POLISH ACADEMY OF SCIENCES
INSTITUTE OF PHYSICS

Established in 1920 by
the Polish Physical Society

ACTA PHYSICA POLONICA

- General Physics
- Atomic and Molecular Physics
- Condensed Matter
- Optics and Quantum Optics
- Quantum Information
- Biophysics
- Applied Physics

Proceedings of the 11th Workshop
on Quantum Chaos
and Localisation Phenomena
Warsaw, Poland, May 25–26, 2023
Online Conference

RECOGNIZED BY THE EUROPEAN
PHYSICAL SOCIETY

Volume 144 — Number 6, Warsaw, December 2023

PL ISSN 0587-4246 ATPLB6 144 (6) 415–504 (2023)

Editor-in-Chief:

Jan Mostowski

Associate Editors:

Anna Ciechan
Elżbieta Guziewicz
Jerzy Pełka
Henryk G. Teisseyre
Łukasz Cywiński
Anna Niedźwiecka
Maciej Sawicki
Andrzej Wawro

Editorial Committee:

Jerzy Kijowski
Jacek Kossut
Andrzej Sobolewski
Maciej Kolwas
Leszek Sirko
Henryk Szymczak

Editorial Council:

Jacek K. Furdyna
Józef Szudy
Ryszard Horodecki
Tadeusz Luty
Jakub Zakrzewski
Karol I. Wysokiński

Managing Editor:

Joanna Pietraszewicz

Executive Editors:

Katarzyna Dug
Marcin Ł. Staszewski

Address of the Publisher:
Instytut Fizyki PAN
al. Lotników 32/46
02-668 Warszawa, Poland
e-mail: appol@ifpan.edu.pl

Printed in Poland:
Drukarnia HAJSTRA Sp. z o.o.
M. Langiewicza 28
05-825 Grodzisk Mazowiecki
drukarnia-hajstra.com
e-mail: hajstra.biuro@gmail.com

POLISH ACADEMY OF SCIENCES
INSTITUTE OF PHYSICS

Established in 1920 by
the Polish Physical Society

ACTA PHYSICA POLONICA

- General Physics
- Atomic and Molecular Physics
- Condensed Matter
- Optics and Quantum Optics
- Quantum Information
- Biophysics
- Applied Physics

Proceedings of the 11th Workshop
on Quantum Chaos
and Localisation Phenomena
Warsaw, Poland, May 25–26, 2023
Online Conference

RECOGNIZED BY THE EUROPEAN
PHYSICAL SOCIETY

Volume 144 — Number 6, Warsaw, December 2023

PL ISSN 0587-4246 ATPLB6 144 (6) 415–504 (2023)

Proceedings of the 11th Workshop on Quantum Chaos and Localisation Phenomena

Warsaw, Poland, May 25–26, 2023
Online Conference

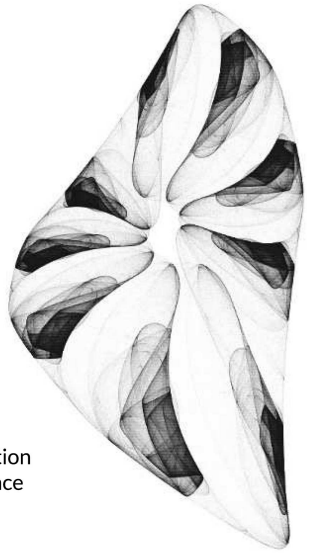

Ministry of Education and Science

PRO PHYSICA

Patronage of Polish Physical Society

Editors of the Proceedings:
Leszek Sirko
Szymon Bauch

WARSAW

POLISH ACADEMY OF SCIENCES
INSTITUTE OF PHYSICS

The Conference was organized by

- Institute of Physics, Polish Academy of Sciences,
- Center for Theoretical Physics, Polish Academy of Sciences,
- Pro Physica Foundation.

Organising Committee

Afshin Akhshani	(IP PAS)
Szymon Bauch	(IP PAS)
Małgorzata Białous	(IP PAS)
Omer Farooq	(IP PAS)
Marek Kuś	(CTP PAS)
Michał Ławniczak	(IP PAS)
Paweł Masiak	(IP PAS)
Adam Sawicki	(CTP PAS)
Leszek Sirko — *Chairman*	(IP PAS)

Objectives

- To assess achievements and to formulate directions of new research on quantum chaos and localisation.
- To bring together prominent experimental and theoretical physicists who share a common interest in quantum chaos and localisation phenomena.

Scope

Presentations will focus on the following topics:

- quantum chaos and nonlinear classical systems,
- quantum and microwave billiards,
- quantum and microwave graphs,
- atoms in strong electromagnetic fields — experiment and theory,
- chaos vs. coherent effects in multiple scattering,
- Anderson localisation,
- random lasers,
- quantum chaos and quantum computing,
- entanglement and noise.

Preface

The 11th Workshop on Quantum Chaos and Localisation Phenomena was held in Warsaw, Poland, on May 25–26, 2023, at the Institute of Physics of the Polish Academy of Sciences. Although the end of the COVID-19 coronavirus pandemic was announced, due to its long-lasting effects and existing threats, the meeting was again fully virtual and took place on the ZOOM platform. The Workshop was organized by the Institute of Physics of the Polish Academy of Sciences, the Center for Theoretical Physics of the Polish Academy of Sciences, and the Foundation "Pro-Physica". The first of these biennial workshops was organized in 2003. Selected articles from the invited lectures, starting from the second Workshop, were published in *Acta Physica Polonica A* [1–9]. The main objectives of the Workshops are to assess achievements and formulate directions for new research on quantum chaos and localisation phenomena.

The Workshop gathered 30 officially registered participants from Afghanistan, China, the Czech Republic, France, Germany, Israel, Poland, Sweden, the United Kingdom, and the USA, representing experimental and theoretical physicists. Additionally, about 20 participants, mainly Ph.D. students and doctors, had the opportunity to join the Workshop via the ZOOM platform. The lectures were also attended by non-registered researchers and Ph.D. students of the Institute of Physics and the Center for Theoretical Physics on the Institute's YouTube channel. During the meeting, 18 invited lectures and 3 posters were presented. The presentations focused on the following topics: quantum chaos and non-linear classical systems, quantum and microwave graphs and billiards, localisation phenomena, topological effects, and physics of low-dimensional systems. In talks and poster presentations, theoretical and experimental problems from various fields of solid state, atomic and molecular, mathematical and statistical physics were discussed. It is noteworthy to mention that although most of the lectures were devoted to the theory of quantum chaos and many-body systems, there were also very interesting new topics, such as topological effects, chiral ensembles, and — for the first time — applications of chaotic systems to modelling metamaterials. The meeting was held online, so scientific discussions that traditionally took place during coffee breaks and social events, this time took place between lectures and during visits to the "rooms" where the posters were displayed.

On behalf of the organizers, we would like to express our gratitude to all the speakers and the authors of poster presentations for their contribution to the success of the Workshop.

We present Proceedings of the 11th Workshop on Quantum Chaos and Localisation Phenomena, in which 11 invited articles of the Workshop participants are published.

The workshop organizers acknowledge the financial support of the Ministry of Education and Science under the program "Doskonała nauka II" under the contract KONF/SN/00702023/01.

Szymon Bauch
Leszek Sirko
Editors of the Proceedings

[1] L. Sirko, S. Bauch, *Acta Phys. Pol. A* **109** (1), (2006)
[2] L. Sirko, S. Bauch, *Acta Phys. Pol. A* **112** (4), (2007)
[3] L. Sirko, S. Bauch, *Acta Phys. Pol. A* **116** (5), (2009)
[4] L. Sirko, S. Bauch, *Acta Phys. Pol. A* **120** (6-A), (2011)
[5] L. Sirko, S. Bauch, *Acta Phys. Pol. A* **124** (6), (2013)
[6] L. Sirko, S. Bauch, *Acta Phys. Pol. A* **128** (6), (2015)
[7] L. Sirko, S. Bauch, *Acta Phys. Pol. A* **132** (6), (2017)
[8] L. Sirko, S. Bauch, *Acta Phys. Pol. A* **136** (5), (2019)
[9] S. Bauch, L. Sirko, *Acta Phys. Pol. A* **140** (6), (2021)

Proceedings of the 11th Workshop on Quantum Chaos and Localisation Phenomena (CHAOS 23)

Control of the Scattering Properties of Complex Systems by Means of Tunable Metasurfaces

J. Erb[a,*], D. Shrekenhamer[b], T. Sleasman[b], T.M. Antonsen[c,d] and S.M. Anlage[a,d]

[a] *Quantum Materials Center, Department of Physics, University of Maryland, College Park, Maryland 20742-4111, USA*
[b] *Johns Hopkins University Applied Physics Laboratory, Laurel, MD, 20723, USA*
[c] *Department of Physics, University of Maryland, College Park, Maryland 20742-4111, USA*
[d] *Department of Electrical and Computer Engineering, University of Maryland, College Park, Maryland 20742-3285, USA*

Doi: 10.12693/APhysPolA.144.421 *e-mail: jmerb@umd.edu

We demonstrate the ability to control the scattering properties of a two-dimensional wave-chaotic microwave billiard through the use of tunable metasurfaces located on the interior walls of the billiard. The complex reflection coefficient of the metasurfaces can be varied by applying a DC voltage bias to varactor diodes on the mushroom-shaped resonant patches, and this proves to be very effective at perturbing the eigenmodes of the cavity. Placing multiple metasurfaces inside the cavity allows us to engineer desired scattering conditions, such as coherent perfect absorption, by actively manipulating the poles and zeros of the scattering matrix through the application of multiple voltage biases. We demonstrate the ability to create on-demand coherent perfect absorption conditions at a specific frequency, and document the near-null of output power as a function of four independent parameters tuned through the coherent perfect absorption point. A remarkably low output-to-input power ratio $P_{\text{out}}/P_{\text{in}} = 3.71 \times 10^{-8}$ is achieved near the coherent perfect absorption point at 8.54 GHz.

topics: coherent perfect absorption (CPA), tunable metasurfaces, scattering zeros and poles

1. Introduction

We consider bounded complex scattering environments, coupled to the outside world through a finite number of scattering channels. Examples include enclosed three-dimensional spaces such as rooms, cabins in a ship or aircraft, or larger enclosed spaces such as warehouses. Other examples include two-dimensional microwave billiards and one-dimensional cable graphs with multiple propagation paths between any two points in the billiard or nodes of the graph. Scattering channels can be coupled to the system through antennas, probes, apertures on the walls of the enclosure, or any means by which wave energy can leave the enclosure and propagate outside it. We assume that these systems are reverberant in the sense that the waves propagate across the length and breadth of the system multiple times before significantly decaying in amplitude. Such systems are characterized by a scattering (S) matrix that relates the set of in-going wave excitations on the channels to the corresponding set of out-going waves on the same channels. Because the scattering environment is complicated and typically lossy, the S-matrix is sub-unitary and has complex matrix elements that are rapid and irregular functions of wave frequency.

The question arises how to control or tame the complex scattering environment so that it can be harnessed to perform specific and useful tasks. Example tasks include establishing and maintaining a robust communication link between two points inside the enclosure, or transferring wave energy to a specific object inside the enclosure with high efficiency and minimal interference. It is our belief that active and tunable metasurfaces can be used to alter the scattering properties of complex structures, thus creating new opportunities to manipulate complex waves. Active metasurfaces have the property that they can alter the reflection coefficient of one portion of the boundary of a scattering environment [1, 2]. This establishes a degree of control of the walls of the enclosure, creating the opportunity to alter the waves everywhere in the enclosure, due to its reverberant nature.

The majority of work on active metasurfaces concerns single-pass reflection or transmission interactions between the waves and the metasurface, or involves metasurface antennas that launch the waves

but do not interact with them again [3]. Here we are concerned with the more challenging situation in which the same waves interact with the same active metasurface multiple times during their propagation. Efforts to control the wave properties of enclosures active and tunable metasurfaces are relatively few in number. Gros et al. [4] showed that three programmable metasurfaces on the walls of a regular six-sided enclosure could be used to effectively stir cavity modes to create a set of uncorrelated cavity configurations. Frazier et al. [5] placed a 240-element tunable binary metasurface inside a 1 m^3 reverberant three-dimensional system, but taking up only 1.5% of the surface area, and demonstrated the ability to create "cold spots" (minima in transmission S_{21}) between two arbitrary points inside the enclosure. That work showed that coherent perfect absorption (CPA) could also be achieved through variation of the metasurface pixel states, as long as the system was already near the CPA condition at the baseline [5]. Earlier, one-port perfect absorption was demonstrated in a reverberant environment using a programmable metasurface [6]. Wavefront shaping with a large number of scattering channels and the creation of CPA states have also been demonstrated in three-dimensional enclosures [7, 8]. The 240-pixel metasurface experiment also utilized a machine learning algorithm that could find the pixel settings on the metasurface required to generate the desired transmission S_{21} spectrum as a function of frequency over a substantial bandwidth [9]. Most recently, an elegant formalism has been created to model the effects of tunable metasurfaces in reverberant environments [10].

The ultimate goal of our experiment is to demonstrate control over all of the scattering parameters of a given microwave billiard system. Often, the functional properties of a cavity are designed into the shape and structure of the cavity, usually including symmetries to help meet the design goals. In our experiments, by contrast, we use a chaotic cavity, which represents the most general wave scattering setting possible, containing no geometrical or hidden symmetries. To gain control over the system, we instead place active metasurfaces inside the cavity, which effectively allow electronic manipulation of the boundary conditions of the cavity. Scattering environments encountered in the real world are usually very complex and lack any symmetries. By demonstrating control over this complex and low-symmetry system, we are moving one step closer to actively controlling the scattering environments of arbitrary real-life systems.

2. Experimental setup

A quasi-two-dimensional wave chaotic quarter bow-tie billiard is loaded with three tunable nonlinear metasurfaces. The billiard has a height of 7.9 mm and an area of 0.115 m^2. Therefore, as long as the cavity is excited at frequencies below approximately 19 GHz, the system supports only one propagating mode, with the electric field polarized in the vertical direction. This billiard has been used before to demonstrate the crossover from Gaussian Orthogonal to Gaussian Unitary ensemble statistics, in both level spacings [11] and eigenfunctions [12, 13], and more recently has been loaded with microwave diodes to act as a reservoir computer [14]. The metasurfaces used in this work were fabricated by the Johns Hopkins University Applied Physics Laboratory [15] and were designed to be used for reflection amplitude variation between 11–18 GHz and reflection phase variation between 14–16 GHz. The metasurfaces are a linear array of 18 varactor-loaded mushroom-shaped resonant elements, where each element is sub-wavelength in size [16]. The PCB material of the metasurfaces is Rogers 5880 and the diode part number is MACOM MAVR-011020-1411. Each metasurface is 1.8 mm thick, 7.9 mm high, and 185 mm long, and is flexible enough to conformally attach to a curved interior wall. The diodes on a given metasurface can be tuned simultaneously with a globally applied DC voltage bias to the metasurface through thin insulated wires that exit the cavity underneath the lid.

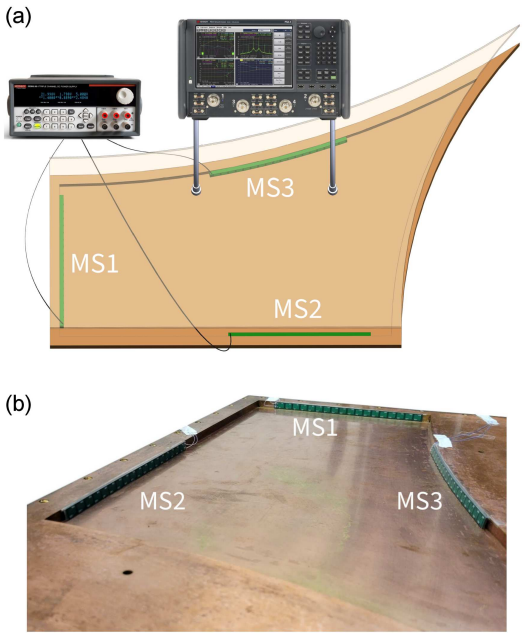

Fig. 1. Quarter bow-tie billiard with three tunable metasurfaces (MS1-3) along the interior walls of the cavity. Panel (a) is a schematic of the quarter bow-tie billiard with the three metasurfaces inside, and the lid lifted off the base. Two antennas are connected to the billiard through the lid and are attached to coaxial transmission lines, representing the scattering channels, and these are connected to the VNA. Panel (b) is a perspective photograph of the interior of the base of the cavity, with the lid removed, showing the three metasurfaces.

As the applied voltage bias increases from 0 to 15 V, the capacitance of the varactor diodes varies from 0.24 to 0.03 pF, thus increasing the resonant frequency of the patches. Note that as the voltage varies, the reflection magnitude and phase of the metasurface changes, in general. Thus, the tuned perturbation has a complex effect on the modes of the cavity. The metasurfaces are placed along three different walls of the billiard and are connected to a Keithley 2230G-30-1 triple channel programmable DC power supply, as shown in Fig. 1. Each of the three metasurfaces cover approximately 12% of the perimeter of the billiard. The quality factor of the billiard with the 3 metasurfaces present is approximately 250 at 9 GHz.

An Agilent Technologies model N5242A or Keysight model N5242B microwave vector network analyzer (VNA) is connected to two ports of the billiard through coaxial cables that support a single mode of propagation, and the 2×2 complex scattering matrix (S) is measured over a chosen frequency range. Through the variation of the reflection coefficient of the metasurfaces, we can manipulate the poles and zeros of the scattering matrix to create conditions for coherent perfect absorption (CPA), among other things. CPA occurs when the zero of the scattering matrix is brought to the real frequency axis [17, 18]. When the system is excited with the S-matrix eigenvector, which corresponds to zero eigenvalue, all of the injected energy is absorbed inside the scattering system and none is reflected or transmitted through any of the scattering channels. The perfect absorption condition requires this very specific type of coherent eigenvector excitation of the billiard, and any deviation causes significant reflection and/or transmission.

CPA requires that the system contain non-zero loss, either in a distributed or localized manner, or both. Waves sent into the system reverberate in such a way as to be completely absorbed, and in addition, so that no energy emerges from any of the ports of the system, either in transmission or reflection. This condition is achieved by exciting all of the ports simultaneously at the (single) CPA frequency, but with appropriate relative amplitudes and phases on the incident waves on all of the ports. With these precise coherent excitation conditions, one can achieve the above-stated outcomes. However, if any of the excitation conditions are modified, the CPA condition is lost — this situation is explored experimentally in detail below. For an arbitrary scattering system, it is very difficult to find coherent excitation conditions for CPA by analytical or numerical methods. We rely on measurements of the scattering matrix and our ability to strongly modify the scattering properties of the cavity using the embedded metasurfaces to establish the CPA conditions. In fact, our approach is so successful that CPA conditions can be established at almost any frequency in the bandwidth of the operation of our experiment.

To establish CPA experimentally, we first choose the frequency range of interest and measure the scattering matrix with the VNA, and with each successive measurement the applied voltage bias of a particular metasurface is increased, usually with a step size of 0.01 V. During a set of measurements, the other metasurfaces in the cavity are held at a fixed applied voltage bias. From this set of measured S-matrices, the complex Wigner–Smith time delay [19] is calculated as a function of frequency at the various applied biases to the metasurface. The conditions for CPA are found by identifying parametric settings where the magnitude of the complex time delay diverges.

Once the conditions for a CPA state are found, the scattering matrix is diagonalized to determine the eigenvalue $\lambda_S = 0 + \mathrm{i}0$ and the corresponding eigenvector $|\psi_{\mathrm{CPA}}\rangle$. For our system, the scattering matrix has two eigenvalues λ_S and eigenvectors $|\psi\rangle$ whose elements are two complex numbers representing the amplitudes of the waves injected at the two ports, but we can determine which one is the CPA excitation by finding the one that has an identically zero eigenvalue. From the CPA eigenvector, the relative amplitude and phase of the required excitation that must be simultaneously injected into the two ports is determined. With this information, the 2-port dual source mode of the VNA is used to inject the CPA eigenvector into the billiard to verify that the conditions for coherent perfect absorption are achieved. For S-parameter measurements, the VNA is calibrated up to the antennas on the billiard. But when the 2-port dual source mode is activated, the calibration is no longer valid. This causes the necessary parameters determining the CPA excitation to be slightly different than those for the calibrated S-parameter measurement. During the CPA injection, we measure the ratio of the outgoing power $P_{\mathrm{out},j}$ to the incident power $P_{\mathrm{in},j}$ on each port j as a function of several parameters near the CPA condition. To do this, the receivers on each VNA port are used to measure both the power that goes into the cavity and the power that comes back out.

3. Complex Wigner–Smith time delay

The Wigner–Smith time delay τ_W is a rough measure of how long a wave lingers in a scattering system before leaving. In unitary systems, the time delay is a real quantity, but for subunitary systems it becomes complex valued [8, 19, 20]. The Wigner–Smith time delay is defined as

$$\tau_W = -\frac{\mathrm{i}}{M}\frac{\partial}{\partial f}\log\left(\det(S)\right), \tag{1}$$

where i is the imaginary number, M is the number of ports connected to the system, f is the frequency, and S is the scattering matrix. Experimentally, the frequency derivative in the Wigner–Smith time delay is calculated using a central difference

formula. It is known that the determinant of S can be written as a Weierstrass factorization extending over the complex frequency plane as [2, 21–28]

$$\det(S(f)) \propto \prod_{n=1}^{N} \frac{f + \mathrm{i}\eta - z_n}{f + \mathrm{i}\eta - \varepsilon_n}, \tag{2}$$

where N is the total number of modes of the closed system, η is the uniform attenuation, and z_n and ε_n are the zeros and poles, respectively, of the scattering matrix. We further define z_n and ε_n as

$$z_n = \mathrm{Re}[z_n] + \mathrm{i}\mathrm{Im}[z_n], \tag{3}$$

$$\varepsilon_n = f_n - \mathrm{i}\Gamma_n, \tag{4}$$

and adopt the convention that $\Gamma_n > 0$ in passive lossy systems. It has been shown [19] that the complex Wigner–Smith time delay associated with each mode n can be written as a sum of two terms for both the real and imaginary parts, one involving the scattering poles and the other the scattering zeros as follows

$$\mathrm{Re}[\tau_W] = \frac{1}{M}\sum_{n=1}^{N}\left[\frac{\mathrm{Im}[z_n] - \eta}{(f - \mathrm{Re}[z_n])^2 + (\mathrm{Im}[z_n] - \eta)^2} + \frac{\Gamma_n + \eta}{(f - f_n)^2 + (\Gamma_n + \eta)^2}\right], \tag{5}$$

$$\mathrm{Im}[\tau_W] = -\frac{1}{M}\sum_{n=1}^{N}\left[\frac{f - \mathrm{Re}[z_n]}{(f - \mathrm{Re}[z_n])^2 + (\mathrm{Im}[z_n] - \eta)^2} - \frac{f - f_n}{(f - f_n)^2 + (\Gamma_n + \eta)^2}\right], \tag{6}$$

Using this formalism, we can see that the Wigner–Smith time delay is divergent at $f = \mathrm{Re}[z_n]$ when the imaginary part of the zero $\mathrm{Im}[z_n]$ of the scattering matrix is equal to the uniform attenuation η of the system. The diverging time delay for the wave propagating inside a lossy system is an indication that the S-matrix zero has crossed the real frequency axis, which is an enabling condition for coherent, perfect absorption [8, 19]. Further, from the measured Wigner–Smith time delay, poles and zeros can be systematically extracted using fits to (5) and (6), and their evolution with the metasurface voltage bias can be visualized. For example, note that the divergent term in the real part of τ_W has a sign that depends on the sign of $\mathrm{Im}[z_n] - \eta$, which changes as the imaginary part of the S-matrix zero is varied. Using information such as this, we can understand how a complex scattering system interacts with incoming waves and use this knowledge to engineer conditions for achieving CPA.

4. Experimental results

For a specific setup of the cavity, we perform measurements in a particular frequency range and voltage bias applied to one of the metasurfaces. Then, the applied bias is swept until the Wigner–Smith time delay shows a near divergence. A typical result

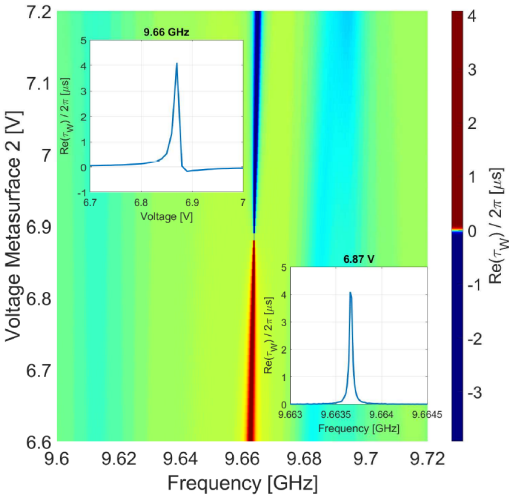

Fig. 2. Real part of the Wigner–Smith time delay $\mathrm{Re}[\tau_W]/(2\pi)$ vs frequency and metasurface $2V$ for a particular cavity realization. We use a nonlinear color scale to help distinguish the areas of small time delay from the areas of very large time delay due to the divergence of the Wigner–Smith time delay at one point in this parameter space. With this color scale, the majority of the colors between blue and red (green–yellow) are concentrated near the mean value of the time delay in this parameter space ($\sim$ 3 ns). The single largest value of the Wigner–Smith time delay measured in this domain has a value of 696.5 μs, but is excluded from this plot for clarity. The Heisenberg time ($\tau_H = 2\pi/\Delta$, with mean mode-spacing $\Delta = c^2/(2\pi f A)$ for this 2D billiard of area A) at 9.66 GHz is $\tau_H \approx 0.49$ μs. Note that τ_W is divided by 2π to convert to seconds. (Left inset) Real Wigner–Smith time delay vs voltage at 9.66 GHz. (Right inset) Real part of Wigner–Smith time delay vs frequency at a fixed voltage of 6.87 V.

is shown in Fig. 2 for the real part of the Wigner–Smith time delay in a narrow range of frequency and voltage. For the mode at 9.66 GHz, the time delay becomes very large in magnitude around the metasurface bias of 6.87 V. This indicates that a CPA state is possibly located at the point of divergence. The left inset of Fig. 2 shows the real part of the time delay as the voltage bias is increased at a fixed frequency of 9.66 GHz, through the point of divergence. The dramatic increase can be explained by the imaginary part of scattering zero ($\mathrm{Im}[z_n]$) decreasing in magnitude toward the value of the uniform attenuation (η) of the system, causing the Wigner–Smith time delay to increase. At the divergence, $\mathrm{Im}[z_n]$ is equal to η, and past the point of divergence, $\mathrm{Im}[z_n]$ has decreased below the value of η, causing the sign of the Wigner–Smith time delay to switch from positive to negative (see (5)). In the right inset of Fig. 2, the voltage is kept fixed at 6.87 V while the frequency increased through the point of divergence. Therefore, a similar increase of

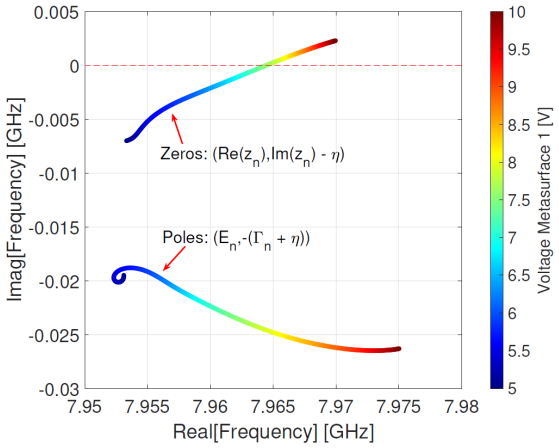

Fig. 3. Zeros and poles of the scattering matrix for a particular mode of the bowtie billiard, extracted from measured complex time delay, plotted in the complex frequency plane as a function of voltage bias applied to metasurface 1. For each successive point from blue to red, the applied bias to metasurface 1 is increased while holding all other parameters fixed. The top curve shows evolution of the S-matrix zero, and the bottom curve shows evolution of the pole.

the real part of the time delay is observed, except that the sign of the Wigner–Smith time delay remains positive through the divergence. The interpretation is that at a fixed voltage bias of 6.87 V, the values of $\mathrm{Im}[z_n]$ and η remain essentially fixed as the frequency is varied, while the divergence arises from the frequency dependence indicated in (5). The variation of $\mathrm{Re}[\tau_W]$ from $+4$ μs to -3.6 μs visible in Fig. 2 occurs diagonally across the frequency and voltage bias because the bias voltage changes both the real and imaginary parts of the S-matrix zero simultaneously.

Using the Wigner–Smith time delay expression as a sum of two terms for the real and imaginary parts, the location of the poles and zeros of the scattering matrix are extracted as functions of applied bias to metasurface 1 for another mode of the bowtie billiard, as shown in Fig. 3. This is accomplished by fitting the Lorentzian expressions (see (5) and (6) for a single mode) to the real and imaginary parts of the experimental data simultaneously, and from the best fitting we extract the pole and zero information of that single mode for each voltage bias. Note that the fit parameters for each mode n are $\mathrm{Re}[z_n]$ and $\mathrm{Im}[z_n] - \eta$ for the zero, and f_n and $\Gamma_n + \eta$ for the pole. Figure 3 shows that as the applied bias is increased, the zeros are observed to move upward in the complex frequency plane toward the real frequency axis, and CPA is enabled at the point where $\mathrm{Im}[z_n] - \eta = 0$. With this information, we now know how to engineer the cavity to have a specific time delay, degree of absorption, etc., for this frequency range.

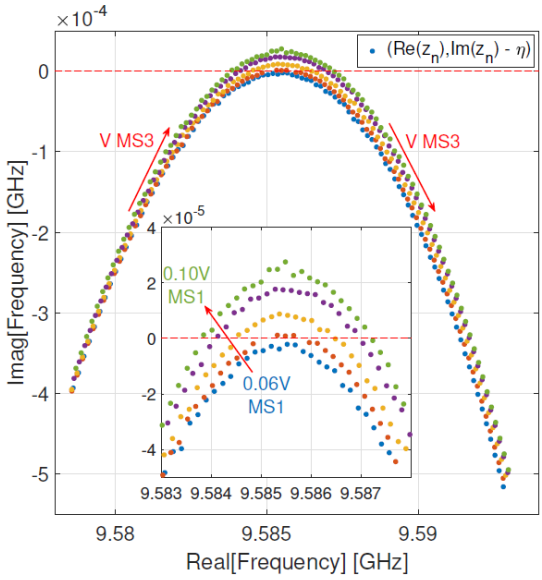

Fig. 4. Zeros of the scattering matrix $(\mathrm{Re}[z_n], \mathrm{Im}[z_n] - \eta)$ for a particular mode of the bowtie billiard, plotted in the complex frequency plane. Each successive point from left to right is a 0.01 V step increase in the voltage applied to metasurface 3 (MS3), and each color represents a different fixed voltage of metasurface 1 (MS1). During these measurements, metasurface 2 was held at a fixed voltage bias. The inset shows a zoomed in view of the real frequency axis near the axis crossings.

Taking measurements of the cavity under different conditions, a particularly interesting case is found where a single mode has a zero that crosses the real axis twice as the voltage bias to metasurface 3 is varied (see Fig. 4). These real frequency-axis crossings for the S-matrix zero correspond to two CPA states in the voltage sweep of one metasurface. Then, using the other two metasurfaces in the cavity, it is possible to raise and lower this parabolic evolution of the zeros in the complex plane, as illustrated in the inset of Fig. 4. This result demonstrates control of the scattering zeros of the system through the additional degrees of freedom that the other metasurfaces offer.

Using the extracted pole and zero locations as a function of voltage, we can use the Lorentzian expression (see (5)) to examine in detail the real part of the Wigner–Smith time delay for one of the curves in Fig. 4. In Fig. 5 we see that there are two locations where the time delay is nearly divergent, and that between the divergences there is a significant peak value of time delay, approximately 9 μs, and its location can be finely tuned in frequency. This delay corresponds to 2.7 km of free space travel, and with the characteristic length scale of the cavity being $\sqrt{A}$ (with cavity area $A = 0.115$ m^2), it corresponds to approximately 8000 bounces around the cavity. It should be noted that at all bias values

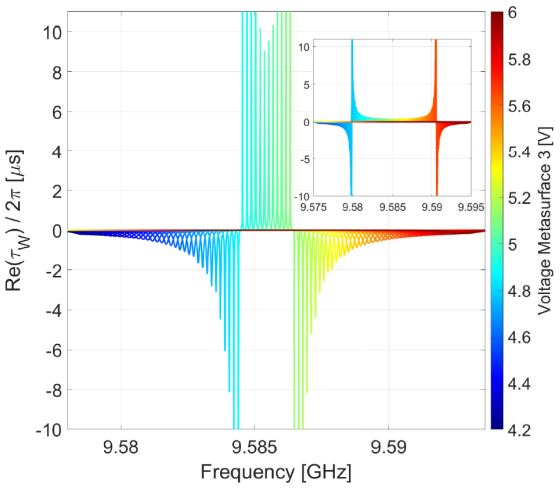

Fig. 5. Real part of the Wigner–Smith time delay $\mathrm{Re}[\tau_W]/2\pi$ vs frequency recovered from a particular curve in Fig. 4 describing the S-matrix zero evolution, and evaluated as a function of frequency using (5). The sign changes of the extreme values of time delay bracket the two CPA points. The lower frequency CPA state has an extreme time delay value around 60 μs, and the upper frequency CPA state has an extreme time delay value near -500 μs, not shown for presentation clarity. The gaps in between the peaks for each color result from the finite metasurface bias voltage resolution of the measurement. The inset shows the real part of Wigner–Smith time delay vs frequency for different fixed values of the metasurface 1 and 2 voltage biases, showing the two CPA points separated by a much larger frequency.

the time delay-bandwidth product is on the order of unity. In Fig. 5, from the inset we can also see that we can move the scattering matrix zeros and push apart the frequencies of the diverging time delay by utilizing other metasurfaces inside the cavity. This also causes the peak time delay between the two zero crossings to decrease.

Once the conditions where the Wigner–Smith time delay diverges are found, we see that the S-matrix has at least one eigenvalue nearly equal to $\lambda_S = 0 + \mathrm{i}0$. We can calculate the eigenvector of the S-matrix corresponding to this eigenvalue. To test for the CPA condition, we must inject this eigenvector excitation into the billiard. The CPA eigenvector can be defined as

$$|\psi_{\mathrm{CPA}}\rangle = \begin{pmatrix} X\,\mathrm{e}^{\mathrm{i}\theta} \\ Y\,\mathrm{e}^{\mathrm{i}\psi} \end{pmatrix}, \tag{7}$$

defining the amplitudes and phases of excitation at the CPA frequency. Hence for CPA excitation, the relative phase of the signal between ports 1 and 2 is $(\psi - \theta)$, and the relative amplitude between ports 1 and 2 is $20\log_{10}\left(\frac{X}{Y}\right)$, when X and Y are measured in linear voltage and need to be converted to dB. The VNA is used to inject this specific excitation into the system at the CPA frequency. The expectation is that the output vector $|\psi_{\mathrm{out}}\rangle = S\,|\psi_{\mathrm{in}}\rangle = 0$ in this case, which means that all of the input energy is perfectly absorbed, and none is reflected or transmitted.

To test this experimentally, we measure both the injected and received powers from the cavity and see how those powers vary as the parameters of the system, and the excitation, are changed. In Fig. 6, the four parameters we have control over are systematically varied to verify that the CPA state is correctly identified. The four parameters are: the voltage applied to the metasurface (which controls the location of the S-matrix zero in the complex frequency plane), the relative amplitudes of the signals on the two input channels, the frequency f, and the relative phase of the signals injected into the two channels. For each parameter sweep, the other parameters are set to their optimal values. We measure the total input power delivered to the system through the two channels, $P_{\mathrm{in}} = P_{\mathrm{in},1} + P_{\mathrm{in},2}$, and the total power that emerges from the cavity, $P_{\mathrm{out}} = P_{\mathrm{out},1} + P_{\mathrm{out},2}$, and form the ratio $P_{\mathrm{out}}/P_{\mathrm{in}}$. This process is carried out in an iterative manner and converges to a point very close to the CPA condition for the system, which corresponds to $P_{\mathrm{out}}/P_{\mathrm{in}} = 0$. For example, in the frequency sweep in Fig. 6c, the ratio of output power to input power changes by approximately seven orders of magnitude for small changes in frequency, with a minimum output to input power ratio of $\frac{P_{\mathrm{out}}}{P_{\mathrm{in}}} = 3.71 \times 10^{-8}$. We observe that the exact conditions of the CPA state slowly drift over time, likely due to temperature fluctuations of the laboratory. We believe this temperature drift to be the limiting factor on how precisely we can measure the CPA state. This illustrates how sensitive the CPA state is to small perturbations to the system, making it attractive for use as a sensor.

5. Discussion

Much of the prior work to controllably alter the scattering matrix of complex systems has been done by mechanical means, mainly for the purpose of perturbing the poles of the scattering matrix [29]. With metasurfaces, the poles and zeros of the scattering matrix can be smoothly varied in the complex frequency plane and placed in determined locations, purely by electronic means. By moving the zero of the scattering matrix to the real frequency axis, we can enable CPA and this is correspondingly seen as a divergence in the real part of the Wigner–Smith time delay. We can inject the zero-eigenvalue eigenvector and observe nearly complete absorption, but this is a singular condition that is only possible at a single point in the parameter space. Suwunnarat et al. [30] have recently shown the creation of a nonlinear CPA by using exceptional point degeneracies of the zeros of the scattering matrix. Work such

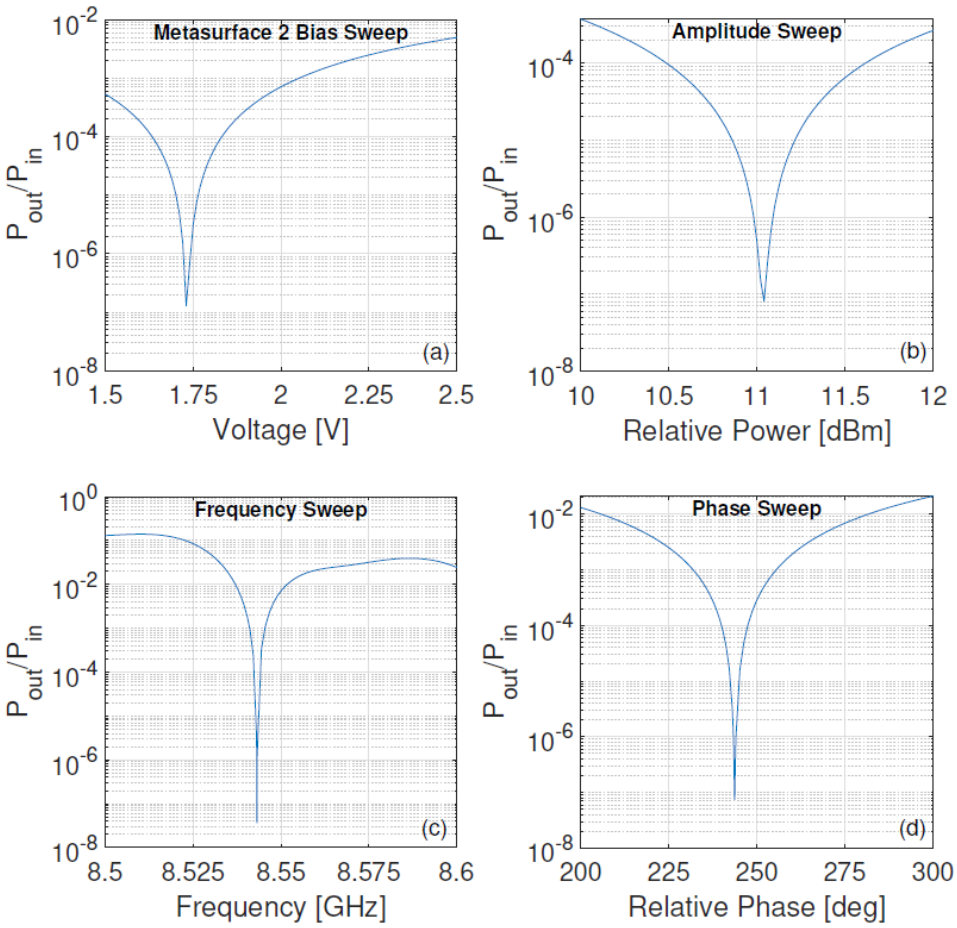

Fig. 6. Evidence of coherent perfect absorption in the ray-chaotic quarter bow-tie microwave billiard, for four independent parametric sweeps. We measure the ratio of the total output power to the total input power, $P_{\text{out}}/P_{\text{in}}$ as a function of parameter variation. The swept voltage bias to metasurface 2 is shown in (a). Small parametric deviations from the CPA input eigenvector $|\psi_{\text{CPA}}\rangle$ are made through the relative power $20\log_{10}\left(\frac{X}{Y}\right)$ (b), frequency (c), and relative phase $(\psi - \theta)$ (d) sweeps.

as [30] shows future possibilities of creating larger parametric regions of coherent near-perfect absorption, which can be beneficial for a variety of applications in communications and wireless power transfer.

6. Conclusions

In this paper, we show that using tunable metasurfaces inside a two-dimensional wave-chaotic cavity, we can control the locations of the scattering poles and zeros in the complex frequency plane. By perturbing the system with metasurfaces, we can drag the scattering zeros across the real frequency axis to create a coherent perfect absorption condition. The demonstration of nearly complete absorption is illustrated in Fig. 6, by having approximately seven orders of magnitude less power leaving the system compared to that injected in the CPA eigenvector. We also demonstrated precise manipulation of the location of the CPA state by applying voltage biases to other metasurfaces in the cavity. This is equivalent to controlling the scattering properties of the system, and this control gives us the ability to engineer specific conditions in the cavity, such as having coherent perfect absorption at a particular frequency, tuning a desired time delay for a signal, having regions of high absorption for unwanted signals, and low absorption for desired signals, etc.

Acknowledgments

We acknowledge insightful discussions with Tsampikos Kottos, Dan Sievenpiper, and Lei Chen. This work was supported by NSF/RINGS under grant No. ECCS-2148318, ONR under grant N000142312507, ONR under grant N0002413D6400, DARPA WARDEN under grant HR00112120021, ONR DURIP FY21 under grant N000142112924, and ONR DURIP FY22 under grant N000142212263.

References

[1] H.T. Chen, A.J. Taylor, N. Yu, *Rep. Prog. Phys.* **79**, 076401 (2016).

[2] M. Elsawy, C. Kyrou, E. Mikheeva, R. Colom, J.-Y. Duboz, K. Zangeneh Kamali, S. Lanteri, D. Neshev, P. Genevet, *Laser Photon. Rev.* **17**, 2200880 (2023).

[3] M. Faenzi, G. Minatti, D. GonzÍaez-Ovejero, F. Caminita, E. Martini, C. Della Giovampaola, S. Maci, *Sci. Rep.* **9**, 10178 (2019).

[4] J.-B. Gros, P. del Hougne, G. Lerosey, *Phys. Rev. A* **101**, 061801 (2020).

[5] B.W. Frazier, T.M. Antonsen, S.M. Anlage, E. Ott, *Phys. Rev. Research* **2**, 043422 (2020).

[6] M.F. Imani, D.R. Smith, P. del Hougne, *Adv. Funct. Mater.* **30**, 2005310 (2020).

[7] P. del Hougne, K. Brahima Yeo, P. Besnier, M. Davy, *Phys. Rev. Lett.* **126**, 193903 (2021).

[8] P. del Hougne, K. Brahima Yeo, P. Besnier, M. Davy, *Laser Photon. Rev.* **15**, 2000471 (2021).

[9] B.W. Frazier, T.M. Antonsen, S.M. Anlage, E. Ott, *Phys. Rev. Appl.* **17**, 024027 (2022).

[10] R. Faqiri, C. Saigre-Tardif, G.C. Alexandropoulos, N. Shlezinger, M.F. Imani, P. del Hougne, *IEEE Trans. Wireless Commun.* **22**, 580 (2023).

[11] P. So, S.M. Anlage, E. Ott, R.N. Oerter, *Phys. Rev. Lett.* **74**, 2662 (1995).

[12] D.H. Wu, J.S.A. Bridgewater, A. Gokirmak, S.M. Anlage, *Phys. Rev. Lett.* **81**, 2890 (1998).

[13] S.H. Chung, A. Gokirmak, D.H. Wu, J.S.A. Bridgewater, E. Ott, T.M. Antonsen, S.M. Anlage, *Phys. Rev. Lett.* **85**, 2482 (2000).

[14] S. Ma, T.M. Antonsen, S.M. Anlage, E. Ott, *Phys. Rev. Research* **4**, 023167 (2022).

[15] T. Sleasman, R. Duggan, R.S. Awadallah, D. Shrekenhamer, *Phys. Rev. Appl.* **20**, 014004 (2023).

[16] D. Sievenpiper, Z. Lijun, R.F.J. Broas, N.G. Alexopolous, E. Yablonovitch, *IEEE Trans. Microw. Theory Tech.* **47**, 2059 (1999).

[17] Y.D. Chong, L. Ge, H. Cao, A.D. Stone, *Phys. Rev. Lett.* **105**, 053901 (2010).

[18] L. Chen, T. Kottos, S.M. Anlage, *Nat. Commun.* **11**, 5826 (2020).

[19] L. Chen, S.M. Anlage, Y.V. Fyodorov, *Phys. Rev. E* **103**, L050203 (2021).

[20] M. Asano, K.Y. Bliokh, Y.P. Bliokh, A.G. Kofman, R. Ikuta, T. Yamamoto, Y.S. Kivshar, L. Yang, N. Imoto, ŞK. Ozdemir, F. Nori, *Nat. Commun.* **7**, 13488 (2016).

[21] V.V. Sokolov, V.G. Zelevinsky, *Nucl. Phys. A* **504**, 562 (1989).

[22] Y.V. Fyodorov, H.J. Sommers, *J. Math. Phys.* **38**, 1918 (1997).

[23] Y.V. Fyodorov, D.V. Savin, in: *The Oxford Handbook of Random Matrix Theory*, Eds. G. Akemann, J. Baik, P. Di Francesco, Oxford University Press, Oxford 2011, chap. 34, p. 703.

[24] U. Kuhl, O. Legrand, F. Mortessagne, *Fortschr. Phys.* **61**, 404 (2013).

[25] V. Grigoriev, A. Tahri, S. Varault, B. Rolly, B. Stout, J. Wenger, N. Bonod, *Phys. Rev. A* **88**, 011803 (2013).

[26] V. Grigoriev, S. Varault, G. Boudarham, B. Stout, J. Wenger, N. Bonod, *Phys. Rev. A* **88**, 063805 (2013).

[27] H. Schomerus, in: *Stochastic Processes and Random Matrices: Lecture Notes of the Les Houches Summer School*, Vol. 104, Oxford University Press, Oxford 2017, chap. 10, p 409.

[28] R. Colom, E. Mikheeva, K. Achouri, J. Zuniga-Perez, N. Bonod, O.J.F. Martin, S. Burger, P. Genevet, *Laser Photon. Rev.* **17**, 2200976 (2023).

[29] B. Dietz, A. Heine, A. Richter, O. Bohigas, P. Leboeuf, *Phys. Rev. E* **73**, 035201 (2006).

[30] S. Suwunnarat, Y. Tang, M. Reisner, F. Mortessagne, U. Kuhl, T. Kottos, *Commun. Phys.* **5**, 5 (2022).

Proceedings of the 11th Workshop on Quantum Chaos and Localisation Phenomena (CHAOS 23)

Berezinskii Approach to Disordered Spin Systems with Asymmetric Scattering and Application to the Quantum Boomerang Effect

J. Janarek[a], N. Cherroret[b,*] and D. Delande[b]

[a] *Instytut Fizyki Teoretycznej, Uniwersytet Jagielloński, Łojasiewicza 11, PL-30-348 Kraków, Poland*
[b] *Laboratoire Kastler Brossel, Sorbonne Université, CNRS, ENS-PSL Research University, Collège de France, 4 Place Jussieu, 75005 Paris, France*

Doi: 10.12693/APhysPolA.144.429 *e-mail: nicolas.cherroret@lkb.upmc.fr

We extend the Berezinskii diagrammatic technique to one-dimensional disordered spin systems, in which time-reversal invariance is broken due to a spin–orbit coupling term inducing left–right asymmetric scattering. We then use this formalism to theoretically describe the dynamics of the quantum boomerang effect, a recently discovered manifestation of Anderson localization. The theoretical results are confirmed by exact numerical simulations of wave-packet dynamics in a random potential.

topics: Anderson localization, disorder scattering, spin–orbit coupling, quantum wave packets

1. Introduction

In the presence of a spatially disordered potential, quantum wave packets may experience, after a transient temporal spreading, a complete freezing of their density distribution due to the proliferation of destructive interference in the multiple scattering process. This phenomenon, which generically occurs in low dimensions, is one of the most representative manifestations of Anderson localization [1]. As such, it has been primarily exploited in the experimental quest for the localization of cold atoms in random potentials [2–5]. Recently, however, a variety of alternative signatures of Anderson localization has been identified. Those include the temporal freezing of the coherent backscattering effect in reciprocal space [6–8] or the universal growth of narrow peak structures in the density profile [9, 10] and momentum distribution [11–13] of spreading wave packets (see [14] for a review).

Recently, yet another unexpected manifestation of Anderson localization, dubbed the quantum boomerang effect (QBE), has been discovered [15]. QBE corresponds to a back-and-forth motion of the mean position of a quantum wave packet launched with a finite velocity in a given direction in a random potential. In one dimension, for instance, if the quantum particle is launched to the right, it will first move to the right over a distance of the order of the mean free path, then make a U-turn and eventually return to its starting point at long time. This phenomenon was also shown to exist in higher-dimensional random or pseudo-random systems [15, 16], as well as in kicked-rotor models [16], where it was recently demonstrated experimentally [17]. While originally described in time-reversal-invariant (TRI) systems, recently QBE was also shown to exist in systems without time-reversal symmetry [18–20]. In [18], in addition, QBE was characterized in the presence of a spin–orbit coupling mechanism inducing left–right asymmetric scattering between different spin states. This is also the scenario addressed in the present paper.

At a theoretical level, describing the temporal dynamics of quantum wave packets in the presence of disorder is a challenging task [21–23]. In one dimension, however, a very powerful analytical approach known as the Berezinskii diagrammatic technique has been developed [24]. Originally, this method was successfully used for calculating the ac conductivity of electronic conductors in the localization regime or the long-time density distribution of spreading wave packets [24–26], the predictions being exact in the limit of weak disorder. More recently, it also allowed the description of QBE in TRI systems [15] and, in the context of electron scattering, was extended to account for the presence of spin–orbit coupling [27].

In this paper, we extend the Berezinskii diagrammatic technique to TRI-broken spin-dependent systems in which a spin–orbit coupling term

induces asymmetric scattering, as recently realized experimentally with cold atoms [28, 29]. This formalism is developed in Sects. 2 and 3. In Sect. 4, we then apply the method to the calculation of a specific observable, namely the mean position of a quantum-mechanical wave packet launched in a random potential with finite velocity. This provides a thorough theoretical description of QBE in spin–orbit coupled systems with asymmetric scattering, complementing results obtained in the recent work [18]. Generally speaking, the formalism presented in this paper provides a practical analytical tool to characterize the dynamics of spinor wave packets in disordered systems with TRI-broken symmetry.

2. Principles of the Berezinskii technique

We start by recalling the main ideas of the original Berezinskii diagrammatic technique used to compute the time-dependent transport properties of one-dimensional disordered systems. The starting point is the single-particle Hamiltonian

$$H = H_0 + V(x), \tag{1}$$

where $V(x)$ is a random (disorder) potential and H_0 is the disorder-free part of the Hamiltonian (e.g., $H_0 = p^2/(2m)$). We suppose that the random potential has a vanishing mean, $\overline{V(x)} = 0$, and follows Gaussian statistics characterized by the two-point correlation function $\overline{V(x)V(x')} = \eta C(x' - x)$, where η is called the disorder strength. Symbol $\overline{(\ldots)}$ here denotes averaging over different disorder realizations. The function $C(x' - x)$ quantifies the range of the spatial correlation of the disorder. In the whole paper, we restrict ourselves to a delta-correlated potential, i.e., $C(x' - x) = \delta(x' - x)$.

In this paper, we aim at describing the time evolution of quantum-mechanical wave packets governed by an Hamiltonian of the type of (1). In the localization problem, this evolution is characterized by considering the disorder-average of observables that depend quadratically on the wave function, such as the density $n(x,t)$ or the mean position $\langle x(t)\rangle = \int \mathrm{d}x \; x\, n(x,t)$ of the wave packet. These observables, by definition, can be expressed in terms of the disorder-averaged correlator $\overline{G^R(x,x',\epsilon)G^A(x'',x,\epsilon-\hbar\omega)}$ [30, 31], where $G^{R/A}(x,x',\epsilon) \equiv \langle x|\left(\epsilon - H \pm \mathrm{i}0^+\right)^{-1}|x'\rangle$ are the single-realization, retarded and advanced Green's functions at energy ϵ associated with Hamiltonian (1). The energy difference $\hbar\omega$ introduced in the correlator allows us to capture the time dependence of observables after an inverse Fourier transform. The precise connection between $\langle x(t)\rangle$ and the Green's function correlator, for instance, will be given in Sect. 3.

Both Green's functions $G^{R/A}$ that appear in the correlator may be computed in a perturbative fashion using the Born expansion [30]

$$\begin{aligned} G^{R/A}(x,x',\epsilon) &= G_0^{R/A}(x,x',\epsilon) \\ &+ \int \mathrm{d}x_1 \; G_0^{R/A}(x,x_1,\epsilon)V(x_1)G_0^{R/A}(x_1,x',\epsilon) \\ &+ \int \mathrm{d}x_1\,\mathrm{d}x_2 \; G_0^{R/A}(x,x_1,\epsilon)V(x_1)G_0^{R/A}(x_1,x_2,\epsilon) \\ &\quad \times V(x_2)G_0^{R/A}(x_2,x',\epsilon) + \ldots, \end{aligned} \tag{2}$$

where

$$G_0^{R/A}(x,x',\epsilon) \equiv \langle x|\left(\epsilon - H_0 \pm \mathrm{i}0^+\right)^{-1}|x'\rangle \tag{3}$$

are the retarded and advanced Green's functions associated with the free part of the Hamiltonian. Physically, the expansion (2) describes a multiple scattering sequence involving scattering events on the random potential at points x_1, x_2, ….

As for the case of the average product $\overline{G^R(x,x',\epsilon)G^A(x'',x,\epsilon-\hbar\omega)}$, it includes all possible correlations between two multiple scattering paths starting at the initial points x' and x'', respectively, and both ending at the final point x. The starting point of the Berezinskii technique is to take advantage of the one-dimensional geometry, which enables us to order the scattering events on a line

$$-\infty < x_1 \le \ldots \le x' \le \ldots \le x \le \ldots \le x_i < \infty. \tag{4}$$

Thanks to this ordering, each contribution to the product $G^R G^A$ may be represented by a diagram, like the one shown in Fig. 1a [24], which combines a retarded (solid lines) and an advanced (dashed lines) multiple scattering sequence, respectively unfolded in the upper and lower parts of the diagram. The scattering events occur at the points x_i. In the example of Fig. 1a, the upper sequence involves 8 scattering events (twice at point x_3), and the lower one — 7 scattering events.

The diagrams effectively contributing to Green's function correlator $\overline{G^R G^A}$ do not have arbitrary shapes. Indeed, because of the assumed Gaussian statistics and the corresponding Wick's theorem, only diagrams whose scattering events can all be paired appear. For instance, the diagram in Fig. 1a vanishes upon averaging because some scattering events cannot be paired. Pairing scattering events at different points would occur in the case of a weakly correlated disorder (for which the correlation length is smaller than the mean free path), a problem previously addressed in [25, 26, 32].

The second important approximation of the Berezinskii technique is to assume that among all possible diagrams contributing to the correlator, only those for which the phase factors induced by free-particle Green functions exactly compensate each other when $\omega \to 0$ matter. This approximation, which holds true in the regime of "weak disorder" (see Sect. 3.3), amounts to imposing that there is exactly the same number of retarded and advanced Green's function in between any two successive scattering events x_i and x_{i+1}. In turn, this yields restrictions on the possible *scattering vertices*, which are building blocks of the

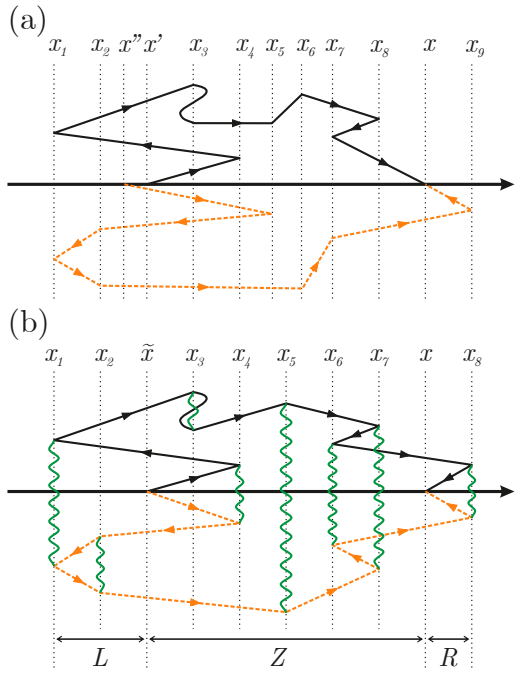

Fig. 1. (a) Example of diagram involved in the product $G^R(x,x',\epsilon)G^A(x'',x,\epsilon-\hbar\omega)$ computed from the Born expansion (2). Solid lines represent free retarded Green's functions G_0^R, and dashed lines — free advanced Green's functions G_0^A. Scattering events occur at points x_i. (b) Example of non-vanishing contribution to the correlator $\overline{G^R(x,\tilde{x},\epsilon)G^A(\tilde{x},x,\epsilon-\hbar\omega)}$. The wavy lines refer to a two-point correlation function of the random potential. At each scattering event, one finds a vertex belonging to the set presented in Fig. 3. The correlation diagram can be divided into three blocks L, Z, and R, separated by the points $\tilde{x}$ and x.

diagrams — aside from the trivial constraint that the solid/dashed lines have to be continuous, all vertices have to be phaseless.

With these conditions implemented, the Berezinskii diagrammatic technique provides a strategy to exactly sum all possible diagrams with nonzero contributions, as we will now detail for the case of a spin–orbit Hamiltonian H_0.

3. Diagrammatic approach without time-reversal symmetry

3.1. Free Hamiltonian and Green's function

In this work, we extend the standard Berezinskii technique to a one-dimensional spin system with spin–orbit coupling and Zeeman splitting breaking all anti-unitary time-reversal symmetries [18, 28, 29]. The corresponding disorder-free Hamiltonian reads

$$H_0 = \frac{\hbar^2 k^2}{2m} + \gamma\hbar k\sigma_z + \frac{\hbar\delta}{2}\sigma_z + \frac{\hbar\Omega}{2}\sigma_x, \qquad (5)$$

where σ_i are the usual Pauli matrices. The Hilbert space is spanned by two-dimensional complex-valued spinors. Further, γ is the strength of the spin–orbit coupling, Ω is the Rabi frequency, and δ is the detuning. Diagonalization of the Hamiltonian H_0 yields two energy bands denoted by $\pm$ with corresponding energies

$$E_\pm(k) = \frac{\hbar^2 k^2}{2m} \pm \frac{\hbar}{2}\sqrt{(2\gamma k+\delta)^2 + \Omega^2}. \qquad (6)$$

Due to this band structure, for a given energy ϵ, the Hamiltonian hosts either 2 or 4 possible eigenstates. From now on, we focus on the case where only two eigenstates are involved, which corresponds to a dynamics operating at energies belonging to the lower band only [18]. We denote by $k_\pm$ the momenta of these two states, and by $v_\pm = \frac{1}{\hbar}|\mathrm{d}E_-(k_\pm)/\mathrm{d}k|$ the associated velocities. As compared to the standard single-particle Hamiltonian $\tilde{H}_0 = p^2/(2m)$, it should be noted that the two involved momenta are not just of opposite sign, i.e., $k_- \neq -k_+$ (and, correspondingly, $v_- \neq v_+$). The left–right symmetry is therefore broken, which, as will be seen below, constitutes the most significant difference as compared to the usual Berezinskii approach. In [27], a much simpler situation was studied, where only the spin–orbit interaction is present (i.e., $\delta = \Omega = 0$); in such a case, the dispersion relation is symmetric with respect to $k \to -k$, so that $v_- = v_+$, and the extension of the Berezinskii technique is rather easy. In contrast, the calculations presented in the present paper are more general and valid when (generalized) TRI is broken.

In the diagrammatic treatment of disorder scattering introduced in the previous section, a fundamental ingredient is the free Green's function (3), which we need to evaluate for the Hamiltonian (5). To this aim, we use the definition

$$G_0^R(x,x',\epsilon) \equiv \int_{-\infty}^{\infty} \frac{\mathrm{d}k}{2\pi}\, \frac{\mathrm{e}^{\mathrm{i}k(x-x')}}{\epsilon - E_-(k) + \mathrm{i}0^+}. \qquad (7)$$

A careful calculation of the integral in momentum space provides us with

$$G_0^R(x,x',\epsilon) = \begin{cases} -\frac{\mathrm{i}}{\hbar v_+}\mathrm{e}^{\mathrm{i}k_+(x-x')}, & x-x'>0, \\ -\frac{\mathrm{i}}{2\hbar}\left(\frac{1}{v_+}+\frac{1}{v_-}\right), & x=x', \\ -\frac{\mathrm{i}}{\hbar v_-}\mathrm{e}^{\mathrm{i}k_-(x-x')}, & x-x'<0, \end{cases} \qquad (8)$$

where, in particular, the diagonal value $G_0^R(x,x,\epsilon)$ is obtained by properly accounting for all the real and complex poles in the denominator in (7). Note that, strictly speaking, when $x-x' \neq 0$, these expressions only hold at distances $|x-x'|$ larger than the de Broglie wavelength $2\pi/|k_\pm|$. This knowledge, however, is sufficient within the weak disorder limit (see (15) given in Sect. 3.3) where the Berezinskii approach operates. Because of translation invariance, the free Green's function $G_0^R(x,x',\epsilon) = G_0^R(x-x',\epsilon)$. Its Fourier transform is therefore

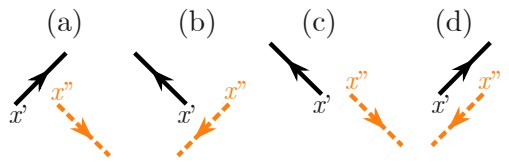

Fig. 2. List of all possible initial vertices. In the limit $\omega \to 0$ they correspond to the factors (a) $(\hbar v_+)^{-1}\,\mathrm{e}^{\mathrm{i}\,k_+(x''-x')}$, (b) $(\hbar v_-)^{-1}\,\mathrm{e}^{\mathrm{i}\,k_-(x''-x')}$, (c) $(\hbar^2 v_- v_+)^{-1/2}\,\mathrm{e}^{\mathrm{i}\,(k_+x''-k_-x')}$, and (d) $(\hbar^2 v_- v_+)^{-1/2}\,\mathrm{e}^{\mathrm{i}\,(k_-x''-k_+x')}$.

diagonal in momentum space, with the diagonal value defined as $G_0^R(k,\epsilon)=\int \mathrm{d}r\,\mathrm{e}^{-\mathrm{i}kr}G_0^R(r,\epsilon)$, where $r=x-x'$. Note that with this definition, (8) implies that $G^{R/A}(k,\epsilon) \neq G^{R/A}(-k,\epsilon)$, contrary to TRI systems. From (8), finally, the advanced Green's function follows from Hermitian conjugation, $G_0^A(x,x',\epsilon) = [G_0^R(x',x,\epsilon)]^*$.

In the following, we will also need the energy-shifted Green's function $G_0^A(x',x,\epsilon-\hbar\omega)$, where $\omega \ll \epsilon/\hbar$. To evaluate this object, we use the Taylor expansions $k_\pm(\epsilon-\hbar\omega) \approx k_\pm \mp \omega/v_\pm$, so that

$$G_0^A(x',x,\epsilon-\hbar\omega) = \begin{cases} \frac{\mathrm{i}}{\hbar v_+}\,\mathrm{e}^{-\mathrm{i}\,(k_+-\omega/v_+)(x-x')}, & x-x'>0, \\ \frac{\mathrm{i}}{2\hbar}\left(\frac{1}{v_+}+\frac{1}{v_-}\right), & x=x', \\ \frac{\mathrm{i}}{\hbar v_-}\,\mathrm{e}^{-\mathrm{i}\,(k_-+\omega/v_-)(x-x')}, & x-x'<0. \end{cases} \quad (9)$$

3.2. Mean free times

Before constructing the diagrammatic approach based on the Hamiltonian $H_0+V(x)$, let us introduce a few important scattering parameters that will be used in the following. The central one is the concept of scattering mean free time, which gives the average time scale between two consecutive scattering events. In the present case, however, two different mean free paths can be defined due to the left–right asymmetry. To find them, let us denote by $|\pm\rangle = |k_\pm\rangle \otimes |\chi_\pm\rangle$ the two eigenstates of H_0, where $|\chi_+\rangle$ and $|\chi_-\rangle$ are the spin state components associated with the wave numbers k_+ and k_-, respectively. This leads us to define τ_+ and τ_-, the scattering mean free times for the processes $|+\rangle \to |-\rangle$ and $|-\rangle \to |+\rangle$, respectively. At weak disorder, they can be evaluated from the Fermi golden rule

$$\frac{1}{\tau_\pm} = \frac{2\pi}{\hbar}\,\overline{\left|\langle\mp|V|\pm\rangle\right|^2}\,\rho\big(E_-(k_\mp)\big), \quad (10)$$

where $\rho(E_-(k_\mp))$ is the density of states evaluated at the energy $E_-(k_\mp)$ of the final state. Using the fact that the disorder is uncorrelated, i.e., $\overline{V(x')V(x)} = \eta\,\delta(x'-x)$ (see Sect. 2), we infer

$$\tau_\pm = \frac{\hbar^2 v_\mp}{2\eta\kappa}, \quad (11)$$

where $\kappa \equiv |\langle\chi_+|\,|\chi_-\rangle|^2$ is the overlap factor of the two spin states. In the following, we will be also led to use the mean free time associated with the weighted sum of the two scattering processes

$$\frac{1}{\tau} = \frac{1}{2}\left(\frac{1}{\tau_+}+\frac{1}{\tau_-}\right), \quad (12)$$

which turns out to be the relevant time scale governing the boomerang effect, as will be shown in Sect. 4. Note that the validity of the Fermi golden rule used above is only guaranteed in the weak disorder limit described in Sect. 3.3 by (15).

3.3. Vertices

At the core of the Berezinskii diagrammatic technique is the idea of transferring the propagating factors from the free Green's functions to the scattering events, called vertices. For example, assuming $x_i > x_j$, the free Green's function can be split as

$$G_0^R(x_i,x_j,\epsilon) = \sqrt{-\frac{\mathrm{i}}{\hbar v_+}}\,\mathrm{e}^{\mathrm{i}\,k_+x_i}\sqrt{-\frac{\mathrm{i}}{\hbar v_+}}\,\mathrm{e}^{-\mathrm{i}\,k_+x_j}, \quad (13)$$

where we formally associate the weights and exponential factors to the vertices at points x_i and x_j. The difference between the TRI system and the TRI-broken case is that these factors depend on the direction of propagation. For example, in the TRI system, the opposite case $x_j > x_i$ would result in just a change of sign of the phase factors in (13), whereas in the system with broken TRI, the velocities also change.

Initial vertices. We start by selecting the relevant initial vertices effectively contributing to the correlator $\overline{G^R(x,x',\epsilon)G^A(x'',x,\epsilon-\hbar\omega)}$. In general, scattering paths may start from any of the 4 vertices shown with their weights in Fig. 2. The vertices with advanced and retarded lines starting into opposite directions, i.e., vertices c and d, carry exponential factors with phases $\mathrm{i}(k_\pm x''-k_\mp x')$. Upon integration over the starting points x' and x'' (see (29) in Sect. 4.1), they typically yield negligible contributions. Thus, we can restrict the analysis to only two classes of initial vertices — a and b. These classes, in turn, correspond to two different types of initial states for the dynamics: (a) with positive (v_+) and (b) with negative (v_-) initial velocity.

A second simplification is based on the assumption that no scattering happens between the initial points x' and x'' [15, 33]. This invites us to introduce the Wigner variables $r = x'-x''$ and $\tilde{x} = (x'+x'')/2$. In the limit $\omega \to 0$, vertices a and b are thus approximated by their counterparts starting from a single point $\tilde{x}$. At the level of Green's functions, this simplification reads [26]

$$\overline{G^R(x,x',\epsilon)G^A(x'',x,\epsilon-\hbar\omega)} \approx \mathrm{e}^{-\mathrm{i}\,k_\epsilon r}\,\overline{G^R(x,\tilde{x},\epsilon)G^A(\tilde{x},x,\epsilon-\hbar\omega)}, \quad (14)$$

where k_ϵ is the wave number satisfying the dispersion relation $\epsilon = E_-(k_\epsilon)$.

Phaseless scattering vertices. Our ultimate goal is to sum all significant contributions to the product of Green's functions $\overline{G^R G^A}$. This formidable task is, in general, out of reach except for the so-called weak-disorder limit

$$k_\epsilon \ell \gg 1, \tag{15}$$

where $\ell = \tau_+ v_+ = \tau_- v_-$ is the scattering mean free path (see also Sect. 3.1). Under this condition, only a limited set of scattering vertices that do not accumulate any phase and, as such, are not vanishingly small upon disorder averaging, should be considered when constructing correlation diagrams. The procedure to identify this set is detailed in Appendix A for clarity. It yields four families of vertices that are listed in Fig. 3. One can easily check that the phase associated with each vertex is zero. For instance, the vertex a_1 originates from a factor of the type $\eta G_0^R(x_i, x_{i-1}) G_0^R(x_i, x_i) G_0^R(x_{i+1}, x_i)$ in the disorder-average of the Born expansion (2). With the help of the splitting procedure (13) and of (8), this corresponds to a vertex weight

$$\eta \sqrt{\frac{-\mathrm{i}}{\hbar v_+}}\, \mathrm{e}^{\mathrm{i} k_+ x_i} \times \frac{-\mathrm{i}}{2\hbar}\left(\frac{1}{v_+}+\frac{1}{v_-}\right) \times \sqrt{\frac{-\mathrm{i}}{\hbar v_+}}\, \mathrm{e}^{-\mathrm{i} k_+ x_i}, \tag{16}$$

whose phase is indeed zero. In turn, the weights of all phaseless scattering vertices are

$$\begin{aligned}
&\mathrm{a}_{1/2}\text{:} && -\frac{\eta}{2\hbar^2 v_\pm}\left(\frac{1}{v_+}+\frac{1}{v_-}\right),\\
&\mathrm{b}_{1/2}\text{:} && -\frac{\eta}{(\hbar v_\pm)^2},\\
&\mathrm{b}_3\text{:} && -\frac{\eta}{(\hbar v_+)(\hbar v_-)},\\
&\mathrm{c}\text{:} && -\frac{\eta\kappa}{(\hbar v_+)(\hbar v_-)},\\
&\mathrm{d}_{1/2}\text{:} && \frac{\eta}{(\hbar v_\pm)^2},\\
&\mathrm{d}_{3/4}\text{:} && \frac{\eta}{(\hbar v_+)(\hbar v_-)},\\
&\mathrm{e}\text{:} && \frac{\eta\kappa}{(\hbar v_+)(\hbar v_-)} \exp\left[\mathrm{i}\omega x\left(\frac{1}{v_+}+\frac{1}{v_-}\right)\right],\\
&\mathrm{f}\text{:} && \frac{\eta\kappa}{(\hbar v_+)(\hbar v_-)} \exp\left[-\mathrm{i}\omega x\left(\frac{1}{v_+}+\frac{1}{v_-}\right)\right].
\end{aligned} \tag{17}$$

Notice that among all diagrams in Fig. 3, the vertices families c, e, and f involve a "backscattering event" in both the retarded and advanced parts. This implies that, in the spin system described by Hamiltonian (5), the associated weights include the spin-state overlap factor $\kappa = |\langle\chi_+|\,|\chi_-\rangle|^2$.

3.4. Correlation diagrams

Knowing all possible phaseless scattering vertices relevant to our problem, we now wish to write down the equations describing the diagrams contributing

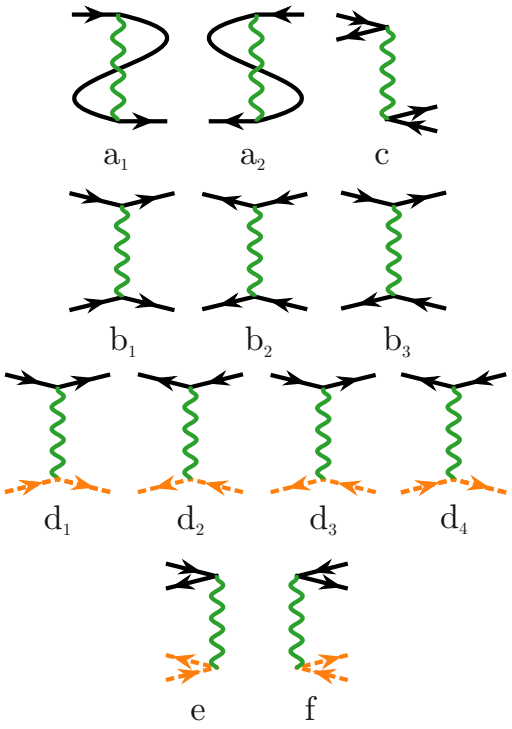

Fig. 3. All possible phaseless scattering vertices to be considered in the Berezinskii technique. Vertices from a, b, and c families have dashed-line counterparts. The weights associated with the vertices are indicated in (17).

to the correlator $\overline{G^R G^A}$. An example of such a correlation diagram is shown in Fig. 1b. Its generic structure can be divided into three left, right, and central blocks denoted by L, R, and Z, as illustrated in Fig. 1b. These different blocks are characterized by their total number of incoming and outgoing solid (retarded) and dashed (advanced) lines.

We first consider the left blocks L. Because the scattering vertices change the number of lines by at most 2, these blocks always have the same even number $2m'$ (with m' being an integer) of retarded and advanced lines attached. For instance, L in Fig. 1b has $m' = 1$. With this property in mind, let us denote by $L_{m'}(\tilde{x})$ the sum of contributions from all L blocks that have their right boundary at point $\tilde{x}$ with $2m'$ lines. To calculate $L_{m'}(\tilde{x})$, we consider how it changes with an infinitesimal change of the boundary position, $\tilde{x} \to \tilde{x} + \delta x$, by counting all possibilities of adding new scattering vertices to $L_{m'}(\tilde{x})$. This counting is detailed in Appendix B for clarity. Taking the limit $\delta x \to 0$, it yields the following differential equation [34]

$$\begin{aligned}
\frac{\mathrm{d}L_{m'}}{\mathrm{d}\tilde{x}} = &-\frac{2m'\eta}{\hbar^2 v_+ v_-} L_{m'}\left(1+(m'-1)\kappa\right) + \frac{m'^2\eta\kappa}{\hbar^2 v_+ v_-}\\
&\times\left[L_{m'+1}\,\mathrm{e}^{\mathrm{i}\omega\tilde{x}\left(\frac{1}{v_+}+\frac{1}{v_-}\right)} + L_{m'-1}\,\mathrm{e}^{-\mathrm{i}\omega\tilde{x}\left(\frac{1}{v_+}+\frac{1}{v_-}\right)}\right].
\end{aligned} \tag{18}$$

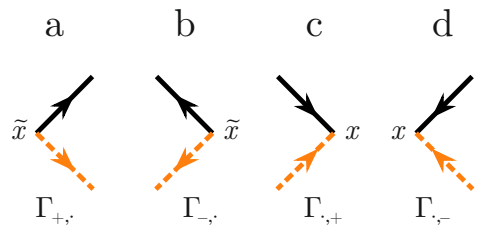

Fig. 4. List of possible initial and final phaseless vertices. They are associated with the following weights (for $\omega \to 0$): (a) $\Gamma_{+,\cdot} = (\hbar v_+)^{-1}$, (b) $\Gamma_{-,\cdot} = (\hbar v_-)^{-1}$, (c) $\Gamma_{\cdot,+} = (\hbar v_+)^{-1}$, and (d) $\Gamma_{\cdot,-} = (\hbar v_-)^{-1}$.

This equation is solved by an ansatz $L_{m'}(\tilde{x}) = \mathcal{L}_{m'} \exp\left[-\mathrm{i}m'\omega\tilde{x}\,(1/v_+ + 1/v_-)\right]$, which leads to an iterative equation for $\mathcal{L}_{m'}$

$$s\mathcal{L}_{m'} + m'\left(\mathcal{L}_{m'+1} - \mathcal{L}_{m'-1} + 2\mathcal{L}_{m'}\right) = 0, \quad (19)$$

where $s = 2 - 2/\kappa + \mathrm{i}\nu$ with $\nu = \omega(v_+ + v_-)\hbar^2/(\kappa\eta)$. The explicit solution of (19) is

$$\mathcal{L}_m(s) = -s\Gamma(m+1)\,\Psi(m+1, 2; -s), \quad (20)$$

with $\Psi(a, b; z)$ being the confluent hypergeometric function of the second kind. Note that in the usual case of spinless TRI systems, $\mathcal{L}_m$ satisfies a similar equation as (19), but with $s_{\mathrm{TRI}} = 2\mathrm{i}\omega v/\eta$, where v is the velocity of the state at energy ϵ [24]. The main difference is that s_{TRI} is fully imaginary, while in our case, s has a finite real part.

The treatment of the right block R is fully analogous. Denoting by $R_m(x)$ the sum of all right-hand blocks that have their left boundary at point x with $2m$ lines (with m an integer), we find that $R_m(x) = L_m(-x)$ and, with a similar ansatz, $\mathcal{R}_m = \mathcal{L}_m$.

Let us finally consider the central block Z. As compared to L and R, this block has one additional line which connects points $\tilde{x}$ and x, i.e., for the left and right blocks that have $2m'$ and $2m$ retarded and advanced lines attached, the central block $Z_{m',m}$ connecting them has $2m'+1$ lines at its left boundary and $2m+1$ lines at its right boundary. For instance, the diagram in Fig. 1b has $2m'+1 = 3$ and $2m+1 = 1$.

To derive a differential equation for $Z_{m',m}(\tilde{x}, x)$, we have to make an assumption on the direction of the extra line. Its type depends on the sign of $x - \tilde{x}$ and introduces a kind of asymmetry because our problem differentiates left and right directions. Here, we assume $\tilde{x} - x < 0$, i.e., that the additional line is going from left to right, like in Fig. 1b. The total derivative of $Z_{m',m}(\tilde{x}, x)$ with respect to x includes the contributions from scattering vertices, but it also has to include the derivative of the final vertex. These final vertices are analyzed analogously to the initial vertices. Out of four possibilities, only two are phaseless and thus contribute to the final sum of diagrams. They correspond to vertices with lines incoming only from a single direction, i.e., both from left or both from right. The list of all phaseless initial and final vertices is summarized in Fig. 4, together with their corresponding weights, denoted by $\Gamma_{\pm,\cdot}$ and $\Gamma_{\cdot,\pm}$ for initial and final vertices, respectively.

Computing the total derivative of the central block at the final point x, assuming $\tilde{x} < x$, we find that

$$\begin{aligned}\frac{\mathrm{d}Z_{m',m}(\tilde{x}, x)}{\mathrm{d}x} &= \pm\frac{\mathrm{i}\omega}{v_\pm} Z_{m',m}(\tilde{x}, x) \\ &- \frac{\eta}{\hbar^2 v_+ v_-}\left(2m^2\kappa + 2m + 1\right) Z_{m',m}(\tilde{x}, x) \\ &+ \frac{\eta\kappa}{\hbar^2 v_+ v_-}\Big[(m+1)^2 Z_{m',m+1}(\tilde{x}, x)\,\mathrm{e}^{\mathrm{i}\omega x(\frac{1}{v_+}+\frac{1}{v_-})} \\ &+ m^2 Z_{m',m-1}(\tilde{x}, x)\,\mathrm{e}^{-\mathrm{i}\omega x(\frac{1}{v_+}+\frac{1}{v_-})}\Big]. \quad (21)\end{aligned}$$

The sign of the first term on the right-hand side depends on the final vertex type, i.e., $\Gamma_{\cdot,+}$ or $\Gamma_{\cdot,-}$. It turns out, on the other hand, that this expression does not depend on the sign of $\tilde{x} - x$. Note that when $v_+ = v_-$ and $\kappa = 1$, (18) and (21) reduce to the known spinless TRI case [24]. While we are not aware of any analytic solution for the differential-recursive equation (21), in general, the direct knowledge of the full function $Z_{m',m}(\tilde{x}, x)$ is not required for the computation of observables. An example of this will be given in the next section when discussing the quantum boomerang effect.

We conclude this section by expressing the Green's function correlator in (14) in terms of the blocks L, R, and Z described above. For $\tilde{x} < x$, and if we suppose that the initial wave function only populates the state with initial velocity v_+ (this is the practical case that will be considered in Sect. 4), the correlator

$$\overline{G^R(x, \tilde{x}, \epsilon)\, G^A(\tilde{x}, x, \epsilon - \hbar\omega)} = \frac{\Gamma_{+,+}^{\tilde{x}<x}}{\hbar^2 v_+^2} + \frac{\Gamma_{+,-}^{\tilde{x}<x}}{\hbar^2 v_+ v_-} \quad (22)$$

is the sum of two contributions corresponding to the two possible final vertices c and d in Fig. 4, with

$$\Gamma_{+,+}^{\tilde{x}<x} = \sum_{m,m'=0}^{\infty} \mathcal{L}_{m'}(\tilde{x}) Z_{m',m}(\tilde{x}, x) \mathcal{R}_m(x), \quad (23)$$

$$\Gamma_{+,-}^{\tilde{x}<x} = \sum_{m,m'=0}^{\infty} \mathcal{L}_{m'}(\tilde{x}) Z_{m',m}(\tilde{x}, x) \mathcal{R}_{m+1}(x). \quad (24)$$

Finally, in the opposite case, i.e., $\tilde{x} > x$, (22) still holds, but with $\Gamma_{+,\pm}^{\tilde{x}<x}$ changed to

$$\Gamma_{+,+}^{\tilde{x}>x} = \sum_{m,m'=0}^{\infty} \mathcal{L}_{m'+1}(x) Z_{m',m}(x, \tilde{x}) \mathcal{R}_{m+1}(\tilde{x}), \quad (25)$$

$$\Gamma_{+,-}^{\tilde{x}>x} = \sum_{m,m'=0}^{\infty} \mathcal{L}_{m'}(x) Z_{m',m}(x, \tilde{x}) \mathcal{R}_{m+1}(\tilde{x}). \quad (26)$$

Together with the solution of (21), (22)–(26) constitute the final solution of the localization problem. In the next section, we will apply this formalism to access the time evolution of a particular observable, the mean position of wave packets, featuring the quantum boomerang effect.

4. Quantum boomerang effect without time-reversal symmetry

We will now apply the above formalism to the theoretical description of a concrete problem, the quantum boomerang effect (QBE). We recall that QBE describes a back-and-forth motion of the mean position of a quantum particle launched with nonzero initial velocity in a disordered potential. Here, we describe this phenomenon based on the TRI-broken Hamiltonian H_0+V, with the free part H_0 defined by (5).

4.1. Mean position

To describe QBE within the Berezinskii technique, we consider for definiteness a wave packet initially launched in a disordered potential with the mean eigen-wave-number k_+ of the Hamiltonian (5) in the corresponding spin state $|\chi_+\rangle$. We denote by $\epsilon_0 = E_-(k_+)$ the associated energy. We thus write the initial wave function as

$$\Psi_0(x) = \frac{1}{(\pi\sigma^2)^{\frac{1}{4}}} \exp\left(-\frac{x^2}{2\sigma^2}+\mathrm{i}k_+x\right)|\chi_+\rangle, \tag{27}$$

where σ is the wave-packet width. As explained in the previous sections, the ensuing dynamics of this state in the disorder gives rise to a coupling with the backward-propagating state of wave number k_- and spin component $|\chi_-\rangle$.

By definition, the disorder-average mean position is

$$\langle x(t)\rangle \equiv \int \mathrm{d}x\; x\overline{|\psi(x,t)|^2}. \tag{28}$$

Using $\psi(x,t) = \int \mathrm{d}x'\, G^R(x,x',t)\,\Psi_0(x')$, we can relate its Fourier transform $\langle x(\omega)\rangle = \int \mathrm{d}t\;\, \mathrm{e}^{\mathrm{i}\omega t}\langle x(t)\rangle$ to the Green's function correlator as

$$\langle x(\omega)\rangle = \frac{1}{2\pi\hbar}\int \mathrm{d}x\,\mathrm{d}x'\,\mathrm{d}x''\,\mathrm{d}\epsilon\;\, \Psi_0(x')\,\Psi_0^*(x'') \times x\;\overline{G^R(x,x',\epsilon)G^A(x'',x,\epsilon-\hbar\omega)}, \tag{29}$$

where we expressed the retarded and advanced Green's functions in the Fourier domain. To simplify this expression, we make use of (14), which leads to

$$\langle x(\omega)\rangle = \int \mathrm{d}x\,\mathrm{d}\tilde{x}\,\mathrm{d}\epsilon\; x\,W(\tilde{x},k_\epsilon) \times \overline{G^R(x,\tilde{x},\epsilon)G^A(\tilde{x},x,\epsilon-\hbar\omega)}, \tag{30}$$

with W being the Wigner distribution of the initial state

$$2\pi\hbar W(\tilde{x},k_\epsilon) = \int \mathrm{d}r\;\, \mathrm{e}^{-\mathrm{i}k_\epsilon r}\,\Psi_0\big(\tilde{x}+\frac{r}{2}\big)\,\Psi_0^*\big(\tilde{x}-\frac{r}{2}\big). \tag{31}$$

For an initial wave function (27) of spatial width σ much smaller than the mean free path, we find $W(\tilde{x},k_\epsilon) \approx \hbar^{-1}\delta(\tilde{x})\delta(k_\epsilon - k_+)$, such that, eventually,

$$\langle x(\omega)\rangle = v_+\int_{-\infty}^{\infty}\mathrm{d}(\Delta x)\;\Delta x\;\overline{G^R(x,\tilde{x},\epsilon_0)G^A(\tilde{x},x,\epsilon_0-\hbar\omega)}, \tag{32}$$

where for convenience we replaced the integral over x by an integral over $\Delta x \equiv x-\tilde{x}$, using that the integrand depends only on $x-\tilde{x}$ due to statistical translational invariance. Equation (32) directly connects the average mean position to the Green's function correlator, which we now compute using the results of the previous section.

4.2. Time evolution of the boomerang effect

Inserting the general Berezinskii result (22) into (32), we infer

$$\langle x(\omega)\rangle = \langle x(\omega)\rangle_+ + \langle x(\omega)\rangle_-, \tag{33}$$

where

$$\langle x(\omega)\rangle_+ = \frac{2\ell}{v_+}\sum_{m'}\big(\mathcal{L}_{m'}S^0_{m'} + \mathcal{L}_{m'+1}S^1_{m'}\big) \tag{34}$$

is the contribution of velocities v_+ (technically, of the final vertex c in Fig. 4), and

$$\langle x(\omega)\rangle_- = \frac{2\ell}{v_-}\sum_{m'}\big(\mathcal{L}_{m'}S^2_{m'} + \mathcal{L}_{m'}S^3_{m'}\big) \tag{35}$$

is the contribution of velocities v_- (final vertex d in Fig. 4). Notice that we here introduced for convenience the mean free path $\ell = \tau_+v_+ = \tau_-v_-$. In (34) and (35), the two terms on the right-hand side are the contributions of $\tilde{x} < x$ and $\tilde{x} > x$, respectively, with the coefficients $\mathcal{L}_m$ defined by (20). The quantities S^i_m, on the other hand, are given by spatial integrals of the block functions $\mathcal{R}_m$ and $Z_{m',m}$. For instance, we have

$$S^0_{m'} = \frac{1}{2\ell}\sum_m\int_0^\infty(\mathrm{d}\Delta x)\;\Delta x\,\mathrm{e}^{-\mathrm{i}\,m'\omega\tilde{x}(\frac{1}{v_+}+\frac{1}{v_-})} \times\; Z_{m',m}(\tilde{x},x)\,\mathrm{e}^{\mathrm{i}\,m\omega x(\frac{1}{v_+}+\frac{1}{v_-})}\mathcal{R}_m. \tag{36}$$

To compute the coefficients $S^0_{m'}$, we perform a partial integration on the right-hand side and use (21) to express the derivative $\mathrm{d}Z_{m',m}(\tilde{x},x)/\mathrm{d}\tilde{x}$ in terms of $Z_{m',m}$. This provides us with the iterative equation

$$2\ell Q^0_m + \mathrm{i}\nu\left(m+\frac{v_-}{v_++v_-}\right)S^0_m - 2\ell\eta\beta_m S^0_m + m^2S^0_{m-1} + (m+1)^2S^0_{m+1} = 0, \tag{37}$$

where $\beta_m \equiv (2\kappa m^2+2m+1)/(\hbar^2v_+v_-)$, and we remind that $\nu \equiv \omega(v_++v_-)\hbar^2/(\kappa\eta)$. The coefficient Q^0_m is defined as

$$Q^0_m = \frac{1}{2\ell}\sum_m\int_0^\infty \mathrm{d}(\Delta x)\;\,\mathrm{e}^{-\mathrm{i}\,m'\omega\tilde{x}(\frac{1}{v_+}+\frac{1}{v_-})} \times Z_{m',m}(\tilde{x},x)\,\mathrm{e}^{\mathrm{i}\,m\omega x(\frac{1}{v_+}+\frac{1}{v_-})}\mathcal{R}_m \tag{38}$$

and is deduced from an iterative equation similar to (37)

$$\mathcal{L}_m + \mathrm{i}\nu\left(m + \frac{v_-}{v_+ + v_-}\right) Q^0_m - 2\ell\eta\beta_m\, Q^0_m$$

$$+m^2\, Q^0_{m-1} + (m+1)^2\, Q^0_{m+1} = 0. \tag{39}$$

The coupled system of equations (37) and (39) is closed, so that at a formal level, it can, in principle, be solved to find the coefficients S^0_m and, in turn, to compute the first sum on the right-hand side of (34). The calculation of the coefficients S^1_m, S^2_m, and S^3_m that appear in (34) and (35) follows the same lines. We provide the corresponding iterative equations they obey in Appendix C for the sake of completeness.

However, instead of exactly computing all the S^i_m coefficients, the mean position can be conveniently evaluated from its short-time expansion using a Padé approximant [33, 34]. The short-time expansion of $\langle x(t)\rangle_+$ and $\langle x(t)\rangle_-$ is systematically obtained by inserting the series $S^i_m(\nu) = \sum_n s^i_{m,n}/(i\nu)^n$ and $Q^i_m(\nu) = \sum_n q^i_{m,n}/(\mathrm{i}\nu)^n$ in the iterative relations (37) and (39) and also (46)–(51) from Appendix C, and computing the $s^i_{m,n}$ and $q^i_{m,n}$ coefficients at arbitrary order in $1/\nu$. This procedure eventually yields the following short-time expansion for the mean position

$$\frac{\langle x(t)\rangle}{v_+\tau} = \frac{t}{\tau} - \frac{t^2}{2\tau^2} + \frac{t^3}{6\tau^3} - \frac{\Big[1 + \Delta\Big(4 + \Delta\big(8 + \Delta(4+\Delta)\big)\Big)\Big] t^4}{24(1+\Delta)^4\,\tau^4} + \mathcal{O}(t^5), \tag{40}$$

where $\Delta \equiv v_-/v_+$ and τ is defined by (12). In Appendix D, we also provide the corresponding expansions for the partial components $\langle x(t)\rangle_+$ and $\langle x(t)\rangle_-$ that respectively describe right- and left-moving particles after the last scattering event. In Fig. 5, we show a comparison between an exact numerical calculation of $\langle x(t)\rangle_\pm$ based on a temporal wave-packet propagation with the disordered Schrödinger equation (details on the numerical simulations are given in the figure caption) and the short-time expansion up to order 11 obtained by solving the Berezinskii equations as explained above. Numerical and theoretical results are in very good agreement without any fit parameter up to $t/\tau \approx 3$. This corresponds to a finite radius of convergence in time, which is also present in the TRI version of the quantum boomerang effect [15]. This radius seems to be dependent on the ratio of velocities Δ. Most importantly, as indicated by (40), the expression of $\langle x(t)\rangle$ is no longer universal because it depends on the velocities' ratio starting from the 4th order. This is a significant difference with the TRI quantum boomerang effect, which solely depends on the dimensionless time scale t/τ at all times. The TRI solution is fully recovered when $v_+ = v_- = v$.

It is also instructive to compare the exact, quantum-mechanical short-time expansion (40) with the classical prediction of the Boltzmann

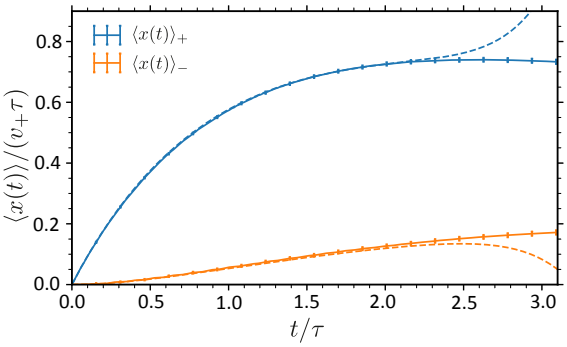

Fig. 5. Numerical (solid lines with error bars) and short-time diagrammatic solution (dashed lines) for the mean position computed up to order $\mathcal{O}(t^{11})$ for a disordered system whose free Hamiltonian part is given by (5). The numerical simulations consist of a temporal propagation of the initial state (27) with the Schrödinger equation. For these simulations, we choose $\sigma = 50$ for the wave-packet width, $\gamma = 0.4$, $\delta = \Omega = 0.4$ for the Hamiltonian parameters, and an energy $\epsilon_0 = 0$. This energy is associated with the two eigen-momenta $k_+ = 1.1850$ and $k_- = -0.6453$. The respective velocities are $v_+ = 0.8014$ and $|v_-| = 0.5307$, and the spin overlap is $\kappa = 0.5050$. We take a disorder strength $\eta = 0.0049$, so that the mean free time is $\tau = 129.4159$. The simulations are done using a system of length $L = 10000$ with a small discretization $\Delta x = 0.2$, and numerical results are averaged over 40960 disorder realizations.

equation, which discards any interference in the multiple scattering process. At a classical level, the mean position is simply given by $\langle x(t)\rangle^{\text{class.}} = \tau v_+(1-\mathrm{e}^{-t/\tau})$, which is essentially the same expression as in TRI systems (see the supplemental material of [18] for details on the classical calculation). This classical result has the short-time expansion

$$\frac{\langle x(t)\rangle^{\text{class.}}}{v_+\tau} = \frac{t}{\tau} - \frac{t^2}{2\tau} + \frac{t^3}{6\tau^3} - \frac{t^4}{24\tau^4} + \mathcal{O}(t^5), \tag{41}$$

which starts to deviate from the quantum-mechanical prediction (40) starting from the 4th order. For completeness, in Appendix D, we also provide the short-time expansions for the classical components $\langle x(t)\rangle^{\text{class.}}_+$ and $\langle x(t)\rangle^{\text{class.}}_-$.

With the short-time expansion (40) at hand, we can infer the $\langle x(t)\rangle$ using a Padé approximant of the full Taylor series [35]. To this aim, we use that, at long time, $\langle x(t)\rangle \propto 1/t^2$ (see below). With this knowledge, we compute the mean position at any time using

$$\langle x(t)\rangle = v_+\tau\left(\frac{\tau}{t}\right)^2 \lim_{n\to\infty} A_n(t), \tag{42}$$

where $A_n(t)$ is a diagonal Padé approximant [35] whose coefficients are computed from the Taylor expansion at a desired order n (e.g., (40) for $n = 4$). In Fig. 6, we compare the exact numerical

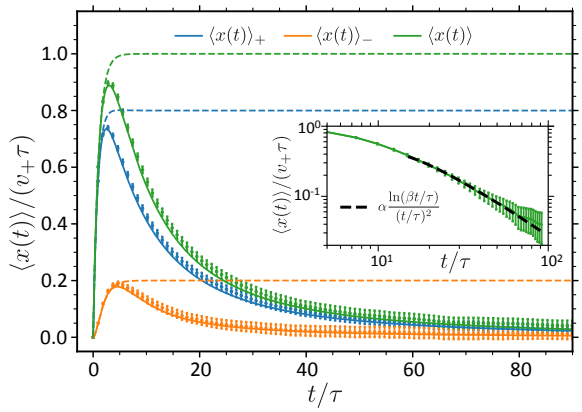

Fig. 6. Mean position as a function of time. The main plot shows numerical data (points with error bars) for $\langle x(t)\rangle_+$, $\langle x(t)\rangle_-$ and $\langle x(t)\rangle = \langle x(t)\rangle_+ + \langle x(t)\rangle_-$, together with the Berezinskii solutions computed with a Padé approximant (solid lines) and the classical solutions (54) and (55) given in Appendix D (dashed lines). Note that no fit parameter is used. The inset shows a log–log scale of $\langle x(t)\rangle$ (points with error bars) and a fitting function $\alpha\log(\beta t/\tau)/(t/\tau)^2$ (black dashed line), with fitted parameters $\alpha = 99.65$ and $\beta = 0.18$. The initial state and parameters of the system are the same as in Fig. 5.

simulations for $\langle x(t)\rangle_+$, $\langle x(t)\rangle_-$ and $\langle x(t)\rangle$ to the corresponding Padé approximants constructed from the Berezinskii technique. The plots reveal the QBE — after a few mean free times, the mean position exhibits a maximum and eventually decays to zero. For all quantities, we find a very good agreement between the simulations and the Berezinskii approach up to long times.

Let us finally come back to the long-time behavior of $\langle x(t)\rangle$. The latter is best visualized in the inset in Fig. 6, which shows the mean position obtained from numerical simulations of the Schrödinger equation in the log–log scale. We find that its long-time asymptotics is well approximated by a function scaling as $\alpha\log(\beta t/\tau)/(t/\tau)^2$, which is of the same form as in spinless TRI Hamiltonians [33]. In the present case of Hamiltonian (5), however, a direct derivation of this asymptotic limit appears to be much more involved and is left for future work.

5. Conclusions

In this paper, we have extended the Berezinskii diagrammatic technique describing the dynamics of Anderson localization in one dimension to TRI-broken disordered Hamiltonians by including a spin–orbit coupling term that induces an asymmetry between right and left scattering processes. Using the formalism, we have computed the time evolution of the mean position of a wave-packet launched in a given direction and recovered the quantum boomerang effect discussed in [18]. As an extension of this work, it would be interesting to extract analytical long-time, asymptotic expansions for the mean position in this system or to characterize the dynamics of other observables such as the mean square width $\langle x^2(t)\rangle$ or the full density distribution of the wave packet.

Acknowledgments

We thank Tony Prat for useful discussions on the Berezinskii technique. N.C. acknowledges financial support from the Agence Nationale de la Recherche (grant ANR-19-CE30-0028-01 CONFOCAL). J.J. acknowledges the support of the French Embassy in Poland through the *Bourse du Gouvernement Français* program.

Appendix

A: Identification of scattering vertices

In this appendix, we briefly explain the procedure used to identify the set of phaseless scattering vertices in Fig. 3. To this aim, let us consider the diagram in Fig. 1a once more. The diagram can be split into spatial intervals lying between consecutive scattering events x_i and x_{i+1}. Each interval contains a specific number of lines. There are in total 4 kinds of lines: retarded lines and advanced lines (both in two possible directions). The numbers of lines are denoted as g_+ and g_- (for retarded lines), and $(g_+)'$ and $(g_-)'$ (for advanced lines), with the index $\pm$ indicating their direction. For example, the interval lying between the points x' and x_3 in the diagram from Fig. 1a has $g_+ = 2$, $g_- = 1$, $(g_+)' = 2$, and $(g_-)' = 1$ lines. Each scattering event induces a definite change in the number of respective lines, which we denote by $\Delta g_\pm$ and $(\Delta g_\pm)'$. These changes determine the phases associated with scattering vertices. To find these phases, we first note that each incoming and outgoing retarded propagator line at point x carries a phase that depends on the direction of the line and on its type:

- every incoming (outgoing) *positive* line, i.e., propagating to the right, carries a k_+x ($-k_+x$) phase;
- every incoming (outgoing) *negative* line, i.e., propagating to the left, carries a $-k_-x$ (k_-x) phase.

For advanced lines, the phases have opposite signs.

For vertices involving only one type of lines, e.g., only retarded Green's functions, the total phase ϕ of a scattering vertex is then calculated from the total change of the number of lines, i.e.,

$$\phi = \pm\big(\Delta g_+ k_+ - \Delta g_- k_-\big)x. \tag{43}$$

Hence, the phaselessness condition of the scattering vertex in the limit of $\omega \to 0$ is that the vertex does not change the total number of incoming and

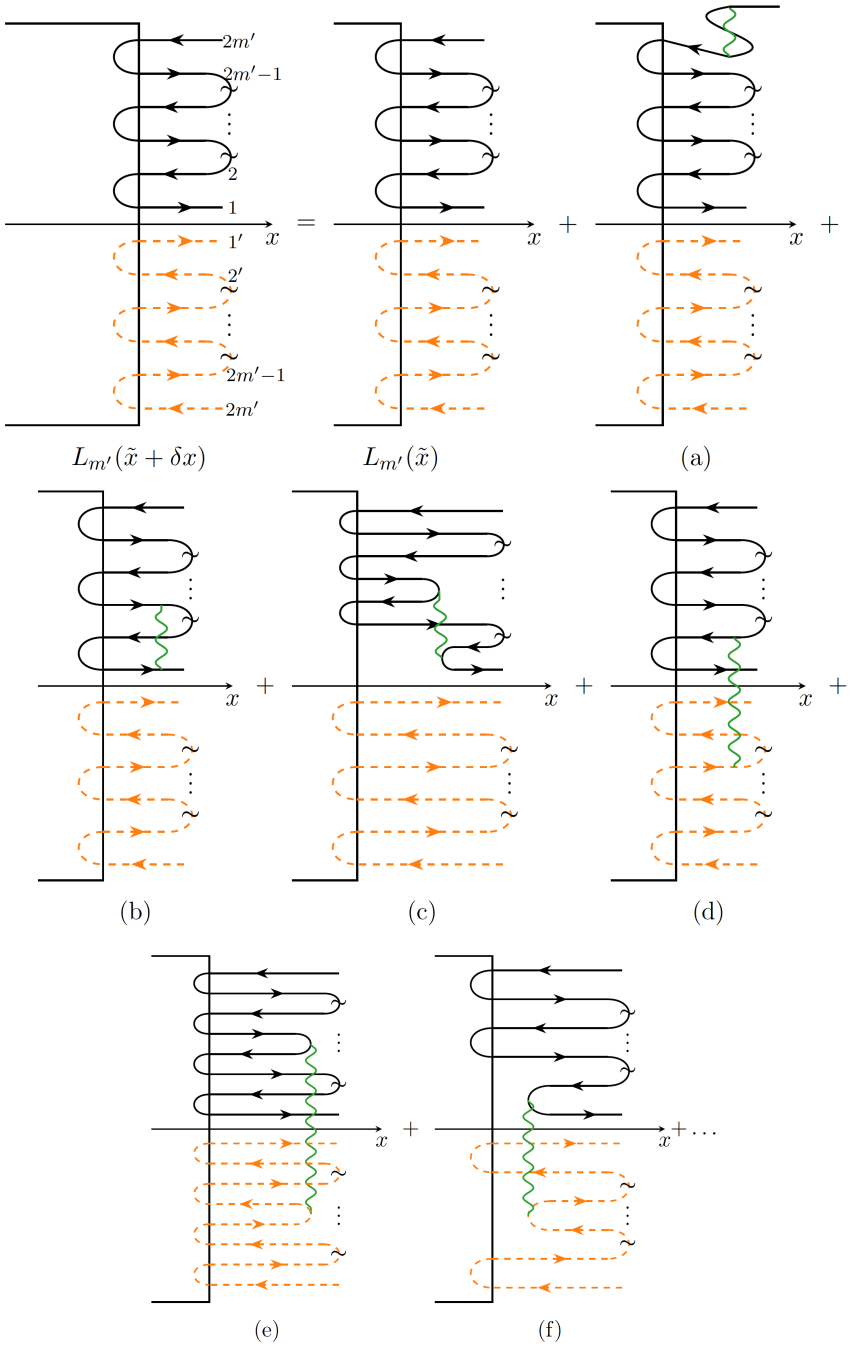

Fig. 7. Schematic representation of (45). Note that $L_{m'}(\tilde{x}+\delta x)$ can be constructed with $L_{m'}(\tilde{x})$ and all possible combinations of the scattering vertices. The figure shows one example for each scattering vertex.

outgoing lines, that is, $\Delta g_{\pm} = 0$. This condition is very similar to the original TRI Berezinskii method, although in our system k_+ and k_- do not cancel each other. In the case of the mixed-line vertices involving both G_0^R and G_0^A, the problem is slightly different — lines from G_0^R and G_0^A may cancel each other. The total phase of a vertex is

$$\phi = \Big[(\Delta g_+ - (\Delta g_+)')\, k_+ - (\Delta g_- - (\Delta g_-)')\, k_- \Big] x. \tag{44}$$

This phase is zero only if $\Delta g_{\pm} - (\Delta g_{\pm})' = 0$.

B: Differential equation for L_m blocks

In this appendix, we provide details about the derivation of the differential equation (18) for the left blocks of correlation diagrams. To calculate $L_{m'}(\tilde{x})$, we consider how it changes with an infinitesimal change of the boundary position, say $\tilde{x} \to \tilde{x} + \delta x$, by adding all possible contributions from different scattering vertices. For this purpose, we have numbered the lines on the boundary by

assigning consecutive numbers to the outgoing and incoming lines, as presented in Fig. 7. The figure also shows a schematic way of adding new vertices to $L_{m'}(\tilde{x})$, bearing in mind that the lines cannot create loops nor cross each other. We get the corresponding equation

$$
\begin{aligned}
L_{m'}(\tilde{x}+\delta x) &= L_{m'}(\tilde{x}) + (-2m')\frac{\eta\delta x}{2} L_{m'}(\tilde{x}) \left(\frac{1}{v_+}+\frac{1}{v_-}\right)^2 \\
&+ \eta\delta x\, L_{m'}(\tilde{x}) \left[-\frac{m'(m'-1)}{v_+^2} - \frac{m'(m'-1)}{v_-^2} - \frac{2m'^2}{v_+v_-} - \frac{2\kappa m'(m'-1)}{v_+v_-} + \frac{m'^2}{v_+^2} + \frac{m'^2}{v_-^2} + \frac{2m'^2}{v_+v_-} \right] \\
&+ \frac{\eta\delta x\,\kappa}{v_+v_-} \left[(m')^2 L_{m'+1}(\tilde{x})\, \mathrm{e}^{\mathrm{i}\omega\tilde{x}\left(\frac{1}{v_+}+\frac{1}{v_-}\right)} + (m')^2 L_{m'-1}(\tilde{x})\, \mathrm{e}^{-\mathrm{i}\omega\tilde{x}\left(\frac{1}{v_+}+\frac{1}{v_-}\right)} \right]. \qquad (45)
\end{aligned}
$$

After taking the limit $\delta x \to 0$ and some simplifications, we finally obtain (18) from the main text.

C: Iterative Berezinskii equations

In this appendix, we provide the coupled equations for the S_m^i coefficients ($i = 1, 2, 3$) that appear in the expressions of the mean position, i.e., (34) and (35) in the main text.

Using the same procedure as for S_m^0, explained in the main text, we find the following coupled iterative equations for the S_m^i, Q_m^i ($i = 1, 2, 3$)

$$
\begin{aligned}
&-2\ell Q_m^1 + \mathrm{i}\nu\left(m+\frac{v_+}{v_++v_-}\right) S_m^1 - 2\ell\eta\beta_m S_m^1 \\
&+m^2 S_{m-1}^1 + (m+1)^2 S_{m+1}^1 = 0, \qquad (46)
\end{aligned}
$$

$$
\begin{aligned}
&\mathcal{L}_{m+1} + \mathrm{i}\nu\left(m+\frac{v_+}{v_++v_-}\right) Q_m^1 - 2\ell\eta\beta_m Q_m^1 \\
&+m^2 Q_{m-1}^1 + (m+1)^2 Q_{m+1}^1 = 0, \qquad (47)
\end{aligned}
$$

$$
\begin{aligned}
&2\ell Q_m^2 + \mathrm{i}\nu\left(m+\frac{v_-}{v_++v_-}\right) S_m^2 - 2\ell\eta\beta_m S_m^2 \\
&+m^2 S_{m-1}^2 + (m+1)^2 S_{m+1}^2 = 0, \qquad (48)
\end{aligned}
$$

$$
\begin{aligned}
&\mathcal{L}_{m+1} + \mathrm{i}\nu\left(m+\frac{v_-}{v_++v_-}\right) Q_m^2 - 2\ell\eta\beta_m Q_m^2 \\
&+m^2 Q_{m-1}^2 + (m+1)^2 Q_{m+1}^2 = 0, \qquad (49)
\end{aligned}
$$

$$
\begin{aligned}
&-2\ell Q_m^3 + \mathrm{i}\nu\left(m+\frac{v_+}{v_++v_-}\right) S_m^3 - 2\ell\eta\beta_m S_m^3 \\
&+m^2 S_{m-1}^3 + (m+1)^2 S_{m+1}^3 = 0, \qquad (50)
\end{aligned}
$$

$$
\begin{aligned}
&\mathcal{L}_{m+1} + \mathrm{i}\nu\left(m+\frac{v_+}{v_++v_-}\right) Q_m^3 - 2\ell\eta\beta_m Q_m^2 \\
&+m^2 Q_{m-1}^3 + (m+1)^2 Q_{m+1}^3 = 0. \qquad (51)
\end{aligned}
$$

D: Partial components $\langle x(t)\rangle_\pm$

We finally provide the short-time expansions for $\langle x(t)\rangle_+$ and $\langle x(t)\rangle_-$, and the exact expressions (valid at any time) of their classical counterparts $\langle x(t)\rangle_+^{\text{class.}}$ and $\langle x(t)\rangle_-^{\text{class.}}$

$$
\begin{aligned}
\frac{\langle x(t)\rangle_+}{v_+\tau} &= \left[\frac{t}{\tau} - \frac{1}{1+\Delta}\frac{t^2}{\tau^2} + \frac{3-\Delta}{6(1+\Delta)}\frac{t^3}{\tau^3}\right. \\
&\left. - \frac{\Delta(\Delta+1)[\Delta(\Delta^2+\Delta-3)-7]-2}{12(\Delta+1)^5}\frac{t^4}{\tau^4}\right] + \mathcal{O}(t^5), \qquad (52)
\end{aligned}
$$

$$
\begin{aligned}
\frac{\langle x(t)\rangle_-}{v_+\tau} &= \left[\frac{1-\Delta}{2(1+\Delta)}\frac{t^2}{\tau^2} - \frac{1-\Delta}{3(1+\Delta)}\frac{t^3}{\tau^3} + \right. \\
&\left. - \frac{\Delta(9-\Delta(\Delta(3\Delta(\Delta+3)+8)-8))+3}{24(\Delta+1)^5}\frac{t^4}{\tau^4}\right] \\
&+ \mathcal{O}(t^5), \qquad (53)
\end{aligned}
$$

$$
\frac{\langle x(t)\rangle_+^{\text{class.}}}{\tau v_+} = \left[\frac{2\Delta}{1+\Delta}\left(1-\mathrm{e}^{-t/\tau}\right) + \frac{1-\Delta}{1+\Delta}\frac{t}{\tau}\mathrm{e}^{-t/\tau}\right], \qquad (54)
$$

$$
\frac{\langle x(t)\rangle_-^{\text{class.}}}{\tau v_+} = \frac{1-\Delta}{1+\Delta}\left(1-\mathrm{e}^{-t/\tau} - \frac{t}{\tau}\mathrm{e}^{-t/\tau}\right). \qquad (55)
$$

References

[1] P.W. Anderson, *Phys. Rev.* **109**, 1492 (1958).

[2] J. Billy, V. Josse, Z. Zuo et al., *Nature* **453**, 891 (2008).

[3] G. Roati, C. D'Errico, L. Fallani, M. Fattori, C. Fort, M. Zaccanti, G. Modugno, M. Modugno, M. Inguscio, *Nature* **453**, 895 (2008).

[4] G. Semeghini, M. Landini, P. Castilho, S. Roy, G. Spagnolli, A. Trenkwalder, M. Fattori, M. Inguscio, G. Modugno, *Nat. Phys.* **11**, 554 (2015).

[5] F. Jendrzejewski, A. Bernard, K. Müller et al., *Nat. Phys.* **8**, 398 (2012).

[6] N. Cherroret, T. Karpiuk, C.A. Müller, B. Grémaud, C. Miniatura, *Phys. Rev. A* **85**, 011604 (2012).

[7] S. Ghosh, D. Delande, C. Miniatura, N. Cherroret, *Phys. Rev. Lett.* **115**, 200602 (2015).

[8] L.A. Cobus, S.E. Skipetrov, A. Aubry, B.A. van Tiggelen, A. Derode, J.H. Page, *Phys. Rev. Lett.* **116**, 193901 (2016).

[9] C. Hainaut, I. Manai, R. Chicireanu, J.F. Clément, S. Zemmouri, J.C. Garreau, P. Szriftgiser, G. Lemarié, N. Cherroret, D. Delande, *Phys. Rev. Lett.* **118**, 184101 (2017).

[10] C. Hainaut, I. Manai, J.-F. Clément, J.C. Garreau, P. Szriftgiser, G. Lemarié, N. Cherroret, D. Delande, R. Chicireanu, *Nat. Commun.* **9**, 1382 (2018).

[11] T. Karpiuk, N. Cherroret, K.L. Lee, B. Grémaud, C.A. Müller, C. Miniatura, *Phys. Rev. Lett.* **109**, 190601 (2012).

[12] S. Ghosh, N. Cherroret, B. Gr'emaud, C. Miniatura, D. Delande, *Phys. Rev. A* **90**, 063602 (2014).

[13] K.L. Lee, B. Grémaud, C. Miniatura, *Phys. Rev. A* **90**, 043605 (2014).

[14] N. Cherroret, T. Scoquart, D. Delande, *Ann. Phys.* **435**, 168543 (2021).

[15] T. Prat, D. Delande, N. Cherroret, *Phys. Rev. A* **99**, 023629 (2019).

[16] L. Tessieri, Z. Akdeniz, N. Cherroret, D. Delande, P. Vignolo, *Phys. Rev. A* **103**, 063316 (2021).

[17] R. Sajjad, J.L. Tanlimco, H. Mas et al., *Phys. Rev. X* **12**, 011035 (2022).

[18] J. Janarek, B. Grémaud, J. Zakrzewski, D. Delande, *Phys. Rev. B* **105**, L180202 (2022).

[19] F. Noronha, J.A.S. Lourenço, T. Macrí, *Phys. Rev. B* **106**, 104310 (2022).

[20] F. Noronha, T. Macrí, *Phys. Rev. B* **106**, L060301 (2022).

[21] L. Sanchez-Palencia, D. Clément, P. Lugan, P. Bouyer, G.V. Shlyapnikov, A. Aspect, *Phys. Rev. Lett.* **98**, 210401 (2007).

[22] S.E. Skipetrov, A. Minguzzi, B.A. van Tiggelen, B. Shapiro, *Phys. Rev. Lett.* **100**, 165301 (2008).

[23] B. Shapiro, *J. Phys. A: Math. Theor.* **45**, 143001 (2012).

[24] V.L. Berezinskii, *Zh. Eksp. Teor. Fiz.* **65**, 1251 (1973) [*Sov. Phys. JETP 38*, 620 (1974)].

[25] A.A. Gogolin, *Sov. Phys. JETP* **44**, 1003 (1976).

[26] J.P.R. Valdes, T. Wellens, *Phys. Rev. A* **93**, 063634 (2016).

[27] B. Suleymanli, E. Nakhmedov, F. Tatardar, B. Tanatar, *Physica E: Low-dimen. Syst. Nanostruct.* **146**, 115550 (2023).

[28] Y.-J. Lin, K. Jiménez-García, I.B. Spielman, *Nature* **471**, 83 (2011).

[29] C. Hamner, Y. Zhang, M.A. Khamehchi, M.J. Davis, P. Engels, *Phys. Rev. Lett.* **114**, 070401 (2015).

[30] E. Akkermans, G. Montambaux, *Mesoscopic Physics of Electrons and Photons*, Cambridge University Press, Cambridge 2007.

[31] C.A. Müller, D. Delande, *Lecture Notes of the Les Houches Summer School in Singapore*, Vol. 91, Oxford University Press, Oxford 2011, p. 441.

[32] A.A. Gogolin, V.L. Mel'nikov, E.I. Rashba, *Sov. Phys. JETP* **42**, 168 (1976).

[33] T. Prat, Ph.D. Thesis, Université Pierre et Marie Curie (Paris), 2017.

[34] J. Janarek, Ph.D. Thesis, Sorbonne Université (Paris), Uniwersytet Jagielloński w Krakowie 2021.

[35] G.A. Baker, *Essentials of Padé approximants*, Academic Press, 1975.

Proceedings of the 11th Workshop on Quantum Chaos and Localisation Phenomena (CHAOS 23)

Toward Remote Physical-Model-Based Fault Localization in Transmission-Line Networks

P. del Hougne*

Univ. Rennes, CNRS, IETR-UMR 6164, F-35000 Rennes, France

Doi: 10.12693/APhysPolA.144.441 *e-mail: philipp.del-hougne@univ-rennes1.fr

We analytically derive the updates of a transmission-line network's interaction matrix and scattering matrix as a consequence of a fault (an interrupted transmission line). We find that the fault alters not only the direct coupling between the two nodes that were previously connected by the faulty cable, but that the fault also alters these nodes' self-interactions in a non-trivial manner. Given the network's topology, it is then possible to *remotely* localize the fault on the faulty cable based on measurements of the faulty network's scattering coefficient(s). Our analytical expressions make it possible to efficiently calculate the expected scattering matrix for different fault locations (orders of magnitude faster than a brute-force evaluation). We report a simple demonstration for which we assume to know the network's topology as well as which cable is faulty; we identify the location of the fault on the faulty cable by comparing the broadband scattering coefficient(s) swept across candidate fault locations to the one(s) measured on the faulty network.

topics: transmission-line network, fault localization, physical-model-based remote sensing, isospectral reduction

1. Introduction

In a simple cable, a fault is easily localized via time-domain analysis of the cable's reflection or transmission coefficient. In this paper, we are interested in the more challenging problem of localizing a fault in a cable that is part of a complex transmission-line network. Thus, we cannot probe the cable in isolation nor directly. We can only probe the cable remotely via asymptotic scattering channels connecting the network to the outside world. In general, asymptotic scattering channels are not directly connected to the faulty cable of interest.

Fault localization in a complex transmission-line network can be understood as a sensing problem inside a complex scattering medium. On the one hand, reverberation in such a complex system can drastically enhance the achievable resolution because it boosts the wave's sensitivity to the perturbation of interest. Indeed, we recently demonstrated a direct link between the resolution with which an object can be localized inside a chaotic cavity and the dwell time of the wave inside the cavity [1]. The chaotic cavity acts essentially like a generalized interferometer, and the resulting interferometric sensitivity can yield orders of magnitude finer resolution than in free space. Deeply subwavelength resolution without capturing evanescent waves is thereby feasible [1]. On the other hand, data analysis inevitably must take into account the complexity of the specific system. In [1], the exact geometry and material composition of the chaotic cavity were unknown such that a calibration dataset had to be measured to characterize the specific system's complexity. In contrast, in the present case of a transmission-line network, the topology is usually known, so that its complexity can be taken into account without the need for calibration measurements.

The considered problem of remotely localizing a network fault is of practical importance, for instance, to diagnose line outages in large networks. Currently, such problems are often studied under simplifying assumptions (e.g., using DC approximation of AC power flow models) and assuming that a line outage simply removes the line from the network topology [2]. Our analytical calculations in the present paper based on a physical model suggest that a fault additionally impacts (in a significant and non-trivial manner) the self-interactions of the nodes that were connected by the faulty line.

Meanwhile, we note that other physics-based remote-sensing approaches for transmission-line networks are currently being explored in the literature. For example, [3] considers the case of an initial network being split at various edges and nodes into two networks; it is shown in [3] that by determining the networks' Euler characteristic from scattering measurements [4], one can determine at how many edges and nodes the initial network was split — even without knowing its topology.

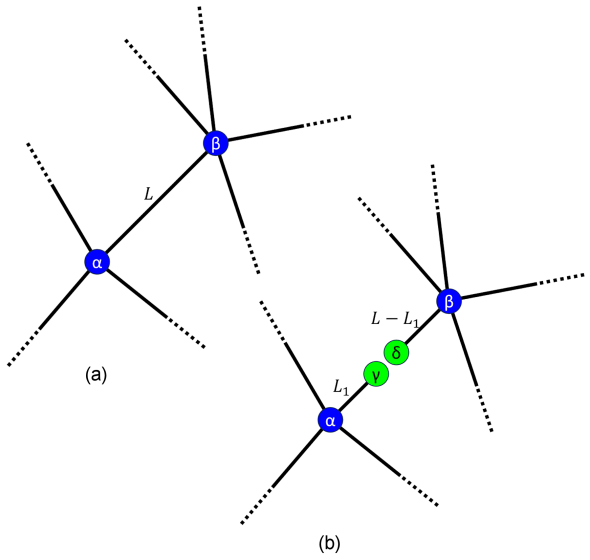

Fig. 1. Considered fault: the cable linking nodes α and β is interrupted (cut) at a distance L_1 from α, creating two new nodes γ and δ. The sketches show (a) an intact cable and (b) a faulty cable of interest within a larger transmission-line network.

Related to the present paper is also a "differential DORT" technique[†] for the detection of *soft* faults in complex wire networks that is similarly based on measuring the scattering matrix of the intact and faulty network, as well as knowledge of the network topology [5]. The signal processing in this "differential DORT" technique consists in identifying the wavefront that focuses on the fault (hence the term "DORT" in the technique's name), computing the field distribution within the network, and comparing it to the baseline field distribution (hence the term "differential" in the technique's name). However, as pointed out in [5], this differential approach relies on the Born approximation (i.e., the amount of power scattered by the fault is small, so there is no significant portion of the wave energy that interacts with the fault more than once). Therefore, the technique is limited to *soft* faults, which only weakly perturb the network. In contrast, the present paper considers *hard* faults, which are open circuits. Hence, many interactions with the fault occur, and, in fact, the resolution improves with the number of interactions [1].

In the present paper, we derive an analytical expression for how a fault alters the interaction matrix of a given network and thereby the observable scattering coefficient(s). We numerically validate the derived expressions and demonstrate their application to remote physical-model-based fault localization.

[†1]DORT — decomposition of the time reversal operator

2. Background

In this section, we recall the well-established background on wave scattering in a transmission-line network on which our subsequent analysis builds.

A transmission-line network, also known as a "quantum graph" [6–8], can be understood as composed of non-resonant scattering entities (its nodes, i.e., junctions) that have certain couplings between each other (its bonds, i.e., cables) and with the outside world (asymptotic scattering channels). Let us consider a system composed of n nodes of which $m \leq n$ are directly connected to the asymptotic scattering channel; we assume that each asymptotic scattering channel is non-dispersively coupled to exactly one node.

The considered transmission-line networks are also known as Neumann quantum graphs, and [7, 9, 10] derived an exact expression relating the system's scattering matrix $S \in \mathbb{C}^{m\times m}$ to the network topology

$$S = I_m - 2\mathrm{i}\, W^\dagger \frac{1}{H + \mathrm{i}WW^\dagger} W. \tag{1}$$

The matrices involved in (1) are defined as follows:

1. $I_m \in \mathbb{B}^{m\times m}$ is the $m \times m$ identity matrix.
2. $W \in \mathbb{B}^{n\times m}$ is the coupling matrix describing the coupling between each node and each asymptotic scattering channel. If the i-th meta-atom is connected to the j-th asymptotic scattering channel, the (i,j)-th entry of W is unity; otherwise, it is zero.
3. $H \in \mathbb{R}^{n\times n}$ is the interaction matrix of the transmission-line network. Its (i,j)-th entry is defined as follows

$$H_{i,j} = \begin{cases} -\sum\limits_{l\neq i} C_{i,l}\, \cot(kL_{i,l}), & \text{if} \quad i = j, \\ C_{i,j}\, \csc(kL_{i,j}), & \text{otherwise.} \end{cases} \tag{2}$$

Here, $C_{i,j}$ is unity if the nodes indexed i and j are directly connected, and zero otherwise; $L_{i,j}$ is the length of the cable connecting the nodes indexed i and j; k is the wavenumber. In the present paper, we limit ourselves to reciprocal bonds, so H is a symmetric matrix. Moreover, its dependence on the wavenumber implies that H, and therefore also S, are frequency dependent.

3. Physics-compliant fault model

The fault considered in this paper is illustrated in Fig. 1, where the cable of length L linking nodes α and β is cut at a distance L_1 from α. This fault implies that the direct link between nodes α and β is interrupted, but this fault is *not* equivalent to just removing the cable between α and β. The waves will still travel along the faulty cable and will be

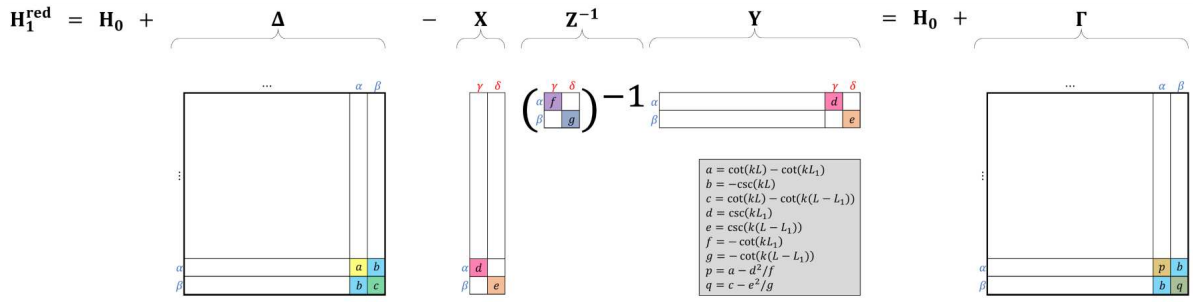

Fig. 2. Fault-induced update of the interaction matrix in the reduced $n \times n$ basis. The update concerns 2×2 block of the interaction matrix involving nodes α and β.

reflected by the fault, which we assume to be an open-circuit end. Therefore, the physics-compliant fault model consists of two modifications of the original network topology:

1. Removal of the cable linking nodes α and β.
2. Creation of two new nodes, γ and δ, which are directly connected to α and β via cables of length L_1 and $L - L_1$, respectively.

Let us denote by H_0 and S_0 the interaction matrix and scattering matrix of the intact transmission-line network of interest, respectively. Assuming the network topology is known, H_0 and S_0 are also known analytically. When a fault appears, the faulty network is described by H_1 and S_1. Note that the dimensions of H_1 are $(n+2) \times (n+2)$ because of the two new nodes γ and δ. (Of course, the dimensions of both S_1 and S_0 are $n \times n$.)

We assume that we know (i) the network topology and (ii) which cable is faulty, and we seek to localize the fault on the faulty cable by estimating L_1. Our next goal is hence to find an analytical expression for $\Delta S = S_1 - S_0$ as a function of the sought-after parameter L_1.

4. Interaction matrix update due to fault

As a first step, we seek to identify in this section how the interaction matrix of our network must be updated to account for the fault. Without loss of generality, we index the nodes of the intact network such that α and β have indices $(n-1)$ and n, respectively.

So far, we have considered the interaction matrix always in the canonical basis, where its dimensions directly correspond to the number of nodes. However, there are equivalent representations reduced to a subset of nodes. Indeed, nodes that are not directly connected to asymptotic scattering channels can equivalently be understood as merely being a non-local coupling mechanism between the remaining nodes. Mathematically, such a reduced-basis representation is based on the block matrix inversion lemma. Calculations of reduced-basis interaction matrices were presented in contexts ranging from tight-binding network engineering [11] to isospectral graph reduction [12]. In particular, we have recently used them to achieve covert symmetry-based wave scattering control by encoding the symmetry in the non-local interactions between "primary" meta-atoms such that the symmetry is "hidden", i.e., the symmetry is only apparent in a reduced basis but not in the canonical basis [13]; very recently, we also used a reduced-basis representation to formulate and calibrate compact physics-compliant models of massively parametrized complex media such as "smart" radio environments [14, 15].

In the present context, the two fault-induced new nodes, γ and δ, are certainly not directly connected to any asymptotic scattering channel (they have only one connection to α or β, respectively). Therefore, we can find an equivalent representation of H_1 in the basis reduced to the n initial nodes. We begin by writing H_1 in block form

$$H_1 = \begin{bmatrix} H_{1,n} & X \\ Y & Z \end{bmatrix}, \tag{3}$$

where $H_{1,n} \in \mathbb{R}^{n \times n}$, $X \in \mathbb{R}^{n \times 2}$, $Y \in \mathbb{R}^{2 \times n}$, and $Z \in \mathbb{C}^{2 \times 2}$. Then, the reduced-basis representation of H_1 is

$$H_1^{\mathrm{red}} = H_{1,n} - XZ^{-1}Y. \tag{4}$$

Since our goal is to express H_1^{red} as an update of H_0, we introduce $\Delta = H_{1,n} - H_0$. Now, we can formulate the impact of the fault as an update of the original interaction matrix

$$H_1^{\mathrm{red}} = H_0 + \Delta - XZ^{-1}Y = H_0 + \Gamma. \tag{5}$$

Next, we seek to define the entries of $\Gamma = \Delta - XZ^{-1}Y$ in terms of L_1. This procedure is illustrated in Fig. 2. The only non-zero entries of Δ are the ones in its bottom right 2×2 block

$$\begin{aligned} \Delta_{n-1,n-1} &= a = \cot(kL) - \cot(kL_1), \\ \Delta_{n-1,n} &= \Delta_{n,n-1} = b = -\csc(kL), \\ \Delta_{n,n} &= c = \cot(kL) - \cot(k(L - L_1)). \end{aligned} \tag{6}$$

The only non-zero entries of $X = Y^T$ are the following two

$$\begin{aligned} X_{n-1,1} &= Y_{1,n-1} = d = \csc(kL_1), \\ X_{n,2} &= Y_{2,n} = e = \csc(k(L - L_1)). \end{aligned} \tag{7}$$

The entries of Z are as follows

$$\begin{aligned} Z_{1,1} &= f = -\cot(kL_1), \\ Z_{1,2} &= Z_{2,1} = 0, \\ Z_{2,2} &= g = -\cot(k(L-L_1)). \end{aligned} \tag{8}$$

Ultimately, we find that only the bottom right 2×2 block of Γ is non-zero, i.e.,

$$\begin{aligned} \Gamma_{n-1,n-1} &= p = a - \tfrac{d^2}{f} = \cot(kL) - \cot(kL_1) \\ &\quad + \frac{(\csc(kL_1))^2}{\cot(kL_1)}, \\ \Gamma_{n-1,n} &= \Gamma_{n,n-1} = b = -\csc(kL), \\ \Gamma_{n,n} &= q = c - \tfrac{e^2}{g} = \cot(kL) - \cot\left(k(L-L_1)\right) \\ &\quad + \frac{\left(\csc\left(k(L-L_1)\right)\right)^2}{\cot\left(k(L-L_1)\right)}. \end{aligned} \tag{9}$$

Therefore, the fault has not only removed the direct coupling between α and β, but it has also changed the self-interactions of α and β in a non-trivial way. One possible interpretation is that in the reduced basis, α and β are now resonant because they have a cable of length L_1 or $L-L_1$, respectively, with open-circuit termination attached to them.

5. Scattering matrix update due to fault

In the previous section, we expressed the impact of the fault as an update (parametrized by L_1) of the interaction matrix. In this section, we now evaluate how the scattering matrix of the network is updated due to the fault. As seen in (1), to go from the interaction matrix H to the scattering matrix S, the matrix $G = H + \mathrm{i}\,WW^\dagger$ must be inverted. We define

$$\begin{aligned} G_1 &= H_1^{\mathrm{red}} + \mathrm{i}\,WW^\dagger = H_0 + \Gamma + \mathrm{i}\,WW^\dagger = \\ &G_0 + \Gamma = G_0 + UDV, \end{aligned} \tag{10}$$

where

$$U = \begin{bmatrix} 0_{n-2,2} \\ Q \end{bmatrix} \quad \text{and} \quad V = \begin{bmatrix} {0_{n-2,2}}^T & Q^{-1} \end{bmatrix}, \tag{11}$$

and where QDQ^{-1} is the eigendecomposition of the bottom right 2×2 block of Γ, and $0_{n-2,2}$ is a $(n-2)\times 2$ matrix of zeros.

Based on the Woodbury matrix identity, we obtain

$${G_1}^{-1} = {G_0}^{-1} - {G_0}^{-1}U\left(D^{-1} + V{G_0}^{-1}U\right)^{-1}V{G_0}^{-1} \tag{12}$$

and hence

$$\begin{aligned} S_1 &= I - 2\mathrm{i}W^\dagger {G_1}^{-1}W = \\ &S_0 + 2\mathrm{i}W^\dagger\left[{G_0}^{-1}U\left(D^{-1} + V{G_0}^{-1}U\right)^{-1}V{G_0}^{-1}\right]W. \end{aligned} \tag{13}$$

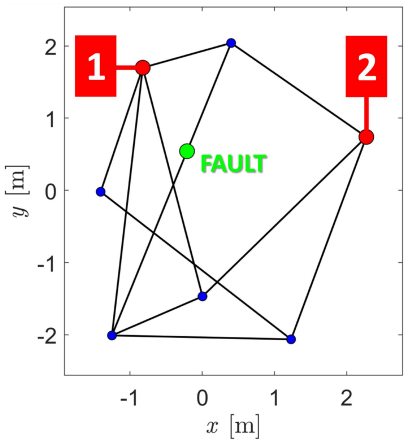

Fig. 3. Considered random transmission-line network. Each of the two red nodes is directly connected to one asymptotic scattering channel. The location of the fault, at which the faulty cable is interrupted, is highlighted in green.

Next, we seek to express Q and D in terms of L_1 so that we can analytically relate the change of the observable scattering coefficient(s) to L_1. The analytical eigendecomposition of the bottom right 2×2 block of Γ yields

$$\begin{aligned} Q &= \begin{bmatrix} \frac{-(q-p+z)}{2b} & \frac{p-q+z}{2b} \\ 1 & 1 \end{bmatrix}, \\ D &= \mathrm{diag}\left(\begin{bmatrix} \frac{p+q-z}{2} & \frac{p+q+z}{2} \end{bmatrix}\right), \end{aligned} \tag{14}$$

where $z = \sqrt{p^2 - 2pq + q^2 + 4b^2}$, and the diag$(\cdot)$ operator constructs a diagonal matrix from a vector.

Equations (13) and (14) are the key result of the present paper, analytically relating the update of S due to the fault to L_1.

6. Application to an example network

In this section, we consider a specific example network (i) to validate the key result of our analytical calculations (i.e., (13)) and (ii) to demonstrate its use for fault localization.

6.1. Numerical validation of (13)

We consider the example random transmission-line network shown in Fig. 3. Two asymptotic scattering channels are connected to the network, and one of the network's inner cables is interrupted by a fault. We assume the wave speed to be 70 % of the speed of light in free space.

In Fig. 4 we plot the frequency-dependent scattering coefficients of the intact (blue) and faulty (red) networks. The fault altered the network's scattering matrix very significantly. The blue and red

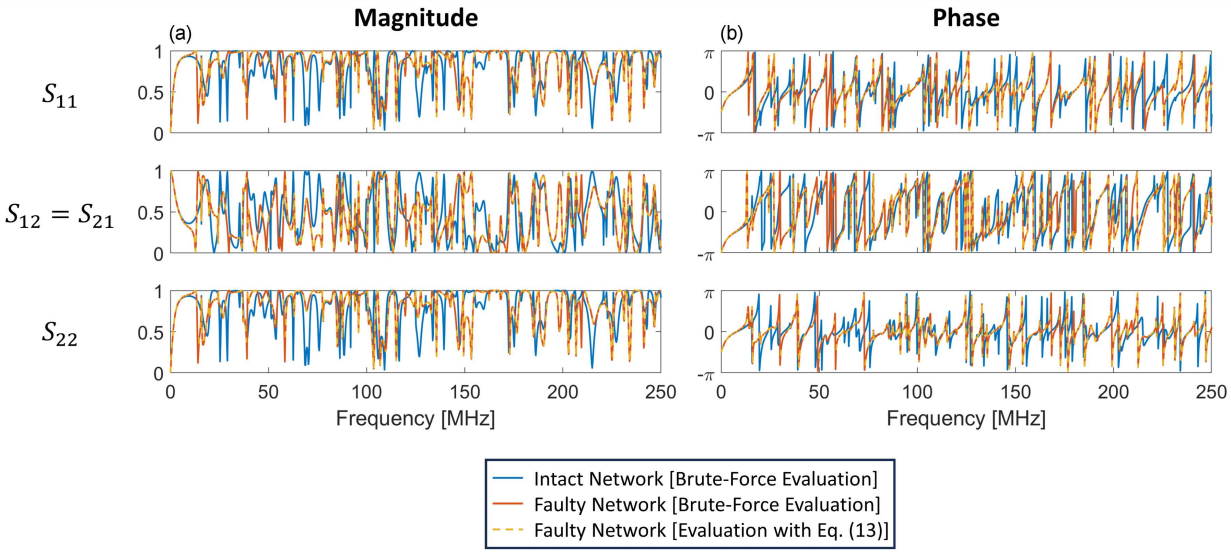

Fig. 4. Comparison of the frequency-dependent scattering coefficients in terms of magnitude (a) and phase (b) for the intact network (blue), the faulty network (red), and the faulty network evaluated with (13) (yellow).

curves are evaluated with the brute-force approach from (2). However, in the case of the faulty network, the scattering coefficients can be more efficiently evaluated as updates of the intact network's scattering coefficients using (13), yielding the yellow lines in Fig. 4. The agreement between red and yellow lines validates the analytical expression from (13).

6.2. Remote model-based fault localization

The faulty network's transmission coefficient $S_{21}(f)$ is a wave fingerprint of the fault's location [1, 16, 17]. Given (13), we can now analytically calculate the expected transmission spectra for different candidate fault locations L_1, in order to identify the one that best explains the measured $S_{21}(f)$ of the faulty network.

For the sake of simplicity, we assume negligible measurement noise. For our analysis, we restrict ourselves to a rather small (arbitrarily chosen) frequency interval, $37.3 < f < 49.8$ MHz, with 50 linearly spaced frequency points. We consider 1000 linearly spaced candidate values of L_1 between zero and the length of the cable connecting α and β in the intact network. For each candidate value of L_1, we compute the correlation coefficient of the transmission spectrum with that measured on the faulty network. Our estimate of L_1 is then simply the candidate value with the highest correlation coefficient. Our results displayed in Fig. 5 provide an accurate estimate of L_1, orders of magnitude better than the smallest measured wavelength (4.2 m for 49.8 MHz).

Of course, the data analysis method can be refined to endow it with robustness against measurement noise [1] and/or environmental perturbations [17], for example by training an artificial neural network for the wave fingerprint identification,

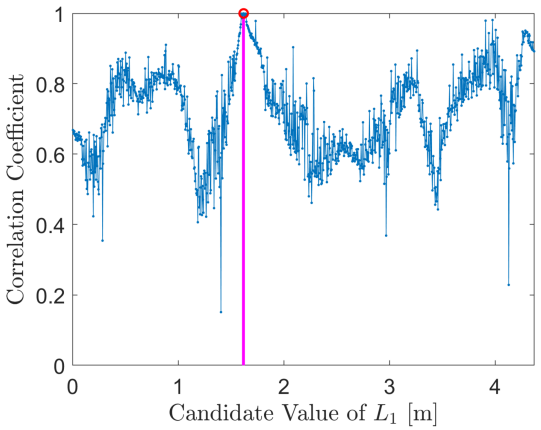

Fig. 5. Demonstration of remote model-based fault localization for the faulty network from Fig. 3. The vertical magenta-colored line indicates the ground-truth value of L_1.

as reported in [1, 17] for localization in a chaotic cavity. The application of these techniques to the localization of faults in transmission-line networks is left for future work. The main purpose of the present work is to demonstrate that in the case of a transmission-line network, wave-fingerprint-based localization techniques can be applied using an efficient physics-compliant model, instead of having to collect experimental calibration data.

7. Conclusions

To summarize, we have derived an analytical expression for the update of a transmission-line network's scattering matrix due to a fault. We found that besides removing the direct connection

between two nodes, a fault also significantly alters the self-interactions of these two nodes in a rather complicated manner. Using the derived physics-compliant model, we *remotely* localized the fault in an example random network with high accuracy based on the faulty network's transmission spectrum. Looking forward, the signal-processing aspects of the methodology can be refined to remove the need for knowing which cable is the faulty one, and to be resilient against noise and environmental perturbations. Naturally, experimental validations at various scales are also envisioned.

References

[1] M. del Hougne, S. Gigan, P. del Hougne, *Phys. Rev. Lett.* **127**, 043903 (2021).

[2] Y. Zhao, J. Chen, H.V. Poor, *IEEE Trans. Smart Grid.* **11**, 555 (2019).

[3] O. Farooq, A. Akhshani, M. Bia lous, S. Bauch, M. Lawniczak, L. Sirko, *Phys. Scr.* **98**, 024005 (2023).

[4] M. Lawniczak, P. Kurasov, S. Bauch, M. Bialous, V. Yunko, L. Sirko, *Phys. Rev. E* **101**, 052320 (2020).

[5] L. Abboud, A. Cozza, L. Pichon, *IEEE Trans. Veh. Technol.* **62**, 1010 (2013).

[6] T. Kottos, U. Smilansky, *Phys. Rev. Lett.* **79**, 4794 (1997).

[7] T. Kottos, U. Smilansky, *J. Phys. A* **36**, 3501 (2003).

[8] O. Hul, S. Bauch, P. Pakoński, N. Savytskyy, K. Zyczkowski, L. Sirko, *Phys. Rev. E* **69**, 056205 (2004).

[9] C. Texier, G. Montambaux, *J. Phys. A* **34**, 10307 (2001).

[10] P. Kuchment, *Waves Random Media* **14**, S107 (2003).

[11] S. Longhi, *Phys. Rev. A* **93**, 022102 (2016).

[12] L. Bunimovich, B. Webb, *Isospectral Transformations*, Springer Monogr. Math., 2014.

[13] J. Sol, M. Röntgen, P. del Hougne, *Adv. Mater.* **2023**, 2303891 (2023).

[14] H. Prod'homme, P. del Hougne, arXiv:2306.00244, 2023, in press at *IEEE Commun. Lett.*.

[15] J. Sol, H. Prod'homme, L. Le Magoarou, P. del Hougne, arXiv:2308.02349, 2023.

[16] P. del Hougne, M.F. Imani, M. Fink, D.R. Smith, G. Lerosey, *Phys. Rev. Lett.* **121**, 063901 (2018).

[17] P. del Hougne, *Phys. Rev. Research* **2**, 043224 (2020).

Proceedings of the 11th Workshop on Quantum Chaos and Localisation Phenomena (CHAOS 23)

On the Density of Complex Eigenvalues of Wigner Reaction Matrix in a Disordered or Chaotic System with Absorption

Y.V. Fyodorov*

King's College London, Department of Mathematics, London WC2R 2LS, United Kingdom

Doi: 10.12693/APhysPolA.144.447 *e-mail: yan.fyodorov@kcl.ac.uk

In an absorptive system, the Wigner reaction K-matrix (directly related to the impedance matrix in acoustic or electromagnetic wave scattering) is non-selfadjoint, hence its eigenvalues are complex. The most interesting regime arises when the absorption, taken into account as an imaginary part of the spectral parameter, is of the order of the mean level spacing. I will show how to derive the mean density of the complex K-matrix eigenvalues for the M-channel reflection problem in disordered or chaotic systems with broken time-reversal invariance. The computations have been done in the framework of the nonlinear σ-model approach, assuming fixed M and the dimension of the underlying Hamiltonian matrix $N \to \infty$. Some explicit formulas are provided for zero-dimensional quantum chaotic system as well as for a semi-infinite quasi-1D system with fully operative Anderson localization.

topics: quantum chaotic scattering, random matrix theory, non-Hermitian matrices.

1. Introduction

Consider the problem of wave scattering from a piece of random medium confined to a spatial domain $\mathcal{D}$ and described by a self-adjoint Hamiltonian H, e.g.,

$$H = \sum_{\boldsymbol{r}\in\boldsymbol{\Lambda}} V(\boldsymbol{r})|\boldsymbol{r}\rangle\langle\boldsymbol{r}| + \sum_{\boldsymbol{r}\sim\boldsymbol{r}'} \Big[t_{\boldsymbol{r}\boldsymbol{r}'}|\boldsymbol{r}\rangle\langle\boldsymbol{r}'| + t_{\boldsymbol{r}'\boldsymbol{r}}|\boldsymbol{r}'\rangle\langle\boldsymbol{r}|\Big], \tag{1}$$

where the second sum runs over nearest neighbours on a lattice $\boldsymbol{\Lambda}$ (assumed to be confined to the domain $\mathcal{D}$). The parameters $t_{\boldsymbol{r}'\boldsymbol{r}}$ are in general complex, satisfying $t^*_{\boldsymbol{r}\boldsymbol{r}'} = t_{\boldsymbol{r}'\boldsymbol{r}}$ to ensure the hermiticity of the Hamiltonian, $H = H^\dagger$, where we use t^* to denote complex conjugation of t and $H^\dagger$ for Hermitian conjugation of H. The disordered nature of the medium is taken into account by choosing the on-site potentials $V(\boldsymbol{r})$ and/or hopping parameters $t_{\boldsymbol{r}'\boldsymbol{r}}$ to be random variables. Such construction is known in the literature as the Anderson model and provides the paradigmatic framework to study single-particle localization phenomena. Note that form (1) can also be used for modelling a quantum particle motion on any graph $\boldsymbol{r} \in \mathfrak{G}$, with $t_{\boldsymbol{r}\boldsymbol{r}'}$ being the elements of the adjacency matrix of graph $\mathfrak{G}$.

The tight-binding representation is convenient as it allows one to think of such a Hamiltonian as described by a large $N \times N$ random matrix H, with N being the number of sites in the lattice or graph. Alternatively, one may think of its continuum analogue, $H = -\frac{\hbar^2}{2m}\nabla^2 + V(\boldsymbol{r})$, $\boldsymbol{r} \in \mathcal{D}$, with the appropriate (e.g., Dirichlet) conditions at the boundary of $\mathcal{D}$. In fact, under appropriate conditions, the essentially random nature of wave scattering can be generated by an irregularly shaped boundary of the domain $\mathcal{D}$, without any intrinsic potential disorder. This is the standard case in the so-called wave billiards, the paradigmatic toy systems for studying the effects of quantum or wave chaos, see, e.g., [1–4]. In such a case, the famous Bohigas–Giannoni–Schmit conjecture [5] allows one to describe universal features of such systems efficiently by replacing the Hamiltonian H with a random $N \times N$ matrix from Gaussian ensembles: Gaussian orthogonal (GOE), Gaussian symplectic (GSE), or Gaussian unitary (GUE), depending on the presence or absence of time-reversal symmetry (and/or other relevant symmetries) in the system.

A very convenient framework for describing the scattering of classical or quantum waves from the disordered or chaotic medium has been formulated in [6] (see, e.g., [7] for more detail). Within such a framework, which is frequently called in the literature the "Heidelberg model", one constructs the unitary $M \times M$ energy-dependent scattering matrix $S(E)$ describing the scattering of waves incident on a random medium at some energy E and then exiting it via M open scattering channels, numbered by $c = 1, \ldots, M$ (see Fig. 1). Unitarity reflects the flux conservation, i.e., the vectors $\boldsymbol{a} = (a_1, \ldots, a_M)$ of incoming and $\boldsymbol{b} = (b_1, \ldots, b_M)$ of outgoing amplitudes are linearly related via $\boldsymbol{b} = S(E)\,\boldsymbol{a}$ and have the same norm.

The relation between $S(E)$ and the medium Hamiltonian H is then provided by the following expression

$$S(E)=\frac{\mathbb{1}-\mathrm{i}K(E)}{\mathbb{1}+\mathrm{i}K(E)},\quad K(E)=W^{\dagger}\frac{1}{E-H}W, \tag{2}$$

where columns W_c ($c=1,\ldots,M$) of an $N\times M$ matrix W of *coupling amplitudes* to M open scattering channels can be taken as fixed vectors satisfying the orthogonality condition

$$\sum_{i=1}^{N} W^{*}_{ci}W_{bi}=\gamma_c\delta_{cb}, \tag{3}$$

with $\gamma_c>0$ $\forall c=1,\ldots,M$ determining the "bare" strength of coupling of a given channel to the scattering system. The resulting $M\times M$ Hermitian matrix $K(E)$ is known in the literature as the Wigner reaction K-matrix. It is the hermiticity of K which implies S-matrix unitarity and, hence, implies the flux conservation. Note that the Wigner K-matrix is experimentally measurable in microwave scattering systems, as it is directly related to the systems impedance matrix, see, e.g., [8–10].

One of the serious challenges related to the theoretical description of scattering characteristics, however, is related to the fact that experimentally measured quantities suffer from inevitable energy losses (absorption), e.g., due to damping in resonator walls and other imperfections. Such losses violate the unitarity of the scattering matrix and are important for interpretation of experiments, hence considerable efforts were directed towards incorporating them into the Heidelberg approach [11]. At the level of the model (1), the losses can be taken into account by allowing the spectral parameter E to have a finite imaginary part by replacing $E\to(E+\mathrm{i}\alpha)\in\mathbb{C}$ with some $\alpha>0$. This replacement violates the hermiticity of the Wigner matrix $K(E+\mathrm{i}\alpha)$; in particular, entries of K now become complex even for real symmetric choice of H and real W. The most interesting, difficult, and experimentally relevant regime occurs when absorption parameter α is comparable with the mean separation $\Delta(E)$ between neighbouring eigenvalues of the wave-chaotic Hamiltonian H. For example, if one uses the Gaussian random matrix model for H, normalized to have the mean eigenvalue density given by Wigner semicircle $\nu(E)=\frac{1}{(2\pi)}\sqrt{4-E^2}$ in a finite interval $|E|<2$, one has $\Delta(E)=(\nu(E)N)^{-1}$ as $N\to\infty$. The statistics of the real and imaginary parts of K-matrix entries in such a regime have been the subject of a considerable number of theoretical papers [12–16] and are by now well-understood and measured experimentally with good precision for systems with preserved time-reversal invariance in microwave cavities [8–10, 17] and microwave simulations of quantum graphs [18–21]. More recently, experimental results for K-matrices in systems with broken time-reversal invariance [22, 23] and eventually symplectic symmetry [24] have been also reported.

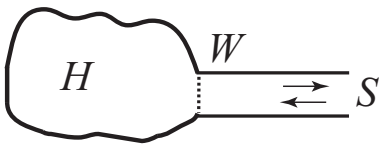

Fig. 1. A sketch of a chaotic wave scattering from a region schematically represented by a cavity and assumed to contain a random medium inside. An operator governing wave dynamics in such a cavity decoupled from the channels is assumed to be effectively described by a large random matrix H. An infinite lead is assumed to support M propagating channels in the considered energy range and is coupled to the cavity region by a matrix/operator W. The ensuing $M\times M$ unitary scattering matrix S can be related to H and W in the framework of the Heidelberg approach and is given by (1).

In the present paper, we will be interested in yet another characteristic of the non-Hermitian Wigner matrix $K(E+\mathrm{i}\alpha)$, the mean density of its complex eigenvalues $K_c=\mathrm{Re}(K_c)-\mathrm{i}\,\mathrm{Im}(K_c)$, $\forall c=1,\ldots,M$, defined as

$$\rho_M(u,v;y)=\left\langle\sum_{c=1}^{M}\delta\big(u-\mathrm{Re}(K_c)\big)\,\delta\big(v-\mathrm{Im}(K_c)\big)\right\rangle, \tag{4}$$

where we suppressed the energy dependence for simplicity, indicating instead explicit dependence on the appropriately scaled absorption parameter $y=\frac{2\pi\alpha}{\Delta}$. Here and henceforth, the angular brackets $\langle\ldots\rangle$ indicate the averaging over ensemble of random Hamiltonians H. Note that selecting the coupling vectors W_c coinciding with the first M basis vectors in N-dimensional space, i.e., $W_1=\boldsymbol{e}_1=(1,0,\ldots,0)$, $W_2=\boldsymbol{e}_2=(0,1,0,\ldots,0)$, etc., converts the K-matrix to $M\times M$ top left corner of the $N\times N$ resolvent matrix $(E+\mathrm{i}\alpha-H)^{-1}$. Physically, this corresponds to M perfectly coupled channels attached to the first M sites. From that angle, we aim to characterize the eigenvalue density for the corner resolvent minor at complex values of the spectral parameter, which is an interesting and potentially rich mathematical problem. We are not aware of any systematic studies in that direction.

Note that in a fully chaotic, zero-dimensional system, the positions of channel attachment do not play any role due to inherent ergodicity. In a more general non-ergodic situation, which may arise due to the presence of Anderson localization phenomena, one may think of such an arrangement as corresponding to a wave reflection problem. In such a setting, the density (4) has appeared recently in paper [25] as an important quantity facilitating the computation of the mean density of S-matrix poles, also known as *resonances*, in the complex energy plane. The latter density is experimentally measurable in wave-chaotic system [26, 27] and is a subject of long-standing theoretical interest, see, e.g., [28–34]. Clearly, the density (4) is also experimentally measurable in principle, provided that accurate experimental data can be sampled for the whole K-matrix. The paper [25] included, without

a proper derivation, an explicit expression for such density, valid for a general class of disordered systems with broken time-reversal invariance, namely for those that can be mapped on the so-called supersymmetric nonlinear σ-model (see [35] and discussions in [25] for more information). The present paper aims to fill that gap by providing a detailed derivation, which involves several steps that are only relatively briefly described in the available literature.

To begin with, for the special simplest case $M = 1$, the K-matrix consists of a single element, and finding the density (4) is equivalent to computing the joint probability density of the real and complex parts of such an element. Such density has been originally addressed in [36] via quite tedious calculations in the σ-model approximation. A much more efficient approach has been proposed later in [14] (see also an account in [11]). Our goal in this paper is to show how to generalize that approach to any number of open channels M, on an example of systems with broken time-reversal invariance. Along these lines, we also try to elucidate some features of the method which were omitted in the exposition in [11, 14].

2. Derivation of the main results

2.1. General exposition of the method

Given two real parameters $p \in \mathbb{R}$ and $q > 0$, we start with defining the following object

$$C_\alpha(p,q) := \Big\langle \mathrm{Tr}\left(z - K\big(E+\mathrm{i}\alpha\big)\right)^{-1} \mathrm{Tr}\left(\overline{z} - K\big(E-\mathrm{i}\alpha\big)\right)^{-1} \Big\rangle, \tag{5}$$

where we denoted $z = p + \mathrm{i}q$, $\overline{z} = p - \mathrm{i}q$ and assumed the real energy E and the absorption parameter $\alpha > 0$ to be fixed. As eigenvalues of the matrices $K(E+\mathrm{i}\alpha)$ and $K(E-\mathrm{i}\alpha)$ are complex conjugates of each other, one can write each trace in terms of $K_c = \mathrm{Re}(K_c) - \mathrm{i}\mathrm{Im}(K_c) := u_c - \mathrm{i}v_c$, with $v_c > 0$, representing (5) as a sum of diagonal and off-diagonal contributions

$$C_\alpha(p,q) = C_\alpha^{(\mathrm{diag})}(p,q) + C_\alpha^{(\mathrm{off})}(p,q), \tag{6}$$

where

$$C_\alpha^{(\mathrm{diag})}(p,q) := \Big\langle \sum_{c=1}^{M} \frac{1}{|z-K_c|^2} \Big\rangle = \Big\langle \sum_{c=1}^{M} \frac{1}{(p-u_c)^2+(q+v_c)^2} \Big\rangle, \tag{7}$$

whereas $C_\alpha^{(\mathrm{off})}(p,q)$ is given by

$$C_\alpha^{(\mathrm{off})}(p,q) := \Big\langle \sum_{c\neq c'}^{M} \frac{1}{(z-K_c)(\overline{z}-\overline{K_{c'}})} \Big\rangle = \Big\langle \sum_{c\neq c'}^{M} \frac{1}{u_c - u_{c'} - \mathrm{i}\,(2q+v_c+v_{c'})} \times \Big[\frac{1}{p-u_c+\mathrm{i}\,(q+v_c)} - \frac{1}{p-u_{c'}-\mathrm{i}\,(q+v_{c'})} \Big] \Big\rangle. \tag{8}$$

In the next step, let us introduce the Fourier transform in variable p,

$$\tilde{C}_\alpha(k,q) := \frac{1}{2\pi} \int_{-\infty}^{\infty} \mathrm{d}p\ \mathrm{e}^{\mathrm{i}pk}\, C_\alpha(p,q). \tag{9}$$

Taking into account $q > 0$, $v_c \geq 0\ \forall c$, we get

$$\tilde{C}_\alpha^{(\mathrm{diag})}(k,q) = \Big\langle \frac{1}{2} \sum_{c=1}^{M} \frac{\mathrm{e}^{\mathrm{i}ku_c - |k|(q+v_c)}}{q+v_c} \Big\rangle, \tag{10}$$

whereas the Fourier-transformed off-diagonal part $\tilde{C}_\alpha^{(\mathrm{off})}(k,q)$ now reads

$$\Big\langle \sum\nolimits_{c\neq c'}^{M} (-\mathrm{i}) \Big[u_c - u_{c'} - \mathrm{i}(2q+v_c+v_{c'}) \Big]^{-1} \times \Big[\theta(-k)\, \mathrm{e}^{\mathrm{i}ku_c + k(q+v_c)} + \theta(k)\, \mathrm{e}^{\mathrm{i}ku_{c'} - k(q+v_{c'})} \Big] \Big\rangle, \tag{11}$$

where $\theta(k) = 1$ for $k \geq 0$ and zero otherwise.

The next step is to continue analytically in the parameter q from positive real values to the whole complex plane slit along the negative real line $q = -v$, $v > 0$, and evaluate the jump across the slit, defined as

$$\delta\tilde{C}_\alpha(k, v{>}0) := \lim_{\epsilon\to 0} \Big(\tilde{C}_\alpha(k, -v - \mathrm{i}\epsilon) - \tilde{C}_\alpha(k, -v + \mathrm{i}\epsilon) \Big). \tag{12}$$

For the diagonal part one finds after straightforward algebra

$$\delta\tilde{C}_\alpha^{(\mathrm{diag})}(k, v>0) = \mathrm{i} \lim_{\epsilon\to 0} \Big\langle \sum_{c=1}^{M} \mathrm{e}^{\mathrm{i}ku_c + |k|(v-v_c)} \left(\frac{\epsilon\cos(\epsilon|k|)}{\epsilon^2 + (v-v_c)^2} - \frac{\sin(\epsilon|k|)(v-v_c)}{\epsilon^2 + (v-v_c)^2} \right) \Big\rangle, \tag{13}$$

which upon using

$$\lim_{\epsilon\to 0} \left[\frac{\epsilon\cos(\epsilon|k|)}{\epsilon^2+(v-v_c)^2} - \frac{\sin(\epsilon|k|)(v-v_c)}{\epsilon^2+(v-v_c)^2} \right] = \pi\, \delta(v-v_c) \tag{14}$$

reduces the diagonal contribution to

$$\delta\tilde{C}_\alpha^{(\mathrm{diag})}(k, v{>}0) = \mathrm{i}\pi \Big\langle \sum_{c=1}^{M} \mathrm{e}^{\mathrm{i}ku_c}\, \delta(v-v_c) \Big\rangle. \tag{15}$$

At the same time, straightforward computations show that assuming that the eigenvalues of the K-matrix are all distinct, i.e., $u_c - \mathrm{i}v_c \neq u'_c - \mathrm{i}v_{c'}$ for $c \neq c'$, the off-diagonal part does not generate any non-vanishing jump across the slit at $q = -v$, $v{>}0$, that is $\delta\tilde{C}_\alpha^{(\mathrm{off})}(k, v{>}0) = 0$. Finally, applying in (15) the inverse Fourier transform in the variable k and comparing with the definition (4) provides the expression for the density of complex eigenvalues of the K-matrix in the form

$$\rho_M(u,v;y) = \int_{-\infty}^{\infty} \frac{\mathrm{d}k}{2\mathrm{i}\pi^2}\ \mathrm{e}^{-\mathrm{i}ku}\, \delta\tilde{C}_{\alpha=\frac{y\Delta}{2\pi}}(k, v{>}0). \tag{16}$$

In this way, the problem of computing the density $\rho_M(u,v;y)$ is reduced to the ability to evaluate explicitly the correlation function $C_\alpha(p, q > 0)$ in (5) and perform the required Fourier transforms

and jump evaluation. Below, we show how this program is executed for those disordered or chaotic systems with broken time-reversal invariance, which can be mapped onto the corresponding nonlinear σ-model.

2.2. Computations for systems with broken time-reversal invariance

Referring the interested reader to [25] and references therein for a detailed discussion of physical assumptions behind such mapping, we only mention here that it provides the most powerful and systematic approaches to addressing universal single-particle features of wave propagation in a disordered medium, including Anderson localization phenomena. Developed in the seminal works by Efetov [35] building on earlier ideas of Wegner [37], the model is defined by specifying a weight function $\mathrm{e}^{-\mathcal{S}[Q]}$, with the action $\mathcal{S}[Q]$ describing interaction between supermatrices $Q(\boldsymbol{r})$ (i.e., matrices with Grassmann/anticommuting/fermionic and ordinary/commuting/bosonic entries) associated to every site $\boldsymbol{r} \in \tilde{\boldsymbol{\Lambda}}$ located on an auxiliary lattice $\tilde{\boldsymbol{\Lambda}}$. The size of the supermatrices involved depends on the underlying symmetries of the Hamiltonian H and in the simplest case of the Hamiltonians with fully broken time-reversal symmetry, denoted in the standard nomenclature as class A with Dyson parameter $\beta = 2$, the supermatrices are of the size 4×4. Physically, such a model provides, in a certain sense, a coarse-grained description of the original microscopic Anderson model or its continuous equivalent, with non-universal features on scales smaller than the mean free path l being effectively integrated out. In such a picture, every (super)matrix $Q(\boldsymbol{r})$ associated with a single lattice site in $\tilde{\boldsymbol{\Lambda}}$ "lumps together" behaviour of the microscopic model on scales of the order of the mean free path l. From this point of view, the billiards in the quantum chaotic regime, where essentially l is of the same order as the system length L, are effectively characterized by nonlinear σ-models with a single matrix Q without any spatial dependence. Such a limit is traditionally called "zero-dimensional". At the same time, all effects of the Anderson localization require considering extended lattices of interacting Q-matrices.

One of the central objects of such theory turns out to be the so-called "order parameter function" (OPF) $F_{\boldsymbol{r}}(Q)$, which is formally defined [38] by integrating the weight $\mathrm{e}^{-\mathcal{S}[Q]}$ over all but one supermatrix $Q(\boldsymbol{r})$. Due to global symmetries of the action, the OPF can be shown to actually depend on only a few real Cartan variables parametrizing Q matrices. In particular, for systems with broken time-reversal symmetry, one has $F_{\boldsymbol{r}}(Q) := \mathcal{F}(\lambda, \lambda_1)$, with $\lambda \in [-1, 1]$ and $\lambda_1 \in [1, \infty]$ being the compact and non-compact coordinates, respectively (we omitted spatial dependence on $\boldsymbol{r}$ for brevity). Note that the OPF characterizes the *closed* system, which (in the absence of absorption) conserves the number of particles, whereas allowing particles/waves at a given energy to be sent via the lead to the random medium and then collecting the reflected waves renders the medium *open*. However, if one makes an assumption of "locality" of the lead, whose transverse extent is assumed to be much smaller than the mean free path l in the disordered medium, then the coupling with it is effectively point-wise at the level of σ-model description. Still, even such point-wise lead may support arbitrarily many propagation channels M, though we will always assume that M remains negligible to the number of sites in the underlying microscopic lattice $\boldsymbol{\Lambda}$.

The power of nonlinear σ-model description in our case lies in our ability to provide an explicit representation for the correlation function $C_\alpha(p, q)$ defined in (5) in terms of the OPF $\mathcal{F}(\lambda, \lambda_1)$ at the point of lead attachment. For systems with broken time-reversal invariance, such computation has already been performed in [7], albeit formally only in the "zero-dimensional" limit, with OPF taking an especially simple form $\mathcal{F}(\lambda, \lambda_1) = \mathrm{e}^{-y(\lambda_1 - \lambda)}$, where, as before, $y = 2\pi\alpha/\Delta$ is the effective absorption parameter. It is, however, straightforward to adapt the calculation for arbitrary nonlinear sigma-model (see Appendix B of [11]), the result being given by the sum of two contributions, the disconnected one

$$C_\alpha^{(\mathrm{disc})}(p, q) = \sum_{c=1}^{M} \frac{1}{p - \gamma_c \frac{E}{2} - \mathrm{i}\left(q + \pi\,\nu(E)\gamma_c\right)} \sum_{b=1}^{M} \frac{1}{p - \gamma_c \frac{E}{2} + \mathrm{i}\left(q + \pi\,\nu(E)\gamma_b\right)} \tag{17}$$

and the connected one

$$C_\alpha^{(\mathrm{con})}(p, q) = \int_{-1}^{1} \mathrm{d}\lambda \int_{1}^{\infty} \mathrm{d}\lambda_1 \, \frac{\mathcal{F}(\lambda, \lambda_1)}{(\lambda_1 - \lambda)^2} \, \mathcal{R}_M(p, q|\lambda, \lambda_1), \tag{18}$$

where the last factor in (18) is given by

$$\mathcal{R}_M(p, q|\lambda, \lambda_1) := \mathcal{L}_{p,q} \prod_{c=1}^{M} \frac{\left(p - \gamma_c \frac{E}{2}\right)^2 + q^2 + 2\pi\,\nu(E)\gamma_c\lambda + \left(\pi\,\nu(E)\,\gamma_c\right)^2}{\left(p - \gamma_c \frac{E}{2}\right)^2 + q^2 + 2\pi\,\nu(E)\,\gamma_c\lambda_1 + \left(\pi\,\nu(E)\gamma_c\right)^2} \tag{19}$$

with the coupling coefficients γ_c defined in (3) and the differential operator $\mathcal{L}_{p,q} := \frac{1}{4}\left(\frac{\partial^2}{\partial p^2} + \frac{\partial^2}{\partial q^2}\right)$.

These expressions provide the basis for implementing the analytic continuation procedure described above. For simplicity, we consider below explicitly only the case $E = 0$, so that $\pi\nu(E) = 1$, and largely concentrate on the simplest, yet important, case of equivalent channels, namely $\gamma_c = \gamma$, $\forall c = 1, \ldots, M$[†1]. The analytic continuation procedure for the disconnected part amounts to a straightforward repetition of our derivation of (16) and yields $\rho^{(\mathrm{disc})}(u,v) = \sum_{c=1}^{M} \delta(u)\,\delta(v-\gamma_c)$. The connected contribution to the density is much less trivial, and we consider it below.

One starts with rewriting (19) in the form

$$\mathcal{R}_M(p,q|\lambda,\lambda_1) = \mathcal{L}_{p,q}\left(1-\tfrac{2q\gamma(\lambda_1-\lambda)}{p^2+q^2+2\gamma_c\lambda_1+\gamma_c^2}\right)^M, \tag{20}$$

which after expanding the binomial reduces to

$$\mathcal{R}_M(p,q|\lambda,\lambda_1) = -\sum_{l=1}^{M}\left(\begin{array}{c} M \\ l \end{array}\right)\tfrac{(\lambda_1-\lambda)^l}{(l-1)!} \times \tfrac{\partial^{l-1}}{\partial\lambda_1^{l-1}}\mathcal{L}_{p,q}\,\tfrac{2q\gamma}{p^2+q^2+2\gamma_c\lambda_1+\gamma_c^2}. \tag{21}$$

The latter form makes it an easy task to perform the Fourier transform in the variable p assuming $q > 0$, which essentially amounts to making in (21) the replacement

$$\mathcal{L}_{p,q}\,\tfrac{2q\gamma}{p^2+q^2+2\gamma_c\lambda_1+\gamma_c^2} \longrightarrow \phi(k,q),$$

$$\phi(k,q) = \tfrac{\pi\gamma}{2}\left(\tfrac{\partial^2}{\partial q^2}-k^2\right) q\,\tfrac{\exp\left[-|k|\sqrt{q^2+2\gamma\lambda_1 q+\gamma^2}\right]}{\sqrt{q^2+2\gamma\lambda_1 q+\gamma^2}}. \tag{22}$$

Following the procedures described in (12), we now continue analytically in the parameter q from positive real values to the whole complex plane slit along the negative real line $q = -v$, $v > 0$ and we evaluate the associated jump across the slit

$$\delta\phi(k,v{>}0) := \lim_{\epsilon\to 0}\Big(\phi(k,-v-\mathrm{i}\epsilon)-\phi(k,-v+\mathrm{i}\epsilon)\Big), \tag{23}$$

which is easily found to be equal to

$$\delta\phi(k,v{>}0)=\pi\gamma\big(\tfrac{\partial^2}{\partial v^2}-k^2\big)\,\tfrac{v\,\cos\left[k\sqrt{2\gamma\lambda_1 v-v^2-\gamma^2}\right]}{\sqrt{2\gamma\lambda_1 v-v^2-\gamma^2}} \times\theta\big(2\gamma\lambda_1 v-v^2-\gamma^2\big). \tag{24}$$

Straightforward inversion of the Fourier transform in the variable k converts the above into

$$\delta\phi(u,v>0) = \frac{\gamma}{2}\left(\frac{\partial^2}{\partial u^2}+\frac{\partial^2}{\partial v^2}\right) v\,\frac{\delta\left(u-\sqrt{2\gamma\lambda_1 v-v^2-\gamma^2}\right)+\delta\left(u+\sqrt{2\gamma\lambda_1 v-v^2-\gamma^2}\right)}{\sqrt{2\gamma\lambda_1 v-v^2-\gamma^2}}\;\theta(2\gamma\lambda_1 v-v^2-\gamma^2) = \frac{1}{2}\left(\frac{\partial^2}{\partial u^2}+\frac{\partial^2}{\partial v^2}\right)\delta\left(\lambda_1-x_\gamma\right), \tag{25}$$

where $x_\gamma := \frac{u^2+v^2+\gamma^2}{2\gamma\, v}$. Next we trade the derivatives over λ_1 for those over x_γ by the identity

$$\frac{\partial^{l-1}}{\partial\lambda_1^{l-1}}\delta\left(\lambda_1-x_\gamma\right) = (-1)^{l-1}\,\frac{\partial^{l-1}}{\partial x_\gamma^{l-1}}\delta\left(\lambda_1-x_\gamma\right) \tag{26}$$

and in this way arrive at replacing (21) with

$$\tilde{\mathcal{R}}_M(u,v|\lambda,\lambda_1) = -\tfrac{1}{2}\left(\tfrac{\partial^2}{\partial u^2}+\tfrac{\partial^2}{\partial v^2}\right) \times\sum_{l=1}^{M}\left(\begin{array}{c} M \\ l \end{array}\right)\tfrac{(-1)^{l-1}(\lambda_1-\lambda)^l}{(l-1)!}\,\tfrac{\partial^{l-1}}{\partial x_\gamma^{l-1}}\,\delta\left(\lambda_1-x_\gamma\right). \tag{27}$$

With this, (16) and (18) imply the density of K-matrix eigenvalues via

$$\rho^{(\mathrm{con})}(u,v)=\int_{-1}^{1}\frac{\mathrm{d}\lambda}{2\pi}\int_{1}^{\infty}\mathrm{d}\lambda_1\,\frac{\mathcal{F}(\lambda,\lambda_1)}{(\lambda_1-\lambda)^2}\,\tilde{\mathcal{R}}_M(u,v|\lambda,\lambda_1), \tag{28}$$

which upon substituting (27) into it and changing the order of integrations yields

$$\rho^{(\mathrm{con})}(u,v)=\frac{1}{4\pi}\left(\frac{\partial^2}{\partial u^2}+\frac{\partial^2}{\partial v^2}\right)\int_{-1}^{1}\mathrm{d}\lambda\,G_M(\lambda|x_\gamma). \tag{29}$$

Here we denoted

$$G_M(\lambda|x_\gamma) := \sum_{l=1}^{M}\left(\begin{array}{c} M \\ l \end{array}\right)\tfrac{(-1)^{l-1}}{(l-1)!} \times\tfrac{\partial^{l-1}}{\partial x_\gamma^{l-1}}\Big[(x_\gamma-\lambda)^l T(\lambda|x_\gamma)\Big], \tag{30}$$

with

$$T(\lambda|x_\gamma) = \frac{\mathcal{F}(\lambda,x_\gamma)}{(x_\gamma-\lambda)^2}. \tag{31}$$

Applying the Leibnitz formula

$$\tfrac{\partial^{l-1}}{\partial x_\gamma^{l-1}}\Big[(x_\gamma-\lambda)^l\,T(\lambda|x_\gamma)\Big] = \sum_{k=0}^{l-1}\left(\begin{array}{c} l-1 \\ k \end{array}\right)\tfrac{l!}{(k+1)!}(x_\gamma-\lambda)^{k+1}\,\tfrac{\partial^k}{\partial x_\gamma^k}\,T(\lambda|x_\gamma) \tag{32}$$

and substituting it back to (30) one may change the order of summation as

$$G_M(\lambda|x_\gamma) = \sum\nolimits_{l=1}^{M} A_l \sum\nolimits_{k=0}^{l-1} B_{k,l}V_k = \sum\nolimits_{-}k=0^{M-1}V_k\sum\nolimits_{l=k+1}^{M}A_l B_{k,l} \tag{33}$$

with $V_k := (x_\gamma-\lambda)^{k+1}\,\frac{\partial^k}{\partial x_\gamma^k}T(\lambda|x_\gamma)$ and

$$A_l := \left(\begin{array}{c} M \\ l \end{array}\right)\frac{(-1)^{l-1}}{(l-1)!},\quad B_{k,l} := \left(\begin{array}{c} l-1 \\ k \end{array}\right)\frac{l!}{(k+1)!}. \tag{34}$$

[†1] However, see expression (42) for two non-equivalent channels.

This gives

$$\sum_{l=k+1}^{M} A_l B_{k,l} = \frac{M!}{k!(k+1)!}\sum_{l=k+1}^{M}\frac{(-1)^{l-1}}{(M-l)!}\frac{1}{(l-k-1)!} = \frac{(-1)^k\, M!}{(M-k-1)!k!(k+1)!}\sum_{n=0}^{M-k-1}(-1)^n\binom{M-k-1}{n} = \frac{(-1)^{M-1}}{(M-1)!}\,\delta_{k,M-1} \tag{35}$$

using the Kronecker symbol $\delta_{k,k'}$, since the sum over n is vanishing for all $0 \le k < M-1$, and is equal to unity at $k = M-1$.

As a result, we get the final expression for the connected part of the mean density of K-matrix eigenvalues in the form

$$\rho_M^{(\mathrm{con})}(u,v) = \frac{1}{4\pi}\frac{(-1)^{M-1}}{(M-1)!}\left(\frac{\partial^2}{\partial u^2}+\frac{\partial^2}{\partial v^2}\right) \times \int_{-1}^{1} \mathrm{d}\lambda\, (x_\gamma-\lambda)^M \frac{\partial^{M-1}}{\partial x_\gamma^{M-1}}\frac{\mathcal{F}(\lambda,x_\gamma)}{(x_\gamma-\lambda)^2}. \tag{36}$$

A few remarks are here in order to help properly interpret and appreciate the content of (36).

Remark 1. Recalling from (25) that

$$x_\gamma = \frac{u^2+v^2+\gamma^2}{2\gamma\, v} \equiv \frac{u^2}{2\gamma\, v} + \frac{1}{2}\left(\frac{v}{\gamma}+\frac{\gamma}{v}\right) \ge 1, \tag{37}$$

one may straightforwardly check that for any smooth enough function $\Phi(x)$ holds

$$\left(\frac{\partial^2}{\partial u^2}+\frac{\partial^2}{\partial v^2}\right)\Phi(x_\gamma) = \frac{1}{v^2}\frac{\partial}{\partial x_\gamma}(x_\gamma^2-1)\frac{\partial}{\partial x_\gamma}\Phi(x_\gamma) \tag{38}$$

for $x_\gamma > 1$. This exact form was used to represent the density in [25].

There is, however, a subtlety in (36) related to its content at $x_\gamma \to 1$. In our derivation, we tacitly assumed $x_\gamma > 1$. However, a more careful analysis shows that the integral in (36) should be pre-multiplied with the step-function factor $\theta(x_\gamma - 1)$ arising as the result of performing integration over $\lambda_1 \in [1,\infty)$ with the factor $\delta(\lambda_1 - x_\gamma)$. The presence of such a seemingly innocent θ-factor has, however, important consequences — when acted upon with the differential operator on the right-hand side of (38), it generates the δ-function factors exactly cancelling the contribution from the disconnected part, $\rho^{(\mathrm{disc})}(u,v) = \sum_{c=1}^{M}\delta(u)\,\delta(v-\gamma_c)$. As a result, the formula (36) as it is written (i.e., without θ-factor) in fact gives the full, properly normalized, eigenvalue density for the K-matrix in absorptive systems. A similar mechanism of cancellation of δ-terms has been first noticed in [39], and we explain in Appendix A how it works in our case using the simplest case of $M = 1$ as an example.

Remark 2. With hindsight, one may notice that one could have arrived at the same expression (36) by a much simpler procedure. Namely, by defining

$$\tilde{x} := \frac{p^2+q^2+\gamma^2}{2\gamma\, q}, \tag{39}$$

Fig. 2. A sketch of the "quasi-1D" model. The left part in grey represents an infinite-length ideal lead supporting M propagating modes. The disordered part is of a finite length L and contains finite concentration of random impurities inside.

rewriting (20) in the form

$$\mathcal{R}_M(p,q|\lambda,\lambda_1) = \frac{1}{4q^2}\frac{\partial}{\partial\tilde{x}}(\tilde{x}^2-1)\frac{\partial}{\partial\tilde{x}}\left(\frac{\tilde{x}+\lambda}{\tilde{x}+\lambda_1}\right)^M. \tag{40}$$

Then one must simply replace $u \to p$, $q \to -v - \mathrm{i}0$, implying $\tilde{x} \to -x_\gamma + \mathrm{i}0$, and calculate the associated jump across the cut using

$$\mathrm{Im}\left[\left(\frac{-x_\gamma+\mathrm{i}0+\lambda}{-x_\gamma+\mathrm{i}0+\lambda_1}\right)^M\right] = (x_\gamma-\lambda)^M\,\frac{(-1)^{M-1}}{(M-1)!} \times\frac{\partial^{M-1}}{\partial x_\gamma^{M-1}}\,\mathrm{Im}\left[\frac{1}{x_\gamma-\lambda_1-\mathrm{i}0}\right] = \pi(x_\gamma-\lambda)^M\,\frac{(-1)^{M-1}}{(M-1)!}\,\frac{\partial^{M-1}}{\partial x_\gamma^{M-1}}\,\delta(x_\gamma-\lambda_1). \tag{41}$$

Such a recipe is exactly the same as the one employed for $M = 1$ in [14], though without a proper explanation provided there or in the review [11].

Armed with such a recipe, one can easily apply it to the case of non-equivalent channels. General formulas in that case look quite complicated, but in the simplest case of two non-equivalent channels with coupling constants $\gamma_1 \ne \gamma_2$, one gets a relatively compact expression

$$\rho_{\gamma_1,\gamma_2}(u,v) = \frac{1}{4\pi}\left(\frac{\partial^2}{\partial u^2}+\frac{\partial^2}{\partial v^2}\right) \times\int_{-1}^{1}\mathrm{d}\lambda\left\{\left[\frac{\mathcal{F}(\lambda,x_1)}{x_2-\lambda_2}+\frac{\mathcal{F}(\lambda,x_2)}{x_1-\lambda_1}\right]-\frac{\left[\mathcal{F}(\lambda,x_1)-\mathcal{F}(\lambda,x_2)\right]}{x_1-x_2}\right\}, \tag{42}$$

where we defined

$$x_1 = \frac{u^2+v^2+\gamma_1^2}{2\gamma_1\, v}, \qquad x_2 = \frac{u^2+v^2+\gamma_2^2}{2\gamma_2\, v}. \tag{43}$$

Remark 3. It is clear that performing further analysis of (36) hinges on our ability to have a good understanding of the OPF $\mathcal{F}(\lambda,x)$ for the closed counterpart of the scattering system, which in general also depends on the (appropriately normalized) absorption parameter α. Such knowledge is currently available mainly in two cases: (i) the "zero-dimensional" limit, with OPF taking an especially simple form $\mathcal{F}^{(0\mathrm{d})}(\lambda,x) = \mathrm{e}^{-y(x-\lambda)}$, where, as before, $y = 2\pi\alpha/\Delta$, and (ii) in a (semi) infinite quasi-one-dimensional wire (see Fig. 2) of length $L \to \infty$, with one edge closed for the waves and second edge attached to an infinite waveguide with M propagating channels.

Such a wire is characterized by a classical microscopic diffusion constant D related to the localization length ξ of the quantum wave problem as

$\xi = 2\pi\nu D$, with ν being, as before, the mean eigenvalue density at a given energy. Note that mathematically such wires can be modelled by a large banded random matrix [40, 41]. In such a system, the OPF at points close to its edges has been originally found in [42] and takes the following form in terms of the modified Bessel functions $I_p(z), K_p(z)$,

$$\mathcal{F}^{(1D)}(\lambda, x) = b\, K_0(a)\, I_1(b) + a\, K_1(a)\, I_0(b), \tag{44}$$

with

$$a = \kappa\sqrt{(x+1)/2}, \qquad b = \kappa\sqrt{(\lambda+1)/2}, \tag{45}$$

where the parameter κ is related to the absorption α as

$$\kappa = \sqrt{8\alpha/\Delta_\xi}, \tag{46}$$

with an important energy scale $\Delta_\xi = (4\pi^2 D\nu^2)^{-1} = D/\xi^2$ giving the mean level spacing in the quasi-one-dimensional wires whose length L is equal to the localization length ξ.

In the "zero-dimensional" limit, due to a simple form of the order parameter function, one can relatively straightforwardly perform the required integrations and differentiations in (36) and get the explicit formulas, which we present below for the simplest cases $M = 1$ and $M = 2$ of equivalent channels

$$\rho_{0D,M=1}(u,v) = \frac{1}{2\pi v^2}\, e^{-x_\gamma} \Big[y\cosh(y) - \sinh(y)(1 - y x_\gamma) \Big] \tag{47}$$

and

$$\rho_{0D,M=2}(u,v) = \frac{1}{2\pi v^2}\, e^{-x_\gamma}\, \sinh(y) \big[y(x_\gamma^2 - 1) - 2x_\gamma \big] + \frac{1}{\pi v^2}\, e^{-x_\gamma} \Big[y\cosh(y) - \sinh(y)\big(1 - y x_\gamma\big) \Big], \tag{48}$$

with the same definition of x_γ (see (37)). The formula equivalent to (47) appeared already in the literature (see Eq. (5) in [13]), but the two-channel case seems to be new. As to the quasi-1D system of infinite length, it turns out that again the results can be found explicitly in the general case. Below we present it only for the simplest case of a single attached channel, when the density acquires quite an elegant form after manipulations outlined in Appendix B of this paper

$$\rho_{1D,M=1}(u,v) = \tfrac{1}{2\pi v^2} P_0(x_\gamma),$$

$$P_0(x) = \tfrac{\kappa^2}{4} \left[I_2(\kappa)\, K_0\left(\kappa\sqrt{\tfrac{x+1}{2}}\right) + I_1(\kappa)\sqrt{\tfrac{x+1}{2}} \times K_1\left(\kappa\sqrt{\tfrac{x+1}{2}}\right) \right]. \tag{49}$$

As is shown in [13], for $M = 1$ and $\gamma = 1$ the variable $r = (x-1)/(x+1)$ is nothing else but the modulus of the reflection coefficient, which in the absorptive system is smaller than one. Correspondingly, the function $P_0(x)$ in (49) provides the distribution for x, hence for r, in a single-channel quasi-1D system with absorption. This complements a result for the same geometry in the case of no absorption inside the sample, but for the second edge of the sample being in contact with perfectly absorbing lead, see Eqs. (12)–(13) in [12]. Note also that it is not difficult to further integrate the variable u, getting an explicit formula for the distribution of variable v, known as the local density of states, corresponding to locations close to the edge of the sample. The latter is an important characteristic of disordered single-particle systems, see [36, 43, 44].

3. Conclusions

In conclusion, we derived the mean density of complex eigenvalues for random Wigner reaction K-matrices for absorptive disordered or chaotic systems with broken time-reversal invariance, in the σ-model approximation. Extension of these results to systems with preserved time-reversal invariance (and then eventually symplectic symmetry) is certainly possible along similar lines, generalizing $M = 1$ results presented in [11]. These subjects are left for future publications.

Acknowledgments

This research has been supported by the EPSRC Grant EP/V002473/1 "Random Hessians and Jacobians: theory and applications".

Appendix A: Cancellation of the disconnected part

Our starting point is the formula (36) with included θ-factor, specified for simplicity and transparency to the case of a single channel $M = 1$ and $\gamma = 1$, so that $x_{\gamma=1} = x$. We write it in the form

$$\rho^{(\mathrm{con})}_{M=1}(u,v) = \frac{1}{4\pi v^2}\, \mathcal{L}_x \left[\theta(x-1)\, \Phi(x) \right], \qquad \Phi(x) = \int_{-1}^{1} \mathrm{d}\lambda\, \frac{\mathcal{F}(\lambda, x)}{(x-\lambda)}, \tag{50}$$

where we introduce the differential operator

$$\mathcal{L}_x := \frac{\partial}{\partial x}(x^2-1)\, \frac{\partial}{\partial x}. \tag{51}$$

Straightforward differentiation then gives

$$\mathcal{L}_x \big[\theta(x-1)\, \Phi(x) \big] = \theta(x-1)\, \mathcal{L}_x\, \Phi(x) + \delta(x-1) \Big[2x\, \Phi(x) + 2(x^2-1)\, \Phi'(x) \Big] + \delta'(x-1) \Big[(x^2-1)\, \Phi(x) \Big]. \tag{52}$$

Further using the integration by parts identity

$$\delta'(x-1) \big[(x^2-1)\, \Phi(x) \big] = -\delta(x-1)\, \frac{\mathrm{d}\left[(x^2-1)\, \Phi(x) \right]}{\mathrm{d}x} = -\delta(x-1) \Big[2x\, \Phi(x) + (x^2-1)\, \Phi'(x) \Big] \tag{53}$$

we conclude that

$$\mathcal{L}_x\big[\theta(x-1)\,\Phi(x)\big] = \delta(x-1)\,\big[(x^2-1)\,\Phi'(x)\big] + \theta(x-1)\mathcal{L}_x\,\Phi(x), \tag{54}$$

so it remains to evaluate $\lim_{x\to 1}[(x^2-1)\,\Phi'(x)]$. To this end, we notice that it can be generally shown that $\lim_{x\to 1}\mathcal{F}(\lambda,x)=1$, hence from (50) we have $\Phi(x\to 1)\approx \int_{-1}^{1}\mathrm{d}\lambda\,\frac{1}{(x-\lambda)} = \ln[\frac{x+1}{x-1}]$, which immediately implies $\lim_{x\to 1}[(x^2-1)\,\Phi'(x)]=-2$. This gives the singular contribution to the density (50) in terms of the variables u,v, as follows

$$-\tfrac{2}{4\pi v^2}\,\delta\left(\tfrac{u^2+v^2+1}{2v}-1\right) = -\tfrac{1}{\pi v}\,\delta\left(u^2+(v-1)^2\right) = -\delta(u)\,\delta(v-1), \tag{55}$$

which exactly cancels the contribution from the disconnected part.

Appendix B

In this appendix, we show how (44), when substituted into (36), implies (49). Throughout this appendix, we again use $x_\gamma = x$ and $\mathcal{L}_x := \frac{\partial}{\partial x}(x^2-1)\frac{\partial}{\partial x}$. First of all, we use the identity (45) from the paper [25], which claims that

$$\tfrac{\partial}{\partial\kappa}\mathcal{F}^{(1\mathrm{D})}(\lambda,x) = -\tfrac{\kappa(x-\lambda)}{2}K_0\left(\kappa\sqrt{\tfrac{x+1}{2}}\right)I_0\left(\kappa\sqrt{\tfrac{\lambda+1}{2}}\right). \tag{56}$$

By differentiating both sides of (36) over κ and using (56) in the right-hand side yields

$$\tfrac{\partial}{\partial\kappa}\rho_{1\mathrm{D},M=1}(u,v) = -\tfrac{1}{8\pi v^2}\mathcal{L}_x\left[\kappa\,K_0\left(\kappa\sqrt{\tfrac{x+1}{2}}\right)\times\int_{-1}^{1}\mathrm{d}\lambda\,I_0\left(\kappa\sqrt{\tfrac{\lambda+1}{2}}\right)\right] \tag{57}$$

and after performing the integral by substitution $\lambda = 2z^2-1$, $z\in[0,1]$ find that

$$\tfrac{\partial}{\partial\kappa}\rho^{(\mathrm{con})}_{1\mathrm{D},M=1}(u,v) = -\tfrac{1}{2\pi v^2}\mathcal{L}_x\left[K_0\left(\kappa\sqrt{\tfrac{x+1}{2}}\right)I_1(\kappa)\right] = -\tfrac{1}{2\pi v^2}\tfrac{\partial}{\partial x}\sqrt{\tfrac{x+1}{2}}\left[\tfrac{1-x}{2}\,\kappa\,I_1(\kappa)\,K_1\left(\kappa\sqrt{\tfrac{x+1}{2}}\right)\right]. \tag{58}$$

In the next step, we employ the following identity (see Sect. 5.54 in p. 624 of [45])

$$\tfrac{1-x}{2}\,\kappa\,I_1(\kappa)K_1\left(\kappa\sqrt{\tfrac{x+1}{2}}\right) = \tfrac{\partial}{\partial\kappa}\left[\kappa I_2(\kappa)K_1\left(\kappa\sqrt{\tfrac{x+1}{2}}\right) + \kappa\sqrt{\tfrac{x+1}{2}}I_1(\kappa)K_2\left(\kappa\sqrt{\tfrac{x+1}{2}}\right)\right]. \tag{59}$$

Using the fact that $\rho^{(\mathrm{con})}_{1\mathrm{D},M=1}(u,v)\to 0$ as $\kappa\to\infty$, we then may conclude that (58) and (59) together imply

$$\rho_{1\mathrm{D},M=1}(u,v) = -\tfrac{1}{2\pi v^2}\tfrac{\partial}{\partial x}\sqrt{\tfrac{x+1}{2}}\kappa\,I_2(\kappa)K_1\left(\kappa\sqrt{\tfrac{x+1}{2}}\right) - \tfrac{1}{2\pi v^2}\tfrac{\partial}{\partial x}\tfrac{x+1}{2}\kappa\,I_1(\kappa)K_2\left(\kappa\sqrt{\tfrac{x+1}{2}}\right) = -\tfrac{1}{2\pi v^2}\left\{\tfrac{I_1(\kappa)}{\kappa}\tfrac{\partial}{\partial x}\left[\kappa^2\tfrac{x+1}{2}K_2\left(\kappa\sqrt{\tfrac{x+1}{2}}\right)\right] + I_2(\kappa)\tfrac{\partial}{\partial x}\left[\kappa\sqrt{\tfrac{x+1}{2}}K_1\left(\kappa\sqrt{\tfrac{x+1}{2}}\right)\right]\right\}. \tag{60}$$

Finally, introducing in the above the variable $z=\kappa\sqrt{\frac{x+1}{2}}$, using the chain rule and the identity (see Sect. 8.846.14 in [45])

$$\frac{\mathrm{d}}{\mathrm{d}z}\big(z^pK_p(z)\big) = -z^pK_{p-1}(z), \tag{62}$$

allows us to bring the density $\rho^{(con)}_{1\mathrm{D},M=1}(u,v)$ to the final form (49).

References

[1] U. Kuhl, O. Legrand, F. Mortessagne, *Fortschr. Phys.* **61**, 414 (2013).

[2] G. Gradoni, J.-H. Yeh, B. Xiao, T.-M. Antonsen, S.-M. Anlage, E. Ott, *Wave Motion* **51**, 606 (2014).

[3] B. Dietz, A. Richter, *Chaos* **25**, 097601 (2015).

[4] H. Cao, J. Wiersig, *Rev. Mod. Phys.* **87**, 61 (2015).

[5] O. Bohigas, M.-J. Giannoni, C. Schmit, *Phys. Rev. Lett.*, **52**, 1 (1984).

[6] J.J.M. Verbaarschot, H.A. Weidenmüller, M.R. Zirnbauer, *Phys. Rep.* **129**, 367 (1985).

[7] Y.V. Fyodorov, H.-J. Sommers, *J. Math. Phys.* **38**, 1918 (1997).

[8] S. Hemmady, X. Zheng, E. Ott, T.M. Antonsen, S.M. Anlage, *Phys. Rev. Lett.* **94**, 014102 (2005).

[9] S. Hemmady, X. Zheng, J. Hart, T.M. Antonsen, E. Ott, S.M. Anlage, *Phys. Rev. E* **74**, 036213 (2006).

[10] X. Zheng, S. Hemmady, T.M. Antonsen, Jr., S. M. Anlage, E. Ott, *Phys. Rev. E* **73**, 046208 (2006).

[11] Y.V. Fyodorov, D.V. Savin, H.-J. Sommers, *J. Phys. A: Math. Gen.* **38**, 10731 (2005).

[12] Y.V. Fyodorov, *JETP Lett.* **78**, 250 (2003).

[13] Y.V. Fyodorov, D.V. Savin, *JETP Lett.* **80**, 725 (2004).

[14] D.V. Savin, H.-J. Sommers, Y.V. Fyodorov, *JETP Lett.* **82**, 544 (2005).

[15] D.V. Savin. Y.V. Fyodorov, H.-J. Sommers, *Acta Phys. Pol. A* **109**, 53 (2006).

[16] S.B. Fedeli, Y.V. Fyodorov, *J. Phys. A Math. Theor.* **53**, 165701 (2020).

[17] R.A. Mendez-Sanchez, U. Kuhl, M. Barth, C.V. Lewenkopf, H.-J. Stöckmann, *Phys. Rev. Lett.* **91**, 174102 (2003).

[18] O. Hul, S. Bauch, P. Pakonski, N. Savytskyy, K. Zyczkowski, L. Sirko, *Phys. Rev. E* **69**, 056205 (2004).

[19] O. Hul, O. Tymoshchuk, S. Bauch, P.M. Koch, L. Sirko, *J. Phys. A* **38**, 10489 (2005).

[20] M. Lawniczak, O. Hul, S. Bauch, P. Seba, L. Sirko, *Phys. Rev. E* **77**, 056210 (2008).

[21] M. Lawniczak, S. Bauch, O. Hul, L. Sirko, *Phys. Rev. E* **81**, 046204 (2010).

[22] M. Lawniczak, L. Sirko, *Sci. Rep.* **9**, 5630 (2019).

[23] M. Lawniczak, B. van Tiggelen, L. Sirko, *Phys. Rev. E* **102**, 052214 (2020).

[24] M. Lawniczak, A. Akhshani, O. Farooq, M. Bialous, S. Bauch, B. Dietz, L. Sirko, *Phys. Rev. E* **107**, 024203 (2023).

[25] Y.V. Fyodorov, M.A. Skvortsov, K.S. Tikhonov, *Ann. Phys.* **460**, 169568 (2024).

[26] U. Kuhl, R. Höhmann, J. Main, H.-J. Stöckmann, *Phys. Rev. Lett.* **100**, 254101 (2008).

[27] L. Chen, S.M. Anlage, Y.V. Fyodorov, *Phys. Rev. Lett.* **127**, 204101 (2021).

[28] V.V. Sokolov, V.G. Zelevinsky, *Nucl. Phys. A* **504**, 562 (1989).

[29] F. Haake, F. Izrailev, N. Lehmann, D. Saher, H.-J. Sommers, *Z. Phys. B Cond. Matt.* **88**, 359 (1992).

[30] Y.V. Fyodorov, H.-J. Sommers, *JETP Lett.* **63**, 1026 (1996).

[31] Y.V. Fyodorov, B.A. Khoruzhenko, *Phys. Rev. Lett.* **83**, 65 (1999).

[32] H.-J. Sommers, Y. V. Fyodorov, M. Titov, *J. Phys. A: Math. Gen.* **32**, L77 (1999).

[33] H. Schomerus, K.M. Frahm, M. Patra, C.W.J. Beenakker, *Physica A* **278**, 469 (2000).

[34] Y.V. Fyodorov, B. Mehlig, *Phys. Rev. E* **66**, 045202(R) (2002).

[35] K.B. Efetov, *Supersymmetry in Disorder and Chaos*, Cambridge University Press, Cambridge 1997.

[36] A.D. Mirlin, Y.V. Fyodorov, *J. de Phys. I* **4**, 655 (1994).

[37] F. Wegner, *Z. Phys. B* **35**, 207 (1979).

[38] M.R. Zimbauer, *Nucl. Phys. B* **265**, 375 (1986).

[39] Y.V. Fyodorov, I. Rozhkov, J.R. Weaver, *Phys. Rev. E* **68**, 016204 (2003).

[40] Y.V. Fyodorov, A.D. Mirlin, *Phys. Rev. Lett.* **67**, 2405 (1991).

[41] Y.V. Fyodorov, A.D. Mirlin, *Int. J. Mod. Phys. B* **8**, 3795 (1994).

[42] M.A. Skvortsov, P.M. Ostrovsky, *Pis'ma Zh. Eksp. Teor. Fiz.* **85**, 79 (2007).

[43] A.D. Mirlin, Y.V. Fyodorov, *Phys. Rev. Lett.* **72**, 526 (1994).

[44] G. Schubert, J. Schleede, K. Byczuk, H. Fehske, D. Vollhardt, *Phys. Rev. B* **81**, 155106 (2010).

[45] L.S. Gradshteyn, I.M. Ryzhik, *Table of Integrals, Series, and Products*, Eds. A. Jeffrey, D. Zwillinger, 6th Ed., Academic Press, 2000.

Proceedings of the 11th Workshop on Quantum Chaos and Localisation Phenomena (CHAOS 23)

On Magnetic Boundary Control for Metric Graphs

P. Kurasov*

Department of Mathematics, Stockholm University, 106 91 Stockholm, Sweden

Doi: 10.12693/APhysPolA.144.456 *e-mail: kurasov@math.su.se

It is investigated how magnetic boundary control can be used to solve inverse problems for Schrödinger operators on metric graphs. Explicit examples show that such reconstruction is sometimes possible, starting from a single contact vertex in the graph.

topics: metric graphs, inverse problems, spectral analysis, boundary control

1. Introduction

The current note is devoted to the boundary control method [1–6] applied to solve inverse problems for magnetic Schrödinger operators on metric graphs [7, 8]. It is well-known that the precise form of the magnetic potential cannot be reconstructed from the spectrum — standard magnetic Schrödinger operators with equal fluxes through the cycles and the same electric potentials are unitary equivalent and hence isospectral. Moreover, the inverse problems for operators with zero magnetic potential cannot always be solved uniquely [9–18] (see also numerous papers devoted to isospectral discrete graphs, e.g., [19–23]). It was proposed in [24] to use magnetic fluxes to enrich the set of spectral data in order to get a unique solution to the inverse problem. The spectral data are given by the spectrum for different values of the magnetic fluxes through the cycles. It was proposed to call this method magnetic boundary control (MBC-method) to underline the role of the magnetic field in the solution of the inverse problem.

In the case of trees (graphs without cycles), the magnetic potential can be removed completely, hence the spectrum is independent of the magnetic potential. The inverse problem is uniquely solvable if the M-function (energy-dependent Dirichlet-to-Neumann map) associated with all degree one vertices is known [25, 26]. The MBC-method for standard operators on graphs with one cycle was considered in [24]. It was proven that the solution to the inverse problem is not unique if the cycle is given by a loop. On the other hand, if the cycle is not a loop, then the solution is unique in the generic case[†1]. Our goal today is to study the MBC-method for graphs with several cycles. It appears that the inverse problem can sometimes be uniquely solved using this new method. We have illustrated our discoveries with a few explicit examples showing both the power of the method and its limitations.

[†1]One should mention that for the lasso graph with other than standard vertex conditions, the inverse problem is uniquely solvable by the MBC-method [27].

2. Metric graphs and standard Schrödinger operators

A finite compact metric graph Γ can be seen as a collection of compact intervals $E_n = [x_{2n-1}, x_{2n}]$, $n = 1, 2, \ldots, N$, called *edges* with the set of end points $\boldsymbol{V} = \{x_j\}_{j=1}^{2N}$ divided into equivalence classes V^m $(m = 1, 2, \ldots, M)$ called *vertices*, so that $\boldsymbol{V} = \bigcup_{m=1}^{M} V^m$ and $V^{m_1} \bigcap V^{m_2} = \emptyset$, provided $m_1 \neq m_2$. Then the metric graph Γ is the union of edges $\Gamma = \bigcup_{n=1}^{N} E_n$ with the end points belonging to the same vertex identified [8].

The corresponding Hilbert space of square-integrable functions on Γ coincides with the orthogonal sum of the spaces of functions on the edges

$$L_2(\Gamma) = \bigoplus_{n=1}^{N} L_2(E_n). \tag{1}$$

Let $q \in L_2(\Gamma)$ and $a \in C(\Gamma \setminus \boldsymbol{V})$ be real-valued electric and magnetic potentials on the edges. Then the standard magnetic Schrödinger operator in $L_2(\Gamma)$ is defined by the differential expression

$$\tau_{q,a} := \left(\mathrm{i}\,\frac{\mathrm{d}}{\mathrm{d}x} + a(x)\right)^2 + q(x) \tag{2}$$

on the functions from

$$W_2^2(\Gamma) = \bigoplus_{n=1}^{N} W_2^2(E_n) \tag{3}$$

satisfying standard vertex conditions at every vertex V^m $(m = 1, 2, \ldots, M)$

$$\begin{cases} u(x_j) = u(u_l), \quad \text{provided} \quad x_j, x_l \in V^m \\ \quad \text{— continuity condition,} \\ \sum_{x_j \in V^m} \partial u(x_j) = 0 \quad \text{— Kirchhoff condition.} \end{cases} \tag{4}$$

Here, $u(x_j)$ and $\partial u(x_j) = (-1)^{j-1} u'(x_j)$ denote the limiting values of the function $u \in W_2^2(\Gamma)$ and its first oriented derivative, respectively. Note that the derivates are taken in the direction pointing inside the corresponding edge and, therefore, are independent of the chosen orientation of the edges.

The main results presented in this paper hold even for potentials $q \in L_1(\Gamma)$, but our presentation will be limited to $L_2(\Gamma)$ potentials for the sake of clarity. The general case has been treated in [8]. We shall also avoid discussing other than standard vertex conditions — the reason is that the elimination of the magnetic potential leads to a change in vertex conditions.

Let us denote the corresponding self-adjoint operator by $L_{q,a}(\Gamma)$. Its spectrum is discrete [7, 8].

The spectrum of $L_{q,a}(\Gamma)$ does not depend on the particular form of the magnetic potential a, but on the magnetic fluxes — the integrals of the magnetic potential along non-trivial cycles C_j in Γ, i.e.,

$$\Phi_j = \int_{C_j} \mathrm{d}y \; a(y), \qquad j = 1, 2, \dots, \beta_1, \tag{5}$$

where β_1 is the first Betti number — the number of independent cycles in Γ.

3. M-function: short introduction

The (scalar) Titchmarsh–Weyl M-function was first introduced to describe spectral properties of one-dimensional Schrödinger operators [28]. For many years, its matrix generalisation has been used to solve inverse problems for operators on metric graphs [25, 29]. It is not our aim to give a rigorous introduction to the theory of M-functions for metric graphs — it is given in [8].

Among all vertices in Γ, we choose a non-empty subset $\partial\Gamma$, which we call the *contact set*. It should be understood that the graph Γ can be approached only via this set. Of course, we are interested in the case when this set is small compared to the set of all vertices in the graph. For any $\lambda \in \mathbb{C} \setminus \mathbb{R}$ consider solutions to the stationary magnetic Schrödinger equation on the edges

$$-\Big(\frac{\mathrm{d}}{\mathrm{d}x} - \mathrm{i}\, a(x)\Big)^2 \psi(\lambda, x) + q(x)\psi(\lambda, x) = \lambda \psi(\lambda, x), \tag{6}$$

satisfying standard conditions (4) at all *internal vertices* $V^m \in \boldsymbol{V} \setminus \partial\Gamma$ and just continuous at the contact vertices $V^m \in \partial\Gamma$. Every such solution is uniquely determined by its values on the contact set. Consider the matrix-valued function, called M-function for the graph Γ and contact set $\partial\Gamma$,

$$M_\Gamma(\lambda) : \boldsymbol{\psi}|_{\partial\Gamma} \mapsto \partial\boldsymbol{\psi}|_{\partial\Gamma}, \tag{7}$$

connecting the values of the solution at the contact vertices $\psi(V^m)$ to the sums of oriented derivatives

$$\partial\boldsymbol{\psi}(V^m) := \sum_{x_j \in V^m} \partial\psi(x_j). \tag{8}$$

This is a matrix-valued Herglotz–Nevanlinna function in λ, i.e., it is analytic outside of the real axis and has a positive imaginary part in the upper half-plane

$$\Im\big(\lambda\big) > 0 \Rightarrow \Im(M_\Gamma(\lambda) := \frac{\big(M_\Gamma(\lambda) - M_\Gamma^*(\lambda)\big)}{2\mathrm{i}} \geq 0. \tag{9}$$

In what follows, we shall also use the Dirichlet Schrödinger operator $L_{q,a}^{\mathrm{D}}(\Gamma)$ — the operator in $L_2(\Gamma)$ defined by the same differential expression, standard vertex conditions at the internal vertices, and Dirichlet conditions at the contact vertices. This operator is again self-adjoint and has a discrete spectrum.

The singularities of the M-function coincide with the spectrum of the Dirichlet operator $L_{q,a}^{\mathrm{D}}(\Gamma)$, while some of the spectrum of $L_{q,a}(\Gamma)$ can be identified using the secular equation $\det M_\Gamma(\lambda) = 0$. The last equation determines those eigenvalues of $L_{q,a}(\Gamma)$, which are not simultaneously eigenvalues of $L_{q,a}^{\mathrm{D}}(\Gamma)$.

The eigenvalues and the normalised (in the original Hilbert space $L_2(\Gamma)$) eigenfunctions of $L_{q,a}(\Gamma)$ and $L_{q,a}^{\mathrm{D}}(\Gamma)$ will be denoted by λ_n, ψ_n and λ_n^{D}, ψ_n^{D}, respectively.

The structure of M-functions for the graph is best seen from the following two explicit formulas [30, 31]

$$M_\Gamma(\lambda) = -\left[\sum_{n=1}^{\infty} \frac{\big\langle \psi_n|_{\partial\Gamma}, \cdot \big\rangle_{\ell_2(\partial\Gamma)} \psi_n|_{\partial\Gamma}}{\lambda_n - \lambda}\right]^{-1}, \tag{10}$$

$$M_\Gamma(\lambda) - M_\Gamma(\lambda') = \sum_{n=1}^{\infty} \frac{\lambda - \lambda'}{(\lambda_n^{\mathrm{D}} - \lambda)(\lambda_n^{\mathrm{D}} - \lambda')} \times \big\langle \partial\psi_n^{\mathrm{D}}|_{\partial\Gamma}, \cdot \big\rangle_{\ell_2(\partial\Gamma)} \partial\psi_n^{\mathrm{D}}|_{\partial\Gamma}. \tag{11}$$

In the above formulas, $\psi_n|_{\partial\Gamma}$ and $\partial\psi_n^{\mathrm{D}}|_{\partial\Gamma}$ denote the function values and the oriented derivative values at the contact vertices, respectively, and $\lambda' \neq \lambda$ is any complex number not lying in the spectra of $L_{q,a}(\Gamma)$ and $L_{q,a}^{\mathrm{D}}(\Gamma)$.

The first formula determines $M_\Gamma(\lambda)$ directly, while the second formula determines only the difference between the values of M-function at two different points. To use the second formula, it is enough to know the degrees d_m of the contact vertices since the M-function possesses the asymptotics

$$M(-s^2) = -s \operatorname{diag}\big\{d_m\big\} + \mathcal{O}(1), \quad s \to \infty. \tag{12}$$

To understand formula (12), consider the boundary control for the Laplace operator ($q(x) = a(x) \equiv 0$). If the boundary control is applied at a degree d_m vertex, then for sufficiently small times the vertex acts as a collection of degree one vertices. The boundary control creates outgoing waves in the

edges joined at the vertex, hence for small times the response is equal to the sum of responses from the degree one vertices. Connectivity between these edges starts to play a role only when the travelling waves return after reflection from the neighbouring vertices. Adding electric and magnetic potentials does not affect the asymptotics.

4. Dissolving a vertex

By solving the inverse problem using the MBC-method, one dissolves high-degree contact vertices. In this section, we shall discuss whether the M-function known for different values of the magnetic fluxes can be used to reconstruct the M-function for the graph where one of the vertices is substituted with several (d_m) degree one vertices.

Definition 1. We say that the metric graph Γ_1 is obtained from a metric graph Γ by dissolving a certain vertex V^0 in Γ if:

- the metric graphs Γ and Γ_1 share the same set of edges $\{E_n\}_{n=1}^N$,
- the end points connected at V^0 in Γ form degree one vertices in Γ_1,
- all other vertices in Γ and Γ_1 coincide.

Let us see Fig. 1, where the dissolving procedure is presented schematically. The green area represents the part of the graph that is not affected by the procedure. The degree four vertex V^0 is substituted with four degree one vertices $V^1, \dots, V^4$.

We restrict our presentation to connected graphs (both Γ and Γ_1 are connected). Then, the number of broken cycles is given by

$$\beta_1(\Gamma) - \beta_1(\Gamma_1) = d_0 - 1. \tag{13}$$

Our goal is to compare the M-functions corresponding to Γ and Γ_1. These functions depend not only on the spectral parameter λ, but on the magnetic fluxes as well. We shall indicate dependence on the fluxes through the broken cycles, assuming that the other fluxes (through preserved cycles) are fixed.

By $V^1, \dots, V^{d_0}$ we denote the pendant vertices in Γ_1 coming from the vertex V^0 in Γ and let C_j be a path connecting V^{d_0} to V^j, $j = 1, 2, \dots, d_0 - 1$. These paths on Γ_1 correspond to the cycles in Γ that are broken under the dissolution. The corresponding fluxes are

$$\Phi_j = \int_{C_j} \mathrm{d}y\ a(y) = \int_{V^{d_0}}^{V^j} \mathrm{d}y\ a(y), \tag{14}$$

where $j = 1, 2, \dots, d_0 - 1$. These fluxes form the vector $\boldsymbol{\Phi}$. It will be convenient to view $\boldsymbol{\Phi}$ as an element of $\mathbb{R}^{d_0}$ despite the fact that only $d_0 - 1$ of its coordinates may be non-zero

$$\boldsymbol{\Phi} = \big(\Phi_1, \Phi_2, \dots, \Phi_{d_0-1}, 0\big). \tag{15}$$

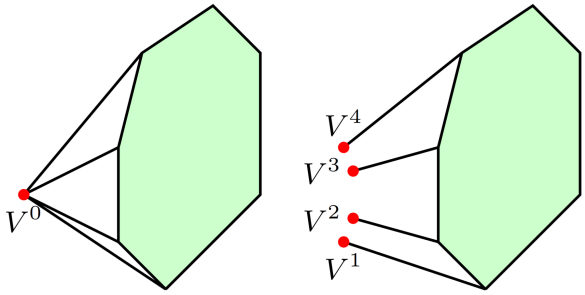

Fig. 1. Dissolving a vertex.

To reconstruct the M-function for Γ_1, it is enough to consider the fluxes equal to 0 and π, therefore we introduce the signs

$$\mu_j := \mathrm{e}^{\mathrm{i}\,\Phi_j}, \qquad j = 1, 2, \dots, d_0;$$
$$\boldsymbol{\mu} = \big(\mu_1, \mu_2, \dots, \mu_{d_0}\big) = \mathrm{e}^{\mathrm{i}\,\boldsymbol{\Phi}}, \tag{16}$$

and consider the M-functions depending on the signs μ_j instead of the phases Φ_j. To get the corresponding spectral data, it is enough to consider the standard operators with zero magnetic potential and additional signing conditions

$$\begin{pmatrix} u(y_j + 0) \\ u'(y_j + 0) \end{pmatrix} = - \begin{pmatrix} u(y_j - 0) \\ u'(y_j - 0) \end{pmatrix} \tag{17}$$

introduced at certain points y_j ($j = 1, 2, \dots, d_0$) on the pendant edges. The sign conditions can be seen as a singular magnetic potential concentrated at the point y_j [32]. These operators will be marked with $L_q^{\mathrm{sign}}(\Gamma)$ and called *signed Schrödinger operators*. We have 2^{d_0-1} different signed operators.

Our first step is to establish the relation between the diagonal element of the M-function associated with Γ and the vertex V^0

$$M_\Gamma^{00}(\lambda, \boldsymbol{\mu}) =: \mathbb{M}(\lambda, \boldsymbol{\mu}) \tag{18}$$

and the diagonal $d_0 \times d_0$ block of the M-function associated with the graph Γ_1 and the degree one vertices coming from V^0. We shall find an explicit relation between the scalar Herglotz–Nevanlinna function $\mathbb{M}(\lambda, \boldsymbol{\mu})$ and the $d_0 \times d_0$ matrix-valued Herglotz–Nevanlinna function $\mathbb{M}_1(\lambda, \boldsymbol{\mu}) := \{M_{\Gamma_1}^{ij}(\lambda, \boldsymbol{\mu})\}_{i,j=1}^{d_0}$.

The dependence of $\mathbb{M}_1(\lambda, \boldsymbol{\mu})$ upon $\boldsymbol{\mu}$ is trivial, namely

$$\mathbb{M}_1(\lambda, \boldsymbol{\Phi}) = \mathrm{diag}\,\{\mu_j\}\,\mathbb{M}_1(\lambda, \mathbf{1})\,\underbrace{\mathrm{diag}\,\{\mu_j\}^{-1}}_{=\mathrm{diag}\,\{\mu_j\}}, \tag{19}$$

where $\mathbf{1} = \big(1, 1, \dots, 1\big)$. To see this, it is enough to eliminate the magnetic potential starting from V^{d_0} using the transformation

$$f(x) \mapsto g(x) = \exp\left[-\mathrm{i}\int_{V^{d_0}}^{x} \mathrm{d}y\ a(y)\right] f(x). \tag{20}$$

The scalar function $\mathbb{M}(\lambda,\boldsymbol{\mu})$ is simply equal to the sum of all entries in $\mathbb{M}_1(\lambda,\boldsymbol{\mu})$

$$\underbrace{\mathbb{M}(\lambda,\boldsymbol{\mu})}_{=M_\Gamma^{00}(\lambda,\boldsymbol{\mu})} = \sum_{i,j=1}^{d_0} \mu_i\mu_j \underbrace{\mathbb{M}_1^{ij}(\lambda,\mathbf{1})}_{=M_{\Gamma_1}^{ij}(\lambda,\mathbf{1})}. \tag{21}$$

This formula determines the M-function for any signed operator on Γ through the M-function for Γ_1.

Let ψ_n^{D} denote the eigenfunction corresponding to zero fluxes through the broken cycles. These eigenfunctions can be chosen to be real-valued. Then, the normal derivatives of the Dirichlet eigenfunctions for non-zero fluxes are given by $\mu_j\partial\psi_n^{\mathrm{D}}(V^j)$, implying in particular that the normal derivative at V^0 is

$$\sum\nolimits_{j=1}^{d_0} \mu_j\partial\psi_n^{\mathrm{D}}(V^j). \tag{22}$$

It follows that the singularity of $\mathbb{M}(\lambda,\boldsymbol{\mu})$ is of the form

$$\mathbb{M}(\lambda,\boldsymbol{\mu}) \underset{\lambda\to\lambda_n^{\mathrm{D}}}{\sim} \frac{1}{\lambda_n^{\mathrm{D}}-\lambda}\sum_{i,j=1}^{d_0}\mu_i\mu_j\,\partial\psi_n^{\mathrm{D}}(V^i)\partial\psi_n^{\mathrm{D}}(V^j) = \frac{1}{\lambda_n^{\mathrm{D}}-\lambda}\left[\sum_{i=1}^{d_0}\left(\partial\psi_n^{\mathrm{D}}(V^i)\right)^2 + \sum_{\substack{i,j=1,\\ i\neq j}}^{d_0}\mu_i\mu_j\,\partial\psi_n^{\mathrm{D}}(V^i)\partial\psi_n^{\mathrm{D}}(V^j)\right], \tag{23}$$

where we have used that $\partial\psi_n^{\mathrm{D}}$ are real-valued.

Introducing the notation $a_j := \partial\psi_n^{\mathrm{D}}(V^j)$, we are faced with the following trivial problem — determine a_j if the numbers

$$(\pm a_1 \pm a_2 \pm \cdots \pm a_{d_0-1} + a_{d_0})^2 \tag{24}$$

are known for all possible combinations of the signs. It is clear that this reconstruction is possible only up to the multiplication of all a_j by -1, which corresponds to the multiplication of the corresponding eigenfunctions by -1.

The sum of the squares can be obtained by averaging over all possible signs

$$\sum_{i=1}^{d_0} a_j^2 = \sum_{\boldsymbol{\mu}\in(\{1,-1\}^{d_0-1},1)} \frac{\left(\mu_1a_1+\mu_2a_2+\ldots+\mu_{d_0-1}a_{d_0-1}+a_{d_0}\right)^2}{2^{d_0-1}}. \tag{25}$$

Hence, we are able to determine the following combinations of a_j's

$$\sum_{\substack{i,j=1,\\ i\neq j}}^{d_0}\mu_i\mu_j\,a_ia_j = \left(\sum_{i=1}^{d_0}\mu_ia_i\right)^2 - \sum_{i=1}^{d_0}a_j^2. \tag{26}$$

We recover the products by averaging a second time

$$a_ka_l = \frac{1}{2^{d_0-1}}\sum_{\substack{\boldsymbol{\mu}\in(\{1,-1\}^{d_0-1},1),\\ \mu_k=\mu_l}}\left(\sum_{\substack{i,j=1,\\ i\neq j}}^{d_0}\mu_i\mu_j\,a_ia_j\right), \tag{27}$$

for $k\neq l$. The product $a_ka_l = a_la_k$ appears in the double sum precisely 2^{d_0-1} times, while all other products cancel since $\mu_i\mu_j$ attains $+1$ and -1 equally many times.

If at least three of the coefficients are non-zero, then the squares a_j^2 are determined as

$$a_i^2 = \frac{(a_ia_j)\,(a_ia_l)}{(a_ja_l)}, \tag{28}$$

provided $a_j, a_l \neq 0$. We are able to recover one non-zero a_j up to a sign, but then all other non-zero coefficients are determined from the products a_ja_i. We conclude that if the squared sums $(\sum_{j=1}^{d_0}\mu_ja_j)^2$ are known for all $\boldsymbol{\mu}$ of the form $\boldsymbol{\mu}\in(\{1,-1\}^{d_0-1},1)$, then the coefficients a_j are determined up to a common sign.

It follows that the diagonal element $\mathbb{M}(\lambda,\boldsymbol{\mu})$ known for all $\boldsymbol{\mu}\in(\{1,-1\}^{d_0-1},1)$ determines the vector

$$\partial\boldsymbol{\psi}_{n\,2}^{\mathrm{D}} := \left(\partial\psi_n^{\mathrm{D}}(V^1),\partial\psi_n^{\mathrm{D}}(V^2),\ldots,\partial\psi_n^{\mathrm{D}}(V^{d_0})\right), \tag{29}$$

up to the common sign, hence the singular part of $\mathbb{M}_1(\lambda,\vec{0})$ is determined, which as before allows us to reconstruct it up to the constant matrix $\mathbb{A}$, yielding

$$\mathbb{M}_1(\lambda,\mathbf{0}) = \mathbb{A} + \sum_{\lambda_n^{\mathrm{D}}(\Gamma_1)}\frac{\lambda-\lambda'}{(\lambda_n^{\mathrm{D}}-\lambda)(\lambda_n^{\mathrm{D}}-\lambda')}\left\langle\boldsymbol{\psi}_{n\,2}^{\mathrm{D}},\cdot\right\rangle\partial\boldsymbol{\psi}_{n\,2}^{\mathrm{D}}. \tag{30}$$

To determine $\mathbb{A}$, we remember that the M-function possesses the asymptotics (12).

We conclude that the M-function for Γ_1 can be recovered, provided the M-functions of all signed operators on Γ are known and the following generically satisfied conditions are fulfilled:

- the spectrum of $L_q^{\mathrm{D}}(\Gamma_1)$ is simple;
- the corresponding eigenfunctions ψ_n^{D} on Γ_1 are either invisible from the involved degree one vertices (all $\partial\psi_n^{\mathrm{D}}(V^j)=0$, $j=1,2,\ldots,d_0$), or at least three normal derivatives $\partial\psi_n^{\mathrm{D}}(V^j)$, $j=1,2,\ldots,d_0$, are different from zero.

5. First examples

In this section, we discuss how to apply the MBC-method to solve inverse problems for metric graphs. We start by presenting examples where the whole graph can be reconstructed starting from a single vertex.

5.1. Example 1

Consider the graph presented in Fig. 2 and assume that the contact set consists of the single vertex V. Let us dissolve the vertex V. The described procedure allows us to determine the M-function associated with the new graph and all its degree one vertices. Conventional boundary control allows us to determine the lengths of the pendant edges and the potential q on them [25]. Then these edges can be peeled away, and we can reduce the inverse problem to a smaller graph, where contact vertices are indicated by red points. By repeating the procedure by dissolving the vertices V' and V'', the inverse problem is reduced to a tree with all pendant vertices in the contact set (see the upper sequence in Fig. 2). The MBC-method allows us to solve the inverse problem for this graph. Note that starting from a single vertex, we recovered both the metric graph Γ and the electric potential q on it.

The inverse problem for this graph can be solved by dissolving the vertices V, V^*, and V^{**} instead (see the lower sequence in Fig. 2). The resulting graph is the cycle with 3 contact points — the inverse problem can again be solved by dismantling the cycle into three intervals.

This example shows that the MBC-method allows us to solve the inverse problem for rather complicated graphs with an arbitrary number of cycles and very few contact points.

5.2. Example 2

Figure 3 presents another graph with a single contact vertex V. After dissolving V and removing the pendant edges, we get the graph with three vertices. We may dissolve only the vertex V' because the remaining two contact vertices have degree two.

This leads to a graph with three contact vertices, namely two degree two vertices and one bottleneck vertex V'' — the dissolution of this vertex would disconnect the graph. The inverse problem for the remaining graph cannot be solved by dismantling it, since the corresponding trees are not independent. Note that the original graph in this example is a slight modification of the graph presented in Fig. 2.

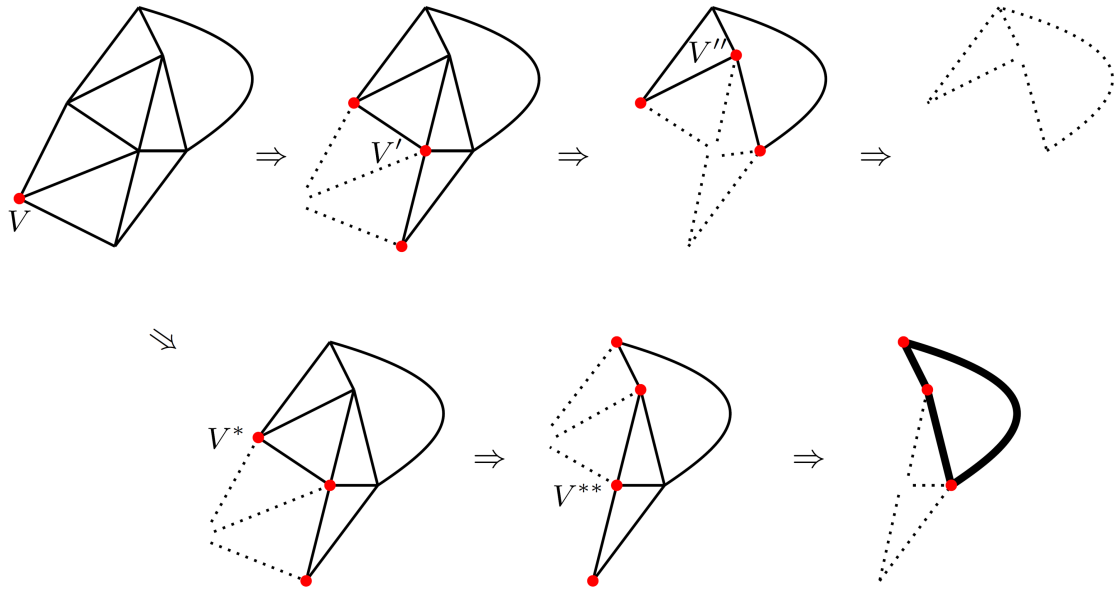

Fig. 2. Reconstruction of the whole graph using the MBC-method.

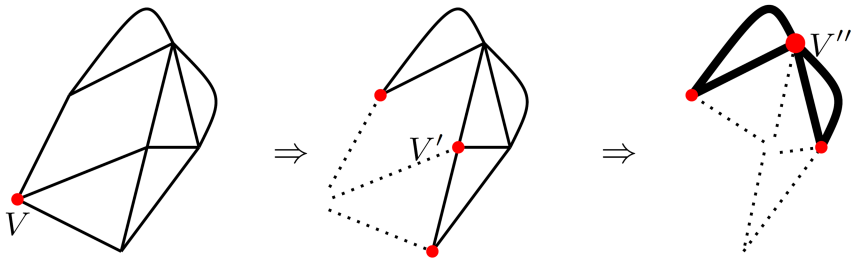

Fig. 3. Reconstruction terminated by the bottleneck.

It is not surprising that not all pendant-free graphs may be reconstructed starting from a single contact vertex — the described procedure may terminate immediately or after a few steps. As the last example shows, there are two reasons for the termination:

- degree two contact vertices,
- bottlenecks.

6. Conclusions

It is shown how magnetic boundary control can be applied to solve inverse problems for Schrödinger equations on metric graphs. It remains to characterise all metric graphs together with contact sets that guarantee solvability of the inverse problem. One may prove explicit theorems characterising the minimal contact sets.

Acknowledgments

This research has been supported by The Swedish Research Council, grant number 2020-03780.

References

[1] S. Avdonin, V. Mikhaylov, A. Rybkin, *Comm. Math. Phys.* **275**, 791 (2007).

[2] M.I. Belishev, *Inverse Probl.* **13**, R1 (1997).

[3] M I Belishev, *Inverse Probl.* **23**, R1 (2007).

[4] M.I. Belishev, *J. Math. Sci.* **155**, 343 (2008).

[5] M.I. Belishev, in: *Dynamical Inverse Problems: Theory and Application*, Vol. 529, Springer Vienna, 2011, p. 85.

[6] A. Rybkin, *Inverse Probl. Imaging* **3**, 139 (2009).

[7] G. Berkolaiko, P. Kuchment, *Introduction to Quantum Graphs, Mathematical Surveys and Monographs*, Vol. 186, American Mathematical Society, Providence (RI) 2013.

[8] P. Kurasov, *Spectral Geometry of Graphs, Operator Theory Advances and Applications*, Birkhäuser/Springer, 2023.

[9] R. Band, G. Berkolaiko, C.H. Joyner, Wen Liu, arXiv:1711.00918 (2017).

[10] R. Band, O. Parzanchevski, G. Ben-Shach, *J. Phys. A* **42**, 175202 (2009).

[11] J. Boman, P. Kurasov, *Adv. Appl. Math.* **35**, 58 (2005).

[12] A. Chernyshenko, V. Pivovarchik, *Integral Equ. Oper. Theory* **92**, 17 (2020).

[13] J. Stewart Fabila-Carrasco, F. Lledó, O. Post, *Anal. Math. Phys.* **13**, 44 (2023).

[14] B. Gutkin, U. Smilansky, *J. Phys. A* **34**, 6061 (2001).

[15] P. Kurasov, J. Muller, *St. Petersburg Math. J.* **35**, 55 (2023).

[16] P. Kurasov, M. Nowaczyk, *J. Phys. A* **38**, 4901 (2005).

[17] P. Kurasov, F. Stenberg, *J. Phys. A* **35**, 101 (2002).

[18] M.-E. Pistol, arXiv:2104.12885v4 (2022).

[19] R. Brooks, *Ann. Inst. Fourier* **49**, 707 (1999).

[20] S. Butler, J. Grout, *Electron. J. Combin.* **18**, 231 (2011).

[21] W.H. Haemers, E. Spence, *Eur. J. Comb.* **25**, 199 (2004).

[22] L. Halbeisen, N. Hungerbühler, *J. Graph Theory* **31**, 255 (1999).

[23] J.J. Seidel, *Proc. K. Ned. Akad. Wet. Ser. A: Math. Sci.* **70**, 188 (1967).

[24] P. Kurasov, *Math. Proc. Cambridge Philos. Soc.* **148**, 331 (2010).

[25] S. Avdonin, P. Kurasov, *Inverse Probl. Imaging* **2**, 1 (2008).

[26] S Avdonin, P. Kurasov, M. Nowaczyk, *Inverse Probl. Imaging* **4**, 579 (2010).

[27] P. Kurasov, *J. Math. Phys.* **54**, 042103 (2013).

[28] H. Weyl, *Math. Ann.* **68**, 220 (1910) (in German).

[29] P. Kurasov, S. Naboko, *Studia Math.* **255**, 303 (2020).

[30] P. Kurasov, *Acta Phys. Pol. A* **132**, 1666 (2017).

[31] P. Kurasov, S. Naboko, "M-functions and Eigenfunctions", 2023.

[32] S. Albeverio, P. Kurasov, *Singular Perturbations of Differential Operators, London Mathematical Society Lecture Note Series*, Vol. 271, Cambridge University Press, Cambridge 2000.

Proceedings of the 11th Workshop on Quantum Chaos and Localisation Phenomena (CHAOS 23)

The Role of the Branch Cut of the Logarithm in the Definition of the Spectral Determinant for Non-Self-Adjoint Operators

J. Lipovský* and T. Macháček

Department of Physics, Faculty of Science, University of Hradec Králové, Rokitanského 62, 50003 Hradec Králové, Czechia

Doi: 10.12693/APhysPolA.144.462 *e-mail: jiri.lipovsky@uhk.cz

The spectral determinant is usually defined using the spectral zeta function that is meromorphically continued to zero. In this definition, the complex logarithms of the eigenvalues appear. Hence, the notion of the spectral determinant depends on the way in which one chooses the branch cut in the definition of the logarithm. We give results for the non-self-adjoint operators that specify when the determinant can and cannot be defined and how its value differs depending on the choice of the branch cut.

topics: spectral determinant, branch cut, spectral zeta function

1. Introduction

When studying the spectral properties of operators, various concepts can be investigated. One of them is the spectral (functional) determinant, corresponding to the product of eigenvalues. It can be viewed as a generalization of the determinant for a square matrix (an operator with finitely many eigenvalues). Since for most of the interesting operators the product of their eigenvalues is not convergent, one defines it using the spectral zeta function, a function of a complex variable s defined through an infinite sum that is usually convergent in a certain half-plane in s (for details, see Sect. 2). Using the fact that the spectral zeta function can be uniquely meromorphically continued to the rest of the complex plane in s, allows us to assign the unique value to its derivative at $s = 0$. This value is then used for the definition of the determinant.

The above definition of the spectral determinant can be traced back to the works of Minakshisundaram and Pleijel [1] and Ray and Singer [2]. Since then, results for various operators have been obtained. Without claiming that the list of works is complete, we mention, e.g., the papers on the determinant for the Sturm–Liouville operators [3–5], Dirichlet Laplacians on balls or polygons [6, 7], or harmonic and anharmonic oscillators [8, 9]. An important application of the spectral determinants can be found in string theory or quantum field theory (see [10] and references therein). A result for more general elliptic operators obtained in [11] was applied for the damped wave equation in [12] or for the polyharmonic operator in [13].

When defining the spectral determinant using the spectral zeta function, complex logarithms of the eigenvalues appear (for more details, see Sect. 2). However, the complex logarithm is not a unique function. When one wants to define it as a unique function, one must choose a certain branch — an interval of the width 2π, from which the arguments of the eigenvalues are taken. As it was already mentioned in [12, 14], the choice of the branch may influence the value of the determinant. The aim of the current note is to shed some light on this problem. For various distributions of the eigenvalues in the complex plane and different choices of the branch cut, we find how the determinant changes when altering the branch cut.

The result in [12] obtained for the linear distribution of the eigenvalues on the imaginary axis is generalized in two ways: we allow for multiple rays along which the eigenvalues are distributed, and we generalize the result to power growth. For this setting, we prove that the determinant changes the sign when the branch cut crosses one of the rays on which the eigenvalues are distributed. Moreover, we prove that for the exponential and the logarithmic growth, the spectral determinant cannot be reasonably defined. Finally, we study the distribution of the eigenvalues on a line not going through the origin, and we compare the results to the previous results on the damped wave equation.

The paper is structured as follows. In Sect. 2, we properly define all notions used in the paper. In Sect. 3, we give an introductory example showing how the choice of the branch cut influences the

determinant. Section 4 gives the main results of the paper; we compare the determinants for different branch cuts and various distributions of the eigenvalues.

2. Definition and preliminaries

Throughout this paper, we will assume an operator A with a discrete spectrum. Operator A can be, in general, non-self-adjoint, and thus its eigenvalues may not be real. To define the spectral determinant for this operator, we have to introduce the spectral zeta function first, which is a function of the complex parameter s.

Definition 1. The spectral zeta function of the operator A is

$$\zeta_A(s) = \sum_{j=1}^{\infty} \lambda_j^{-s}, \tag{1}$$

where λ_j's are the eigenvalues of the operator A.

This definition is a generalization of the Riemann zeta function $\zeta_{\mathrm{R}}(s) = \sum_{j=1}^{\infty} j^{-s}$. We stress that, similarly to the Riemann zeta function, the sum in the spectral zeta function is typically not convergent for all complex s. However, for the most common operators (as, for instance, the Sturm–Liouvile operators), the sum is typically convergent in the half-plane $\mathrm{Re}(s) > c$.

Since it will be used in Sect. 4.4, we also introduce the Hurwitz zeta function.

Definition 2. Hurwitz zeta function is a function of two complex parameters, s and a, defined by the formula

$$\zeta_{\mathrm{H}}(s, a) = \sum_{j=0}^{\infty} \frac{1}{(j+a)^s}, \tag{2}$$

Now, we can define the spectral determinant.

Definition 3. The spectral determinant for the operator A is defined as

$$\det\big[A\big] = \exp\big(-\zeta_A'(0)\big), \tag{3}$$

where prime denotes the complex derivative of the zeta function with respect to s.

Notice that $s = 0$ is the point where the sum (1) is not convergent, as it consists of infinitely many ones. However, one can bypass this issue if the sum is properly defined in the above-mentioned half-plane. We use the fact that the function can be uniquely meromorphically continued from the half-plane to the rest of the complex plane, and the needed derivative at zero is computed using this continuation.

For the reader's convenience, we introduce the well-known notions from complex analysis (see, e.g., [15, 16]).

Definition 4. We say that a complex function of the complex variable $f(z)$ is *holomorphic* in an open set $\Omega \subset \mathbb{C}$ if there exists its complex derivative $f'(z)$ for every $z_0 \in \Omega$. The function which is holomorphic in Ω up to the set of isolated points is called *meromorphic*. The function is *complex analytic* at z_0 if it is infinitely many times differentiable and equal to its Taylor series in the neighbourhood of z_0.

Theorem 1. For functions on an open ball, the function is holomorphic if and only if it is analytic.

Theorem 2. Two functions that are complex analytic in $\tilde{\Omega}$ and coincide on some set with an accumulation point in $\tilde{\Omega}$ are identical.

Hence, if we have a meromorphic function in an open set Ω, we can meromorphically continue it to the whole complex plane. The zeta function in Definition 3 is thus understood as the unique meromorphic continuation to zero from the above-mentioned set where the sum in the definition of the zeta function converges.

At the end of this section, let us mention a property that will be important in the following sections. There appears the term λ_j^{-s} in the definition of the spectral zeta function. Let us stress that both λ_j and s are complex and that the expression can be rewritten as $\exp(-s \ln(\lambda_j))$. Hence, the spectral zeta function (and through it also the spectral determinant) is dependent on the definition of the complex logarithm of the eigenvalues. The complex logarithm can be regarded as a multivalued function, with the imaginary part having values that can differ by multiples of 2π. When one wants to define the logarithm as a single-valued function, one must specify the interval of the width 2π and take the arguments of the numbers in the argument of the logarithm from that interval. Thus, one chooses one particular *branch* of the logarithm. Then, the ray in the complex plane where the arguments are discontinuous is called the *branch cut*.

As it was found in [12] and earlier in Examples 11 and 12 [14], the choice of the branch cut of the logarithm can influence the value of the spectral determinant. In the next sections, we will investigate this issue deeper and try to elucidate under which conditions the spectral determinant changes and how.

3. Example — damped wave equation

In this section, we will reproduce an example from [12]. In the mentioned paper, the spectral determinant for the damped wave equation on an interval of the length T was studied. On this interval, the equation

$$\frac{\partial^2 v(t,x)}{\partial t^2} + 2a(x)\frac{\partial v(t,x)}{\partial t} = \frac{\partial^2 v(t,x)}{\partial x^2}, \tag{4}$$

is investigated, where $a(x) \in \mathcal{C}([0,T])$ is the damping function. The Dirichlet boundary conditions $v(0) = v(T) = 0$ and certain initial conditions are assumed. The problem can be rewritten into the form of a matrix equation

$$\frac{\partial}{\partial t}\begin{pmatrix} v_0(t,x) \\ v_1(t,x) \end{pmatrix} = \begin{pmatrix} 0 & 1 \\ \frac{\partial^2}{\partial x^2} & -2a(x) \end{pmatrix}\begin{pmatrix} v_0(t,x) \\ v_1(t,x) \end{pmatrix}. \tag{5}$$

It is easy to find that after the substitution for v_1, the variable v_0 satisfies (4). Furthermore, the ansatz $v_0(t,x) = \mathrm{e}^{\lambda t}u_0(x)$, $v_1(t,x) = \mathrm{e}^{\lambda t}u_1(x)$ leads to the alternative formulation of the problem — finding the eigenvalues for the matrix operator

$$A_{\mathrm{DWE}} = \begin{pmatrix} 0 & 1 \\ \frac{\partial^2}{\partial x^2} & -2a(x) \end{pmatrix}. \tag{6}$$

Then, (5) translates to

$$A_{\mathrm{DWE}}\begin{pmatrix} u_0(x) \\ u_1(x) \end{pmatrix} = \lambda\begin{pmatrix} u_0(x) \\ u_1(x) \end{pmatrix}. \tag{7}$$

The spectral determinant for the operator A_{DWE} was found in [12], and it was proven that it does not depend on the damping. The effect of the choice of the branch cut that is found in [12] is visible already for the case without damping ($a(x) \equiv 0$), i.e., the operator with the eigenvalues $\lambda_{j\pm} = \pm\frac{j\pi}{T}\mathrm{i}$, $j \in \mathbb{N}$. We will study the spectral determinant for the branch cuts in the negative and the positive real axis. For the former, the interval of the arguments of the eigenvalues will be chosen from the interval $(-\pi, \pi)$, and the eigenvalues can be rewritten as

$$\lambda_{j+} = \frac{j\pi}{T}\mathrm{e}^{\mathrm{i}\frac{\pi}{2}}, \qquad \lambda_{j-} = \frac{j\pi}{T}\mathrm{e}^{-\mathrm{i}\frac{\pi}{2}}. \tag{8}$$

The spectral zeta function can be then written as

$$\begin{aligned}\zeta_A(s) &= \sum_{j=1}^{\infty}\left[\left(\frac{j\pi}{T}\mathrm{e}^{\mathrm{i}\frac{\pi}{2}}\right)^{-s} + \left(\frac{j\pi}{T}\mathrm{e}^{-\mathrm{i}\frac{\pi}{2}}\right)^{-s}\right] = \\ &\sum_{j=1}^{\infty}\left(\frac{j\pi}{T}\right)^{-s}\left(\mathrm{e}^{-\mathrm{i}\frac{\pi}{2}s} + \mathrm{e}^{\mathrm{i}\frac{\pi}{2}s}\right) = \\ &\sum_{j=1}^{\infty}2\left(\frac{j\pi}{T}\right)^{-s}\cos\left(\frac{\pi s}{2}\right) = \\ &2\mathrm{e}^{s\log\left(\frac{T}{\pi}\right)}\cos\left(\frac{\pi s}{2}\right)\zeta_{\mathrm{R}}(s),\end{aligned} \tag{9}$$

where ζ_{R} is the Riemann zeta function.

The Riemann zeta function is well defined in the half-plane $\mathrm{Re}(s) > 1$ and thus can be meromorphically continued to the rest of the complex plane with the known values

$$\zeta_{\mathrm{R}}(0) = -\frac{1}{2}, \quad \zeta_{\mathrm{R}}'(0) = -\frac{1}{2}\log(2\pi). \tag{10}$$

Differentiating (9) and using (10), we get

$$\zeta_A'(0) = 2\log\frac{T}{\pi}\zeta_{\mathrm{R}}(0) + 2\zeta_{\mathrm{R}}'(0) = -\log(2T). \tag{11}$$

Hence, the determinant is

$$\det\big[A\big] = \mathrm{e}^{\log(2T)} = 2T. \tag{12}$$

For the choice of the cut on the positive real axis, one has to take the arguments of the eigenvalues from the interval $(0, 2\pi)$. Hence, we plug into the formula for the zeta function the values

$$\lambda_{j+} = \frac{j\pi}{T}\mathrm{e}^{\mathrm{i}\frac{\pi}{2}}, \quad \lambda_{j-} = \frac{j\pi}{T}\mathrm{e}^{\mathrm{i}\frac{3\pi}{2}} \tag{13}$$

and, using similar manipulations as above, we obtain the result

$$\zeta_A(s) = 2\mathrm{e}^{-\mathrm{i}\pi s}\mathrm{e}^{s\log\left(\frac{T}{\pi}\right)}\cos\left(\frac{\pi s}{2}\right)\zeta_{\mathrm{R}}(s). \tag{14}$$

Thus, the derivative at zero differs by the factor of $i\pi$, i.e.,

$$\begin{aligned}\zeta_A'(0) = -2\mathrm{i}\pi\zeta_{\mathrm{R}}(0) + 2\log\frac{T}{\pi}\zeta_{\mathrm{R}}(0) + 2\zeta_{\mathrm{R}}'(0) = \\ \mathrm{i}\pi - \log(2T).\end{aligned} \tag{15}$$

This results in the spectral determinant that has a different sign, i.e.,

$$\det\big[A\big] = \mathrm{e}^{-\mathrm{i}\pi+\log(2T)} = -2T. \tag{16}$$

This result shows that the change of the branch cut can, in some cases, cause a difference in the spectral determinant, for instance, in its sign. The analysis provided in this section illustrates that to get a proper value of the spectral determinant, one must clearly specify which branch of the logarithm is assumed in its definition. Even in this simple example inspired by a physical problem, the value of the spectral determinant differs; this drives us to investigate this problem further and find how the determinant changes in different geometrical settings of the eigenvalues of the problem.

4. Results

In this section, we try to generalize this result for different and more general types of operators, or in other words, distributions of eigenvalues. We start with a result already mentioned in [12], concerning the shift of the branch cut through finitely many eigenvalues.

Theorem 3. If the branch cut of the logarithm moves so that it crosses finitely many eigenvalues of the operator A, its spectral determinant does not change.

We generalize the result of Sect. 3 in two directions. First, the eigenvalue distances from the origin grow at a different rate (as a power of j, exponentially or logarithmically). Secondly, we allow for more rays on which the eigenvalues are situated.

4.1. Power growth

One of the main results of the paper is the following theorem concerning the power growth of the eigenvalues.

Theorem 4. Let us have a finite number of angles α_ℓ, such that $0 < \alpha_1 < \alpha_2 < \cdots < \alpha_N < 2\pi$. Let us assume that the eigenvalues of the operator A are

$$\begin{aligned}
&\lambda_j^{(1)} = c_1 j^{c_2}\,\mathrm{e}^{\mathrm{i}\alpha_1},\\
&\lambda_j^{(2)} = c_1 j^{c_2}\,\mathrm{e}^{\mathrm{i}\alpha_2},\\
&\vdots\\
&\lambda_j^{(N)} = c_1 j^{c_2}\,\mathrm{e}^{\mathrm{i}\alpha_N}
\end{aligned} \tag{17}$$

(see Fig. 1), where $c_1, c_2 \in \mathbb{R}_+$. If the branch cut is moved so that it passes n half-lines with angles α_ℓ, the determinant will be $(-1)^n$-multiple of the former determinant.

Proof. Let us define angles β_ℓ, $\ell = 1, \ldots, N+1$ such that $0 < \beta_1 < \alpha_1 < \beta_2 < \alpha_2 < \beta_3 < \cdots < \beta_N < \alpha_N < \beta_{N+1} < 2\pi$ and assume the branch cuts on the half-lines under the angles β_ℓ. For a particular branch cut under the angle β_ℓ, the arguments of the eigenvalues will be in the interval $(\beta_\ell, \beta_\ell + 2\pi)$. It is clear that the arguments of the eigenvalues in the particular rays are successively $\alpha_1 + 2\pi$, $\alpha_2 + 2\pi$, $\ldots$, $\alpha_{\ell-1} + 2\pi$, α_ℓ, $\alpha_{\ell+1}$, $\ldots$, α_N. The spectral zeta function is

$$\begin{aligned}
\zeta_A(s) = {}& \textstyle\sum_{j=1}^{\infty} (c_1 j^{c_2})^{-s} \Big[\mathrm{e}^{-\mathrm{i}\alpha_1 s - 2\pi\mathrm{i}s} + \mathrm{e}^{\mathrm{i}\alpha_2 s - 2\pi\mathrm{i}s}\\
&+ \ldots + \mathrm{e}^{-\mathrm{i}\alpha_{\ell-1} s - 2\pi\mathrm{i}s} + \mathrm{e}^{-\mathrm{i}\alpha_\ell s} + \ldots + \mathrm{e}^{-\mathrm{i}\alpha_N s} \Big] =\\
&\mathrm{e}^{-s\log c_1} \zeta_{\mathrm{R}}(c_2 s) \Big[\mathrm{e}^{-\mathrm{i}\alpha_1 s - 2\pi\mathrm{i}s} + \mathrm{e}^{-\mathrm{i}\alpha_2 s - 2\pi\mathrm{i}s} + \ldots\\
&+ \mathrm{e}^{-\mathrm{i}\alpha_{\ell-1} s - 2\pi\mathrm{i}s} + \mathrm{e}^{-\mathrm{i}\alpha_\ell s} + \ldots + \mathrm{e}^{-\mathrm{i}\alpha_N s} \Big].
\end{aligned} \tag{18}$$

The sum is convergent for $\mathrm{Re}(s) > c_2^{-1}$, hence, we can continue it to the rest of the complex plane. The derivative of the spectral zeta function at zero is

$$\begin{aligned}
\zeta_A'(0) = {}& -\log(c_1)\,\zeta_{\mathrm{R}}(0) N + c_2 \zeta_{\mathrm{R}}'(0) N + \zeta_{\mathrm{R}}(0)(-\mathrm{i})\\
&\times \left[2\pi(\ell - 1) + \sum_{k=1}^{N} \alpha_k \right] = \frac{N}{2}\log(c_1) - \frac{N}{2} c_2 \log(2\pi)\\
&+ \mathrm{i}\pi(\ell - 1) + \mathrm{i}\tfrac{1}{2} \sum_{k=1}^{N} \alpha_k.
\end{aligned} \tag{19}$$

The determinant is then, according to (3), equal to

$$\det\big[A\big] = (-1)^{\ell-1} c_1^{-\frac{N}{2}} (2\pi)^{\frac{c_2 N}{2}} \exp\left[-\frac{\mathrm{i}}{2} \sum_{k=1}^{N} \alpha_k \right], \tag{20}$$

If the branch cut is changed so that it crosses n rays of eigenvalues, i.e., we move from the index ℓ to the index $\ell + n$, the ratio of the determinants is clearly from the previous formula $(-1)^n$, and hence we have

$$\det\Big[A_{\ell+n}\Big] = \det\big[A_\ell\big](-1)^n, \tag{21}$$

where $\det[A_\ell]$ is the determinant for the branch cut under the angle β_ℓ and $\det[A_{\ell+n}]$ is the determinant for the branch cut under the angle $\beta_{\ell+n}$. □

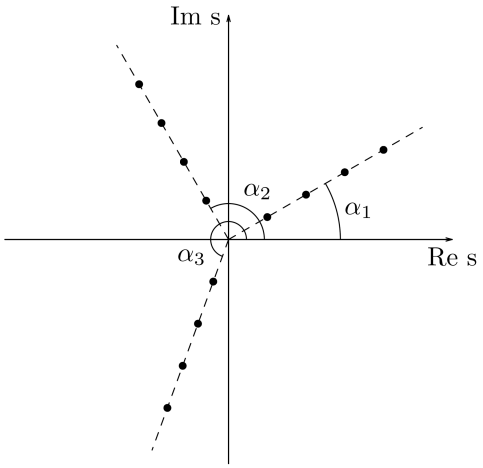

Fig. 1. Power growth of the eigenvalues on more half-lines.

Let us stress that even for the cut on the same place in the complex plane but with the angle different by 2π, the determinant does not have to be the same. If the number of rays of the eigenvalues is odd, the determinant changes the sign.

4.2. Exponential growth

This subsection is devoted to the exponential behaviour of the eigenvalues.

Theorem 5. If a ray of eigenvalues behaving as $\lambda_j = c_1\,\mathrm{e}^{c_2 j}\,\mathrm{e}^{\mathrm{i}\alpha}$, $c_1, c_2 \in \mathbb{R}_+$ is present, the spectral determinant diverges to $+\infty$.

Proof. We will restrict ourselves to the case when there is only the above-mentioned ray of eigenvalues, although the presence of other eigenvalues (either finitely many or infinitely many with power growth) does not influence the result. First, we write down the spectral zeta function

$$\begin{aligned}
\zeta_A(s) = {}& \sum_{j=1}^{\infty} c_1^{-s}\,\mathrm{e}^{-c_2 j s}\,\mathrm{e}^{-\mathrm{i}\alpha s} =\\
&c_1^{-s}\,\mathrm{e}^{-\mathrm{i}\alpha s} \sum_{j=1}^{\infty} \mathrm{e}^{-c_2 j s} = c_1^{-s}\,\mathrm{e}^{-\mathrm{i}\alpha s} \frac{\mathrm{e}^{-c_2 s}}{1 - \mathrm{e}^{-c_2 s}} =\\
&\mathrm{e}^{-s\log(c_1)}\,\mathrm{e}^{-\mathrm{i}\alpha s} \tfrac{1}{\mathrm{e}^{c_2 s} - 1},
\end{aligned} \tag{22}$$

where we use the sum for the geometric series that converges for $\mathrm{Re}(s) > 0$. Its derivative is

$$\begin{aligned}
\zeta_A'(s) = {}& -\log c_1\,\mathrm{e}^{-s\log(c_1)}\,\mathrm{e}^{-\mathrm{i}\alpha s} \frac{1}{\mathrm{e}^{c_2 s} - 1}\\
&-\mathrm{i}\alpha\,\mathrm{e}^{-s\log(c_1)}\,\mathrm{e}^{-\mathrm{i}\alpha s} \frac{1}{\mathrm{e}^{c_2 s} - 1}\\
&-c_2\,\mathrm{e}^{-s\log(c_1)}\,\mathrm{e}^{-\mathrm{i}\alpha s} \tfrac{\mathrm{e}^{c_2 s}}{(\mathrm{e}^{c_2 s} - 1)^2}.
\end{aligned} \tag{23}$$

Both ζ_A and ζ_A' diverge as $s = 0$; the limit of the derivative at zero is $-\infty$. Hence, the spectral determinant diverges to $+\infty$. □

4.3. Logarithmic growth

In this subsection, we study the case where the eigenvalues on a ray grow logarithmically or slower.

Theorem 6. Let log denote the natural logarithm. If a ray of eigenvalues behaving as $\lambda_j = \omega_j \mathrm{e}^{\mathrm{i}\alpha}$, $\omega_j \in \mathbb{R}_+$, $\omega_j \leq c_1 \log(c_2 j)$, $c_1 \in \mathbb{R}_+$, $c_2 \geq 1$ is present, the spectral zeta function is not defined.

Proof. The spectral zeta function can be constructed similarly to the previous cases, i.e.,

$$\zeta_A(s) = \mathrm{e}^{-\mathrm{i}\alpha s} \sum_{j=1}^{\infty} \omega_j^{-s}. \tag{24}$$

Now, we prove that $\sum_{j=1}^{\infty} \omega_j^{-s}$ diverges for all $s \in \mathbb{R}$ with $s > 0$ (for $s \leq 0$, the claim is obvious)

$$\sum_{j=1}^{\infty} \omega_j^{-s} \geq c_1^{-s} \sum\nolimits_{j=1}^{\infty} (\log(c_2 j))^{-s} = c_1^{-s} \sum\nolimits_{j=1}^{\infty} (\log(c_2) + \log(j))^{-s}. \tag{25}$$

The last sum diverges by the integral criterion. For any given $s > 0$, there exists $c > 1$ such that $\frac{1}{x} < \log(x)^{-s}$ for $x > c$. Moreover, there exists $\tilde{c} > 0$ such that $(\log(c_2) + \log(x))^{-s} \geq (2\log x)^{-s} \geq \tilde{c}\,(\log x)^{-s}$ for $x > c$. Then,

$$\int_1^{\infty} \mathrm{d}x\ (\log(c_2) + \log(x))^{-s} \geq \int_c^{\infty} \mathrm{d}x\ (\log(c_2) + \log(x))^{-s} \geq \int_c^{\infty} \mathrm{d}x\ \tilde{c} \log(x)^{-s} > \int_c^{\infty} \mathrm{d}x\ \frac{\tilde{c}}{x} = \infty, \tag{26}$$

and hence the sum diverges. Therefore, there is no half-plane $\mathrm{Re}(s) > \text{const.}$ such that the zeta function is defined in this half-plane, and hence the spectral determinant cannot be reasonably defined. □

4.4. Eigenvalues on a vertical line outside the origin

The next example illustrates that the ratio of the determinants for different branch cuts is not always 1 or −1. We consider the example from Sect. 3 with the eigenvalues shifted horizontally. The eigenvalues will be $\lambda_j = b + \mathrm{i}j$, $j \in \mathbb{Z}\backslash\{0\}$ (see Fig. 2).

We will choose the branch cut in the following way. The first one will be on the positive real axis or just above it, hence, the arguments of the eigenvalues will be taken from the interval $(0, 2\pi)$. The second branch cut will be chosen on the negative real axis, and the arguments of the complex numbers will be taken from the interval $(\pi, 3\pi)$. Note that the eigenvalues in the lower half-plane will have the same arguments for both choices of the branch cut.

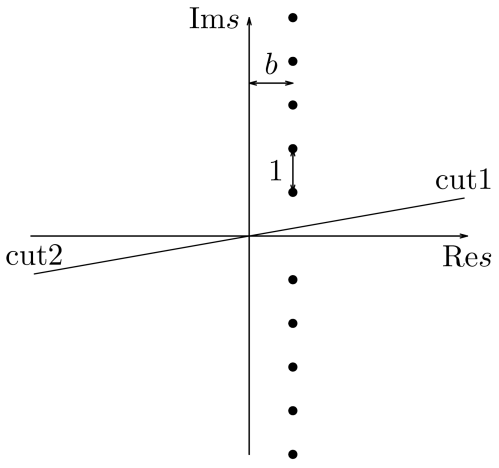

Fig. 2. Eigenvalues on a vertical line outside the origin.

The spectral zeta functions can be written using the Hurwitz zeta functions in the following way

$$\zeta_1(s) = \mathrm{e}^{-\frac{\pi}{2}\mathrm{i}s} \zeta_{\mathrm{H}}(s, 1-\mathrm{i}b) + \mathrm{e}^{-\frac{3\pi}{2}\mathrm{i}s} \zeta_{\mathrm{H}}(s, 1+\mathrm{i}b) \tag{27}$$

for the first choice of the branch cut and

$$\zeta_2(s) = \mathrm{e}^{-\frac{5\pi}{2}\mathrm{i}s} \zeta_{\mathrm{H}}(s, 1-\mathrm{i}b) + \mathrm{e}^{-\frac{3\pi}{2}\mathrm{i}s} \zeta_{\mathrm{H}}(s, 1+\mathrm{i}b) \tag{28}$$

for the second choice. For this construction, we have rotated the set of points $j \pm \mathrm{i}b$, $j = 1, \ldots, \infty$ by corresponding angles. Note that in the definition of the Hurwitz zeta function, the sum goes from 0, while in the definition of the spectral zeta function, it starts from 1. This results in the factor of 1 in the second argument of ζ_{H}.

Differentiating the expressions (27) and (28), one obtains

$$\begin{aligned} \zeta_1'(0) &= -\tfrac{\pi}{2}\mathrm{i}\,\zeta_{\mathrm{H}}(0, 1-\mathrm{i}b) + \left.\tfrac{\partial \zeta_{\mathrm{H}}(s, 1-\mathrm{i}b)}{\partial s}\right|_{s=0} \\ &\quad -\tfrac{3\pi}{2}\mathrm{i}\,\zeta_{\mathrm{H}}(0, 1+\mathrm{i}b) + \left.\tfrac{\partial \zeta_{\mathrm{H}}(s, 1+\mathrm{i}b)}{\partial s}\right|_{s=0}, \\ \zeta_2'(0) &= -\tfrac{5\pi}{2}\mathrm{i}\,\zeta_{\mathrm{H}}(0, 1-\mathrm{i}b) + \left.\tfrac{\partial \zeta_{\mathrm{H}}(s, 1-\mathrm{i}b)}{\partial s}\right|_{s=0} \\ &\quad -\tfrac{3\pi}{2}\mathrm{i}\,\zeta_{\mathrm{H}}(0, 1+\mathrm{i}b) + \left.\tfrac{\partial \zeta_{\mathrm{H}}(s, 1+\mathrm{i}b)}{\partial s}\right|_{s=0}. \end{aligned} \tag{29}$$

Let us denote by $\det_1$ and $\det_2$ the determinant for the first and the second cut, respectively. The ratio of both determinants is

$$\frac{\det_1}{\det_2} = \mathrm{e}^{-\zeta_1'(0) + \zeta_2'(0)} = \mathrm{e}^{-2\mathrm{i}\pi\zeta_{\mathrm{H}}(0, 1-\mathrm{i}b)}. \tag{30}$$

Our final task is to find the value of the Hurwitz zeta function $\zeta(0, 1-\mathrm{i}b)$. We can use the following formula (see, e.g., Eq. (1.10.7) in [17])

$$\zeta_{\mathrm{H}}(s, a) = \frac{1}{2}a^{-s} + \frac{a^{1-s}}{s-1} + 2\int_0^{\infty} \mathrm{d}x\ \frac{\sin(s \arctan(x/a))}{(a^2 + x^2)^{s/2}\,(\mathrm{e}^{2\pi x} - 1)}. \tag{31}$$

Applying this formula for $s = 0$ and $a = 1-\mathrm{i}b$, one finds that the sine and hence also the integral vanish, and we obtain

$$\zeta_{\mathrm{H}}(0, 1-\mathrm{i}b) = \frac{1}{2} + \frac{1-\mathrm{i}b}{-1} = -\frac{1}{2} + b\mathrm{i}. \tag{32}$$

Substitution to (30) yields

$$\frac{\det_1}{\det_2} = \mathrm{e}^{-2\mathrm{i}\pi(-\frac{1}{2}+b\mathrm{i})} = -\mathrm{e}^{2b\pi}. \tag{33}$$

Remark 1. We can see that unlike in [12], the determinant not only changes the sign, but the ratio of the determinants depends on the parameter b. Another example can be found in Examples 11 and 12 [14]. A more detailed analysis of the eigenvalues of our system and the damped wave equation in [12] for the general value of the damping shows that, on the one hand, the eigenvalue distribution looks very similar and, on the other hand, there are differences in the higher terms of the eigenvalue asymptotics. For the damped wave equation on the interval of length 1 with the damping $a(x)$, the large j eigenvalue asymptotics is

$$\lambda_j \approx \pi j\mathrm{i} - \langle a\rangle + \frac{\langle a^2\rangle}{2\pi\mathrm{i}j} + \frac{1}{2\pi^2 j^2}\Big[\langle a^3\rangle - \langle a\rangle\langle a^2\rangle + \frac{1}{2}\big(a'(1) - a'(0)\big)\Big] + \dots \tag{34}$$

(see [18]). The correct choice of the length of the interval supporting the damped wave equation (in particular, equal to π) and $b = -\langle a\rangle$ gives the same first two terms of the asymptotics as in our example. However, the higher-order terms differ. This results in different behaviour of the determinant; in [12], the determinant did not depend on the damping, while in the present example, it depends exponentially. One can deduce that even small changes in the eigenvalue asymptotics can influence the spectral determinant.

5. Conclusions

In this paper, we have illustrated the subtleties of the spectral determinant and the spectral zeta function. The spectral zeta function, used for defining the spectral determinant, is a function of a complex variable s and (in general, infinitely many) complex eigenvalues λ_j. In the variable s, one may find a certain region in which the infinite sum in its definition converges, and the zeta function is well-defined and may be meromorphically continued into the rest of the s-complex plane. On the other hand, the situation in the complex plane in which the eigenvalues λ_j "live" is more complicated. The value of the spectral zeta function depends on the choice of the interval from which the arguments of the eigenvalues are taken. This may result in the discontinuities of the spectral zeta function in the λ-plane. If the branch cut moves through infinitely many eigenvalues (or, from the other perspective, if we perturb the eigenvalues so that they move through the branch cut), the spectral zeta function (and hence also the spectral determinant) may change.

Although this phenomenon was mentioned earlier in [12, 14], to the best of our knowledge, it has not been studied in detail previously. In the current paper, we have given new Theorems 4, 5, and 6 that specify for eigenvalues on rays with power, exponential, and logarithmic behaviour, respectively, whether the zeta function and the spectral determinant can be defined, and if yes, how the determinant changes when moving the branch cut. Moreover, in Sect. 4.4, we studied in detail the example of an operator with the eigenvalues on the line not including the origin. Such a distribution of eigenvalues is close to the distribution of eigenvalues of the damped wave equation on an interval. However, we show that the behaviour of the spectral determinants for both operators differs significantly. Our result demonstrates that the higher terms of the asymptotics of the eigenvalues for the damped wave equation are crucial for the behaviour of some of its spectral properties, e.g., the spectral determinant.

Acknowledgments

The authors were supported by the Czech Science Foundation within the project 22-18739S. We thank the reviewer for useful remarks that improved the presentation of the paper.

References

[1] S. Minakshisundaram, Å. Pleijel, *Can. J. Math.* **1**, 242 (1949).

[2] D.B. Ray, I.M. Singer, *Adv. Math.* **7**, 145 (1971).

[3] S. Levit, U. Smilansky, *Proc. Am. Math. Soc.* **65**, 299 (1977).

[4] F. Gesztesy, K. Kirsten, *J. Funct. Anal.* **276**, 520 (2019).

[5] C. Aldana, J.-B. Caillau, P. Freitas, *J. Éc. Polytech. Math.* **7**, 803 (2020).

[6] M. Bordag, B. Geyer, K. Kirsten, E. Elizalde, *Commun. Math. Phys.* **179**, 215 (1996).

[7] E. Aurell, P. Salomonson, *Commun. Math. Phys.* **165**, 233 (1994).

[8] P. Freitas, *Math. Ann.* **372**, 1081 (2018).

[9] A. Voros, *Nuclear Physics B* **165**, 209 (1980).

[10] G.V. Dunne, *J. Phys. A: Math. Theor.* **41**, 304006 (2008).

[11] D. Burghelea, L. Friedlander, T. Kappeler, *Proc. Amer. Math. Soc.* **123**, 3027 (1995).

[12] P. Freitas, J. Lipovský, *Acta Phys. Pol. A* **136**, 817 (2019).

[13] P. Freitas, J. Lipovský, *J. Funct. Anal.* **279**, 108783 (2020).

[14] J.R. Quine, S.H. Heydari, R.Y. Song, *Trans. Am. Math. Soc.* **338**, 213 (1993).

[15] W. Rudin, *Real and complex analysis*, 3rd ed., McGraw Hill, Singapore 1986, p. 483.

[16] L.V. Ahlfors, *Complex analysis*, 3rd ed., McGraw Hill, 1979, p. 336.

[17] A. Erdélyi, W. Magnus, F. Oberhettinger, F.G. Tricomi, *Higher Transcendental Functions*, Vol. I, McGraw-Hill Book Company, New York 1953.

[18] D. Borisov, P. Freitas, *J. Diff. Eq.* **247**, 3028 (2009).

Proceedings of the 11th Workshop on Quantum Chaos and Localisation Phenomena (CHAOS 23)

Experimental Distributions of the Reflection Amplitude for Networks with Unitary and Symplectic Symmetries

M. Ławniczak*, A. Akhshani, O. Farooq,
S. Bauch and L. Sirko

Institute of Physics, Polish Academy of Sciences, al. Lotników 32/46, PL-02668 Warsaw, Poland

Doi: 10.12693/APhysPolA.144.469 *e-mail: lawni@ifpan.edu.pl

We present the experimental study of the distributions of the reflection amplitudes $r_i = |S_{ii}|$ of the two-port scattering matrix $\hat{S}$ for networks with unitary and symplectic symmetries for the intermediate absorption strength parameter γ. The experimental results confirm the theoretical predictions obtained within the framework of the Gaussian unitary and symplectic ensembles of the random matrix theory.

topics: random matrix theory, gaussian unitary ensemble, gaussian symplectic ensemble, chaotic scattering

1. Introduction

The theory of quantum chaotic scattering in large complex quantum systems was developed more than seventy years ago [1–3]. However, controllable experimental investigations of such systems due to the effects of decoherence are still extremely difficult. Therefore, many of physical problems from the field of quantum chaos are experimentally undertaken with the help of microwave networks simulating quantum graphs [4–7].

This article shows how microwave networks can be applied to obtain the experimental results on the distributions $P(r)$ of the reflection amplitudes $r_i = |S_{ii}|$ of the two-port scattering matrix

$$\hat{S} = \begin{bmatrix} S_{11} & S_{12} \\ S_{21} & S_{22} \end{bmatrix} \tag{1}$$

for networks with unitary and symplectic symmetries. The experimental results are compared to the exact random matrix theory (RMT) solutions of this problem [8].

The concept of quantum graphs constructed from a set of vertices connected by one-dimensional quantum wires was introduced more than 80 years ago by Linus Pauling [9]. They are not only basic mathematical objects but are also indispensable in modeling physical networks in the limit where the lengths of the wires are much larger than their widths [4, 10]. Quantum graphs are invaluable tools for studying open quantum systems exhibiting chaotic scattering [11–14]. They have been used to describe a large variety of systems and models, e.g., superconducting quantum circuits [15], quantum circuits in tunnel junctions [16], and the realization of high-dimensional multipartite quantum states [17].

Quantum graphs can be simulated by microwave networks because of the formal equivalence of the Schrödinger equation describing quantum graphs and the telegraph equation of the corresponding microwave networks [4–6]. It was demonstrated that microwave networks can experimentally simulate systems whose fluctuation properties can be described by all three fundamental ensembles in RMT. In the case of the systems characterized by T-invariance, they are the Gaussian orthogonal ensemble (GOE, symmetry index β=1 in RMT) [4, 12, 18–23] and the Gaussian symplectic ensemble (GSE, symmetry index β=4) [7, 14, 24, 25]. For systems for which T-invariance is broken, this is the Gaussian unitary ensemble (GUE, symmetry index β=2) [4–6, 26–28].

It should be emphasized that the other complex quantum systems can be simulated by microwave plane billiards [29–45] and atoms excited in strong microwave fields [46–55].

2. Theoretical outline

The distribution of the amplitude of the diagonal elements S_{ii} of the scattering matrix $\hat{S}$, $P(r)$, where $r = |S_{ii}|$, is an important but

very rarely studied characteristic of chaotic systems. The distribution of the reflection amplitude $P(r)$ in the GOE system and in the system with partially violated time reversal invariance was experimentally studied using microwave chaotic cavities [29, 56].

Recently, substantial progress has been made in the investigation of open chaotic systems with violated time reversal invariance (symmetry index $\beta = 2$). The distributions of Wigner's reaction K-matrix in the case of high absorption were for the first time experimentally studied in [6]. Finally, the experimental investigation of distributions of the off-diagonal elements of the two-port scattering and the Wigner's $\hat{K}$ matrices were investigated in [28]. However, the distribution of the reflection amplitude $P(r)$ has not been studied yet.

For open chaotic systems with symplectic symmetry (symmetry index $\beta = 4$), the distribution of the rescaled reflection amplitude $P(\tilde{r})$, where $\tilde{r} = \frac{r}{\langle r \rangle}$ and $\langle r \rangle$ is the average value of r, has been studied in [7].

In this article, we present the first experimental study of the distribution of the reflection amplitude $P(r)$ for an open GUE system. These results are compared with the ones obtained for the GSE system. The openness of the systems will be described by the dimensionless parameter $\gamma = 2\pi\Gamma/\Delta$, characterizing the absorption strength [8, 57], where Γ and Δ are the width of resonances and the mean level spacing, respectively.

The diagonal elements of the scattering matrix $\hat{S}$ can be expressed as $S_{ii} = r_i \mathrm{e}^{\mathrm{i}\theta_i}$, where r_i and θ_i are the reflection amplitude and the phase measured at the i-th port of the network. The relationship between the diagonal elements S_{ii}^{exp} of the two-port scattering matrix $\hat{S}^{\mathrm{exp}}$ measured directly in the experiment and the diagonal entries S_{ii} of the matrix $\hat{S}$ will be discussed later.

In the experimental investigations, quantum graphs with unitary symmetry were modeled by microwave networks with the circulators [5, 6] (see Fig. 1). The GSE microwave networks with symplectic symmetry contained two connected microwave subnetworks with unitary symmetry (see Fig. 2). The time reversal invariance violation was induced by T-shaped circulators of opposite orientation introduced at corresponding vertices. The connections between the subnetworks were realized by two phase shifters in order to maintain the signal phase difference of π (see Fig. 2) and to enforce the appearance of Kramer's doublets specific to the GSE systems [7].

3. Experiment

In this article, the distributions of the reflection amplitudes $P(r)$ are tested for the intermediate values of the absorption parameter $\gamma = 5.1 \pm 0.5$ and $\gamma = 5.6 \pm 0.2$ ($\Gamma \simeq \Delta$) for the networks with unitary and symplectic symmetries, respectively. In order to achieve such values of the parameter, in addition to the microwave cables, 4 circulators and 4 phase shifters were introduced into the unitary microwave network (see Fig. 1). The microwave network with symplectic symmetry contained altogether 20 1 dB attenuators, 2 circulators, and 4 phase shifters, i.e., 10 1 dB attenuators, 1 circulator, and 1 phase shifter for each connected by 2 phase shifters microwave subnetwork with unitary symmetry (see Fig. 2).

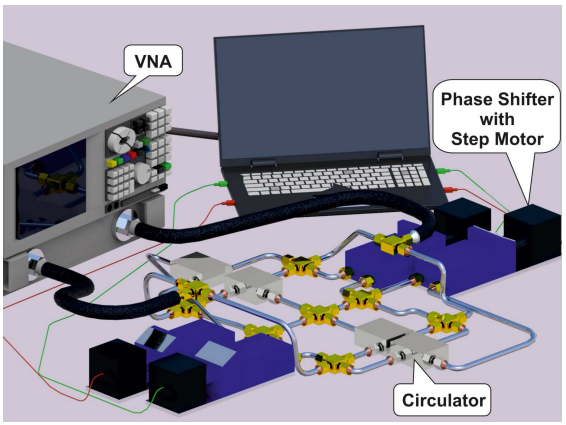

Fig. 1. The scheme of the experimental set-up for measuring the scattering matrix $\hat{S}$ of the 9-vertex microwave networks with violated T-invariance (GUE system) and absorption. The T-violation was induced using four Anritsu PE8403 microwave circulators. Absorption in the networks was caused by the internal absorption of microwave cables, 4 phase shifters, and 4 circulators.

The two-port scattering matrices $\hat{S}^{\mathrm{exp}}$ of the microwave networks with unitary and symplectic symmetries required for the evaluation of the normalized two-port scattering matrix $\hat{S}$ and the distributions $P(r)$, were measured using a vector network analyzer (VNA), Agilent E8364B (see Figs. 1 and 2). The networks were connected to VNA through the leads — HP 85133-616 and HP 85133-617 flexible microwave cables. The T-violation in the unitary network and in the subgraphs of the main GSE network was induced with Anritsu PE8403 and Aerotek microwave circulators with low insertion loss, which operate in the frequency ranges $\nu \in$ (7–14) GHz and $\nu \in$ (3.5–7.5) GHz, respectively. The circulators are non-reciprocal three-port passive devices. A wave that enters the circulator through port 1, 2, or 3 exits through port 2, 3, or 1, respectively.

4. Basic formulas

For systems with GUE and GSE invariance ($\beta = 2$ and $\beta = 4$), the analytic expression for the distribution of the reflection amplitude r can be expressed by the distribution of the reflection

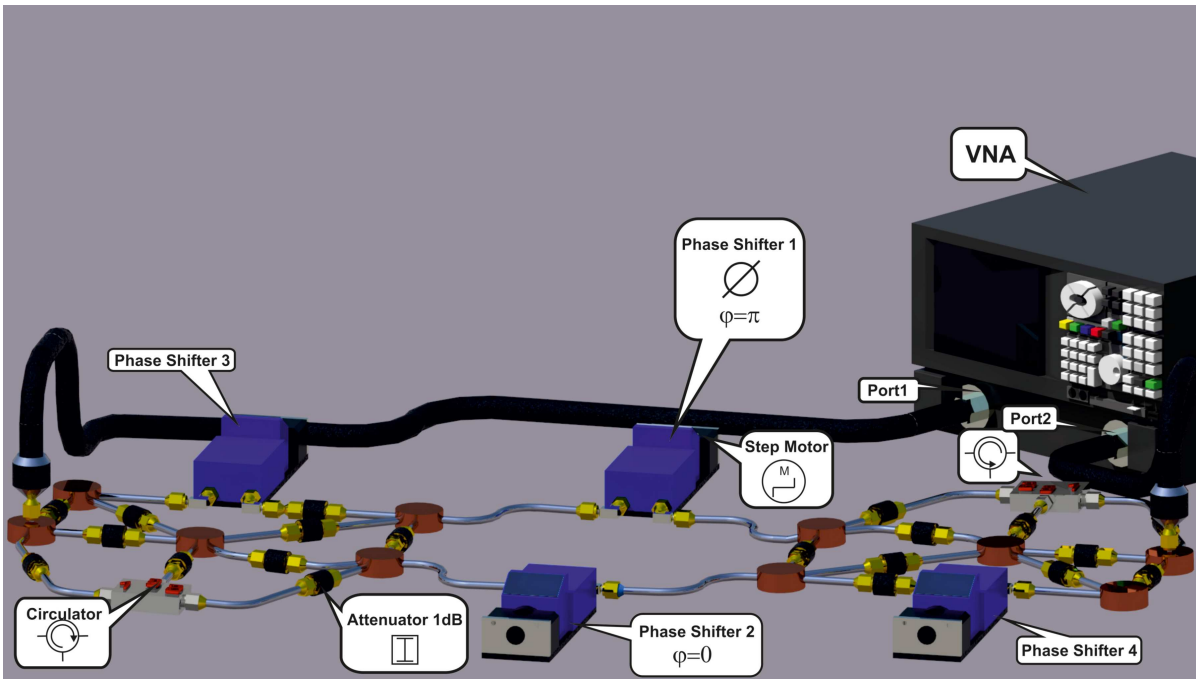

Fig. 2. The scheme of the microwave network with symplectic symmetry. The microwave network is constructed from two GUE subgraphs. Time reversal invariance violation is induced by T-shaped circulators. The subgraphs are connected by two phase shifters (No. 1 and No. 2) that induce a relative phase π. Different realizations of the GSE graph were realized by increasing the lengths of two corresponding bonds with phase shifters (No. 3 and No. 4) by the same amount. The absorption strength parameter γ in the GSE network was controlled by 20 1 dB attenuators.

coefficient $R = r^2$ given by [8]

$$P(r) = \frac{4r}{(1-r^2)^2} P_0\left(\frac{1+r^2}{1-r^2}\right). \tag{2}$$

The probability distribution $P_0(x)$ for GUE systems is given by the expression

$$P_0(x) = \frac{1}{2}\left[A^{\mathrm{GUE}}\left(\frac{\alpha}{2}(x+1)\right)^{\beta/2} + B^{\mathrm{GUE}}\right] \times \exp\left(-\frac{\alpha}{2}(x+1)\right), \tag{3}$$

where $\alpha = \gamma\beta/2$, $A^{\mathrm{GUE}} = \mathrm{e}^{\alpha} - 1$, and $B^{\mathrm{GUE}} = 1 + \alpha - \mathrm{e}^{\alpha}$.

While, in the case of GSE symmetry, the probability distribution $P_0(x)$ is defined by

$$P_0(x) = \frac{1}{2}\left[A^{\mathrm{GSE}}\gamma(x+1) + B^{\mathrm{GSE}}\right] \mathrm{e}^{-\gamma(x+1)} + C(x,\gamma)\mathrm{e}^{-\gamma x}\int_0^{\gamma} \mathrm{d}t\, \frac{\sinh(t)}{t}, \tag{4}$$

where $A^{\mathrm{GSE}} = \mathrm{e}^{2\gamma} - 1$, $B^{\mathrm{GSE}} = 1 + 2\gamma - \mathrm{e}^{2\gamma}$, and $C(x,\gamma) = \frac{1}{2}\gamma^2(x+1)^2 - \gamma(\gamma+1)(x+1) + \gamma$.

For each realization of a microwave network, the absorption parameter $\gamma = \frac{1}{2}\sum_{i=1}^{2}\gamma_i$ was evaluated by fitting the theoretical mean reflection coefficient

$$\langle r^2\rangle^{\mathrm{th}} = \int_0^1 \mathrm{d}r\; r^2 P(r) \tag{5}$$

to the experimental one, $\langle r_i^2\rangle = \langle S_{ii}S_{ii}^{\dagger}\rangle$, obtained after eliminating the direct processes, where the index $i = 1, 2$ denotes the port 1 or 2. In particular, the diagonal elements S_{ii} of the scattering matrix $\hat{S}$ of a network for the perfect coupling case were obtained by removing the direct processes present in the diagonal elements S_{ii}^{exp} of the scattering matrix $\hat{S}^{\mathrm{exp}}$ using the impedance approach [41].

5. Results

In Fig. 3a, the experimentally obtained distribution of the reflection coefficient $P(r) = \frac{1}{2}\sum_{i=1}^{2} P_i(r)$ for the microwave networks with unitary symmetry is shown for the effective absorption strength $\gamma = 5.1 \pm 0.5$ (red dots). The results are obtained by averaging over 700 realizations of the network, which were generated by increasing and decreasing the length of different pairs of network bonds by the same amount, while keeping the total optical length of the network constant at 3.61 m. The corresponding theoretical distribution $P(r)$ calculated from (2) and (3) for the parameter $\gamma = 5.1$ is represented by a red dashed line. A good overall agreement of the experimental distribution $P(r)$ with the theoretical one is observed. For comparison, we also show the theoretical distribution $P(r)$ calculated for GSE systems with the same absorption strength $\gamma = 5.1$ (blue solid line).

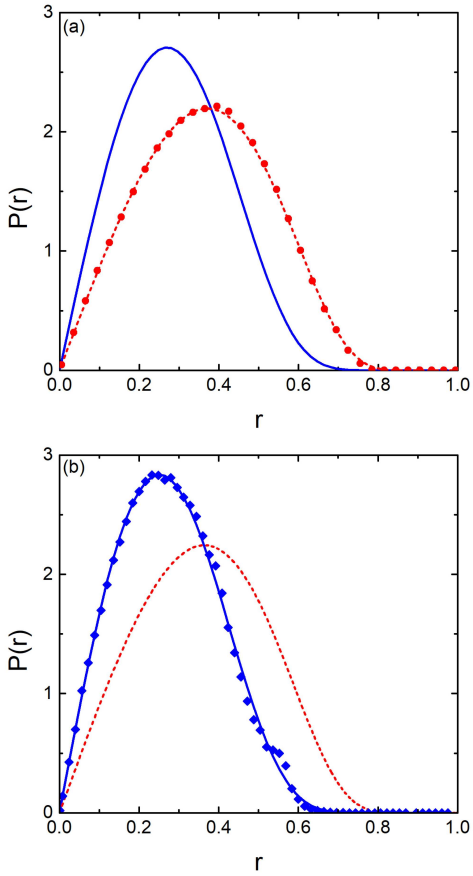

Fig. 3. (a) The experimental distribution of the reflection amplitude $P(r)$ for the microwave network with unitary symmetry for $\gamma = 5.1 \pm 0.5$ (red dots). It is compared with the theoretical ones for GUE (red dashed line) and for GSE (blue full line) calculated for $\gamma = 5.1$. (b) The experimental distribution of the reflection amplitude $P(r)$ for the microwave network with symplectic symmetry for $\gamma = 5.6 \pm 0.2$ (blue diamonds). It is compared with the theoretical ones for GSE (blue full line) and for GUE (red dashed line) for $\gamma = 5.6$.

The experimental distribution of the reflection coefficient $P(r)$ for the microwave networks with symplectic symmetry for the effective absorption strength $\gamma = 5.6 \pm 0.2$ (blue diamonds) is shown in Fig. 3b. The results were obtained by averaging over 30 realizations of the networks. The total optical length of the networks varied from 7.09 to 7.17 m. In Fig. 3b, we also show the corresponding theoretical distribution $P(r)$ (blue full line) calculated from (2) and (4) for the parameters $\gamma = 5.6$. The good overall agreement of the experimental distribution $P(r)$ with the theoretical one confirms that the procedure leading to the determination of the absorption parameter γ using (5) also works very well for the networks with symplectic symmetry. Additionally, the distribution $P(r)$ predicted for GUE systems ($\gamma = 5.6$) is shown with the red dashed line.

6. Conclusions

In conclusion, we have reported on the measurements of the distribution $P(r)$ of the amplitude of the diagonal elements $r = |S_{ii}|$ of the two-port scattering matrix $\hat{S}$ for the unitary and symplectic microwave networks for intermediate loss parameters $\gamma = 5.1 \pm 0.5$ and $\gamma = 5.6 \pm 0.2$, respectively. The experimental results were compared with the theoretical ones [8], showing good overall agreement. Thus, our experimental results validated the theoretical ones.

Acknowledgments

This work was supported in part by the National Science Centre, Poland, Grant No. UMO-2018/30/Q/ST2/00324.

References

[1] E.P. Wigner, *Ann. Math.* **53**, 36 (1951).
[2] F. Haake, *Quantum Signatures of Chaos*, Springer-Verlag, Heidelberg 2001.
[3] H.A. Weidenmüller, G.E. Mitchell, *Rev. Mod. Phys.* **81**, 539 (2009).
[4] O. Hul, S. Bauch, P. Pakoński, N. Savytskyy, K. Życzkowski, L. Sirko, *Phys. Rev. E* **69**, 056205 (2004).
[5] M. Ławniczak, S. Bauch, O. Hul, L. Sirko, *Phys. Rev. E* **81**, 046204 (2010).
[6] M. Ławniczak, L. Sirko, *Sci. Rep.* **9**, 5630 (2019).
[7] M. Ławniczak, A. Akhshani, O. Farooq, M. Białous, S. Bauch, B. Dietz, L. Sirko, *Phys. Rev. E* **107**, 024203 (2023).
[8] Y.V. Fyodorov, D.V. Savin, *JETP Lett.* **80**, 725 (2004).
[9] L. Pauling, *J. Chem. Phys.* **4**, 673 (1936).
[10] T. Kottos, U. Smilansky, *Phys. Rev. Lett.* **79**, 4794 (1997).
[11] T. Kottos, U. Smilansky, *Phys. Rev. Lett.* **85**, 968 (2000).
[12] M. Ławniczak, O. Hul, S. Bauch, P. Seba, L. Sirko, *Phys. Rev. E* **77**, 056210 (2008).
[13] Z. Pluhař, H. A. Weidenmüller, *Phys. Rev. Lett.* **112**, 144102 (2014).
[14] J. Che, J. Lu, X. Zhang, B. Dietz, G. Chai, *Phys. Rev. E* **103**, 042212 (2021).
[15] H.Z. Jooya, K. Reihani, S.-I. Chu, *Sci. Rep.* **6**, 37544 (2016).
[16] O.F. Namarvar, G. Dridi, C. Joachim, *Sci. Rep.* **6**, 30198 (2016).
[17] M. Krenn, X. Gu, and A. Zeilinger, *Phys. Rev. Lett.* **119**, 240403 (2017).

[18] O. Hul, M. Ławniczak, S. Bauch, A. Sawicki, M. Kuś, L. Sirko, *Phys. Rev. Lett* **109**, 040402 (2012).

[19] M. Ławniczak, S. Bauch, O. Hul, L. Sirko, *Phys. Scr.* **T147**, 014018 (2012).

[20] M. Ławniczak, S. Bauch, L. Sirko, in: *Handbook of Applications of Chaos Theory*, Eds. C. Skiadas, C. Skiadas, CRC Press, Boca Raton (FL) 2016, p. 559.

[21] B. Dietz, V. Yunko, M. Białous, S. Bauch, M. Ławniczak, L. Sirko, *Phys. Rev. E* **95**, 052202 (2017).

[22] M. Ławniczak, J. Lipovský, L. Sirko, *Phys. Rev. Lett.* **122**, 140503 (2019).

[23] M. Ławniczak, P. Kurasov, S. Bauch, M. Białous, V. Yunko, L. Sirko, *Phys. Rev. E* **101**, 052320 (2020).

[24] A. Rehemanjiang, M. Allgaier, C.H. Joyner, S. Müller, M. Sieber, U. Kuhl, H.-J. Stöckmann, *Phys. Rev. Lett.* **117**, 064101 (2016).

[25] J. Lu, J. Che, X. Zhang, B. Dietz, *Phys. Rev. E* **102**, 022309 (2020).

[26] M. Ławniczak, S. Bauch, O. Hul, L. Sirko, *Phys. Scr.* **T143**, 014014 (2011).

[27] M. Białous, V. Yunko, S. Bauch, M. Ławniczak, B. Dietz, L. Sirko, *Phys. Rev. Lett.* **117**, 144101 (2016).

[28] M. Ławniczak, B. Tiggelen, L. Sirko, *Phys. Rev. E* **102**, 052214 (2020).

[29] B. Dietz, T. Friedrich, H.L. Harney, M. Miski-Oglu, A. Richter, F. Schäfer, H.A. Weidenmüller, *Phys. Rev. E* **81**, 036205 (2010).

[30] J.-H. Yeh, Z. Drikas, J. Gil Gil, S. Hong, B.T. Taddese, E. Ott, T.M. Antonsen, T. Andreadis, S.M. Anlage, *Acta Phys. Pol. A* **124**, 1045 (2013).

[31] X. Zheng, S. Hemmady, T.M. Antonsen Jr., S.M. Anlage, E. Ott, *Phys. Rev. E* **73**, 046208 (2006).

[32] H.-J. Stöckmann, J. Stein, *Phys. Rev. Lett.* **64**, 2215 (1990).

[33] S. Sridhar, A. Kudrolli, *Phys. Rev. Lett.* **72**, 2175 (1994).

[34] L. Sirko, P.M. Koch, R. Blümel, *Phys. Rev. Lett.* **78**, 2940 (1997).

[35] S. Bauch, A. Błędowski, L. Sirko, P.M. Koch, R. Blümel, *Phys. Rev. E* **57**, 304 (1998).

[36] Y. Hlushchuk, A. Kohler, Sz. Bauch, L. Sirko, R. Blümel, M. Barth, H.-J. Stöckmann, *Phys. Rev. E* **61**, 366 (2000).

[37] Y. Hlushchuk, A. Błędowski, N. Savytskyy, L. Sirko, *Physica Scripta* **64**, 192 (2001).

[38] Y. Hlushchuk, L. Sirko, U. Kuhl, M. Barth, H.-J. Stöckmann, *Phys. Rev. E* **63**, 046208 (2001).

[39] A. Dhar, D.M. Rao, U. Shankar, S. Sridhar, *Phys. Rev. E* **68**, 026208 (2003).

[40] N. Savytskyy, O. Hul, L. Sirko, *Phys. Rev. E* **70**, 056209 (2004).

[41] S. Hemmady, X. Zheng, E. Ott, T.M. Antonsen, S.M. Anlage, *Phys. Rev. Lett.* **94**, 014102 (2005).

[42] O. Hul, N. Savytskyy, O. Tymoshchuk, S. Bauch, L. Sirko, *Phys. Rev. E* **72**, 066212 (2005).

[43] B. Dietz, A. Richter, *CHAOS* **25**, 097601 (2015).

[44] B. Dietz, T. Klaus, M. Miski-Oglu, A. Richter, M. Wunderle, *Phys. Rev. Lett.* **123**, 174101 (2019).

[45] M. Białous, B. Dietz, L. Sirko, *Phys. Rev. E* **100**, 012210 (2019).

[46] R.V. Jensen, S.M. Susskind, M.M. Sanders, *Phys. Rep.* **201**, 1 (1991).

[47] M. Bellermann, T. Bergemann, A. Haffmann, P.M. Koch, L. Sirko, *Phys. Rev. A* **46**, 5836 (1992).

[48] A. Buchleitner, D. Delande, *Phys. Rev. Lett.* **71**, 3633 (1993).

[49] L. Sirko, M.R.W. Bellermann, A. Haffmans, P.M. Koch, D. Richards, *Phys. Rev. Lett.* **71**, 2895 (1993).

[50] J.E. Bayfield, S.-Y. Luie, L.C. Perotti, M.P. Skrzypkowski, *Physica D: Nonlinear Phenomena* **83**, 46 (1995).

[51] L. Sirko, P.M. Koch, *Appl. Phys. B* **60**, S195 (1995).

[52] L. Sirko, A. Haffmans, M.R.W. Bellermann, P.M. Koch, *Europhys. Lett.* **33**, 181 (1996).

[53] J. Bayfield, L. Pinnaduwage, *J. Phys. B* **18**, L49 (1985).

[54] L. Sirko, S.A. Zelazny, P.M. Koch, *Phys. Rev. Lett.* **87**, 043002 (2001).

[55] A. Arakelyan, J. Nunkaew, T.F. Gallagher, *Phys. Rev. A* **94**, 053416 (2016).

[56] M. Białous, B. Dietz, L. Sirko, *Phys. Rev. E* **102**, 042206 (2020).

[57] D.V. Savin, H.-J. Sommers, Y.V. Fyodorov, *JETP Lett.* **82**, 544 (2005).

Proceedings of the 11th Workshop on Quantum Chaos and Localisation Phenomena (CHAOS 23)

Entanglement and Absorbing State Transitions in $(d+1)$-Dimensional Stabilizer Circuits

P. Sierant[a,*] and X. Turkeshi[b,c]

[a] *ICFO-Institut de Ciències Fotòniques, The Barcelona Institute of Science and Technology, Av. Carl Friedrich Gauss 3, 08860 Castelldefels (Barcelona), Spain*
[b] *Institut für Theoretische Physik, Universität zu Köln, Zülpicher Strasse 77, 50937 Köln, Germany*
JEIP, USR 3573 CNRS, Collège de France, PSL Research University, 11 Place Marcelin Berthelot, 75321 Paris Cedex 05, France

Doi: 10.12693/APhysPolA.144.474 *e-mail: Piotr.Sierant@icfo.eu

We study the influence of feedback operations on the dynamics of $(d+1)$-dimensional monitored random quantum circuit. Competition between unitary dynamics and measurements leads to an entanglement phase transition, while feedback steers the dynamics towards an absorbing state, yielding an absorbing state phase transition. Based on previous results in one spatial dimension (Phys. Rev. Lett. **130**, 120402 (2023)), we discuss the interplay between the two types of transitions for $d \geq 2$ in the presence of (i) short-range feedback operations or (ii) additional global control operations. In both cases, the absorbing state transition belongs to the d-dimensional directed percolation universality class. In contrast, the entanglement transition depends on the feedback operation type and reveals dynamics' inequivalent features. The entanglement and absorbing state phase transition remain separated for short-range feedback operations. When global control operations are applied, we find the two critical points coinciding; nevertheless, the universality class may still differ, depending on the choice of control operation.

topics: entanglement, monitored quantum dynamics, feedback operations, random circuits

1. Introduction

Monitored many-body quantum systems provide a natural perspective for understanding the progress in quantum simulations [1] and noisy intermediate-scale quantum technologies [2, 3]. Repeated measurements introduce non-unitary effects on the otherwise unitary evolution of quantum systems, leading to dynamics that can be described by stochastic quantum trajectories [4–8]. Most importantly, there is a striking distinction between the average and typical properties of the trajectory ensemble. While the former lead to quantum channels and Lindbladian evolution, the latter reveal a rich structure, including fingerprint phenomena like measurement-induced transitions (MIT) [9–14].

The distinction between average and typical trajectory is of central importance for the observability of these transitions. While average dynamics is experimentally feasible, extraction of typical features of quantum trajectories requires post-selection over the measurement results — a task of outstanding difficulty for generic systems and observables [15–24]. Indeed, to perform the post-selection for a given quantum trajectory, one has to ensure that each of the conducted measurements yields the desired result. MIT is observed in settings where the number of measurements scales proportionally to the space-time volume of the considered system. Since quantum measurements are inherently stochastic, the probability of obtaining a given trajectory is exponentially suppressed, or in other words, the resources needed to perform an experiment scale exponentially with the size of the system. Thus, without fine-tuning (cf. [25–29]), avoiding or mitigating post-selection is a central open problem in monitored quantum dynamics.

Recently, it has been proposed to use feedback operations that condition the system's dynamics on measurement outcomes to circumvent this post-selection problem. Indeed, conditional operations alter the average dynamics [30–32], and, in principle, can encode non-linear features of quantum trajectories, such as MIT, even at the averaged density matrix level. This idea has been successful for monitored free fermions and certain models of quantum chaos [33, 34], but the introduction of feedback

does not necessarily imply that MIT is observable on the level of average state. For instance, when a feedback mechanism introduces an absorbing state to the system, i.e., a state that is a fixed point of the dynamics, the resulting absorbing phase transition (APT) and MIT are generally distinct [35–38]. Nevertheless, for carefully chosen feedback operations [39], fluctuations of the order parameter of APT and the entanglement entropy can be coupled. In that case, the entanglement entropy undergoes a dynamical transition that inherits the universal features of APT. However, even when the critical points of MIT and APT coincide, the universal content of APT may differ from that of MIT, depending on the renormalization group relevance of the underlying feedback operations [39, 40].

These previous works investigate one-dimensional systems and leave the role of dimensionality in monitored systems with feedback essentially unexplored. Indeed, higher dimensional systems are generally challenging from a numerical perspective. The extensive entanglement generated by weakly monitored dynamics poses severe limitations to tensor network methods [41]. Similarly, the exponential growth of the Hilbert space with system size limits the exact simulations to a few tens of qubits. An important exception is stabilizer circuits, which are efficiently simulable via the Gottesman–Knill theorem [42, 43], and have been recently investigated in $(d+1)$ random circuits with [44–46] and without monitoring [47].

This paper investigates the interplay between APT and MIT in $(d+1)$-dimensional stabilizer circuits. We employ the flagged Clifford circuits [37, 39, 40], showing that short-range feedback operations lead to distinct APT and MIT critical points and investigating their properties. Subsequently, we also include a global feedback-control operation. In that case, the critical points of APT and MIT coincide. We unravel the similarities between the time evolution of the order parameter of APT and the entanglement entropy at any dimension d investigated. Finally, we discuss the range of validity of our results.

This manuscript is structured as follows. In Sect. 2, we review flagged stabilizer circuits, discuss the interplay between monitoring and feedback in a heuristic manner, and detail our implementation in $d \geq 2$. The core section of our work is Sect. 3, which discusses our numerical findings. Specifically, in Sect. 3.1 we study the order parameter behavior for APT, highlighting its direct percolation (DP) universality class through numerical results in $2 \leq d \leq 4$. In Sect. 3.2, we compare those findings with the entanglement dynamics for different choices of feedback operation. Section 3.3 discusses the order parameter and entanglement entropy at a fixed circuit depth (time) $t \propto L$, revealing additional aspects of APT and MIT. Our conclusions, with further discussions and outlooks, are presented in Sect. 4.

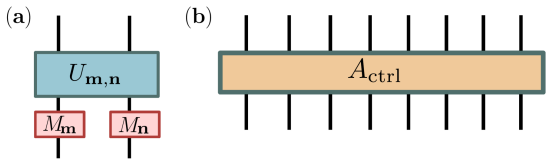

Fig. 1. Gates building a layer $K = A_{\mathrm{ctrl}}K_0$ of the considered quantum circuit. The K_0 layer consists of gates $U_{\boldsymbol{m},\boldsymbol{n}}$ applied to neighboring qubits $\boldsymbol{m}$ and $\boldsymbol{n}$, depicted in panel (a). These gates include a two-body Clifford gate $U_{\boldsymbol{m},\boldsymbol{n}}$, conditioned on the flags $f_{\boldsymbol{m}}$ and $f_{\boldsymbol{n}}$ (as discussed in Sect. 2.1), as well as measurements $M_{\boldsymbol{m}}$ and $M_{\boldsymbol{n}}$ of the $Z_{\boldsymbol{m}}$ and $Z_{\boldsymbol{n}}$ operators. These measurements are performed with a probability of p. (b) Feedback-control operation A_{ctrl} is a global Clifford gate that acts non-trivially on all lattice sites at which $f_{\boldsymbol{m}} = 0$.

2. Feedback-controlled and flagged stabilizer circuits

This section reviews the concept of flagged stabilizer circuits and details our numerical implementation of d-dimensional circuits. We also discuss the phenomenology of our system here.

2.1. Flagged stabilizer circuits

We consider a $(d+1)$ dimensional quantum circuit defined on a d-dimensional spatial lattice Λ, comprising of T layers that intersperse unitary dynamics and projective measurements of the local magnetization $Z_{\boldsymbol{m}}$. The lattice Λ is fixed as as hyperrectangular $L_1 \times \cdots \times L_d$ lattice, where $L_1 = L$ and $L_2 = \ldots = L_d = L/2$. We assume periodic boundary conditions in all directions and denote by $|X|$ the number of sites in a sublattice X. Throughout this manuscript, we denote Pauli operators by $X_{\boldsymbol{m}}$, $Y_{\boldsymbol{m}}$, $Z_{\boldsymbol{m}}$, while $|1_{\boldsymbol{m}}\rangle$ and $|0_{\boldsymbol{m}}\rangle$ are the $+1$ and -1 eigenvectors of $Z_{\boldsymbol{m}}$, and $\boldsymbol{m}$ labels the lattice sites. We consider two types of circuits: (i) with short-range feedback control, in this case each layer of the circuit is given as $K = K_0$, with K_0 comprised of local measurements and unitary gates; (ii) with global control-feedback operations for which each layer of the circuit is arranged as $K = A_{\mathrm{ctrl}}K_0$, where A_{ctrl} is a global feedback operation described below.

The measurement/unitary layer K_0 is built of $|\Lambda|/2$ two-body gates $U_{\boldsymbol{m},\boldsymbol{n}}$ presented in Fig. 1a. The two-body gate $U_{\boldsymbol{m},\boldsymbol{n}}$ acts on the *nearest neighboring* sites $\boldsymbol{m}, \boldsymbol{n}$ of the lattice. The first index, $\boldsymbol{m}$, is chosen with uniform probability, without repetitions, over the whole lattice Λ. In turn, the second index is set as $\boldsymbol{n} = \boldsymbol{m} + \boldsymbol{e}_u$, where $\boldsymbol{e}_u$ is the unit vector in a randomly chosen direction $u = 1, \ldots, d$. The gate $U_{\boldsymbol{m},\boldsymbol{n}}$ consists of the measurements $M_{\boldsymbol{m}}$, $M_{\boldsymbol{n}}$ of $Z_{\boldsymbol{m}}$, $Z_{\boldsymbol{n}}$ operators, and acts on system's state

$|\psi\rangle$ via

$$M_{\boldsymbol{m}}|\Psi\rangle = \begin{cases} \frac{1+Z_{\boldsymbol{m}}}{2}\frac{|\Psi\rangle}{\sqrt{p_+}}, & \text{with probability } p_+. \\ \\ \frac{1-Z_{\boldsymbol{m}}}{2}\frac{|\Psi\rangle}{\sqrt{p_-}}, & \text{with probability } p_-, \end{cases} \tag{1}$$

with $p_\pm = \langle\Psi|1 \pm Z_{\boldsymbol{m}}|\Psi\rangle/2$ being the Born rule probability of a given measurement outcome. Each of the measurements is performed with the *measurement probability* (or *rate*) p, which is the control parameter that allows tuning the considered quantum circuit between various dynamical phases. The measurements are followed by the action of a two-body gate $U_{\boldsymbol{m},\boldsymbol{n}}$ selected, with uniform probability, from the 2-qubit Clifford group. The gate $U_{\boldsymbol{m},\boldsymbol{n}}$ is conditioned on the classical labels $f_{\boldsymbol{m}}$ in a way specified below. The procedure of creating the layer K_0 consists of a random generation of $|\Lambda|/2$ two-body gates $U_{\boldsymbol{m},\boldsymbol{n}}$ that is performed independently during the construction of each of the circuit layers.

To introduce feedback in our system, we fix $|\mathrm{ABS}\rangle \equiv \bigotimes_{\boldsymbol{m}\in\Lambda}|1_{\boldsymbol{m}}\rangle$ as the absorbing state, i.e., we require that $|\mathrm{ABS}\rangle$ is a fixed point of the dynamics of our circuit, $K|\mathrm{ABS}\rangle = |\mathrm{ABS}\rangle$. For this purpose, the two-body gates $U_{\boldsymbol{m},\boldsymbol{n}}$ should preserve the states $|1_{\boldsymbol{m}}1_{\boldsymbol{n}}\rangle$. Since Clifford gates fulfilling this condition do not generate genuine quantum correlations, we introduce, following [39], the classical flags $f_{\boldsymbol{m}} = 0, 1$ at each site $\boldsymbol{m} \in \Lambda$ to establish the feedback mechanism in our stabilizer circuits. The system is initialized in the state $|\Psi_0\rangle = \bigotimes_{\boldsymbol{m}\in\Lambda}|0_{\boldsymbol{m}}\rangle$ and we initially set $f_{\boldsymbol{m}} = 0$ for all $\boldsymbol{m} \in \Lambda$. After each measurement, we change the flag to $f_{\boldsymbol{m}} = 1$ when the outcome is $+1$ (otherwise the flag remains unchanged, $f_{\boldsymbol{m}} = 0$). The two-body gate $U_{\boldsymbol{m},\boldsymbol{n}}$ acts on the sites $\boldsymbol{m}, \boldsymbol{n}$ only when $f_{\boldsymbol{m}} f_{\boldsymbol{n}} = 0$. Otherwise, $U_{\boldsymbol{m},\boldsymbol{n}}$ is replaced by the two-site identity matrix.

The short-range feedback mechanism is present in a circuit comprised solely of layers K_0 due to the flag mechanism built in the two-body gates $U_{\boldsymbol{m},\boldsymbol{n}}$. It is straightforward to verify that $|\mathrm{ABS}\rangle$ is indeed an absorbing state, $K_0|\mathrm{ABS}\rangle = |\mathrm{ABS}\rangle$.

Finally, to introduce the global control operation to our system, we consider A_{ctrl}, see Fig. 1b, which is a global random Clifford unitary that acts non-trivially only on the subset $\tilde{\Lambda} = \{\boldsymbol{m} \in \Lambda : f_{\boldsymbol{m}} = 0\} \subset \Lambda$ of unflagged sites. This construction of the feedback-control operation A_{ctrl} ensures that our stabilizer circuit can generate extensive entanglement in the presence of monitoring while preserving $|\mathrm{ABS}\rangle$ as an absorbing state. In the following, we will compare and contrast the properties of the circuit built of layers of $K = K_0$ with the time evolution of the circuit $K = A_{\mathrm{ctrl}}K_0$ composed of the global feedback-control operation A_{ctrl} and the measurement/unitary layer K_0.

We note that with these specifications, the described setups are amenable to efficient numerical simulations for $d \geq 2$ [45, 47] that scale polynomially in the system size L. Our simulations of flagged stabilizer circuits are implemented in a state-of-the-art package STIM [43] and use an asymptotically fast [48, 49] algorithm for computation of rank with complexity $\mathcal{O}(N^3/\log_2(N))$ [50], where $N = |\Lambda|$ is the number of qubits in the lattice.

2.2. Post-selection: linear and non-linear functions of the density matrix

Before proceeding to the systematic numerical analysis of the next section, we would like to highlight some vital physical aspects of the dynamics of the considered quantum circuits with feedback. Performing numerical simulations of the quantum dynamics of the flagged stabilizer circuits, we obtain the time-evolved state $|\Psi_t\rangle \equiv \prod_t K_t|\Psi_0\rangle$ and the corresponding density matrix $\rho_t \equiv |\Psi_t\rangle\langle\Psi_t|$. We are interested in quantities that are averaged over the circuit realizations. This leads to a crucial difference between physical quantities concerning their dependence on the density matrix ρ_t:

- Linear functions of ρ_t, for instance, a defect density

$$n_{\mathrm{def}}(\Psi_t) = 1 - \mathrm{Tr}\left(\rho_t \sum_{\boldsymbol{m}} \frac{1+Z_{\boldsymbol{m}}}{2N}\right), \tag{2}$$

  where $N = |\Lambda| = L(L/2)^{d-1}$ is the total number of sites in the lattice. Taking the average (denoted by the overline) over the circuit realizations of the defect density yields $n_{\mathrm{def}} \equiv \overline{n_{\mathrm{def}}(\Psi_t)}$, which, due to the linearity of the considered quantity, amounts to

$$n_{\mathrm{def}} = 1 - \mathrm{Tr}\left(\overline{\rho_t} \sum_{\boldsymbol{m}} \frac{1+Z_{\boldsymbol{m}}}{2N}\right), \tag{3}$$

  i.e., the average defect density n_{def} is determined solely by the average density matrix $\overline{\rho_t}$.

- Non-linear functions of ρ_t, for instance, entanglement entropy

$$S_X(\Psi_t) = \overline{-\mathrm{Tr}_X\Big(\rho_X(t)\log_2\rho_X(t)\Big)}, \tag{4}$$

  where $\rho_X(t) = \mathrm{Tr}_{X_c}(\rho_t)$ is the reduced density matrix for the subsystem X [8] obtained by tracing out the degrees of freedom of its complement X_c ($\Lambda = X \cup X_c$). Due to the non-linearity of (4), the average entanglement entropy, $S_X(t) \equiv \overline{S_X(\Psi_t)}$, has to be calculated directly by evaluating $S_X(\Psi_t)$ and by averaging the result over the circuit realizations. In other words, there is generally no functional dependence between $S_X(t)$ and the average density matrix $\overline{\rho_t}$.

The dichotomy between linear and non-linear functions of ρ_t is reflected at the level of physical quantities and phenomena that can be captured with the two types of quantities. Averages of linear functions of ρ_t are amenable to experiments as they do not

require post-selection and are dependent solely on the average density matrix $\overline{\rho_t}$. The defect density n_{def} captures APT in the system. Conversely, non-linear functionals of the state, such as the entanglement entropy $S_X(t)$, reveal phenomena occuring at the level of individual trajectories of the system, such as MIT, and require post-selection. Indeed, to calculate $S_X(\Psi_t)$, we have first to ensure that we consider a fixed final state $|\Psi_t\rangle$ that depends on the outcomes of the performed measurements, then evaluate $S_X(\Psi_t)$ by repeatedly preparing the same final state $|\Psi_t\rangle$, and only then we can average the result over the circuit realizations.

2.3. Phenomenology of feedback-monitored systems with an absorbing state

In our system, due to the presence of a feedback mechanism, we expect that $\lim_{t\to\infty}\rho = |\text{ABS}\rangle\langle\text{ABS}|$. Indeed, if in a particular region λ of the lattice Λ the measurements of $Z_{\boldsymbol{m}}$ yield the result of 1, the flags in the region λ are set to unity, $f_{\boldsymbol{m}} = 1$. Hence, due to the feedback used, the unitary gates $U_{\boldsymbol{m},\boldsymbol{n}}$ can act non-trivially only on the edges of the λ region. In contrast, in the bulk of the subsystem λ the state is already locally ferromagnetically ordered, as in the absorbing $|\text{ABS}\rangle$. Hence, as our system evolves, the lattice Λ becomes covered with ordered domains in which the spins are aligned as in the absorbing state, $\langle\Psi_t|Z_{\boldsymbol{m}}|\Psi_t\rangle = 1$, and defect regions in which the spins are not aligned in that way, $\langle\Psi_t|Z_{\boldsymbol{m}}|\Psi_t\rangle \neq 1$, as schematically presented in Fig. 2. The fraction of sites in the defect regions is precisely given by n_{def} defined in (2).

Since $|\text{ABS}\rangle$ is invariant under each K layer of the circuit, the ordered domains, on average, grow. This introduces ordering to the system, which finally reaches the absorbing state. The timescale for reaching $|\text{ABS}\rangle$ is altered by p. At high measurement rates ($p > {p_c}^{\text{APT}}$), ordered regions develop quickly and the defect density n_{def} decays exponentially in time. Conversely, at small measurement rates ($p < p_c^{\text{APT}}$), the system is in a non-absorbing phase. The unitary gates scramble information, while still competing with the measurements. This leads to a non-vanishing defect density n_{def}, prevails to time scales exponentially large in the system size L. Close to the APT critical point $p \approx p_c^{\text{APT}}$, ordering in the system develops so that the defect density decays in a characteristic power-law fashion, which is a signature of absorbing phase transition (APT).

The dynamics of APT can be observed at the level of the average state $\overline{\rho_t}$. In contrast, the entanglement properties of the system unravel a richer structure observable at the level of individual trajectories $|\psi_t\rangle$.

Notably, the entanglement content of the system is fixed by the presence/absence of the feedback-control operation A_{ctrl}, which, by construction, does not affect the dynamics of the average state $\overline{\rho_t}$. Without the control operation ($a = 0$, $K = K_0$), the feedback mechanism is solely short-ranged, and no-long range entanglement is generated between distant disordered regions, see Fig. 2a. Indeed, the unitaries $U_{\boldsymbol{m},\boldsymbol{n}}$ generate quantum correlations only among degrees of freedom within or close to the boundary of defect regions. The absorbing state is a product state. Hence, we expect that MIT occurs before APT (i.e., $p_c^{\text{MIT}} < p_c^{\text{APT}}$) in such a way that the state can follow the area-law of entanglement entropy while the system is not yet in an absorbing phase. For instance, the state may host isolated single-site defects. Such a state is not volume-law entangled but is still not an absorbing state.

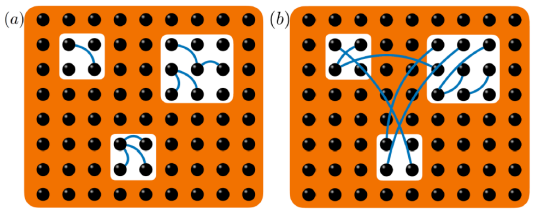

Fig. 2. Conditioning of the unitary gates on the measurement outcomes by the flags mechanism leads to the emergence of ordered domains (highlighted in orange) and defect regions. (a) Short-range control operations only entangle degrees of freedom within the same defect regions. (b) An additional global feedback-control operation A_{ctrl} generates long-range entanglement, coupling distant disordered areas. The blue lines pictorially represent entangled degrees of freedom.

When the global feedback-control operation A_{ctrl} is used, it globally couples all defect regions, creating long-range entanglement between distant defects, see Fig. 2b. In this case, we expect $p_c^{\text{MIT}} = p_c^{\text{APT}}$ since any arbitrarily separated qubits in a defect state will be correlated by A_{ctrl} and only a fully ordered state hosts no entanglement. This heuristic discussion was corroborated for $d = 1$ dimensional systems in [39]. We confirm this picture with a systematic numerical analysis for $d \geq 1$ in the following sections.

3. Numerical results

In this section, we discuss numerical results for the described circuit architecture and various space dimensions $d \leq 4$, considering the average dynamics reflected by the defect density n_{def} as well as non-linear functions of ρ_t. Specifically, we investigate the entanglement entropy dynamics $S_X(t)$ for setups with short-range feedback mechanisms and with the additional global feedback-control operation A_{ctrl}. Lastly, we investigate the system's entanglement and average state features at a fixed circuit depth.

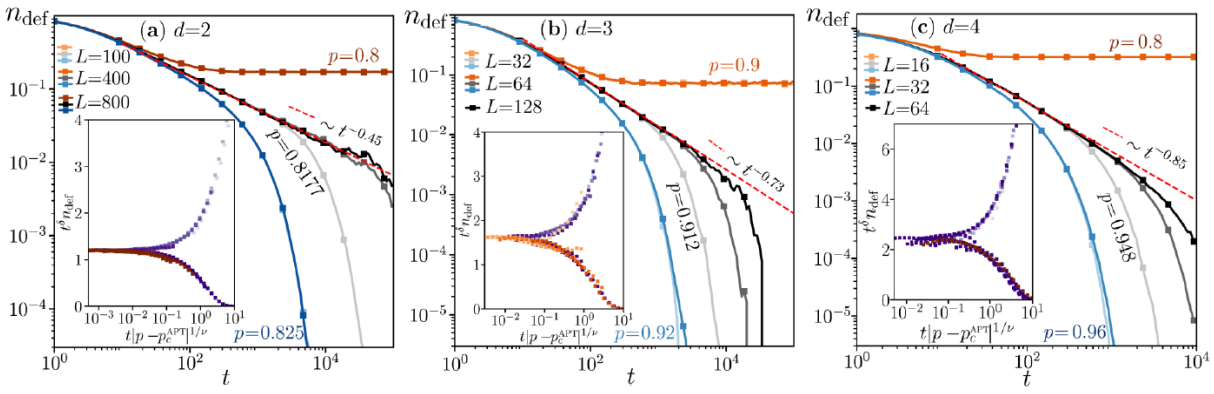

Fig. 3. Absorbing state phase transition in $d = 2, 3, 4$ dimensional circuits. The time evolution of the defect density n_{def} was obtained by considering PCA for average dynamics (see text). Panels (a, b, c) show the n_{def} as a function of time t for measurement rate below/close to/above APT. Darker colors correspond to increasing system sizes. For $d = 2$ (a), we consider $L = 100, 400, 800$, for $d = 3$ (b) $L = 32, 64, 128$, and for $d = 4$ (c) $L = 16, 32, 64$. In the vicinity of APT, we observe characteristic power-law decays $n_{\mathrm{def}} \propto t^{-\delta}$ with exponents δ close to the exponents for the DP class. The insets show $t^{\delta} n_{\mathrm{def}}$ plotted as functions of $t|p - p_c^{\mathrm{APT}}|^{1/\nu}$, demonstrating data collapses with exponents consistent with the DP class, see Table I for exponent values.

3.1. Dynamics of the order parameter

We begin by analyzing the dynamics of the average state $\overline{\rho}_t$. Following standard techniques, see e.g. [35, 36, 39, 40], the average dynamics can be analytically mapped to a probabilistic cellular automaton. Appendix A2 details a short discussion about this mapping which we use to calculate quantities depending on $\overline{\rho}_t$, such as the defect density n_{def}. Computing the classical average dynamics is more efficient than calculating the full quantum dynamics of the circuit with stabilizer formalism, which allows us to simulate systems in $2 \leq d \leq 4$. Focusing on the evolution of the defect density n_{def} over time t (circuit depth) close to APT, we average the results over no less than $N_{\mathrm{real}} = 200$ realizations of the circuit and study the behavior n_{def} in systems of size up to $L = 800$ in $d = 2$, $L = 128$ in $d = 3$, and $L = 64$ in $d = 4$ dimensions. Our results are summarized in Fig. 3.

Our results for $d = 2$ and systems of size $L \geq 100$ are shown in Fig. 2a. At $p = 0.8$, the defect density attains a non-zero stationary value that persists on time scales that increases exponentially with L, indicating that the system is in the non-absorbing phase. In stark contrast, a hallmark of the absorbing phase is visible for $p = 0.825$ — the defect density decays to zero exponentially with time t independently of the system size L. The critical point that separates the two phases is located at the measurement rate $p_c^{\mathrm{APT}} = 0.8175(2)$ at which a power-law decay $n_{\mathrm{def}} \propto t^{-\delta}$ with an exponent $\delta = 0.45(1)$ emerges. This behavior is characteristic for the DP universality class in dimension $d = 2$. Varying the measurement rate around $p = p_c^{\mathrm{APT}}$, we observe a collapse of $t^{\delta} n_{\mathrm{def}}$ plotted as a function of $t|p - p_c^{\mathrm{APT}}|^{1/\nu}$, see inset in Fig. 3a, with exponent $\nu = 1.30(3)$, which is in agreement with the $d = 2$ DP universality class [51, 52].

Our results for the average dynamics in $d = 3$ are presented in Fig. 3b. In the non-absorbing phase, the defect density n_{def} attains a non-zero stationary value up to a time scale which grows exponentially with L, as exemplified by the results displayed for $p = 0.9$. In the absorbing phase, n_{def} decreases exponentially to zero, as demonstrated by the data for $p = 0.92$. At APT in $d = 3$, at $p_c^{\mathrm{APT}} = 0.912(1)$, we notice a power-law decay $n_{\mathrm{def}} \propto t^{-\delta}$, with the exponent $\delta = -0.73(2)$, compatible with the $d = 3$ DP universality class. Moreover, as the inset in Fig. 3b illustrates, we find a collapse of $t^{\delta} n_{\mathrm{def}}$ versus $t|p - p_c^{\mathrm{APT}}|^{1/\nu}$, with $\nu = 1.11(4)$ consistently, within error bars, with the critical exponents for the $d = 3$ DP universality class [51, 52].

As shown in Fig. 3c, the defect density n_{def} in the $d = 4$ dimensional system behaves in a quantitatively similar fashion in the non-absorbing phase (e.g., at $p = 0.8$) and in the absorbing phase (e.g., at $p = 0.96$). The two phases are separated by a phase transition at which the power-law decay of the defect density emerges. At the considered system size $L = 64$, we find that the decay of n_{def} is well approximated by a decay with an exponent $\delta = 0.85(1)$ at $p_c^{\mathrm{APT}} = 0.948(2)$. However, by comparing this exponent with the results for $L = 16$ and $L = 32$, we notice a persistent increase of our estimate of δ as L increases. For instance, at $L = 16$, the power-law decay persists for the longest time for $p = 0.945$ with exponent $\delta = 0.79(1)$. Hence, the effects of finite system size introduce a systematic error into our numerical analysis, preventing us from quantitatively confirming the mean-field critical exponents $\delta = 1$ and

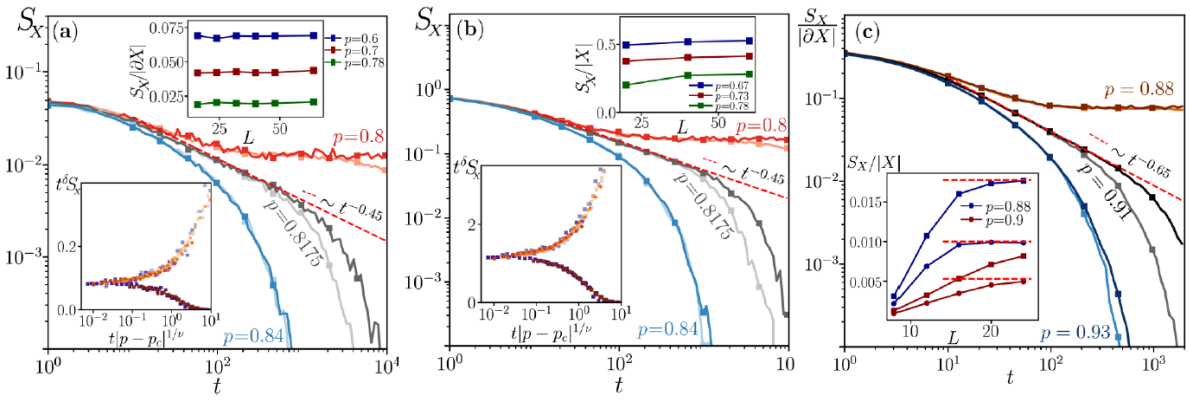

Fig. 4. Entanglement entropy S_X without the control operation (a) and with the control operation $A_{\rm ctr}$ (b) close to APT in the $d = 2$ dimensional system. Panel (c) shows S_X for $d = 3$ with $A_{\rm ctrl}$. Darker (lighter) tones correspond to $L = 60$ ($L = 40$) for $d = 2$ and $L = 24$ ($L = 16$) for $d = 3$, while the colors represent the measurement rate p. For $d = 2$, at $p = 0.8175 \approx p_c^{\rm APT}$, we observe the power-law decays with exponent $\delta = 0.45(1)$ characteristic for the DP class in $d = 2$. The bottom insets in (a, b) show collapses of data with exponents consistent with DP class in $d = 2$, see Table I. The upper insets in (a, b) present the value of entanglement entropy S_X at time $t = 4L$ for $p < p_c^{\rm APT}$ as a function of the size of the subsystem boundary ∂X, where (a) indicates an area-law $S_X \propto |\partial X|$, while (b) exhibits a volume-law behavior, $S_X \propto |X|$. For $d = 3$ in (c), we find a power law behavior with $\delta = 0.65(4)$ around the critical point $p_c^{\rm APT} = 0.912(1)$. In the inset, we reveal the emerging volume-law scaling, $S_X \propto |X|$. Results are averaged over more than 10^3 circuit realizations.

TABLE I

Summary of critical exponents characterizing dynamical transitions in flagged Clifford circuits. The column denoted by "DP class" shows the expectations of the directed percolation theory [51, 52]. The column "Unitary Dyn." presents the exponents obtained in studies of the full quantum dynamics of the flagged stabilizer circuits. At the same time, the column "Average Dyn." reports the results obtained from the simulation of the probabilistic cellular automaton and they correspond to the average dynamics of the flagged stabilizer circuits. The results of our numerical simulations are consistent with the DP universality class, except for the average dynamics results for $d = 4$, which are subject to significant system size drifts and hence are denoted by the asterisks.

	DP class		Unitary Dyn.		Average Dyn.	
d	δ	ν	δ	ν	δ	ν
2	0.450(5)	1.295(6)	0.45(2)	1.30(5)	0.45(1)	1.30(3)
3	0.73(1)	1.11(1)	0.65(4)*	–	0.73(2)	1.09(4)
4	1	1	–	–	0.85(5)*	1.0(1)*

$\nu = 1$ expected for the DP universality class at $d = 4$ [53]. Nevertheless, the trends characterizing our results suggest that the mean-field critical exponents may describe the considered system when the time scales and sizes of the system are sufficiently large.

3.2. Entanglement evolution

Now, we switch to full quantum dynamics of the circuit and calculate the time-evolved state $|\Psi_t\rangle$. We focus on non-linear functions of the density matrix ρ_t, which grasp physics beyond average state properties. We consider the average entanglement entropy $S_X(t)$ for the subsystem X, which is a hyper rectangle of dimensions $l_x \times L/2 \times \ldots \times L/2$ (recall that the full system has dimensions $L \times L/2 \times \ldots \times L/2$). We set the value of l_x as $L/4$, which allows us to distinguish between area-law and volume-law scaling of entanglement entropy when the system size L is increased.

Without the feedback-control operation $A_{\rm ctrl}$, i.e., in the presence of only short-range feedback control, the system undergoes measurement-induced transitions (MIT) at $p_c^{\rm MIT} = 0.255(3)$ between phases with volume-law and area-law entanglement entropy, with properties fully analogous to MIT reported in $d = 2$ systems without feedback [45].

In Fig. 4a, we present the time evolution of the entanglement entropy $S_X(t)$ at measurement rates p close to APT, which occurs at $p_c^{\rm APT} = 0.8175(2)$. The entanglement entropy $S_X(t)$ saturates at $p < p_c^{\rm APT}$ to a finite value, decays exponentially with time t when $p > p_c^{\rm APT}$ and follows a power-law

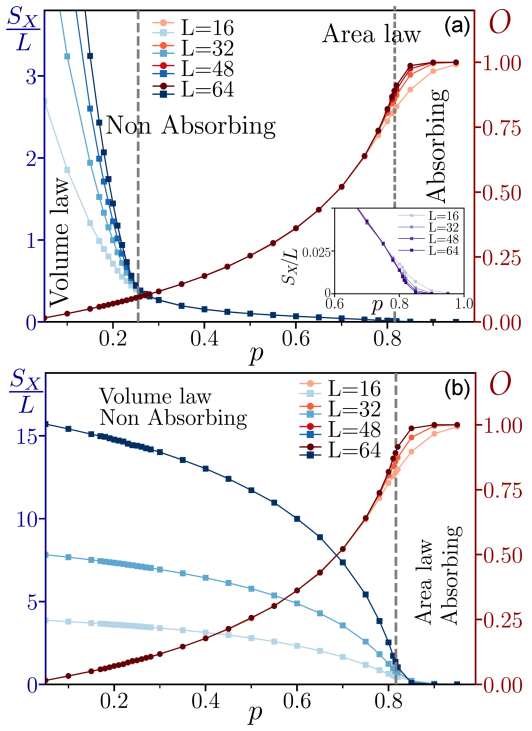

Fig. 5. Properties of the system at time $t = 4L$ as a function of the measurement rate p for the dimensional system $d = 2$. Panel (a) presents results with short-range feedback only (i.e., without the control $A_{\rm ctrl}$) and demonstrates a volume-law phase of entanglement $S_A \propto L^2$ at $p < p_c^{\rm MIT} = 0.255(3)$ and an area-law phase $S_A \propto L$ at $p > p_c^{\rm MIT}$. The order parameter $O \equiv 1 - n_{\rm def}$ is smaller than unity for $p < p_c^{\rm APT} = 0.8165(19)$ and approaches 1 in the $L \to \infty$ limit for $p > p_c^{\rm APT}$. The inset in panel (a) shows the area-to-area law transition of the entanglement entropy S_X at $p = p_c^{\rm APT}$. The panel (b) presents the same, but in the presence of the global feedback-control operation $A_{\rm ctrl}$. APT and MIT merge in a single transition at which the volume-to-area law entanglement transition accompanies the ordering transition reflected by O.

decay when $p \simeq p_c^{\rm APT}$. This behavior is analogous to the behavior of the defect density $n_{\rm def}$ near APT. Moreover, as shown in the lower inset of Fig. 4a, the entanglement entropy has the same dynamical scaling as $n_{\rm def}$, with compatible critical exponents, see Table I. Importantly, the entanglement entropy presents an area-law behavior and scales proportionally to the number of sites at the boundary ∂X of the region X, $S_X \propto |\partial X|$ at any measurement probability $p > p_c^{\rm APT}$, as illustrated in the upper inset in Fig. 4a. Consequently, at $p = p_c^{\rm APT}$, there is an area-to-area law entanglement transition at time $t \propto L$, in full analogy with the $d = 1$ case [39].

In the presence of the feedback-control operation $A_{\rm ctrl}$, the dynamical behavior of the entanglement entropy $S_X(t)$ at a fixed subsystem size is entirely analogous to the short-range feedback case, as shown in Fig. 4b. However, in the presence of $A_{\rm ctrl}$, the entanglement entropy has the volume-law scaling with the subsystem size at all $p < p_c^{\rm APT}$. This is demonstrated in the upper inset in Fig. 4b, which shows that $S_X/|X|$ approaches a constant as the subsystem size increases. Thus, at measurement rate $p = p_c^{\rm APT}$, the system undergoes an entanglement transition between volume-law scaling and area-law scaling of entanglement entropy at time $t \propto L$ (see the next section for further discussion of this point).

Finally, the results for $d = 3$, presented in Fig. 4c, exhibit an analogous behavior. We note that the power-law decay of $S_X/|X|$ close to APT is governed by an exponent $\delta \approx 0.65(4)$, slightly smaller than the value for the DP class for $d = 3$. This is a finite-size effect caused by the limitations of the largest system size, $L = 24$, available to our full quantum dynamics simulation. In contrast, calculations of average dynamics were performed for systems of size up to $L = 128$ at $d = 3$ and yielded the result consistent with the DP class in $d = 3$. The presence of the feedback-control operation $A_{\rm ctrl}$ ensures that the entanglement entropy follows a volume-law $S_X \propto |X|$, as indicated by the saturation of the curves shown in the inset of Fig. 4c. Consequently, at $t \propto L$, the system undergoes an entanglement transition between volume-law and area-law scaling of the entanglement entropy.

The critical features of the entanglement entropy dynamics reported in this section for systems in dimensions $d = 2$ and $d = 3$ are entirely analogous to the results for $d = 1$ discussed in [39]. By analogy, we expect similar results to extend to $d = 4$, the upper critical dimension for the DP universality class [53]. Nevertheless, our present capabilities of the simulation of Clifford circuits prevent us from a quantitative confirmation of this conjecture.

3.3. Absorbing and entanglement phase transition at time $t \propto L$

As we argued in Sect. 2.2, the presence of a feedback mechanism in our system implies that $\lim_{t\to\infty} \rho_t = |{\rm ABS}\rangle\langle{\rm ABS}|$ in any finite system size L. In other words, if the limit of large time is taken, we will always find our system in the trivial, ordered, product state $|{\rm ABS}\rangle\langle{\rm ABS}|$. However, fixing a specific time scale at which we observe the system, for instance, setting $t = 4L$ (which we will use henceforth in this section), allows us to uncover manifestations of the dynamical phase transitions described above.

In Fig. 5, we compare the results for $d = 2$ by considering both short-range feedback and including the global feedback-control operation $A_{\rm ctrl}$. A clear signature of APT is the fact that the order parameter $O \equiv 1 - n_{\rm def}$ approaches its maximal value $O \to 1$ at $p > p_c^{\rm APT}$ when the system size increases, while $O < 1$ for $p < p_c^{\rm APT}$, as demonstrated by the

red lines in Fig. 5. We reiterate that the behavior of the order parameter is the same in the presence and absence of A_{ctrl} by the construction of our feedback mechanism.

In the presence of the short-range feedback only, see the top panel in Fig. 5, we observe two separate transitions, namely (i) MIT between phases with volume-law and area-law entanglement entropy at the measurement rate $p = p_c^{\mathrm{MIT}} = 0.255(3)$ and (ii) APT at $p = p_c^{\mathrm{APT}}$. We note that area-law scaling for $d = 2$ implies that $S_X \propto L$. Notably, at $p = p_c^{\mathrm{APT}}$, there is a second entanglement transition between the area-law phase characterized by $S_X \propto L$ and the area-law phase with $S_X \to 0$ as demonstrated by the inset in the top panel of Fig. 5.

However, when the global feedback-control operation A_{ctrl} is present, the entanglement entropy S_X behavior parallels that of the defect number n_{def}. Consequently, in that case, there is only a single volume-law to area-law entanglement transition in our system at $p = p_c^{\mathrm{APT}}$, as shown in the lower panel of Fig. 5.

The behavior of entanglement entropy presented at time $t = 4L$ has its roots in the separation of time scales of the approach to the absorbing state that occurs at APT. Since the dynamical behavior of entanglement entropy in $d = 3$ is parallel to the results for $d = 2$, the entanglement entropy has analogous behavior to that presented in Fig. 5 in the presence and absence of the global feedback control operation in $d = 3$ at time $t \propto L$ (data not shown).

4. Conclusions

In this work, we analyzed the role of dimensionality in the dynamics of monitored stabilizer circuits with a feedback control mechanism introduced by classical labels (flags), which gives rise to an absorbing state of the dynamics. While dimensionality changes the universal content of APT and MIT, the phenomenological understanding presented of one-dimensional circuits is generalized straightforwardly to higher dimensions d. In particular, similarly to the $d = 1$ dimensional case [39], the range of feedback-control operations is a crucial ingredient for the interplay between entanglement and absorbing state transition. We find that circuits with short-range feedback control exhibit two entanglement transitions at circuit depths proportional to the system size, namely a volume-to-area law transition at the MIT critical point and an area-to-area law transition at the APT transition point. Instead, when global feedback-control operations are present, there is only a single volume-to-area MIT which coincides with APT. For the employed global unitary operation, MIT inherits the properties of the underlying APT universality class. In our implementation, the latter is unaffected by the feedback control operations range and always leads to the critical behavior described by directed percolation universality class in d dimensions, as summarized in Table I. The average dynamics results are consistent with the expectation that $d = 4$ is the upper critical dimension beyond which the mean-field critical exponents capture the properties of APT. In contrast, the upper critical dimension for MIT in setups without feedback mechanisms is $d_c = 6$ [45].

Similarly to the one-dimensional case, our work concludes that the post-selection problem can be mitigated if appropriate feedback-control operations are chosen. The behavior of the entanglement entropy at the area-to-area law phase transition in the setup with short-range feedback control and the volume-to-area law phase transition in the setup with global control operation can be observed by measurements of the defect density, which does not require the post-selection. However, the crucial caveat is that the correspondence between the dynamics defect density and the entanglement entropy does not generally hold but requires the choice of a sufficiently strongly entangling control operation (see [39] for explicit examples). In other words, the post-selection problem is mitigated only by meeting stringent control operations requirements. Moreover, introducing global control operations may significantly alter the trajectory ensemble. As a result, feedback control drives the original measurement-induced transition (present in the system without feedback control) onto a different universality class. We expect similar conclusions to hold for generic (Haar) circuits. While numerical methods are ineffective, a generalization of the arguments in [40] may lead to a formal proof of the distinct APT and MIT when $q \gg 1$ dimensional qudits are considered. Similarly, we expect that our arguments generalize to a monitored fermionic model with conditional feedback control in higher dimensions and variable-range interactions, which we will extensively discuss in a future contribution [54]. An interesting future direction is to enhance our understanding of the interplay between absorbing states, topological state preparation, and shallow circuits [55–62]. We leave these questions as subjects of further explorations.

Acknowledgments

XT acknowledges support from the ANR grant "NonEQuMat." (ANR-19-CE47-0001) and computational resources on the Collége de France IPH cluster. PS acknowledges support from: ERC AdG NOQIA, Ministerio de Ciencia y Innovation Agencia Estatal de Investigaciones (PGC2018-097027-B-I00/10.13039/501100011033, CEX2019-000910-S/10.13039/501100011033, Plan National FIDEUA PID2019-106901GB-I00, FPI, QUANTERA MAQS PCI2019-111828-2, QUANTERA DYNAMITE PCI2022-132919, Proyectos de I+D+I "Retos Colaboración" QUSPIN RTC2019-007196-7); MICIIN with funding from European Union

NextGenerationEU(PRTR-C17.I1) and by Generalitat de Catalunya; Fundació Cellex; Fundació Mir-Puig; Generalitat de Catalunya (European Social Fund FEDER and CERCA program, AGAUR Grant No. 2017 SGR 134, QuantumCAT U16-011424, co-funded by ERDF Operational Program of Catalonia 2014–2020); EU Horizon 2020 FET-OPEN OPTOlogic (Grant No. 899794); EU Horizon Europe Program (Grant Agreement 101080086 — NeQST), National Science Centre, Poland (Symfonia Grant No. 2016/20/W/ST4/00314); ICFO Internal "QuantumGaudi" project; European Union's Horizon 2020 research and innovation program under the Marie-Skłodowska-Curie grant agreement No. 101029393 (STREDCH) and No. 847648 ("La Caixa" Junior Leaders fellowships ID100010434: LCF/BQ/PI19/11690013, LCF/BQ/PI20/11760031, LCF/BQ/PR20/11770012, LCF/BQ/PR21/11840013).

Views and opinions expressed in this work are, however, those of the author(s) only and do not necessarily reflect those of the European Union, European Climate, Infrastructure and Environment Executive Agency (CINEA), nor any other granting authority. Neither the European Union nor any granting authority can be held responsible for them.

Appendix: Additional details

For self-consistency, this appendix presents additional technical details. After a more formal discussion on flagged Clifford circuits, we discuss the mapping of average dynamics to the classical model. We briefly review the Gottesman–Knill theorem and how stabilizer simulations are performed.

A1. Flagged Clifford circuits

Our discussion follows closely the paper [39], to which we refer for additional details. At a formal level, flagged Clifford circuits extend our many-body quantum state to $|\Psi\rangle \mapsto |\Phi\rangle = |\Psi\rangle \otimes |\mathcal{F}\rangle$. The flag vector $|\mathcal{F}\rangle = \otimes_{\boldsymbol{m}\in\Lambda}|f_{\boldsymbol{m}}\rangle$ registers the post-measurement polarizations and determines the action of the unitary gates at each time step. As in the main text, we fix $|\mathrm{ABS}\rangle = |1_{\boldsymbol{m}}\rangle$ as the absorbing state.

The key idea is that flagged sites $\boldsymbol{m}$ (i.e., for which $f_{\boldsymbol{m}} = 1$) are unchanged by the measurement layer M and by the global unitary A. Furthermore, depending on the nearest neighbors flags $f_{\boldsymbol{n}}$, two-body gates $U_{\boldsymbol{m},\boldsymbol{n}}$ act trivially or as a random Clifford transformation. (Here $\boldsymbol{n} = \boldsymbol{m} + \hat{\boldsymbol{e}}_\mu$, with $\hat{\boldsymbol{e}}_\mu$ being the versor in the randomly chosen direction $\mu = 1, \ldots, d$.)

In the doubled Hilbert space, the absorbing state $|\Phi_{\mathrm{abs}}\rangle = |\mathrm{ABS}\rangle \otimes |1_{\boldsymbol{m}}\rangle^{\otimes_{\boldsymbol{m}}}$ is the fixed point of the dynamics, while the initial state is $|\Phi_0\rangle = |\Psi_0\rangle \otimes |0_{\boldsymbol{m}}\rangle^{\otimes_{\boldsymbol{m}}}$. The non-trivial control operation A_{ctrl}, when present, is given by

$$A_{\mathrm{ctrl}}|\Phi\rangle = \left(C_{\{\boldsymbol{m}:f_{\boldsymbol{m}}=0\}}|\Psi\rangle\right) \otimes |\mathcal{F}\rangle \tag{5}$$

with $C_{\{\boldsymbol{m}:f_{\boldsymbol{m}}=0\}}$ being a global Clifford unitary acting only on unflagged sites. On the other hand, the projective measurement and two-body gates are given respectively by

$$P_{\boldsymbol{m}}|\Phi\rangle = \begin{cases} \frac{1}{\sqrt{p_-}}\left(\frac{1-Z_{\boldsymbol{m}}}{2}|\Psi\rangle\right) \otimes \left[\left(X_{\boldsymbol{m}} - \mathrm{i}Y_{\boldsymbol{m}}\right)^{f_{\boldsymbol{m}}}|\mathcal{F}\rangle\right], & \text{outcome } -1, \\ \frac{1}{\sqrt{p_+}}\left(\frac{1+Z_{\boldsymbol{m}}}{2}|\Psi\rangle\right) \otimes \left[\left(X_{\boldsymbol{m}} + \mathrm{i}Y_{\boldsymbol{m}}\right)^{1-f_{\boldsymbol{m}}}|\mathcal{F}\rangle\right], & \text{otherwise}, \end{cases} \tag{6}$$

and

$$U_{\boldsymbol{m},\boldsymbol{n}}|\Phi\rangle = \begin{cases} C_{\boldsymbol{m},\boldsymbol{n}}|\Psi\rangle \otimes \left[\left(X_{\boldsymbol{m}} - \mathrm{i}Y_{\boldsymbol{m}}\right)^{f_{\boldsymbol{m}}}\left(X_{\boldsymbol{n}} - \mathrm{i}Y_{\boldsymbol{n}}\right)^{f_{\boldsymbol{n}}}|\mathcal{F}\rangle\right], & \text{if } f_{\boldsymbol{m}}f_{\boldsymbol{n}} = 0, \\ |\Phi\rangle, & \text{otherwise}, \end{cases} \tag{7}$$

for the nearest neighboring sites $\boldsymbol{m}$ and $\boldsymbol{n}$.

A2. Mapping of average dynamics to classical model

As discussed in the previous section, the flagged Clifford circuit acts in a formally doubled Hilbert space. We now discuss the dynamics of the average state over Clifford gates. More importantly, the average dynamics of the observables linear in a state, such as n_{def}, is fully encoded in the mean state $R_t = \mathbb{E}_{\mathrm{Clifford}}[|\Phi_t\rangle\langle\Phi_t|]$, with t — depth/time of the circuit. The core idea is that the average dynamics over the Clifford unitaries corresponds to a probabilistic cellular automaton (PCA). The average state requires independently drawn Clifford operations C, each of them acting on a single bra and ket, namely

$$I \equiv \int_{\mathrm{Clifford}} \mathrm{d}C\; C|\Psi\rangle\langle\Psi|C^\dagger. \tag{8}$$

However, the integral I is easily performed using the 2-design property of the Clifford group [63] as the Haar integral

$$I = \int_{\text{Haar}} \mathrm{d}C\ C|\Psi\rangle\langle\Psi|C^\dagger = \frac{1}{2^w}\mathbb{1}_C \otimes P^\perp|\Psi\rangle\langle\Psi|P^\perp, \tag{9}$$

where $\mathbb{1}_C$ is the sites where C acts non-trivially, and $P^\perp$ is the projection on its complementary space. By introducing the indices $k_{\boldsymbol{m}} = 0, \pm 1$, the on-site mixed state $\rho_{\boldsymbol{m}}^{(0)} = \frac{1}{2}\mathbb{1}_{\boldsymbol{m}}$, and the on-site projectors $\rho_{\boldsymbol{m}}^{(\pm 1)} = \frac{1}{2}(\mathbb{1}_{\boldsymbol{m}} \pm Z_{\boldsymbol{m}})$, it follows that the Clifford averaged state is

$$R_t = \mathbb{E}_{\text{Clifford}}[|\Phi_t\rangle\langle\Phi_t|] = \left(\bigotimes_{\boldsymbol{m}\in\Lambda} \rho_{\boldsymbol{m}}^{(f_{\boldsymbol{m}})}\right) \otimes \left(\bigotimes_{\boldsymbol{m}\in\Lambda} \rho_{\boldsymbol{m}}^{(-1)^{f_{\boldsymbol{m}}+1}}\right). \tag{10}$$

Since the physical state and the flags are in one-to-one correspondence, the average dynamics correspond to a probabilistic cellular automaton of the flags. The average dynamics over measurement locations, measurement outcomes, and unitary locations can be written down analogously. This corresponds to a discrete master equation for R_t, that we do not detail for presentation purposes, cf. also [39].

A3. Brief review on the simulation of stabilizer circuits

We conclude by briefly reviewing ideas for stabilizer simulations and refer to [42, 45] for additional details. The stabilizer state on the lattice Λ is fixed by L^d independent Pauli strings $g_{\boldsymbol{m}}$ such that $g_{\boldsymbol{m}}|\Psi\rangle = |\Psi\rangle$. Each Pauli string is parametrizes as

$$g_{\boldsymbol{m}} = \mathrm{e}^{\mathrm{i}\pi\phi_{\boldsymbol{m}}} \prod_{\boldsymbol{j}\in\Lambda} (X^{a_{\boldsymbol{m}}^{\boldsymbol{i}}} Z^{b_{\boldsymbol{m}}^{\boldsymbol{i}}}) \tag{11}$$

where $\phi_{\boldsymbol{m}}, a_{\boldsymbol{m}}^{\boldsymbol{i}}, b_{\boldsymbol{m}}^{\boldsymbol{i}} = 0, 1$ are the $\mathbb{Z}_2$ numbers. The group $\mathcal{G}$ generated by the Pauli strings $g_{\boldsymbol{m}}$ is abelian and fixes the state as $|\Psi\rangle\langle\Psi| = \sum_{g\in\mathcal{G}} g/2^{L^d}$. Therefore, the state is completely determined by the matrix $G = (\phi_{\boldsymbol{m}}|a_{\boldsymbol{m}}^{\boldsymbol{i}}, b_{\boldsymbol{m}}^{\boldsymbol{i}})$, whose rows fix the generators of the group $\mathcal{G}$.

Stabilizer circuits involve stabilizer states that evolve under the Clifford gates and projective measurements. By definition, Clifford unitaries transform a Pauli string into a single Pauli string. Hence, they correspond to a transformation of the $L^d \times (L^d + 1)$ matrix G to the new matrix G' [42]. Similarly, projective measurements onto Pauli strings transform G in a new matrix G''. If the projecting Pauli string g^* is already in the group $\mathcal{G}$, then $G \mapsto G$. (Finding the measurement outcome requires a Gaussian elimination, cf. [42].) Viceversa, if the operator g^* is not in the group $\mathcal{G}$, then there exist a set I_{anti} of anticommuting operators g_μ such that $\{g^*, g_\mu\} = 0$ for each $\mu \in I_{\text{anti}}$. The measurement outcome is randomly and uniformly ± 1, and the state collapses after the measurement onto the resulting string $\pm g^*$. One can verify that the updated matrix $G \mapsto G''$ is given by g_ν such that $[g^*, g_\nu] = 0$, together with g^* and the transformed set $g_{\tilde{\mu}} \cdot g_\mu$ for $\tilde{\mu} \in I_{\text{anti}}$ and $\mu \in I_{\text{anti}}/\{\tilde{\mu}\}$. The above statement summarizes the Gottesman–Knill theorem and illustrates how the system is efficiently simulable with polynomial classical resources of the number of N qubits. Lastly, given a bipartition $X \cup X_c$, the entanglement of a stabilizer state $|\Psi\rangle$ can be computed efficiently [64, 65] using

$$S_X(|\Psi\rangle) = |X| - \log_2|\mathcal{G}_X|, \tag{12}$$

where $\mathcal{G}_X$ is a subgroup of all elements in $\mathcal{G}$ that act trivially on X_c, and $|X|$ is the number of qubits in X. The calculation of $\log_2|\mathcal{G}_X|$ reduces to the calculation of the rank of the appropriate submatrix of the matrix G over the $\mathbb{Z}_2$ field for which we use the algorithm of [48–50]. We note that participation entropies of stabilizer states can be calculated in a similar way, see [14].

References

[1] J. Fraxanet, T. Salamon, M. Lewenstein, *The Coming Decades of Quantum Simulation*, arXiv:2204.08905, 2022.

[2] J. Preskill, *Quantum* **2**, 79 (2018).

[3] K.J. Ferris, A.J. Rasmusson, N.T. Bronn, O. Lanes, *Quantum Simulation on Noisy Superconducting Quantum Computers*, arXiv:2209.02795, 2022.

[4] H. Carmichael, *An open systems approach to quantum optics* (Springer, Berlin, Germany, 1993).

[5] J. Dalibard, Y. Castin, K. Mølmer, *Phys. Rev. Lett.* **68**, 580 (1992).

[6] K. Mølmer, Y. Castin, J. Dalibard, *J. Opt. Soc. Am. B* **10**, 524 (1993).

[7] H.M. Wiseman, G.J. Milburn, *Quantum Measurement and Control* (Cambridge University Press (Cambridge, UK), 2009).

[8] H.P. Breuer, F. Petruccione, *The theory of open quantum systems* (Oxford University Press (Oxford, UK), 2002).

[9] X. Cao, A. Tilloy, A.D. Luca, *SciPost Phys.* **7**, 024 (2019).

[10] B. Skinner, J. Ruhman, A. Nahum, *Phys. Rev. X* **9**, 031009 (2019).

[11] Y. Li, X. Chen, M.P.A. Fisher, *Phys. Rev. B* **98**, 205136 (2018).

[12] Y. Li, X. Chen, M.P.A. Fisher, *Phys. Rev. B* **100**, 134306 (2019).

[13] A. Chan, R.M. Nandkishore, M. Pretko, G. Smith, *Phys. Rev. B* **99**, 224307 (2019).

[14] P. Sierant, X. Turkeshi, *Phys. Rev. Lett.* **128**, 130605 (2022).

[15] J.M. Koh, S.-N. Sun, M. Motta, A.J. Minnich, *Experimental Realization of a Measurement-Induced Entanglement Phase Transition on a Superconducting Quantum Processor*, arXiv:2203.04338, 2022.

[16] M.P.A. Fisher, V. Khemani, A. Nahum, S. Vijay, *Random Quantum Circuits*, arXiv:2207.14280, 2022.

[17] A.C. Potter, R. Vasseur, *Entanglement dynamics in hybrid quantum circuits, in Entanglement in Spin Chains: From Theory to Quantum Technology Applications*, edited by A. Bayat, S. Bose, H. Johannesson (Springer, Cham, 2022) pp. 211-249.

[18] O. Lunt, J. Richter, A. Pal, *Quantum simulation using noisy unitary circuits and measurements, in Entanglement in Spin Chains: From Theory to Quantum Technology Applications*, edited by A. Bayat, S. Bose, and H. Johannesson (Springer, Cham, 2022) pp. 251-284.

[19] R. Vasseur, A.C. Potter, Y.-Z. You, A.W.W. Ludwig, *Phys. Rev. B* **100**, 134203 (2019).

[20] C.-M. Jian, Y.-Z. You, R. Vasseur, A.W.W. Ludwig, *Phys. Rev. B* **101**, 104302 (2020).

[21] A. Nahum, S. Roy, B. Skinner, J. Ruhman, *PRX Quantum* **2**, 010352 (2021).

[22] Y. Bao, S. Choi, E. Altman, *Phys. Rev. B* **101**, 104301 (2020).

[23] M.J. Gullans, D.A. Huse, *Phys. Rev. X* **10**, 041020 (2020).

[24] S.J. Garratt, E. Altman, *Probing post-measurement entanglement without post-selection*, arXiv:2305.20092, 2023.

[25] S.J. Garratt, Z. Weinstein, E. Altman, *Phys. Rev. X* **13**, 021026 (2023).

[26] J.C. Hoke, M. Ippoliti, D. Abanin et al., *Quantum information phases in space-time: measurement-induced entanglement and teleportation on a noisy quantum processor*, arXiv:2303.04792 (2023).

[27] C. Noel, P. Niroula, D. Zhu, A. Risinger, L. Egan, D. Biswas, M. Cetina, A.V. Gorshkov, M.J. Gullans, D.A. Huse, C. Monroe, *Nature Physics* **18**, 760 (2022).

[28] M. Ippoliti, V. Khemani, *Phys. Rev. Lett.* **126**, 060501 (2021).

[29] G. Passarelli, X. Turkeshi, A. Russomanno, P. Lucignano, M. Schirò, R. Fazio, *Post-selection-free measurement-induced phase transition in driven atomic gases with collective decay*, arXiv:2306.00841, 2023.

[30] A.J. Friedman, O. Hart, R. Nandkishore, *Measurement-induced phases of matter require feedback*, arXiv:2210.07256, 2023.

[31] S. Roy, J.T. Chalker, I.V. Gornyi, Y. Gefen, *Phys. Rev. Res.* **2**, 033347 (2020).

[32] M. McGinley, S. Roy, S.A. Parameswaran, *Phys. Rev. Lett.* **129**, 090404 (2022).

[33] M. Buchhold, T. Müller, S. Diehl, *Revealing measurement-induced phase transitions by pre-selection*, arXiv:2208.10506, 2022.

[34] T. Iadecola, S. Ganeshan, J.H. Pixley, J.H. Wilson, *Phys. Rev. Lett.* **131**, 060403 (2023).

[35] N. O'Dea, A. Morningstar, S. Gopalakrishnan, V. Khemani, *Entanglement and Absorbing-State Transitions in Interactive Quantum Dynamics*, arXiv:2211.12526, 2022.

[36] V. Ravindranath, Y. Han, Z.-C. Yang, X. Chen, *Entanglement Steering in Adaptive Circuits with Feedback*, arXiv:2211.05162, 2022.

[37] V. Ravindranath, Z.-C. Yang, X. Chen, *Free fermions under adaptive quantum dynamics*, arXiv:2306.16595, 2023.

[38] N. Makki, N. Lang, H.P. Büchler, *Absorbing state phase transition with clifford circuits*, arXiv:2303.05317, 2023.

[39] P. Sierant, X. Turkeshi, *Phys. Rev. Lett.* **130**, 120402 (2023).

[40] L. Piroli, Y. Li, R. Vasseur, A. Nahum, *Phys. Rev. B* **107**, 224303 (2023).

[41] U. Schollwöck, *Annals of Physics* **326**, 96 (2011).

[42] S. Aaronson, D. Gottesman, *Phys. Rev. A* **70**, 052328 (2004).

[43] C. Gidney, *Quantum* **5**, 497 (2021).

[44] X. Turkeshi, R. Fazio, M. Dalmonte, *Phys. Rev. B* **102**, 014315 (2020).

[45] P. Sierant, M. Schirò, M. Lewenstein, X. Turkeshi, *Phys. Rev. B* **106**, 214316 (2022).

[46] O. Lunt, M. Szyniszewski, A. Pal, *Phys. Rev. B* **104**, 155111 (2021).

[47] P. Sierant, M. Schirò, M. Lewenstein, X. Turkeshi, *Entanglement growth and minimal membranes in (d+1) random unitary circuits*, arXiv:2306.04764, (2023).

[48] D. Andrén, L. Hellström, K. Markström, *Adv. Appl. Math.* **39**, 428 (2007).

[49] M.R. Albrecht, G.V. Bard, C. Pernet, *Efficient Dense Gaussian Elimination over the Finite Field with Two Elements*, arXiv:1111.6549, 2011.

[50] E. Bertolazzi, A. Rimoldi, *J. Comput. Appl. Math.* **260**, 519 (2014).

[51] M.A. Muñoz, R. Dickman, A. Vespignani, S. Zapperi, *Phys. Rev. E* **59**, 6175 (1999).

[52] H. Hinrichsen, *Advances in Physics* **49**, 815 (2000).

[53] M. Henkel, *Non-equilibrium phase transitions* (Springer, 2008).

[54] P. Sierant, M. Schirò, M. Lewenstein, X. Turkeshi (in preparation).

[55] A. Lavasani, Y. Alavirad, M. Barkeshli, *Nature Phys.* **17**, 342 (2021).

[56] A. Lavasani, Y. Alavirad, M. Barkeshli, *Phys. Rev. Lett.* **127**, 235701 (2021).

[57] G.-Y. Zhu, N. Tantivasadakarn, A. Vishwanath, S. Trebst, R. Verresen, *Nishimori's cat: stable long-range entanglement from finite-depth unitaries and weak measurements*, arXiv:2208.11136, 2022.

[58] S. Sang, T.H. Hsieh, *Phys. Rev. Research* **3**, 023200 (2021).

[59] J.Y. Lee, W. Ji, Z. Bi, M.P.A. Fisher, *Decoding Measurement-Prepared Quantum Phases and Transitions: from Ising model to gauge theory, and beyond*, arXiv:2208.11699, 2022.

[60] K. Klocke, M. Buchhold, *Phys. Rev. B* **106**, 104307 (2022).

[61] G.-Y. Zhu, N. Tantivasadakarn, S. Trebst, *Structured volume-law entanglement in an interacting, monitored majorana spin liquid*, arXiv:2303.17627, (2023).

[62] K. Klocke, M. Buchhold, *Majorana loop models for measurement-only quantum circuits*, arXiv:2305.18559, (2023).

[63] D. Gross, S. Nezami, M. Walter, *Communications in Mathematical Physics* **385**, 1325 (2021).

[64] A. Hamma, R. Ionicioiu, P. Zanardi, *Phys. Rev. A* **71**, 022315 (2005).

[65] A. Nahum, J. Ruhman, S. Vijay, J. Haah, *Phys. Rev. X* **7**, 031016 (2017).

Proceedings of the 11th Workshop on Quantum Chaos and Localisation Phenomena (CHAOS 23)

Engineering Metamaterial Interface Scattering Coefficients via Quantum Graph Theory

T.M. Lawrie[a], G. Tanner[a,*] and G.J. Chaplain[b]

[a] *School of Mathematical Sciences, University of Nottingham, NG7 2RD, United Kindom*
[b] *Centre for Metamaterial Research and Innovation, Department of Physics and Astronomy, University of Exeter, Exeter EX4 4QL, United Kindom*

Doi: 10.12693/APhysPolA.144.486 *e-mail: gregor.tanner@nottingham.ac.uk

For layered metamaterial devices, the reflection and transmission coefficients at an interface typically depend on the properties of the coupling between different layers. In this paper, we set out to engineer the reflection/transmission behaviour at boundaries to obtain desirable properties such as achieving total reflection and transmission. Based on the quantum graph formulation for modelling metamaterials developed in *Sci. Rep.* **12(1)**, 18006 (2022), we tailor the interface reflection and transmission coefficients by patterning the boundary with resonant elements at each interface vertex. By tuning the internal lengths of the resonant elements, we demonstrate both minimization and maximization of the reflection coefficient via a scattering formulation. In addition, we present an interface set-up incorporating beyond-nearest-neighbour connections, which yields narrow-band transmission for certain angles only, creating an angular filtering interface.

topics: quantum graph theory, wave scattering, metamaterials, wave propagation

1. Introduction

Over recent decades, the field of metamaterial research has grown rapidly with the intent of engineering materials with special electromagnetic and acoustic wave properties, see for example [1] for an overview. Typically, metamaterial properties are given by a unit cell resonant or phase modulating characteristics. Recently, also non-local or beyond-nearest-neighbour interactions [2] have been investigated. These structures have additional coupling terms due to connections that extend beyond the periodic unit cell; numerical and experimental realisations have been studied both in an acoustics and elasticity setting [3–6]. Customisation procedures have been developed to engineer the dispersion behaviour of metamaterials using competing channels of the power flowing through the structure [7]. In numerical simulations, the governing models have, so far, been based on analogies to systems of coupled masses and springs akin to the canonical model used by Brillouin [8]. In this paper, we model metamaterials via quantum graph theory instead, first introduced by Lawrie et al. [9]. The wave dynamics takes place here along one-dimensional edges coupled at vertices on an infinite periodic graph network. Resonant characteristics can be introduced in the form of vertex scattering conditions. The model provides a fast and flexible tool for designing metamaterials and for uncovering new and interesting wave phenomena.

Quantum graph theory was initially formulated by Kottos and Smilansky [10] in order to study the quantum mechanical properties of complex systems; for a comprehensive introduction, see [11, 12]. The simple mathematical construction of quantum graphs naturally leads to a great number of interdisciplinary applications, such as the study of quantum chaos [11], modelling the vibrations of coupled plates [13], formulating quantum random walks [14, 15] and quantum search algorithms [16]. The graph formalism allows the eigenvalue conditions to be written in terms of a secular equation for a matrix of finite dimension. Similarly, the scattering matrix of an open quantum graph can be given as a closed-form expression involving finite dimensional matrices. Closed-form expressions of the Green's function of a quantum graph have been given in [17]. Infinite periodic quantum graphs allow for a spectral analysis where an underlying graph "decoration" can be chosen to create spectral gaps [18]. For such infinite periodic graph structures, it has furthermore been shown by Exner et al. [19] that the spectrum of the graph Hamiltonian converges to the corresponding Schrödinger operator on the Euclidean space in the continuum limit. This makes the mathematical language of quantum graph theory an ideal tool for modelling metamaterial set-ups using a continuum limit formulation.

Describing wave coupling between different media is a key problem in metamaterial research and the motivation for this work. The ability to efficiently

model such an interface permits an additional degree of freedom for metamaterial design, which has recently received attention in the context of homogenisation [20]. At a metamaterial interface, the boundary reflection coefficients depend strongly on the properties of the interface layer connecting the two metamaterials. In order to tune the reflection behaviour, we use and expand on tools introduced in [9]. We tailor the interface scattering coefficients by decorating the boundary with resonant elements at each interface vertex. By varying the underlying graph structure, we demonstrate the tunability of the reflection/transmission behaviour ranging from total reflection to total transmission. This formulation is then used to construct a beam splitting and steering device with minimal reflection — a primitive cloak. In addition, we present scattering effects when introducing a beyond-nearest-neighbour structure at the boundary. We find rapid switching between full reflection and transmission as a function of the angle of incident, that is, the interface acts as an angular filtering device.

The paper is structured as follows: In Sect. 2, we introduce the general quantum graph formalism for modelling metamaterials based on the theory developed in [9]. In Sect. 2.1, the wave dynamics on the graph is defined, and in Sect. 2.2, it is shown how the compact portions of the graph at each vertex are reduced to simple frequency-dependent point scatterers. The eigenfunction solutions on the periodic quantum graph are introduced in Sect. 2.3 and combined to form Gaussian beam solutions in Sect. 2.4. In Sect. 3, we derive the scattering matrix for a boundary layer or interface connecting two metamaterials. We demonstrated the efficiency and flexibility of the quantum graph approach by showing various example set-ups in Sect. 3.2. In particular, modifications for obtaining resonant interfaces giving zero and full reflection, as well as a configuration displaying both beam splitting and reconfiguration, are shown in Sect. 3.2.1. Finally, in Sect. 3.2.2, the effects of introducing a beyond-nearest-neighbour interface are formulated, showing interesting angle filtering properties.

2. Metamaterials: The quantum graph formalism

2.1. General set-up

We will provide a brief introduction to the quantum graph model for metamaterials here; for more details, see [9]. Typically, metamaterials are constructed from a periodic arrangement of sub-wavelength resonant elements. We consider each such element as an open quantum graph $\Gamma(\mathcal{V}, \mathcal{E}, L)$, where $\mathcal{V}$ is a finite set of vertices with imposed boundary conditions connected by a finite set of bidirectional edges $\mathcal{E}$ with metric length $L = \{\ell_j : j \in \mathcal{E}\}$. Edges of finite length will be called bonds

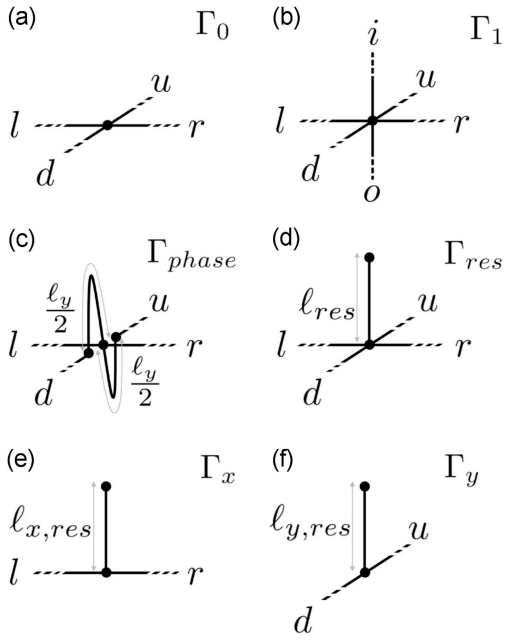

Fig. 1. Six examples of sub-wavelength resonant or phase modulating elements are shown labelled here as Γ_x, Γ_y, Γ_0, Γ_1, Γ_{res}, and Γ_{phase}. The bond lengths are shown as $\ell_{x,res}$, $\ell_{y,res}$, ℓ_{res}, and ℓ_y. In turn, the lead directions are given by l, r, d, u, i, and o. The graph in (c) represents a phase modulator, the graph in (d) represents a resonator on a vertex, and (e) and (f) resonant resonators on an edge.

$\mathcal{B}$ with coordinate $z_j = [0, \ell_j]$ with reverted edge coordinate given by $\tilde{z}_j = \ell_j - z_j$. Edges of infinite length will be called leads $\mathcal{L}$ with coordinate $z_j = [0, \infty)$ and no reverted edge coordinate. Naturally, $\mathcal{E} = \mathcal{B} \cup \mathcal{L}$. The resonant characteristics of an element are determined by treating the compact portion of the graph as a scattering site, as shown in Fig. 1. The construction of the corresponding scattering matrix is described in Sect. 2.2. The open graphs are then arranged and connected to form a mesh with square periodic topology embedded in $\mathbb{R}^2$ and discussed in more detail in Sect. 2.3. For this construction, four leads $\mathcal{L} = \mathcal{L}_l, \mathcal{L}_r, \mathcal{L}_d, \mathcal{L}_u$ are imposed on the compact portion of the graph in the left (l), right (r), down (d), and up (u) directions. In the example in Fig. 1b, two additional leads, $\mathcal{L}_i$ and $\mathcal{L}_o$, have been added, heading in (i) and out (o) of the plane and allowing for beyond-nearest-neighbour connections discussed in more detail in Sect. 3.1. All edges in $\mathcal{E}$ are endowed with the Helmholtz wave equation with wave number k, i.e.,

$$\left(\frac{\partial^2}{\partial z_j^2} + k^2\right)\psi_j(z_j) = 0. \tag{1}$$

The solutions are given as a superposition of counter-propagating plane waves on a given edge $j \in \mathcal{E}$, i.e.,

$$\psi_j(z_j) = \mathrm{e}^{\mathrm{i}kz_j} a_j^{\mathrm{out}} + \mathrm{e}^{-\mathrm{i}kz_j} a_j^{\mathrm{in}}. \tag{2}$$

Here, $a_j^{\text{out/in}}$ represents the complex wave amplitudes heading out of or into a vertex. The edge solutions can then be concatenated to form the vector $\boldsymbol{\Psi}(\hat{Z}) = (\boldsymbol{\Psi}_{\mathcal{L}}(\hat{Z}), \boldsymbol{\Psi}_{\mathcal{B}}(\hat{Z}))^{\mathrm{T}}$ of all lead and bond solutions, where

$$\boldsymbol{\Psi}(\hat{Z}) = \mathrm{e}^{\mathrm{i}k\hat{Z}}\boldsymbol{a}^{\text{out}} + \mathrm{e}^{-\mathrm{i}k\hat{Z}}\boldsymbol{a}^{\text{in}}. \tag{3}$$

Here, $\boldsymbol{a}^{\text{out/in}} = (\boldsymbol{a}_{\mathcal{L}}^{\text{out/in}}, \boldsymbol{a}_{\mathcal{B}}^{\text{out/in}})^{\mathrm{T}}$ represents the vector of all complex wave amplitudes, and $\hat{Z}$ is a diagonal matrix of all edge coordinates. Given the general solutions, we can treat the compact portion of the graph as a scattering site and thus derive a resonant element scattering matrix $\hat{S}_{\Gamma}$.

2.2. The unit cell scattering matrix

Wave transport along each bond can be modelled by mapping the outgoing wave amplitudes at vertices to the incoming wave amplitudes at adjacent vertices by a matrix $\hat{P}(k;L)$,

$$\boldsymbol{a}_{\mathcal{B}}^{\text{in}} = \hat{P}(k;L)\,\boldsymbol{a}_{\mathcal{B}}^{\text{out}}. \tag{4}$$

The matrix elements of $\hat{P}$ take account of the phase $\mathrm{e}^{\mathrm{i}k\ell_j}$ accumulated by the wave as it travels along a given bond j. The wave amplitudes on different edges are mapped from incoming to outgoing wave amplitudes at the vertices via a vertex scattering matrix $\hat{\sigma}$ that satisfies the imposed vertex boundary conditions, i.e.,

$$\boldsymbol{a}^{\text{out}} = \hat{\sigma}\,\boldsymbol{a}^{\text{in}}, \qquad \text{or in block form}$$
$$\left(\begin{array}{c}\boldsymbol{a}_{\mathcal{L}}^{\text{out}}\\ \hline \boldsymbol{a}_{\mathcal{B}}^{\text{out}}\end{array}\right) = \left(\begin{array}{c|c}\hat{\sigma}_{\mathcal{L}\mathcal{L}} & \hat{\sigma}_{\mathcal{L}\mathcal{B}}\\ \hline \hat{\sigma}_{\mathcal{B}\mathcal{L}} & \hat{\sigma}_{\mathcal{B}\mathcal{B}}\end{array}\right)\left(\begin{array}{c}\boldsymbol{a}_{\mathcal{L}}^{\text{in}}\\ \hline \boldsymbol{a}_{\mathcal{B}}^{\text{in}}\end{array}\right). \tag{5}$$

For this work, we assume Neumann–Kirchhoff boundary conditions [11] at each vertex, giving the pq-th matrix element of $\hat{\sigma}$ associated with vertex V_j as

$$\left[\hat{\sigma}_{V_j}\right]_{pq} = \frac{2}{v_{V_j}} - \delta_{pq}. \tag{6}$$

Note that the index j runs now over the number of vertices $\mathcal{V}$ in Γ. Here, δ_{pq} is the Kronecker delta, and v_{V_j} is the valency (number of attached edges) at vertex V_j. From here, a graph scattering matrix $\hat{S}_{\Gamma}$ can be determined, which performs the mapping between the leads only, i.e.,

$$\boldsymbol{a}_{\mathcal{L}}^{\text{out}} = \hat{S}_{\Gamma}(k;L)\,\boldsymbol{a}_{\mathcal{L}}^{\text{in}}. \tag{7}$$

Now, $\hat{S}_{\Gamma}$ can be constructed from $\hat{\sigma}$ and $\hat{P}$ by

$$\hat{S}_{\Gamma}(k;L) = \hat{\sigma}_{\mathcal{L}\mathcal{L}} + \hat{\sigma}_{\mathcal{L}\mathcal{B}}\left[\hat{\mathbb{I}} - \hat{P}(k;L)\hat{\sigma}_{\mathcal{B}\mathcal{B}}\right]^{-1}\hat{P}(k;L)\hat{\sigma}_{\mathcal{B}\mathcal{L}}, \tag{8}$$

where $\hat{\mathbb{I}}$ is the identity matrix; see [9] for more details.

Below are the results of solving (8) for each resonant element shown in Fig. 1, i.e.,

$$\hat{S}_{\Gamma_0} = \tfrac{1}{2}\hat{\mathbb{E}}^{(4\times4)} - \hat{\mathbb{I}}^{(4\times4)}, \tag{9}$$

$$\hat{S}_{\Gamma_1} = \tfrac{1}{3}\hat{\mathbb{E}}^{(6\times6)} - \hat{\mathbb{I}}^{(6\times6)}, \tag{10}$$

$$\hat{S}_{\Gamma_{phase}}(k;\ell_y) = \tfrac{1}{2}\begin{pmatrix} -1 & 1 & \mathrm{e}^{\frac{\mathrm{i}k\ell_y}{2}} & \mathrm{e}^{\frac{\mathrm{i}k\ell_y}{2}} \\ 1 & -1 & \mathrm{e}^{\frac{\mathrm{i}k\ell_y}{2}} & \mathrm{e}^{\frac{\mathrm{i}k\ell_y}{2}} \\ \mathrm{e}^{\frac{\mathrm{i}k\ell_y}{2}} & \mathrm{e}^{\frac{\mathrm{i}k\ell_y}{2}} & -\mathrm{e}^{\mathrm{i}k\ell_y} & \mathrm{e}^{\mathrm{i}k\ell_y} \\ \mathrm{e}^{\frac{\mathrm{i}k\ell_y}{2}} & \mathrm{e}^{\frac{\mathrm{i}k\ell_y}{2}} & \mathrm{e}^{\mathrm{i}k\ell_y} & -\mathrm{e}^{\mathrm{i}k\ell_y} \end{pmatrix}, \tag{11}$$

$$\hat{S}_{\Gamma_{res}}(k;\ell_{res}) = \frac{2\cos(k\ell_{res})}{3\cos(k\ell_{res}) + \mathrm{e}^{-\mathrm{i}k\ell_{res}}}\hat{\mathbb{E}}^{(4\times4)} - \hat{\mathbb{I}}^{(4\times4)}, \tag{12}$$

$$\hat{S}_{\Gamma_x}(k;\ell_{x,res}) = \frac{2\cos(k\ell_{x,res})}{\cos(k\ell_{x,res}) + \mathrm{e}^{-\mathrm{i}k\ell_{x,res}}}\hat{\mathbb{E}}^{(2\times2)} - \hat{\mathbb{I}}^{(2\times2)}, \tag{13}$$

$$\hat{S}_{\Gamma_y}(k;\ell_{y,res}) = \frac{2\cos(k\ell_{y,res})}{\cos(k\ell_{y,res}) + \mathrm{e}^{-\mathrm{i}k\ell_{y,res}}}\hat{\mathbb{E}}^{(2\times2)} - \hat{\mathbb{I}}^{(2\times2)}. \tag{14}$$

Here, $\hat{\mathbb{E}}^{(n\times n)}$ represents a square matrix of all ones of dimension n. Having defined the scattering matrices associated with each resonant element, one can now construct the full metamaterial.

2.3. Eigenfunction solutions of the periodic graph

From here, the compact portions of the above graphs are treated simply as frequency-dependent point scatterers. Each scatterer is arranged into a square periodic 2D mesh, where the open leads of each resonant element are truncated to form connections of length ℓ between each compact graph. In addition, resonant elements of the type Γ_x and Γ_y, as shown in Fig. 1, can be placed halfway along an edge in the x- and y-direction, respectively (see Fig. 2). This allows for more freedom in constructing interesting wave dispersion curves. The periodic construction means that all wave solutions at the central vertex of any unit cell nm are translationally invariant up to a phase obeying Bloch's theorem [8],

$$\boldsymbol{\Psi}_{nm}(0) = \mathrm{e}^{\mathrm{i}(\kappa_x n + \kappa_m m)\ell}\,\boldsymbol{\Psi}(0). \tag{15}$$

Here, κ_x and κ_y represent the quasi-momentum. The symmetry in each connecting edge allows the horizontal and vertical edge scattering due to Γ_x and Γ_y to be evaluated at $z_r = \ell/2$ and $z_u = \ell/2$, respectively, and we obtain

$$\begin{pmatrix} a_l^{\text{in}} \\ a_r^{\text{in}} \end{pmatrix} = \hat{M}_x(k;\ell_{res})\begin{pmatrix} a_l^{\text{out}} \\ a_r^{\text{out}} \end{pmatrix},$$
$$\begin{pmatrix} a_d^{\text{in}} \\ a_u^{\text{in}} \end{pmatrix} = \hat{M}_y(k;\ell_{res})\begin{pmatrix} a_d^{\text{out}} \\ a_u^{\text{out}} \end{pmatrix}, \tag{16}$$

where

$$\hat{M}_j(k;\ell_{j,res}) := \mathrm{e}^{\mathrm{i}k\ell}\begin{pmatrix} \mathrm{e}^{-\mathrm{i}\kappa_j\ell} & 0 \\ 0 & 1 \end{pmatrix}\hat{S}_{\Gamma_j}(k;\ell_{j,res})\begin{pmatrix} \mathrm{e}^{\mathrm{i}\kappa_j\ell} & 0 \\ 0 & 1 \end{pmatrix} \tag{17}$$

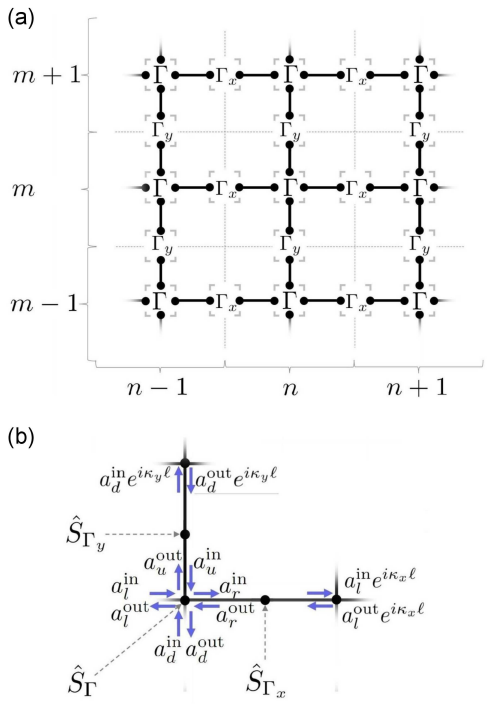

Fig. 2. Panel (a) shows the square periodic arrangement of some arbitrary graph Γ (such as the examples Γ_0, Γ_{phase}, or Γ_{res}) with mesh indices n, m, spaced by edges of length ℓ. Resonators Γ_x and Γ_y may be placed on both the horizontal and vertical edges. Panel (b) shows the local edge wave amplitudes $a_j^{\text{out/in}}$ represented by blue arrows in the neighbourhood of the central vertex.

with $j = x$ or y and $\ell_{j,res}$ is the resonator length of the edge scattering elements Γ_j. By substitution of (16) into (7), one obtains

$$\left[\hat{\mathbb{I}} - \hat{U}(k, \kappa_x, \kappa_y; L)\right] \boldsymbol{a}_{\mathcal{L}}^{\text{in}}(k, \kappa_x, \kappa_y; L) = \mathbf{0}, \quad (18)$$

where $\hat{U}$ represents the quantum map and is explicitly given as

$$\hat{U} := \begin{pmatrix} \hat{M}_x & 0 \\ 0 & \hat{M}_y \end{pmatrix} \hat{S}_{\Gamma}. \quad (19)$$

The spectrum of dispersion curves relating k, κ_x, and κ_y are given by solving the secular equation

$$\det\left[\hat{\mathbb{I}} - \hat{U}(k, \kappa_x; \kappa_y, L)\right] = 0. \quad (20)$$

Note that $\hat{U}$ is implicitly a function of the chosen graph metric L. By varying these metric parameters and by changing the topology of the graph Γ, one has great control over the possible wave properties of the metamaterial. We will briefly discuss the examples shown in Fig. 1. A metamaterial constructed purely of elements Γ_0 (i.e., $\ell_{j,res} = 0$ for $j = x$ and y) has in the low-frequency limit an approximately circular dispersion curve modelling free space propagation. As the frequency increases, the underlying square periodic topology becomes "noticeable", leading to square iso-frequency contours and directional band gaps. The properties of a metamaterial constructed purely of elements Γ_{res} are similar in shape to that of Γ_0, however, the presence of the edge of length ℓ_{res} opens band gaps, thus forcing high-frequency material properties into the low-frequency domain. The same can be said for the elements Γ_x and Γ_y, where the opening of band gaps is then directional. As for graphs constructed from elements Γ_{phase}, waves travelling from down(up) to up(down) accumulate an additional phase $\mathrm{e}^{\mathrm{i}k\ell_y}$. This can be thought of as compressing a lattice of period ℓ by $\ell + \ell_y$ to a lattice of period ℓ by ℓ, while maintaining the edge lengths between cells, see Fig. 3. Such a construction breaks the vertex scattering symmetry and allows for negative refraction without relying on resonant characteristics as shown in [9].

2.4. Gaussian beams from graph eigenfunctions

To construct the allowed eigenfunction solutions, we consider a single frequency k and wave number κ_y, leaving in general a choice of two wave numbers κ_x. Naturally, this choice defines the direction of the energy flow. To delineate between waves travelling in opposite horizontal directions, the following notation is used: Eigenfunction solutions with energy flux J_x pointing in the positive x-direction are given an index $\rightarrow$, and the corresponding eigenvector in (18) is redefined as $\boldsymbol{a}^{\text{out/in}} := \boldsymbol{a}^{\text{out/in}}(k, \kappa_x^{\rightarrow}, \kappa_y)$. Eigenfunction solutions with energy flux J_x pointing in the negative x-direction are given an index $\leftarrow$, and the corresponding eigenvector in (18) is redefined as $\boldsymbol{b}^{\text{out/in}} := \boldsymbol{a}^{\text{out/in}}(k, \kappa_x^{\leftarrow}, \kappa_y)$. Explicitly, we write

$$\boldsymbol{\Psi}_{nm} := \begin{cases} \boldsymbol{\Psi}_{nm}^{\rightarrow}(\hat{Z}; k, \kappa_y) = \mathrm{e}^{\mathrm{i}(\kappa_x^{\rightarrow} n + \kappa_y m)}\left(\mathrm{e}^{\mathrm{i}k\hat{Z}}\boldsymbol{a}^{\text{out}} + \mathrm{e}^{-\mathrm{i}k\hat{Z}}\boldsymbol{a}^{\text{in}}\right), & J_x > 0, \\ \boldsymbol{\Psi}_{nm}^{\leftarrow}(\hat{Z}; k, \kappa_y) = \mathrm{e}^{\mathrm{i}(\kappa_x^{\leftarrow} n + \kappa_y m)}\left(\mathrm{e}^{\mathrm{i}k\hat{Z}}\boldsymbol{b}^{\text{out}} + \mathrm{e}^{-\mathrm{i}k\hat{Z}}\boldsymbol{b}^{\text{in}}\right), & J_x < 0. \end{cases} \quad (21)$$

For fixed k and κ_y, we thus obtain an eigenfunction solution on the mesh as

$$\Upsilon_{nm}(\hat{Z}; k, \kappa_y) = A(k, \kappa_y)\, \boldsymbol{\Psi}_{nm}^{\rightarrow}(\hat{Z}; \kappa_y, k) + B(k, \kappa_y)\, \boldsymbol{\Psi}_{nm}^{\leftarrow}(\hat{Z}; \kappa_y, k), \quad (22)$$

where A and B are wave amplitudes associated with right-hand and left-hand moving waves, respectively. They are both functions of k and κ_y as they will later represent incident and scattered field amplitudes at an interface.

From here, one can construct Gaussian beam solutions $\boldsymbol{\Phi}_{nm}$ by integrating over the Brillouin zone ($\mathbb{BZ}$) of a given metamaterial

$$\boldsymbol{\Phi}_{nm}(\boldsymbol{z};k) = \frac{1}{\sqrt{2\pi}} \int_{\mathbb{BZ}} \mathrm{d}\kappa_y \; \alpha(\kappa_y)\, \Upsilon_{nm}(\hat{Z}, \kappa_y; k), \tag{23}$$

where α is a κ_y-dependent expansion coefficient chosen here to give a Gaussian mode profile, and is defined as

$$\alpha(\kappa_y; \kappa_y', w) = \gamma \exp\left[-\frac{\left(\kappa_y - \kappa_y'\right)^2}{2\, w^2} \right]. \tag{24}$$

Here, κ_y' determines the direction of the beam relative to the x, y coordinate system, w defines the width of the beam, and γ is a normalisation constant.

3. Wave behaviour at interfaces

3.1. Engineering interface boundary conditions

In previous work [9], the boundary conditions between two different metamaterials modelled by periodic quantum graphs were fixed by satisfying an equivalence condition on the joining edges. In this section, we will demonstrate how to influence the reflection and transmission behaviour at such an interface by introducing an additional boundary layer $\mathfrak{B}$, as illustrated in Fig. 4a. For this, we consider two infinite half-spaces, each constructed from a square periodic quantum graph with an identical period, as defined in the previous section.

The left half-space represents metamaterial 1 with unit cell $\Gamma^{(1)}$, while the right half-space represents metamaterial 2 with unit cell $\Gamma^{(2)}$. The two metamaterials are coupled via a periodic boundary along the y-direction constructed from either $\Gamma^{(\mathfrak{B})} = \Gamma_{res}$ and $\Gamma^{(\mathfrak{B})} = \Gamma_{y,res}$ or a simple point scatterer with beyond-nearest-neighbour connections, $\Gamma^{(\mathfrak{B})} = \Gamma^{(1)}$, as discussed in [2], see Fig. 4b and c.

The wave properties of the boundary are defined by a scattering matrix $\hat{S}_{\mathfrak{B}}(k, \kappa_y; L)$, which performs the horizontal (H) mapping,

$$\boldsymbol{a}_H^{\mathrm{out}} = \hat{S}_{\mathfrak{B}}(k, \kappa_y; L)\, \boldsymbol{a}_H^{\mathrm{in}}. \tag{25}$$

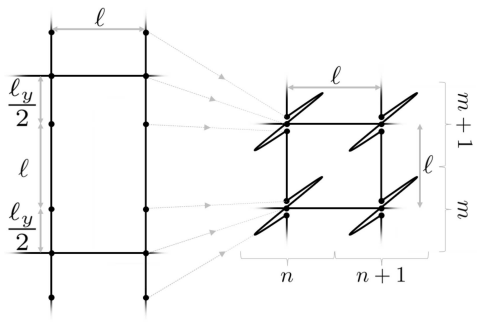

Fig. 3. Illustration of the relationship between the vertex and edge length scale in the case of Γ_{phase} giving rise to non-trivial wave effects.

Here, $\boldsymbol{a}_H^{\mathrm{out/in}} = (\alpha_l^{\mathrm{out/in}}, \alpha_r^{\mathrm{out/in}})^{\mathrm{T}}$ represents the (to be determined) vector wave amplitudes heading out of or into the boundary vertex on the left (l) or right (r). The boundary scattering matrix is constructed from the underlying vertex scattering matrix as defined in (7), along with the vertical periodicity conditions defined in (16). By decomposing (7) into horizontal (H) and vertical (V) dynamics, one can write

$$\left(\begin{array}{c} \boldsymbol{a}_H^{\mathrm{out}} \\ \hline \boldsymbol{a}_V^{\mathrm{out}} \end{array}\right) = \left(\begin{array}{c|c} \hat{S}_{HH} & \hat{S}_{HV} \\ \hline \hat{S}_{VH} & \hat{S}_{VV} \end{array}\right) \left(\begin{array}{c} \boldsymbol{a}_H^{\mathrm{in}} \\ \hline \boldsymbol{a}_V^{\mathrm{in}} \end{array}\right). \tag{26}$$

One obtains

$$\hat{S}_{\mathfrak{B}} = \hat{S}_{HH} + \hat{S}_{HV} \left[\hat{\mathbb{I}} - \hat{M}_y \hat{S}_{VV}\right]^{-1} \hat{M}_y \hat{S}_{VH}. \tag{27}$$

From this definition, we can determine how the boundary scatters the global wave fields of incident amplitude $A^{(1)}$, $B^{(2)}$ to give the global scattered field of amplitude $A^{(2)}$, $B^{(1)}$. To do this, we construct the global boundary scattering matrix $\hat{\Sigma}_{\mathfrak{B}}(k, \kappa_y; \boldsymbol{L})$, which performs the mapping,

$$\begin{pmatrix} B^{(1)} \\ A^{(2)} \end{pmatrix} = \hat{\Sigma}_{\mathfrak{B}} \begin{pmatrix} A^{(1)} \\ B^{(2)} \end{pmatrix}. \tag{28}$$

To do this, one substitutes the x component of the eigenfunction solutions (22) on the left and right side of the interface, i.e., at $z_l = z_r = 0$ at the location of the boundary $n = n_{\mathfrak{B}}$ for any m, that is,

$$\begin{aligned} \alpha_l^{\mathrm{out/in}} &= A^{(1)}\, \mathrm{e}^{\mathrm{i}(\kappa_x^{(1)\rightarrow} n_{\mathfrak{B}} + \kappa_y m)\ell} a_l^{(1)\mathrm{out/in}} \\ &\quad + B^{(1)}\, \mathrm{e}^{\mathrm{i}(\kappa_x^{(1)\leftarrow} n_{\mathfrak{B}} + \kappa_y m)\ell} b_l^{(1)\mathrm{out/in}}, \\ \alpha_r^{\mathrm{out/in}} &= A^{(2)}\, \mathrm{e}^{\mathrm{i}(\kappa_x^{(2)\rightarrow} n_{\mathfrak{B}} + \kappa_y m)\ell} a_r^{(2)\mathrm{out/in}} \\ &\quad + B^{(2)}\, \mathrm{e}^{\mathrm{i}(\kappa_x^{(2)\leftarrow} n_{\mathfrak{B}} + \kappa_y m)\ell} b_r^{(2)\mathrm{out/in}}, \end{aligned} \tag{29}$$

into (25). After some algebra, we get

$$\begin{aligned} \hat{\Sigma}_{\mathfrak{B}} = &\begin{pmatrix} \mathrm{e}^{-\mathrm{i}\kappa^{(1)} n_{\mathfrak{B}} \ell} & 0 \\ 0 & \mathrm{e}^{\mathrm{i}\kappa^{(2)} n_{\mathfrak{B}} \ell} \end{pmatrix} \left[\begin{pmatrix} a_l^{(1)\mathrm{out}} & 0 \\ 0 & b_r^{(2)\mathrm{out}} \end{pmatrix} - \hat{S}_{\mathfrak{B}} \begin{pmatrix} a_l^{(1)\mathrm{in}} & 0 \\ 0 & b_r^{(2)\mathrm{in}} \end{pmatrix} \right]^{-1} \\ &\times \left[\hat{S}_{\mathfrak{B}} \begin{pmatrix} b_l^{(1)\mathrm{in}} & 0 \\ 0 & a_r^{(2)\mathrm{in}} \end{pmatrix} - \begin{pmatrix} b_l^{(1)\mathrm{out}} & 0 \\ 0 & a_r^{(2)\mathrm{out}} \end{pmatrix} \right] \begin{pmatrix} \mathrm{e}^{-\mathrm{i}\kappa^{(1)} n_{\mathfrak{B}} \ell} & 0 \\ 0 & \mathrm{e}^{\mathrm{i}\kappa^{(2)} n_{\mathfrak{B}} \ell} \end{pmatrix}. \end{aligned} \tag{30}$$

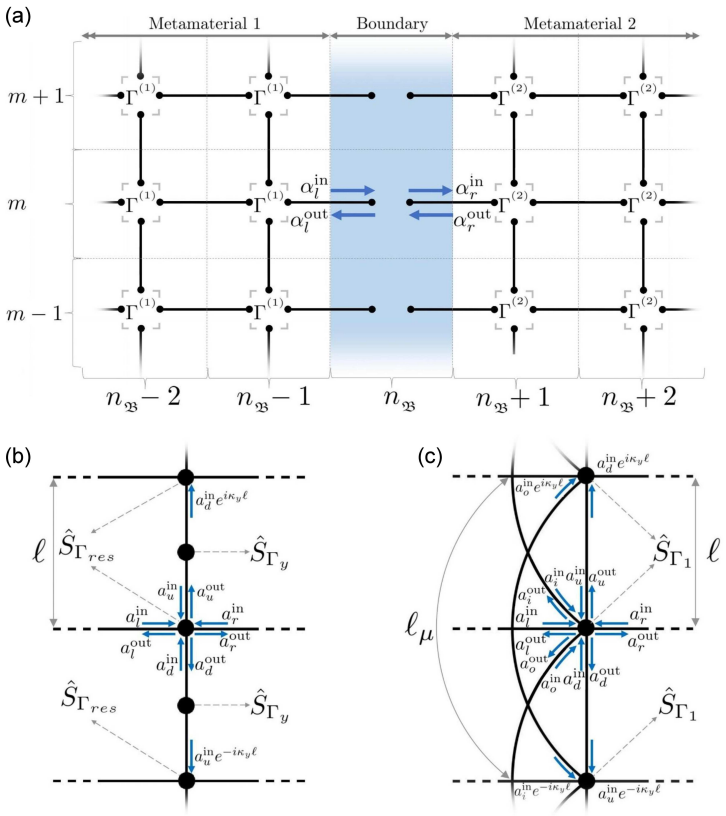

Fig. 4. (a) The boundary region between metamaterials 1 and 2 with amplitudes $\alpha_l^{\text{out/in}}$ and $\alpha_r^{\text{out/in}}$ related by the boundary scattering matrix $\hat{S}_{\mathfrak{B}}$. (b) Boundary constructed of resonators Γ_{res} and Γ_y. (c) Boundary with beyond-nearest-neighbour connections with l_μ, the length of this connection, and μ giving the distance in terms of unit cells; (in the example shown, $\mu = 2$).

3.2. Examples

In the following, we will discuss a few examples leading to interesting reflection/transmission behaviour at interfaces.

3.2.1. Non-reflecting boundaries, beam splitting and steering

In the first example, we will consider how to construct non-reflective interfaces using boundary elements, as shown in Fig. 4b. Here, metamaterial 1 is constructed from elements defined by Γ_0, while metamaterial 2 is constructed from elements defined by Γ_{res} for $l_{res} = 1.1995\ell$. The corresponding dispersion curves of the two materials are shown in Fig. 5a at $k = 1$. Note that the particular value of l_{res} leads to a square-like dispersion pattern of material 2 with singular behaviour for vanishing κ_x or κ_y. The third plot in Fig. 5a shows the chosen expansion coefficient α giving rise to a beam with width $w = 0.0575$ centred at $\kappa_y' = 1$, which yields an incident Gaussian beam angle of $\theta' = \pi/4$. The chosen boundary is constructed exclusively from Γ_{res}, for $l_{res} = 0\ell$, $l_{res} = 0.9667\ell$, and $l_{res} = \pi\ell/2$ in Fig. 5b–d, respectively.

The transmission $|A^{(2)}|^2$ and reflection coefficients $|B^{(1)}|^2$ of the beam $\boldsymbol{\Psi}_{nm}$ are shown on the RHS of Fig. 5 for panels (b), (c), and (d) as a function of the incident angle θ. This demonstrates that we can obtain both complete transmission and total internal reflection by varying the boundary properties in terms of l_{res}. In particular, total internal reflection happens when $l_{res} = \pi/(2k)$. At this length, the vertex is in resonance, and the boundary conditions reduce to Dirichlet $\hat{S}_{res} = -\hat{\mathbb{I}}$, making the boundary completely reflective.

With this knowledge, we set out to construct a layered metamaterial set-up that will allow us to steer an incoming beam at normal incident around an object. We can do this with minimal reflection at the boundaries using the techniques described above. The example shown in Fig. 6 is made up of four different metamaterials connected by interface layers of the type used in the example shown in Fig. 5. Metamaterials 1 and 4 are identical and are made up of resonant elements Γ_{res} with $\ell_{res} = 0.725\ell$. The corresponding dispersion curves at $k = 1$ are shown in Fig. 6a. Metamaterial 2 is constructed from both Γ_0 and Γ_y with $\ell_{y,res} = 0.909175\ell$; note that the material exhibits a corner singularity in its dispersion curve for normal incident giving rise to the beam split-

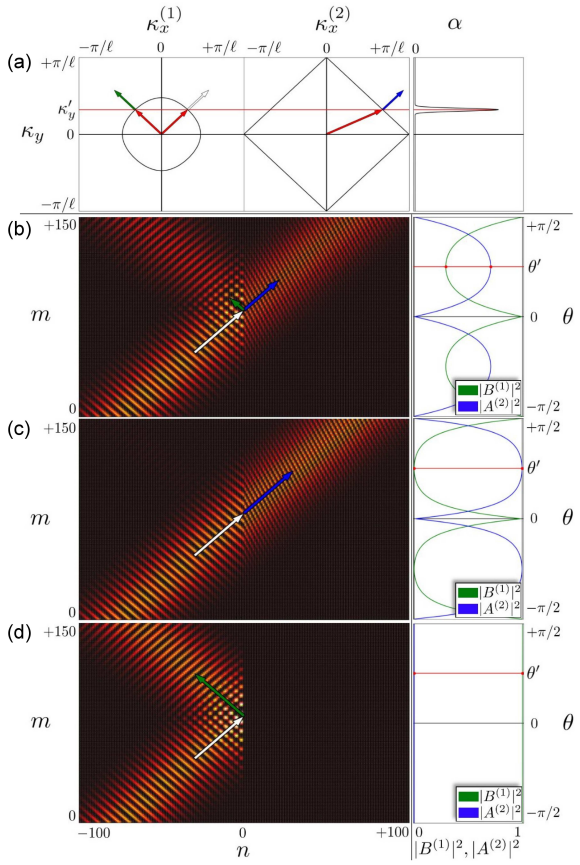

Fig. 5. (a) Isofrequency contours associated with metamaterial 1 and 2 for $k = 1$ together with the Gaussian beam expansion coefficients α. (b)–(d) Reflection behaviour of the beam for different l_{res} chosen at the boundary, see text for details.

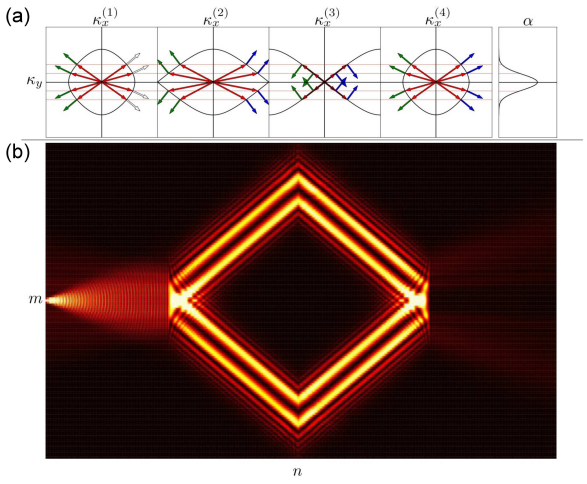

Fig. 6. The plots in (a) show the isofrequency contours associated with metamaterials 1, 2, 3, and 4, while the 5th plot shows the chosen expansion coefficient α for the incident beam. The plot in (b) displays the resulting norm squared wave amplitude of the incoming and scattered beam $|\boldsymbol{\Phi}_{nm}|^2$. The material interfaces are optimized to give minimal reflection.

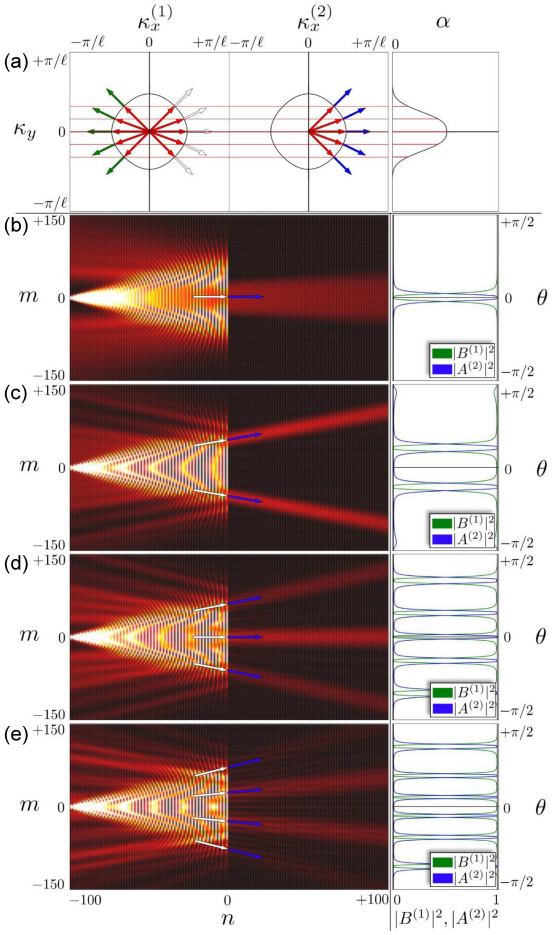

Fig. 7. (a) Dispersion curves of metamaterials 1 and 2 together with the beam shape α for the beam incoming from the LHS. (b)–(e) Wave patterns given by $|\boldsymbol{\Phi}_{nm}|^2$, for different configurations (left) and the reflection/transmission coefficients at the interface as function of the incoming angle θ (right); the parameters are (b) $\mu = 3$, $l_{\mu=3} = 6.32757\ell$; (c) $\mu = 6$, $l_{\mu=6} = 9.3\ell$; (d) $\mu = 10$, $l_{\mu=10} = 12.41818\ell$; (e) $\mu = 12$, $l_{\mu=12} = 15.96\ell$.

ting behaviour observed in Fig. 6b. Metamaterial 3 is constructed from Γ_{phase} and Γ_x for $\ell_y = 4.64\ell$ and $\ell_{x,res} = 2.7955\ell$. The metamaterial is designed in such a way as to reverse the beam splitting behaviour yielding negative reflection (see the relevant dispersion curve). We may regard such a device as a primitive cloak in the sense that one can hide or shield an object from normal incidence.

3.2.2. An angle filtering boundary

In the previous example, only nearest-neighbour coupling has been used in the vertical direction of the boundary such as shown in Fig. 4b, that is, a cell m is coupled to cells $m \pm 1$ only. We will now study the properties of an interface boundary made up of the elements shown in Fig. 4c, i.e., we consider $\Gamma^{(\mathfrak{B})} = \Gamma_1$, and we connect up the vertices by

using beyond-nearest-neighbour interaction. In the example in Fig. 4c, the next-to-nearest-neighbour coupling is used, that is, in addition to the nearest neighbours, cell m is also coupled to cells $m\pm\mu$ with $\mu = 2$, here. We will later also consider $\mu > 2$.

By introducing the additional coupling, the valency of a boundary vertex increases by two. The vertex conditions are then given by the vertex scattering matrix $\hat{S}_{\Gamma_1}$ in (10) with Γ_1 shown in Fig. 1b. To obtain $\hat{S}_{\mathbb{B}}$, we must now redefine $\hat{M}_y$ to include the additional coupling. The structure inherits the same Bloch phase as the unit cell has, and the wave amplitudes as such obey the following conditions

$$\begin{aligned} a_u^{\text{in}} &= \mathrm{e}^{\mathrm{i}k\ell}\mathrm{e}^{-\mathrm{i}\kappa_y\ell}a_d^{\text{out}} \\ a_d^{\text{in}} &= \mathrm{e}^{\mathrm{i}k\ell}\mathrm{e}^{\mathrm{i}\kappa_y\ell}a_u^{\text{out}} \\ a_i^{\text{in}} &= \mathrm{e}^{\mathrm{i}k\ell_\mu}\mathrm{e}^{-\mathrm{i}\kappa_y\mu\ell}a_o^{\text{out}} \\ a_o^{\text{in}} &= \mathrm{e}^{\mathrm{i}k\ell_\mu}\mathrm{e}^{\mathrm{i}\kappa_y\mu\ell}a_i^{\text{out}} \end{aligned} \tag{31}$$

and $\hat{M}_y$ becomes

$$\hat{M}_y = \begin{pmatrix} 0 & \mathrm{e}^{\mathrm{i}(k-\kappa_y)\ell} & 0 & 0 \\ \mathrm{e}^{\mathrm{i}(k+\kappa_y)\ell} & 0 & 0 & 0 \\ 0 & 0 & 0 & \mathrm{e}^{\mathrm{i}(k\ell_\mu-\kappa_y\mu\ell)} \\ 0 & 0 & \mathrm{e}^{\mathrm{i}(k\ell_\mu+\kappa_y\mu\ell)} & 0 \end{pmatrix}. \tag{32}$$

Here, l_μ represents the length of the lead connecting element m to element $m\pm\mu$. Naturally $\ell_\mu \geq \mu\ell$. This is a free parameter that alters the phase accumulation for the wave propagation along the y-direction. In Fig. 7, we show various examples of the wave behaviour at such an interface. In all cases, metamaterials 1 and 2 are identical here and given by simple point scatters Γ_0, as shown in Fig. 1a. We have chosen a relatively broad beam profile of the incoming beam, covering a wide range of κ_y values and giving the beam a cone-like appearance. A range of μ and corresponding ℓ_μ values are tested.

Surprisingly, the interface acts as an invisible aperture or angle filtering device, letting the incoming wave pass only at certain angles of incident. The number of incoming directions able to pass the interface increases with the connectivity index μ, as demonstrated in Fig. 7b–e; see the figure caption for details regarding the chosen parameters μ and ℓ_μ. The filtering behaviour is brought about by a transmission function being zero for most angles θ apart from narrow-band transmission windows, see the RHS of Fig. 7. Note that these transmission windows exist here although there are no resonant elements present at either vertices or edges and seem to be an interference effect of the competing vertical channels. We report this behaviour here without further analysis, which will be provided in a forthcoming publication.

4. Conclusions

We have demonstrated applications of a quantum graph approach to modelling metamaterials coupled through structured interfaces, thus providing a fast and efficient tool for aiding the design process for layered metamaterial devices. The reflection and transmission coefficients of complex interfaces can be explicitly calculated in our approach, and the freedom in choosing the vertex scattering matrices and edge lengths provides a large parameter space for constructing desired material properties. We show in particular that interfaces with minimal reflection or transmission can be designed. Beyond-nearest-neighbour coupling along the interface has been incorporated, which can be used as a single-frequency angular filter, allowing for energy transmission only at specific angles and potentially providing a possibility for a tunable aperture or filter. The examples highlight the potential of quantum graph-based metamaterial and interface design. The tuning of edge lengths and the freedom in assigning the vertex scattering matrices are unique to the graph model presented here and enable an open system description that is cumbersome in other conventional mass-spring models, where either the construction of Green's function or a full time-domain simulation is required.

Acknowledgments

The author(s) would like to thank the Isaac Newton Institute for Mathematical Sciences, Cambridge, for support and hospitality during the program Multiple Wave Scattering supported by EPSRC grant no EP/R014604/1. TML and GT would like to acknowledge funding from the Clean Sky 2 Joint Undertaking under the European Union's Horizon 2020 research and innovation programme under grant agreement number 882842 (Silentprop). GJC gratefully acknowledges financial support from the Royal Commission for the Exhibition of 1851 in the form of a Research Fellowship.

References

[1] R. Kumar, M. Kumar, J. Singh Chohan, S. Kumar, *Mater. Today* **56**, 3016 (2022).

[2] Y. Chen, M. Kadic, M. Wegener, *Nature Commun.* **12**, 3278 (2021).

[3] J.A.I. Martínez, M.F. Groß, Y. Chen, T. Frenzel, V. Laude, M. Kadic, M. Wegener, *Sci. Adv.* **7**, eabm2189 (2021).

[4] D.B. Moore, J.R. Sambles, A.P. Hibbins, T.A. Starkey, G.J. Chaplain, *Phys. Rev. B* **107**, 144110 (2023).

[5] G.J. Chaplain, I.R. Hooper, A.P. Hibbins, T.A. Starkey, *Phys. Rev. Appl.* **19**, 044061, (2023).

[6] Y. Chen, J.L.G. Schneider, M.F. Groß, K. Wang, S. Kalt, P. Scott, M. Kadic, M. Wegener, *Adv. Funct. Mater.* **33**, 2302699 (2023).

[7] A. Kazemi, K.J. Deshmukh, F. Chen, Y. Liu, B. Deng, H. Chien Fu, P. Wang, *Phys. Rev. Lett.* **131**, 176101 (2023).

[8] L. Brillouin, *Wave Propagation and Group Velocity*, Academic Press, New York 1960.

[9] T. Lawrie, G. Tanner, D. Chronopoulos, *Sci. Rep.* **12**, 18006 (2022).

[10] T. Kottos, U. Smilansky, *Ann. Phys.* **274**, 76 (1999).

[11] S. Gnutzmann, U. Smilansky, *Adv. Phys.* **55**, 527 (2006).

[12] G. Berkolaiko, P. Kuchment, *Introduction to Quantum Graphs*, Vol. 186, American Mathematical Soc., 2013.

[13] C. Brewer, S.C. Creagh, G. Tanner, *J. Phys. A Math. Theor.* **51**, 445101 (2018).

[14] J. Kempe, *Contemp. Phys.* **44**, 307 (2003).

[15] G.K. Tanner, in: *Non-Linear Dynamics and Fundamental Interactions: Proceedings of the NATO Advanced Research Workshop on Non-Linear Dynamics and Fundamental Interactions*, Tashkent 2004, Springer, 2006, p. 87.

[16] B. Hein, G. Tanner, *Phys. Rev. Lett.* **103**, 260501 (2009).

[17] T. Lawrie, S. Gnutzmann, G. Tanner, arXiv:2309.11251, 2023.

[18] P. Kuchment, *J. Physics A Math. General* **38**, 4887 (2005).

[19] P. Exner, S. Nakamura, Y. Tadano, *Lett. Math. Phys.* **112**, 83(2022).

[20] M. Touboul, Ph.D. thesis, Aix-Marseille Université, 2021.

Proceedings of the 11th Workshop on Quantum Chaos and Localisation Phenomena (CHAOS 23)

Numerical Simulation of Radiative Transfer of Electromagnetic Angular Momentum

B.A. van Tiggelen* and R. Le Fournis

Univ. Grenoble Alpes, CNRS, LPMMC, 38000 Grenoble, France

Doi: 10.12693/APhysPolA.144.495 *e-mail: Bart.Van-Tiggelen@lpmmc.cnrs.fr

We present numerical simulations of the light emitted by a source and scattered by surrounding electric dipoles with Zeeman splitting. We calculate the leakage of electromagnetic angular momentum to infinity.

topics: radiative transfer, magneto-optics

1. Introduction

Optical sources radiate electromagnetic energy at a rate that depends on the local density of radiative states (LDOS) near the source and at the emitted frequency of the source [1, 2]. This statement is classically true and recalls Fermi's golden rule in quantum mechanics [3]. LDOS is affected by the environment and can be either dielectric, structured, gapped in frequency, or disordered. If the environment is magneto-active, induced by the presence of an externally applied magnetic field $\boldsymbol{B}_0$, the source can also radiate angular momentum (AM) with direction $\boldsymbol{B}_0$ into space.

The first study of this phenomenon [4] used the phenomenological concept of radiative transfer and, in particular, the role of the radiative boundary layer of an optically thick medium to argue that the Poynting vector has two components in the far field. The first is the usual energy flux, purely radial, that decays with distance r from the object as $1/r^2$. The second is magneto-transverse and circulates energy around the object (see Fig. 1). This component decays faster, as $1/r^3$, but has finite angular momentum constant with distance that travels away from the object. Our second study [5] demonstrated that this leakage is not restricted to multiple scattering and also exists when a homogeneous magneto-birefringent environment surrounds the source. In this case: (i) the radiation of AM results in a torque on the source and not on the environment, (ii) it depends sensitively on the nature of the source with huge differences between, e.g., an electric dipole source and a magnetic dipole source; and (iii) geometric "Mie" resonances can enhance the effect much like the Purcell effect does in nano-antennas [6, 7].

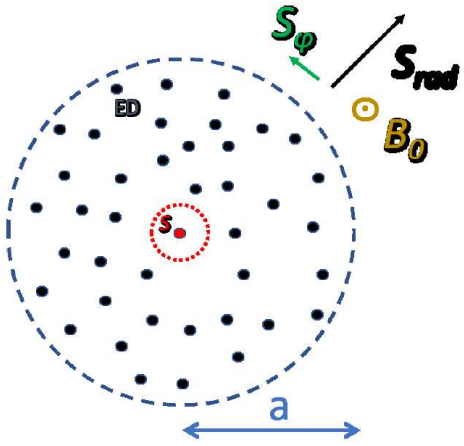

Fig. 1. The geometry considered in this work. A source emits light into a disordered environment containing N electric dipole scatterers. In the presence of a magnetic field $\boldsymbol{B}_0$, a magneto-transverse component $\boldsymbol{S}_\phi$ of the Poynting vector appears outside the medium that carries electromagnetic angular momentum. This angular momentum propagates to infinity, and a torque is exerted on scatterers and source.

Our latest study [8] considered numerically a spherical environment filled with small resonant electric dipole scatterers. When the optical thickness increases at a fixed frequency, the total leakage rate of AM is seen to increase. Upon varying the optical thickness, we investigated separately the role of photonic spin and orbital momentum, the two essential constituents of electromagnetic AM [9], and found both to co-exist. The torque on the source was also seen to increase with dipole density but

hardly with optical thickness. In this work, we study the frequency dependence of the dipole scatterers. Especially for large detuning from their resonance, the scattering from one dipole becomes weak, so to keep reasonable optical thicknesses, we require more dipoles, typically thousands, and this takes more CPU time and memory.

2. Leakage of angular momentum

For a monochromatic electric dipole source with electric dipole moment $\boldsymbol{d}$ at frequency $\omega = kc_0$, positioned at $\boldsymbol{r} = 0$, the radiated electric field at position $\boldsymbol{r}$ is given by

$$\boldsymbol{E}(\boldsymbol{r},\omega) = -4\pi k^2\, \boldsymbol{G}\big(\boldsymbol{r},0,\omega+\mathrm{i}0\big)\cdot\boldsymbol{d}(\omega) \tag{1}$$

with $G_{kk'}(\boldsymbol{r},\boldsymbol{r}',\omega)$, the vector Green's function, associated with the Helmholtz equation for the electric field. This Green's function contains full information about the environment. The slightly positive imaginary part of the frequency $\omega + \mathrm{i}0$ guarantees outward propagation of the light. The power P (radiated energy per second) radiated by the electric dipole is equal to its dissipation rate $\mathrm{Re}(\boldsymbol{J}^*\cdot\boldsymbol{E})/2$ [10]. Since $\boldsymbol{J} = -\mathrm{i}\omega\boldsymbol{d}$, we find, after averaging over the orientation of the dipole source, that

$$P = -\frac{2\pi}{3}k^3c_0\big|\boldsymbol{d}\big|^2\,\mathrm{Im}\Big[\mathrm{Tr}\,\boldsymbol{G}(0,0)\Big]. \tag{2}$$

We recognize $\rho(k) \sim -\mathrm{Im}[\,\mathrm{Tr}\,\boldsymbol{G}(0,0)]$ as LDOS at the source position. The balance equation for the angular momentum can be written as [5]

$$\frac{\mathrm{d}}{\mathrm{d}t}J_{i,\mathrm{mec}} = M_i = \frac{R^3}{8\pi}\epsilon_{ijk}\,\mathrm{Re}\left[\int_{4\pi}\mathrm{d}\hat{\boldsymbol{r}}\;\hat{r}_l\hat{r}_j\big(E_l^*E_k + B_l^*B_k\big)(R\hat{\boldsymbol{r}})\right], \tag{3}$$

with $\boldsymbol{J}_{\mathrm{mec}}$ being the mechanical AM of the matter and with implicit summation over repeated indices. This formula expresses that the torque $\boldsymbol{M}$ exerted on the matter is radiated away as AM to infinity ($r > R$), thereby assuming a source that has been constant during a time longer than R/c_0. In this picture, the radiative AM inside the environment enclosed by the sphere of radius R is constant in time, and AM leaks to infinity somewhere around $r(t) \sim c_0 t > R$. The cycle-averaged torque acts on both the source and its environment, $\boldsymbol{M} = \boldsymbol{M}_S + \boldsymbol{M}_E$. The latter is

$$\boldsymbol{M}_E = \frac{1}{2}\mathrm{Re}\left[\int \mathrm{d}^3r\;(\boldsymbol{P}^*\times\boldsymbol{E} + P_m^*(\boldsymbol{r}\times\nabla)E_m)\right]. \tag{4}$$

This torque vanishes for a rotationally-invariant environment around the source but not when this symmetry is broken by structural heterogeneity, as will be discussed here. The torque on a source with an electric dipole moment $\boldsymbol{d}(\omega)$ is given by [10]

$$\boldsymbol{M}_S = \frac{1}{2}\mathrm{Re}\big[(\boldsymbol{d}^*\times\boldsymbol{E})\big]. \tag{5}$$

With the electric field given by (1), an expression similar to (2) can be obtained, i.e.,

$$M_{S,i} = -\frac{2\pi}{3}k^2\big|\boldsymbol{d}\big|^2\;\mathrm{Re}\Big[\epsilon_{ijk}G_{kj}(0,0)\Big]. \tag{6}$$

This torque vanishes for an (on average) spherical environment with isotropic optical response [11].

Alternatively, the leak of AM given by the right-hand side of (3) can be split up into parts associated with photonic spin and orbital momentum [9]

$$\boldsymbol{M} = \frac{R^2}{8\pi k}\,\mathrm{Im}\left[\int_{r=R}\mathrm{d}^2\hat{\boldsymbol{r}}\;\;(\boldsymbol{E}^*\times\boldsymbol{E} + E_m^*(\boldsymbol{r}\times\nabla)E_m)\right]. \tag{7}$$

In particular, the existence of orbital AM expressed by the second term is interesting since polarized radiation by a source subjected to a magnetic field may be more intuitive to accept in view of the Faraday effect.

3. Environment of N dipoles with Zeeman shift

The Helmholtz Green's function for light scattering from N electric dipoles can be found in the literature [12–14]. Because of the point-like nature of the dipoles, it reduces to a $3N\times3N$ complex-symmetric non-hermitian matrix. The magnetic response of the dipoles — due to the Zeeman splitting of their internal resonance — can be extracted in linear order so that the AM linear in the external field can be calculated numerically, given the N positions of the dipoles. The polarizability of a single dipole is given by

$$\boldsymbol{\alpha}(\omega,\boldsymbol{B}_0) = \alpha(0)\frac{\omega_0^2}{\omega_0^2 - (\omega+\omega_c\,\mathrm{i}\boldsymbol{\epsilon}\cdot\hat{\boldsymbol{B}}_0)^2 - \mathrm{i}\gamma\omega} \tag{8}$$

in terms of the radiative damping rate γ, the resonant frequency ω_0 and the cyclotron frequency $\omega_c = eB_0/(2mc_0)$. The second rank operator $\mathrm{i}\boldsymbol{\epsilon}\cdot\hat{\boldsymbol{B}}_0$ has three eigenvalues $0, \pm1$ corresponding to 3 Zeeman levels that make the environment linearly magneto-birefringent. The external magnetic field $\boldsymbol{B}_0$ is assumed homogeneous across the environment, but this can easily be altered in future work, e.g., to describe an environment surrounding a magnetic dipole. The detuning parameter is defined as $\delta \equiv (\omega-\omega_0)/\gamma$. It is also useful to introduce the dimensionless material parameter $\mu = (12\pi/(\alpha(0)k^3))\times\omega_c/\omega_0$ that quantifies the magnetic birefringence induced by one dipole and typically small (for the $1S$–$2P$ transition in atomic hydrogen one can estimate $\mu \sim 7\cdot10^{-5}$ Gauss^{-1}). The mean free path ℓ is another important length scale and follows from $1/\ell = nk\,\mathrm{Im}[\alpha(\omega)]$ if we neglect recurrent scattering, with $n = 3N/(4\pi a^3)$ the density of dipoles. Without a magnetic field, the polarizability can be written as $\alpha = -(3\pi/k^3)/(\delta + \mathrm{i}/2)$.

The leak of AM is calculated by performing the surface integral in (3) numerically for different realizations in which dipole positions are averaged over a sphere with a given radius a at homogeneous average density throughout the sphere. For more details we refer to [8]. It was explicitly checked that the surface integral did not depend on the choice of $R > a$ as required by the conservation of AM. Once verified, it is convenient to evaluate (3) in the far field $R \gg a$ where the fields simplify. Our code was also tested on flux conservation and obeys the optical theorem.

4. Numerical results

In this paper, we focus on numerical results obtained for different detunings δ and relatively large optical depths $\tau \equiv a/\ell$ in the hope of seeing major trends that can be extrapolated to even larger detunings. This regime becomes rapidly challenging since $\tau \sim \frac{9}{4}N/(ka \times \delta)^2$, so for $\delta \gg 1$ and $\tau \gg 1$ we need a large N. Typically, for $\delta = 2$, the best we have done so far, and $\tau = 5$, we already need $N = 2000$ in a sphere of 13 inverse wave numbers in radius ($ka = 13$). These numbers imply a value for the number of dipoles per optical volume $\eta \equiv 4\pi n/k^3 = 3N/(ka)^3 \sim 2.5$, i.e., the dipoles are largely located in each other's near field. Nevertheless, for a detuning $\delta = 2$, dipoles still scatter more or less independently because $k\ell \sim 2\delta^2/\eta = 3 > 1$ [15], but this is no longer true for $\eta = 6$. This implies that completely unknown effects, such as weak localization, may affect the radiative transfer of AM.

After an ideal average over all N dipole positions, the magnetic field is the only orientation left in the problem, and we expect that $\boldsymbol{M} = \kappa \hat{\boldsymbol{B}}_0$ with κ a real-valued scalar to be calculated that can have both signs. Following earlier works [4, 5, 8], we normalize the leakage of AM by the radiated amount of energy and introduce the dimensionless AM $\kappa\omega/P$, with P being the radiated amount of energy per second. This number is linear in the material parameter μ introduced earlier and can directly be related to the Hall angle of the Poynting vector in the far field of the sphere. Alternatively, the number quantifies the amount of leaked angular momentum expressed in $\hbar$, normalized per emitted photon.

In Figs. 2 and 3, we show the normalized AM leakage for an optically thin sphere as a function of detuning. The bars in all figures denote the typical support of the full probability distribution function (PDF) when calculating the torque for 1000 different realizations of the dipole positions. Except for the spin leakage rate, they are large, and all AM related to source and orbital momentum are genuine mesoscopic parameters. The optical depth $\tau = 1.9$ and average density $\eta = 0.3$ are kept constant, which means that both the number N of dipoles and the radius a of the sphere change as δ is varied. It is seen that the dimensionless AM depends

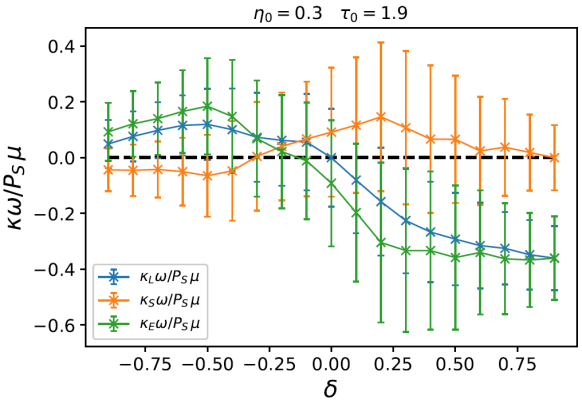

Fig. 2. Total normalized leakage rate of angular momentum (blue) as a function of detuning $\delta = (\omega - \omega_0)/\gamma$ from the dipole resonance, separated into torque on the source(orange) and torque on the environment (green). The optical depth is $\tau = 1.9$, and the dimensionless dipole density is $\eta = 0.3$.

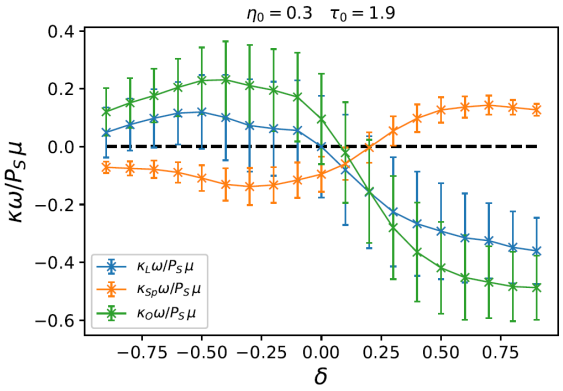

Fig. 3. As in previous figure with same fixed parameters $\tau = 1.9$ and $\eta = 0.3$, but this time, the total leakage has been split up into leakage of orbital angular momentum (green) and leakage of spin (orange).

significantly on detuning and changes sign near the resonance at $\delta = 0$. In this weakly scattering regime, single scattering is still dominant. For a thin layer in the far field of the source, we can derive a profile $\kappa\omega/P \sim \eta\,\mathrm{Im}[\alpha^2] \sim -\eta\delta/(\delta^2 + 1/4)^2$ independent of distance. This corresponds more or less to the observed profile of total AM in Figs. 2 and 3 that are nevertheless affected by higher-order scattering events. Both figures also show how total AM leakage splits up into either spin + orbital AM (Fig. 2) or torque on source + torque on the environment (Fig. 3). All are of the same order of magnitude but are not always of same sign. In particular, for this set of parameters, both decompositions have opposite signs.

The picture changes significantly in the multiple scattering regime. Figures 4 and 5 show the same normalized leakage of AM for optical depth $\tau = 4.6$

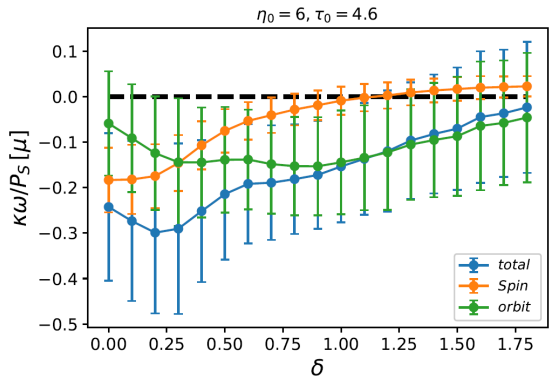

Fig. 4. Total leakage of optical angular momentum (blue) as a function of detuning. The orange and green curves represent spin and orbital momentum. The optical depth and average density are kept constant ($\tau = 4.6$ and $\eta = 6$). The calculations have been done only for $\delta > 0$, i.e., blue-shifted from the resonance.

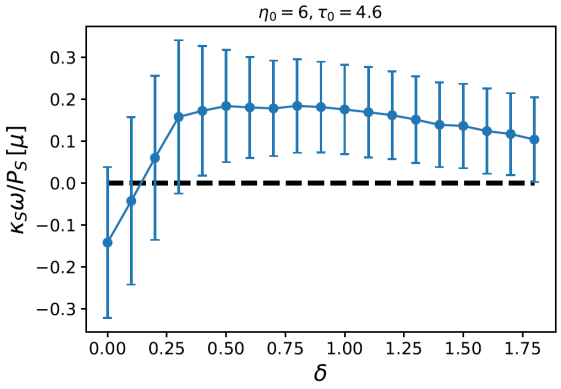

Fig. 5. As in Fig. 4, for clarity only the torque on the source has been shown. Bars denote the support of the full probability distribution (PDF) over 1000 realizations.

and dimensionless density as large as $\eta = 6$. Going to smaller values of η would require too large a value for N. The total leakage is now negative for all (positive) detunings, and spin leakage and orbital leakage have the same sign. Except for near resonance, it is dominated by leaks in orbital AM. In Fig. 5, we see that the torque on the source is mainly positive, but changes sign with detuning near resonance. This implies again that for most detunings, source and environment are subject to opposite torques. A normalized torque on the source around 0.1–0.2 is not much different than that found for $\eta = 0.3$ [8]. For low densities, this torque increased with η but seems to saturate for $\eta > 0.3$. The numbers for total leakage rate (-0.2 ± 0.1) are almost one order of magnitude less than what we found for $\eta = 0.03$ and $\tau \approx 2$ in [8], and one may speculate about the possibility of some process related to "weak localization" that reduces the transfer of angular momentum.

To get an order of magnitude for this effect, we consider a homogenous gas with atoms of mass $Z\,m_H$ in a sphere of size a. For an ideal gas at room temperature, the density is roughly $n_0 = 40\ \mathrm{mol/m^3}$. If we assume that all leaked angular momentum after a time interval Δt is transferred homogeneously to the mechanical momentum of the sphere, we can estimate that its angular velocity is

$$\Omega\left[\frac{\mathrm{rad}}{\mathrm{s}}\right] = 5.7\frac{\kappa\omega}{P\mu}\,\frac{\mu}{Z}\,\frac{\left(\frac{P}{10\,\mathrm{W}}\right)\left(\frac{\lambda}{500\,\mathrm{nm}}\right)\left(\frac{\Delta t}{\mathrm{days}}\right)}{\left(\frac{a}{1\,\mathrm{cm}}\right)^5\left(\frac{n}{n_0}\right)}. \tag{9}$$

For $\kappa\omega/P\mu = 0.3$, $\mu/Z \sim 10^{-5}$, the angular rotation is typically of the order of 1 mrad/s after 100 days.

5. Conclusions

In this work, we have reported an exact numerical study of the radiation of electromagnetic angular momentum by a light source imbedded in a disordered and magneto-active environment described by resonant electric dipoles with Zeeman splitting that scatter light elastically. The angular momentum is directed along the magnetic field, and its transfer is directed radially outward from the source. It is, in general, composed of both spin transport and transport of orbital angular momentum. The first implies polarization of radiated light, the second is related to an energy flux circulating around the object and the magnetic field. Leakage of angular momentum has been quantified by a dimensionless parameter that is essentially the ratio of angular momentum leakage rate (with physical unit Joule) and the energy of the source emitted during one optical cycle. The number can be seen to be equal to the angular momentum, expressed in $\hbar$, transferred per emitted photon to the source and environment. It is proportional to the product of a pure material parameter μ associated with the magneto-scattering of the dipoles and the numbers that can be found in the figures that result from scattering. By conservation of angular momentum, this transfer gives rise to torques on both the emitting source and the scattering environment. All parameters are seen to be of the same order, can have mutually opposite signs, and depend on the detuning from the resonance.

The regime of Thompson scattering is interesting for astrophysical applications and is a major scattering mechanism in our Sun. It corresponds to large detunings, where the phase shift between the incident and scattered field becomes negligible. The out-of-phase response seems essential for the leakage to exist, even for large optical depths. The amount of multiple scattering, quantified by optical depth, certainly affects the radiative transfer of angular momentum, but it is difficult at this point to deduce general trends. Our simulations are clearly in need of a radiative transport theory for angular

momentum in magnetic fields, which, to our knowledge, does not exist. From our simulations, we suspect that different parts of the environment undergo different torques. We also expect that as the optical thickness of the environment increases, the precise nature of the source becomes of less importance, quite opposite to what was found for a homogeneous environment.

Indeed, this picture may possibly apply to stellar atmospheres, globally exposed to the magnetic dipole fields of their nuclei. Although all ingredients are present for leakage of angular momentum to exist, lots of extra complications, such as broadband radiation, Doppler broadening, etc., make quantitative predictions difficult.

Acknowledgments

This work was funded by the Agence Nationale de la Recherche (Grant No. ANR-20-CE30-0003 LOLITOP).

References

[1] D. Kleppner, *Phys. Rev. Lett.* **47**, 233 (1981).

[2] E. Yablonovitch, *Phys. Rev. Lett.* **58**, 2059 (1987).

[3] R. El-Dardiry, S. Faenz, A. Lagendijk, *Phys. Rev. A* **83**, 031801 (2011).

[4] B.A. van Tiggelen, G.L.J.A. Rikken, *Phys. Rev. Lett.* **125**, 133901 (2020).

[5] B.A. van Tiggelen, *Opt. Lett.* **48**, 41 (2023).

[6] E.M. Purcell, *Phys. Rev.* **69**, 681 (1946).

[7] D.G. Baranov, R.S. Savelev, S.V.Li, A.E. Krasnok, A. Alu, *Laser Photon. Rev.* **11**, 1600268 (2017).

[8] R. Le Fournis, B.A. van Tiggelen, *Phys. Rev. A* **108**, 053713 (2023).

[9] C. Cohen-Tannoudji, J. Dupont-Roc, G. Grynberg, *Photons and Atoms*, Wiley, 1989.

[10] J.D. Jackson, *Classical Electrodynamics*, Wiley, Hoboken (NJ) 1999.

[11] L.D. Landau, E.M. Lifshitz, *The Classical Theory of Fields*, Pergamon, 1975, p. 193.

[12] M. Rusek, A. Orlowski, J. Mostowski, *Phys. Rev. E* **56**, 4892 (1997).

[13] F.A. Pinheiro, M. Rusek, A. Orlowski, B.A. van Tiggelen, *Phys. Rev. E* **69**, 026605 (2004).

[14] O. Leseur, R. Pierrat, J.J. Saenz, R. Carminati, *Phys. Rev. A* **90**, 053827 (2014).

[15] A. Lagendijk, B.A. van Tiggelen, *Phys. Rep.* **270**, 143 (1996).

Proceedings of the 11th Workshop on Quantum Chaos and Localisation Phenomena (CHAOS 23)

Multifractality for Intermediate Quantum Systems

H. Ueberschär*

Sorbonne Université, Université Paris Cité, CNRS, IMJ-PRG, F-75006 Paris, France

Doi: 10.12693/APhysPolA.144.500 *e-mail: henrik.ueberschar@imj-prg.fr

While quantum multifractality has been widely studied in the physics literature and is by now well understood from the point of view of physics, there is little work on this subject in the mathematical literature. I will report on the proof of multifractal scaling laws for arithmetic Šeba billiards. I will explain the mathematical approach to defining the Rényi entropy associated with a sequence of eigenfunctions and sketch how arithmetic methods permit us to obtain a precise asymptotic in the semiclassical regime and how this allows us to compute the fractal exponents explicitly. Moreover, I will discuss how the symmetry relation for the fractal exponent is related to the functional equation of certain zeta functions.

topics: quantum multifractality, intermediate systems, Seba billiard

1. Introduction

Many dynamical systems are in a state of transition between two regimes. In models of the brain, such as neural networks, the firing patterns of neurons may undergo a transition from isolated firing to avalanches of firing neurons. In the quantum physics of disordered electronic systems, the system may be in an insulating or a conducting phase. The former phase corresponds to electronic states, which are localized (no transport), whereas the latter phase corresponds to extended states (diffusive dynamics). The study of phase transitions, and in particular the critical states at the transition between these different regimes, is central to understanding important phenomena such as the functioning of our brain or the properties of semi-conducting materials.

One of the key features of systems in a critical state is that they often display a self-similarity in a certain scaling regime, which is so complex that it cannot be captured by a single fractal exponent but only by a continuous spectrum of fractal exponents. This phenomenon is known as multifractality.

Multifractality in quantum systems has been studied in the physics literature since the 1980s and has become an extremely active field in theoretical and experimental physics [1–8]. However, the abundance of results in the physics literature is in stark contrast with a glaring absence of rigorous mathematical results. One of the key difficulties in obtaining a mathematical proof is to formulate the problem in a concise mathematical way and then develop the mathematical methods which permit its resolution.

In joint work with Keating, we recently proved the existence of multifractal eigenfunctions for arithmetic Šeba billiards [9] as well as quantum star graphs [10]. The key idea which permitted this advance was an approach to associate a quantity, known as Rényi's entropy — in some sense, a generalization of Shannon's entropy — with each eigenfunction. We were able to obtain asymptotic estimates of the Rényi entropy along a typical sequence of eigenfunctions. This permitted the derivation of explicit formulae for the fractal exponents and led to the derivation of a multifractal scaling law for this system.

Multifractal self-similarity typically emerges at the transition between two physical regimes. Examples of such intermediate quantum systems are disordered systems at the Anderson or quantum Hall transitions from a localized to a delocalized phase [1, 2]. In the field of quantum chaos, pseudo-integrable systems [11] are intermediate between integrability and chaos in the sense that their dynamics in phase space is not constrained to tori but rather to handled spheres (e.g., rational polygonal billiards). One often includes in this class toy models of pseudointegrable dynamics such as parabolic automorphisms of the torus [12], quantum star graphs [13–16], and Šeba billiards (rectangular billiards with a Dirac delta potential) [17].

The morphology of eigenfunctions with multifractal self-similar structures is far more complex than being purely localized or delocalized. Numerical and experimental studies of a large class of quantum systems have resulted in numerous conjectures in the physics literature [4, 6–8], such as predictions of a symmetry relation for the fractal exponents D_q around the critical value $q = 1/4$.

2. The gap between localization and delocalization

Much of the mathematical literature on quantum chaos over the past 40 years has focused on the classification of limit measures which arise in the high-frequency limit from eigenfunctions of quantized chaotic systems. One of the key results of the field is the quantum ergodicity theorem, which states that on a Riemannian manifold without boundary, whose geodesic flow is ergodic with respect to the Liouville measure, a typical sequence of eigenfunctions gives rise to Liouville measure as the only semiclassical defect measure along this sequence.

Quantum ergodicity (QE) was first proved in the 1980s by Zelditch and Colin de Verdière [18, 19], who completed the earlier work of Snirelman [20]. QE was later generalized to manifolds with boundary by Gérard–Leichtnam [21] and Zelditch–Zworski [22]. The quantum unique ergodicity (QUE) conjecture put forward by Rudnick and Sarnak in 1994 [23] asserts that the only such measure should be the Liouville measure. Lindenstrauss [24] proved this conjecture in 2006 for arithmetic hyperbolic surfaces and was awarded the Fields Medal for his work. Moreover, Anantharaman [25] ruled out localization on points or geodesic segments for Anosov manifolds. De Bièvre–Faure–Nonnenmacher [26] demonstrated the existence of partially localized limit measures for the eigenstates of quantized hyperbolic automorphisms of tori with minimal periods.

While rigorous mathematical work has largely focused on the proof of localization and delocalization results for the probability densities which arise from quantum eigenfunctions (Q(U)E, scarring, Anderson localization), the key feature of intermediate quantum systems is the multifractal self-similarity of their eigenfunctions. This feature to this day remains poorly understood from a mathematical point of view.

3. Multifractality for quantum billiards

Consider the Dirichlet problem for the positive Laplacian $-\Delta = -\partial_x^2 - \partial_y^2$ on a compact domain $D \subset \mathbb{R}^2$ with a piece-wise smooth boundary. We have discrete spectrum accumulating at infinity associated with eigenfunctions ψ_j

$$(\Delta + \lambda_j)\psi_j = 0, \qquad \psi_j|_{\partial D} = 0, \tag{1}$$

where $0 = \lambda_0 < \lambda_1 \leq \cdots \leq \lambda_j \leq \cdots \to +\infty$.

Our goal is to prove a multifractal scaling law for a subsequence of eigenfunctions $\{\lambda_{j_k}\}_{k=0}^{\infty}$, as $\lambda_{j_k} \to +\infty$. The general idea is to embed the domain in a rectangle and expand with respect to an eigenbasis of complex exponentials. The key point is that the scaling law should be independent of rotations and scaling of the rectangle in which the domain is embedded. The scaling parameter will then arise from the number of $O(1)$ contributions in this expansion, as the eigenvalue tends to infinity.

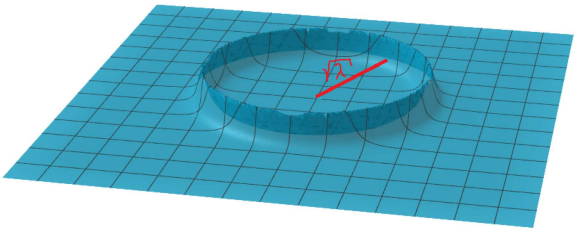

Fig. 1. The measure μ_λ is concentrated on lattice points, which lie inside a thin annulus of central radius $\sqrt{\lambda}$. The width of this annulus grows with λ on a logarithmic scale. The number of lattice points inside the annulus is subject to subtle fluctuations.

We will illustrate this in detail using the case of toral Schrödinger operators. Let $\mathbb{T}^d = 2\pi\mathbb{R}^d/\mathbb{Z}^d$ and $V \in C^0(\mathbb{T}^d)$. We consider L^2-normalized solutions of the stationary Schrödinger equation on $\mathbb{T}^d$,

$$(-\Delta + V)\psi_\lambda = \lambda\psi_\lambda, \qquad ||\psi_\lambda||_{L^2(\mathbb{T}^d)} = 1. \tag{2}$$

We can expand the eigenfunctions into Fourier series

$$\psi_\lambda(x) = \frac{1}{2\pi} \sum_{\xi \in \mathbb{Z}^d} \hat{\psi}_\lambda(\xi)\, \mathrm{e}^{\mathrm{i}\xi x}. \tag{3}$$

By Parseval's identity, we obtain a discrete probability measure on $\mathbb{Z}^d$, namely $\mu_\lambda(\xi) := |\hat{\psi}_\lambda(\xi)|^2$.

For $q > 1$, we define the moment sum

$$M_q(\mu_\lambda) = \sum_{\xi \in \mathbb{Z}^d} \mu_\lambda(\xi)^q. \tag{4}$$

A fractal scaling law, in the semiclassical limit $\lambda \to \infty$, is a power law

$$M_q(\mu_\lambda) \sim N_\lambda^{(1-q)D_q}, \tag{5}$$

where N_λ denotes the number of $O(1)$-contributions in (4), as $\lambda \to \infty$, and D_q denotes the fractal exponent.

We note that, in the case of the torus, the mass of the probability measure μ_λ is concentrated on lattice points which lie inside a thin annulus of central radius $\sqrt{\lambda}$ and whose width depends on the spectral parameter λ (see Fig. 1). In the semiclassical limit, as $\lambda \to \infty$, the number of $O(1)$-contributions will grow slowly (in fact on a logarithmic scale) with λ. However, this number fluctuates a lot, as the number of lattice points in thin annuli is subject to strong fluctuations (this is due to the scale of the width being of much lower order than the error term in the Gauss circle law). In order to compute N_λ, as a function of λ, one must perform a spectral average. This is the first challenge, from a mathematical point of view, to be able to prove a fractal scaling law. As we will see below, for particularly simple choices of potential, where the measure μ_λ takes a simple and explicit form, it is possible to perform this calculation. For generic potentials, it is expected to be a much more challenging task.

In order to compute the fractal exponent associated with a sequence of eigenfunctions, we introduce the Rényi entropy of the measure μ_λ, i.e.,

$$H_q(\mu_\lambda) = \frac{1}{1-q}\log\big(M_q(\mu_\lambda)\big), \quad q>1. \tag{6}$$

The Rényi entropy may be thought of as a generalization of the Shannon entropy, which is familiar from information theory, in the sense that the latter is recovered in the limit as $q \to 1$

$$\lim_{q\to 1} H_q(\mu_\lambda) = -\left[\frac{\mathrm{d}}{\mathrm{d}q}\log\big(M_q(\mu_\lambda)\big)\right]_{q=1} = -\sum_{\xi\in\mathbb{Z}^d}\mu_\lambda(\xi)\log\big(\mu_\lambda(\xi)\big). \tag{7}$$

Provided one can obtain an asymptotic for the Rényi entropy in the limit, $\lambda\to\infty$, possibly by restricting oneself to a subsequence of eigenvalues, and tackle the problem of determining the scaling parameter (by averaging out the fluctuations mentioned above), then one might hope to be able to compute the fractal exponent D_q for $q>1$.

For a generic choice of the potential V, this problem can be very hard. To give an idea of the challenges involved: if one picks a potential model of a disordered system in a scaling regime that corresponds to the thermodynamical limit (e.g., taking a large torus and scaling back to the standard torus), the occurrence of multifractal scaling appears to be related to the onset of a phase transition between localized and delocalized regimes (in $d\geq 3$).

For a simple choice of potential, however, which allows for explicit expressions of the eigenfunctions and, thus, the measure μ_λ, it is possible to overcome these challenges.

4. Multifractality for an arithmetic Šeba billiard

In a 1990 paper [17], Petr Šeba introduced rectangular billiards with a Dirac delta potential placed in the interior as a toy model for more complicated pseudo-integrable billiards, whose dynamics is in some sense intermediate between integrable and chaotic dynamics. In this section, we will consider a slightly modified version of this billiard, namely a square torus with a delta potential. We will refer to this as an arithmetic Šeba billiard because the Laplace spectrum is of an arithmetic nature. It is given, up to a factor, by integers representable as a sum of two squares:

$$\sigma(-\Delta_{\mathbb{T}^2}) = \big\{n = x^2+y^2 \mid (x,y)\in\mathbb{Z}^2\big\}. \tag{8}$$

We note that the Laplace eigenvalues have multiplicities, which are given by the arithmetic function

$$r_2(n) = \#\big\{(x,y)\in\mathbb{Z}^2 \mid n = x^2+y^2\big\}, \tag{9}$$

which counts the number of lattice points on the circle of radius $\sqrt{n}$.

Employing self-adjoint extension theory, one can show that the spectrum of the Šeba billiard consists of two types of eigenvalues. There are old Laplace eigenvalues, with multiplicity reduced by 1, which correspond to co-dimension 1 subspaces of eigenfunctions, which vanish at the position of the potential. There are also new eigenvalues, with multiplicity 1, corresponding to new eigenfunctions which feel the potential. These new eigenvalues interlace with the Laplace eigenvalues.

Moreover, self-adjoint extension theory yields explicit formulae for these new eigenfunctions, which in turn give rise to an explicit expression for the Fourier coefficients and, hence, the measure μ_λ

$$\mu_\lambda(\xi) = \frac{\big(|\xi|^2-\lambda\big)^{-2}}{\sum_{\xi'\in\mathbb{Z}^2}\big(|\xi'|^2-\lambda\big)^{-2}}. \tag{10}$$

Moreover, we note that $\lambda\notin\sigma(-\Delta)$, because of the interlacing property of the new eigenvalues.

The moment sums associated with the measure μ_λ, for a new eigenvalue λ, are of the form

$$M_q(\mu_\lambda) = \frac{\zeta_\lambda(2q)}{\zeta_\lambda(2)^q}, \tag{11}$$

where we introduce the shifted zeta function

$$\zeta_\lambda(s) = \sum_{n\geq 0}\frac{r_2(n)}{|n-\lambda|^s}, \qquad \Re(s)>1. \tag{12}$$

4.1. Weak coupling: a monofractal regime

It is instructive to look at the physically trivial case of weak coupling (fixed self-adjoint extension). In this regime, λ is typically close to a neighbouring Laplace eigenvalue m (see [27]). Let us denote by Δ_j the distance between a new eigenvalue and the nearest Laplace eigenvalue.

For a given $x\gg 1$, we define the mean distance up to threshold x as

$$\langle\Delta_j\rangle_x = \frac{1}{\#\{\lambda_k\leq x\}}\sum_{\lambda_k\leq x}\Delta_k. \tag{13}$$

In the case of the square torus, we have $\langle\Delta\rangle_x = O((\log(x))^{-1/2})$ (which is a special case of a more general estimate derived in [27]), where we note that in this case, the average spacing of the Laplace eigenvalues is of order $\sqrt{\log(x)}$ due to the multiplicities in the Laplace spectrum.

Thus, only one term (or one circle in the lattice with radius $\sqrt{m}$) contributes. The sum scales as follows along the subsequence of typical eigenvalues

$$M_q(\mu_\lambda) = \frac{\zeta_\lambda(2q)}{\zeta_\lambda(2)^q} \sim \frac{r_2(m)\,|m-\lambda|^{-2q}}{\big(r_2(m)\,|m-\lambda|^{-2}\big)^q} = r_2(m)^{1-q}. \tag{14}$$

The number of terms that contribute is simply the number of lattice points on the circle $|\xi|^2=m$.

The Rényi entropy has asymptotics

$$H_q(\mu_\lambda) \sim \frac{1}{1-q}\log\big(r_2(m)^{1-q}\big) = \log\big(r_2(m)\big). \tag{15}$$

It can be shown that for a full-density subsequence of Laplace eigenvalues, we have for any m ($m \to +\infty$) in this subsequence

$$r_2(m) = \big[\log(n)\big]^{\frac{1}{2}\log(2)+o(1)}. \tag{16}$$

Hence,

$$N_\lambda = \big[\log(m)\big]^{\log(2)/2}, \tag{17}$$

which is known as the normal order of r_2.

We note that the fluctuations of the arithmetic function $r_2(n)$ are very subtle. It is a classical theorem of Landau from 1907 that the number of integers less or equal than x grows like $cx/\sqrt{\log(x)}$, which implies that on average the multiplicities are of order $\sqrt{\log(x)}$. The smaller exponent $\frac{1}{2}\log(2)$ arises along a typical (as in full density) subsequence, because there is a very sparse subsequence, where $r_2(n)$ grows much faster (of order $n^{o(1)}$ for some slowly decaying exponent function). Moreover, there are also sparse subsequences where r_2 remains bounded.

From the Rényi entropy, one can now readily obtain the fractal exponent

$$D_q = \lim_{\lambda\to\infty} \frac{H_q(\mu_\lambda)}{\log\big(N_\lambda\big)} = 1. \tag{18}$$

In particular, we note that the fractal exponent does not vary with q, because, due to the weakness of coupling strength, only the nearest circle contributes.

4.2. Strong coupling: a multifractal regime

The physically interesting regime requires a renormalization of the extension parameter in the semiclassical limit. This allows us to consider stronger coupling strength. We can measure the strength of the perturbation by computing the mean distance between old and new eigenvalues. For a suitable renormalization, one obtains

$$\langle \Delta_j \rangle = \big[\log(x)\big]^{\alpha+o(1)}, \quad \alpha \in \big(-\tfrac{1}{2}, \tfrac{1}{2}\big], \tag{19}$$

where the exponent α is a measure of the strength of the perturbation.

Because in such regimes the new eigenvalues lie farther away from the neighbouring Laplace eigenvalues (on the scale of the mean spacing of the eigenvalues), many more circles contribute. In fact, all lattice points in a thin annulus of central radius $\sqrt{\lambda}$ must be taken into account.

We have the following theorem, proven jointly with Keating in [9], which computes the fractal exponents associated with a full density subsequence of new eigenvalues in a strong coupling regime. For a range of exponents q, which depends on the coupling strength α associated with the subsequence, we derive an explicit formula for the fractal exponent, which shows how it varies with q, thereby proving multifractality.

Theorem 1. *Let Λ be a sequence of new eigenvalues in a strong coupling regime such that $\alpha(\Lambda) \in (\frac{1}{4}, \frac{1}{2})$. There exists a full-density subsequence $\Lambda' \subset \Lambda$ such that for any q in the range*

$$\frac{1-\log(2)}{2-4\alpha} < q \leq \frac{1}{2-4\alpha} \tag{20}$$

we have the following formula for the fractal exponents associated with the sequence Λ'

$$D_q(\Lambda') = \frac{1}{2\alpha}\left(1-\frac{1}{2q}\right)\log(2). \tag{21}$$

4.3. The ground state regime

Instead of studying a high-frequency regime, where $\lambda \to \infty$, one might as well consider a low-frequency regime, where $\lambda \to 0$. In this regime, there is no relationship expected between the intermediate type of dynamics and the occurrence of multifractality. Rather, multifractality in such regimes is expected to occur for a much wider class of systems.

However, in the case of Šeba billiards, there is a very interesting link with Epstein's zeta function associated with quadratic forms. This link occurs for general tori, not just arithmetic ones. We introduce the following modified version of the shifted zeta function above

$$\zeta^*_\lambda(s) = \sum_{n\in\mathcal{N}} \frac{r_Q(n)}{|n-\lambda|^s}, \qquad \Re(s) > 1, \tag{22}$$

where $\mathcal{N}$ denotes the Laplace spectrum on a general unimodular rectangular tori, given by the set of values taken by the quadratic form $Q(x,y) = a^2x^2 + a^{-2}y^2$; $(x,y)^2$, and $a > 0$. Moreover, r_Q denotes the representation number of Q.

We introduce the modified moment sums $M^*_q(\lambda) = \zeta^*_\lambda(2q)$ for $q > 1$. Note that we need to remove the first term, as this blows up in the limit $\lambda \to 0$. We are, thus, interested in the fluctuations around this blow-up term, which motivates the study of the modified moment sums.

For $q > 1$ we define the fractal exponents

$$\begin{aligned} D^*_q &= \frac{d^*_q - q d^*_1}{q-1}, \\ d^*_q &= \lim_{\lambda\to 0} \zeta^*_\lambda(2q) = \zeta_Q(2q), \end{aligned} \tag{23}$$

where we denote Epstein's zeta function associated with the quadratic form Q as

$$\zeta_Q = \sum_{(m,n)\in\mathbb{Z}^2\setminus\{0\}} Q(m,n)^{-s}, \qquad \Re(s) > 1. \tag{24}$$

We also note that we have the following functional equation

$$\zeta_Q(1-s) = \varphi_Q(s)\zeta_Q(s), \tag{25}$$

where φ_Q denotes a certain meromorphic function associated with Q.

The first prediction of symmetry relations for the fractal exponents of multifractal systems is due to Mirlin, Fyodorov, Mildenberger, and Evers for the case of the Anderson model in [28]. The following symmetry relation was proved in [9].

Theorem 2. *The fractal exponent D_q^* admits an analytic continuation to the full complex plane. It satisfies the following symmetry relation with respect to the critical point $q = 1/4$*

$$D^*_{\frac{1}{2}-q} = \frac{1-q}{\frac{1}{2}+q}\left[D^*_q + \frac{\log\varphi_Q(2q)+(2q-\frac{1}{2})\log\zeta_Q(2)}{1-q}\right]. \tag{26}$$

5. Conlusions

Multifractal scaling is an important property of quantum systems that are intermediate between two physical regimes, and many important systems, such as the Anderson model and pseudo-integrable quantum billiards, fall into this category. However, understanding the rigorous mathematical underpinning of multifractality goes far beyond the study of intermediate quantum systems. In fact, multifractal scaling appears to be related to deep and important mathematical problems in a number of models in mathematical physics. Another highly interesting type of models are nonlinear partial differential equations (PDE), such as the Euler and Navier–Stokes equations, which model the dynamics of incompressible fluids. In this case, it turns out that the occurrence of multifractal scaling is related to the deep and difficult question of the regularity or blow-up of solutions to these nonlinear PDE, which is the subject of a forthcoming article [29].

References

[1] B.L. Altshuler, V.E. Kravtsov, I.V. Lerner, *JEPT Lett.* **43**, 441 (1986).

[2] M. Schreiber, H. Grussbach, *Phys. Rev. Lett.* **67**, 607 (1991).

[3] V.E. Kravtsov, K.A. Muttalib, *Phys. Rev. Lett.* **79**, 1913 (1997).

[4] J. Martin, I. Garcia-Mata, O. Giraud, B. Georgeot, *Phys. Rev. E* **82**, 046206 (2010).

[5] E. Bogomolny, O. Giraud, *Phys. Rev. E* **84**, 036212 (2011).

[6] Y.Y. Atas, E. Bogomolny, *Phys. Rev. E* **86**, 021104 (2012).

[7] A. Bäcker, M. Haque, I.M. Khaymovich, *Phys. Rev. E* **100**, 032117 (2019).

[8] A.M. Bilen, I. Garcia-Mata, B. Georgot, O. Giraud, *Phys. Rev. E* **100**, 032223 (2020).

[9] J.P. Keating, H. Ueberschär, *Comm. Math. Phys.* **389**, 543 (2022).

[10] J.P. Keating, H. Ueberschär, arXiv:2202.13634 (2022).

[11] P.J. Richens, M.V. Berry, *Physica D* **2**, 495 (1981).

[12] J. Marklof, Z. Rudnick, *Geom. Funct. Anal.* **10**, 1554 (2000).

[13] G. Berkolaiko, J.P. Keating, *J. Phys. A* **32**, 7827 (1999).

[14] G. Berkolaiko, E.B. Bogomolny, J.P. Keating, *J. Phys. A* **34**, 335 (2001).

[15] J.P. Keating, J. Marklof, B. Winn, *Comm. Math. Phys.* **241**, 421 (2003).

[16] G. Berkolaiko, J.P. Keating, B. Winn, *Commun. Math. Phys.* **250**, 259 (2004).

[17] P. Seba, *Phys. Rev. Lett.* **64**, 1855 (1990).

[18] Y. Colin de Verdiere, *Comm. Math. Phys.* **102**, 497 (1985).

[19] S. Zelditch, *Duke Math. J.* **55**, 919 (1987).

[20] A.I. Snirelman, *Uspehi Mat. Nauk* **29**, 181 (1974).

[21] P. Gérard, E. Leichtnam, *Duke Math. J.* **71**, 559 (1993).

[22] S. Zelditch, M. Zworski, *Commun. Math. Phys.* **175**, 673 (1996).

[23] Z. Rudnick, P. Sarnak, *Comm. Math. Phys.* **161**, 195 (1994).

[24] E. Lindenstrauss, *Ann. Math.* **163**, 165 (2006).

[25] N. Anantharaman, *Ann. Math.* **168**, 435 (2008).

[26] F. Faure, S. Nonnenmacher, S. de Bievre, *Comm. Math. Phys.* **239**, 449 (2003).

[27] Z. Rudnick, H. Ueberschär, *Ann. Henri Poincaré* **15**, 1 (2014).

[28] D.A. Mirlin, Y. Fyodorov, A. Mildenberg, F. Evers, *Phys. Rev. Lett.* **97**, 046803 (2006).

[29] H. Ueberschär, "Multifractal scaling and Euler's equations on $\mathbb{R}^3/\mathbb{Z}^3$", in preparation.

Subscription terms/Warunki prenumeraty — 2023

Acta Physica Polonica is issued as two separate journals, namely *A* and *B*, in Warszawa and Kraków, respectively. Each of the periodicals is published in the indicated scope and sold by its respective Publisher (see details below). A subscription order should be submitted to the relevant Publisher.

◇ The subscription price of *Acta Physica Polonica A* (*APPA*) is **450 EUR** (surface mail delivery, priority mail on demand with extra **90 EUR** postage rate).

The Publisher of *Acta Physica Polonica A*:

The Director of Institute of Physics
Polish Academy of Sciences
al. Lotników 32/46
02-668 Warsaw, Poland
e-mail: appol@ifpan.edu.pl

bank account BGK S.A. Warszawa:
PL 35 1130 1017 0013 4373 9820 0027
(int. bank code SWIFT: GOSKPLPW)

The archival *APPA* issues (if still available) can be purchased at the Editorial Board of *APPA*.

◇ Cena prenumeraty rocznej *Acta Physica Polonica A* wynosi **2100 PLN** (netto).

Prenumeratę przyjmuje Wydawca:

Dyrektor Instytutu Fizyki
Polskiej Akademii Nauk
al. Lotników 32/46
02-668 Warszawa, Polska
e-mail: appol@ifpan.edu.pl

konto bankowe BGK S.A. Warszawa:
89 1130 1017 0013 4373 9820 0025

◇ The subscription price of *Acta Physica Polonica B* can be obtained by contacting its Publisher:

Institute of Physics
Jagiellonian University
Łojasiewicza 11
30-348 Kraków, Poland
e-mail: acta.phys.pol.b@uj.edu.pl

ACTA PHYSICA POLONICA A
Volume 144 — Number 6

Proceedings of the 11th Workshop on Quantum Chaos and Localisation Phenomena (CHAOS 23), Warsaw, Poland, May 25–26, 2023, Online Conference